# Production and Characterization of Three-Dimensional, Cellular, Metal-Filled Ceramics

Duncan Cree

A Thesis
In the Department
of
Mechanical and Industrial Engineering

Presented in Partial Fulfillment of the Requirements
For the Degree of Doctor of Philosophy (Mechanical Engineering) at
Concordia University
Montreal, Quebec, Canada

September 2009

*Your file Votre référence*
*ISBN:* 978-0-494-63360-1
*Our file Notre référence*
*ISBN:* 978-0-494-63360-1

## ABSTRACT

**Production and Characterization of Three-Dimensional, Cellular, Metal-Filled Ceramics**

Duncan Cree, Ph.D.
Concordia University, 2009

This research focuses on the infiltration of two porous structures. In the first, two different silicon sources were used to infiltrate structures derived from different Canadian pine, beech and maple species for the production of silicon carbide (SiC). This allows the use of a precursor structure that is already available, thus saving time, energy and cost of manufacturing. Carbonized wood species measuring 15 mm x 11 mm x 13 mm were used as precursors for the production of silicon carbide (SiC) using two silicon sources (sol and powder) in order to produce a porous SiC structure mimicking that of wood. The liquid sol was vacuum infiltrated into the pyrolyzed wood species, dried and reacted at 1575 °C under a 70 L/h flow of argon. Scanning electron microscopy (SEM) showed SiC grains formed on the interior of the tracheid walls and a high density of SiC whiskers were discovered in certain tracheids of pine and vessels of beech and maple. Both cyclic and repeated infiltration processes were undertaken. In addition, infiltration of carbonized pine wood with molten silicon was carried out in order to obtain a porous SiC structure. Infiltration was based on capillary forces within the preform and the infiltration depth was measured. Optical microscope, SEM, EDS and XRD were used for microstructure characterization and phase identification.

In the second part of this work, a liquid A356 aluminum alloy was infiltrated into a porous silicon carbide foam structure. Three dimensional silicon carbide (SiC) ceramic foams were employed as reinforcement for producing an aluminum alloy metal matrix

composite with potential as a base plate material in electronic packaging. These are commonly manufactured with aluminum/silicon carbide (Al/SiC) particulate materials, nickel-iron and copper alloys. A base plate provides mechanical strength to the integrated circuit design, as well as aids in transfering the heat from the chip to the heat sink. Packaging base plate materials are required to have low coefficient of thermal expansion (CTE), high thermal conductivity, and low density. A356 aluminum alloy was vacuum infiltrated into a 100 PPI (pores per inch), silicon carbide (SiC) foam network, at 775°C using an in-house built apparatus. It has been shown that this metal matrix composite has similar properties to traditional packaging materials with the added benefit of a lower density. CTE and thermal conductivity are within the range of commercially available materials, with porosity levels of 7%, using this method. Flexural strength and Young's modulus of the composite provide reasonable values as a result of the low reinforcement concentration employed. Secondary Electron Microscopy (SEM) was used to investigate the fractured surfaces of the Charpy, flexural strength and compression tests. In the Charpy and flexural strength samples, the A356 aluminum-silicon alloy matrix shows signs of mixed fracture; cleavage regions and some dimpling. In the network structure, the majority of the failure is from SiC layers debonding from the aluminum matrix with some SiC layer peeling (inter-delamination). Compressive loading showed internal damage in the form of failed SiC struts. X-ray Diffraction (XRD) analysis did not detect any brittle aluminum carbide at the Al/SiC interface. The Rule of Mixtures (ROM) is used for a first rough estimate of certain mechanical and thermal properties.

# DEDICATION

Dedicated to my late father

## ACKNOWLEDGEMENTS

I would like to thank my advisor, Dr. Martin Pugh for his support and advice during my graduate research studies. I am grateful to him, for allowing me to work autonomously while offering guidance when required. Above all, I would like to thank him for providing me an opportunity to work on my doctoral thesis with him.

I would like to thank the administrative staff who were very helpful and always cheerful; Sophie Merineau, Sabrina Poirier and Arlene Zimmerman. Also Robert Oliver for his technical assistance with the Instron, MTS and other valuable suggestions during manufacturing of the composites. Heng Wang for his assistance with thermal analysis and nano-indentation measurements.

I would like to acknowledge NSERC (Natural Science and Engineering Council of Canada) for support of this research. I would like to thank Alcan Inc. for their kind donation of the aluminum ingot and Louise Pelletier from the University of Montreal for donating the microtome.

I would like to acknowledge Robin A.L. Drew's Ceramics and Materials group from the Department of Mining and Materials Engineering at McGill University. They were all very helpful in providing assistance operating various equipment and made me feel as I was part of their group. Moreover, I would like to thank Helen Campbell for her support and interpretation of the scanning electron microscopy results as well as Paula Mercedes Proa Flores for her assistance in demonstrating the preparation techniques and chemical solutions for nickel coating.

Thanks to my office mates for their support and friendship. I will always remember the laughter and good times we had together.

**Table of Contents**

## List of Figures

## List of Tables

## List of Acronyms

**Abbreviations**

A356 Aluminum alloy

$Al_4C_3$ Aluminum carbide

AlN Aluminum nitride

$Al_2O_3$ alumina

C Carbon

CO Carbon monoxide

$CO_2$ Carbon dioxide

CVD Chemical vapor deposition

CVI Chemical vapor infiltration

CCA Chromate copper arsenate

CTE Coefficient of thermal expansion

Cu Copper

DSC Differential scanning calorimeter

EDS or EDX Energy Dispersive X-Ray Spectroscopy

GaAs Gallium arsenide

HS Hashin-Shtrikman bounds

IC Integrated circuits

ID Inner diameter

IPC Interpenetrating phase composite

LOM Laminated object manufacturing

MMC Metal matrix composite

Mo Molybdenum

Ni Nickel

OD Outer diameter

PPI Pores per linear inch

RBSC Reaction-bonded silicon carbide

ROM Rule of Mixtures

SEM Scanning electron microscope

Si Silicon

SiC Silicon carbide

SiO Silicon monoxide

$SiO_2$ Levasil 50 silica sol

TEOS Tetraethyl-orthosilicate sol

3-D Three-dimensional

2-D Two dimensional

TMA Thermo-mechanical analyzer

W Tungsten

XRD X-ray diffraction

**List of Symbols**

$\alpha$ Thermal diffusivity

$\alpha_c$ Composite CTE

$\alpha_m$ Matrix CTE

$\alpha_r$ Fiber/reinforcement CTE

c Composite

$C_p$ Specific heat capacity

D Dry weight

$\rho$ Density of melt

$\rho_{bulk}$ Bulk density

$\rho_{comp}$ Al/SiC composite density

$\rho_{theo}$ Theoretical density

$\rho_{SiC}$ Theoretical CVD SiC density

$\rho_c$ Theoretical vitreous carbon density

$\rho_{theo.\ strut}$ Two phase theoretical strut solid density

E Young elastic modulus of composite

$E_{c3}$ Three-phase composite modulus

$E_{cp}$ Composite modulus with porosity

$E_c^L$ Transverse or lower limit composite modulus

$E_m$ Young modulus of the matrix

$E_o$ Young's modulus of the solid material

$E_r$ Young modulus of the reinforcement

$E_c^U$ Longitudinal or upper limit composite modulus

G Bulk shear modulus

$G_c^L$ Lower bound bulk shear modulus

Gm Bulk shear modulus of matrix

Gr Bulk shear modulus of reinforcement

$G_c^U$ Upper bound for bulk shear modulus

h Infiltration depth

k The thermal conductivity

K Bulk modulus

$K_c^L$ Lower bound for the bulk modulus

$K_m$ Bulk modulus of matrix

$K_r$ Bulk modulus of reinforcement

$K_c^U$ Upper bound for the bulk modulus

m Matrix

P Porosity volume fraction of the composite

$P_{atm}$ Atmospheric pressure

$P_{closed}$ Closed porosity

$P_{open}$ Open porosity

$P_{total}$ Total porosity

$P_{vac}$ Vacuum pressure

r Reinforcement

$\theta$ Contact (or wetting) angle

$\gamma$ Surface tension

$\gamma_{sv}$ Surface tension of the solid-vapor interface

$\gamma_{sl}$ Surface tension of the liquid-solid interface

$\gamma_{lv}$ Surface tension of the liquid-vapor interface

V Volume fraction of each phase

$V_c$ Volume fraction of carbon

$V_m$ Matrix volume fraction

$V_r$ Fiber volume fraction

$V_{SiC}$ Volume fraction of SiC

# Chapter 1 Introduction

Examples of infiltrated cellular structures date back millions of years to the production of petrified wood. During the petrification process, water with various minerals, enters the wood and fills the hollow three dimensional organic structures. Over time and under a certain temperature and pressure, the initial wood transforms to a more rigid, stronger structure. In a similar approach, this research focuses on the infiltration of a porous pyrolyzed wood structure with two different silicon sources to form a SiC network structure, as well as liquid A356 aluminum alloy (Al) infiltration into a porous silicon carbide (SiC) foam structure.

## 1.1 Background

Maintaining the principle of petrified wood, the goal of this research initially focused on the production of a porous SiC structure mimicking that of wood following the work of other authors for subsequent infiltration, e.g. to form an aluminum metal matrix composite (MMC). The motivating aspect for this research was to use an initial structure that is already available; it does not have to be manufactured. In addition, there are significant advantages of using an ecological, renewable resource to produce a range of multi-purpose composite materials with much needed properties for lightweight applications in the transportation industry.

Following a similar line of investigation, manufactured three-dimensional (3-D) SiC ceramic foams were also employed as a 3-D network reinforcement for producing an aluminum alloy A356 MMC. Foams have the advantage of being lightweight due to their

high porosity and in many cases they are made of low density materials. They are commercially available with different porosities, thus the amount of reinforcement can be tailored to a particular engineering application. In addition, the two inter-connecting phases in this composite become synergetic to one another. The aluminum phase may improve mechanical properties, for example ductility, while the silicon carbide phase may reduce the coefficient of thermal expansion (CTE) of the composite.

### 1.2 Motivation

In this research, an aluminum MMC is created with an aluminum alloy for the matrix and a SiC as the reinforcement. Aluminum alloys are preferred for their low-density, age-hardening capabilities and reasonably low melting points for easy manufacturing. The role of SiC is to provide increased strength, modulus, and wear resistance in addition to lowering the thermal expansion of the composite, in order to reduce the risk of thermal stresses on electronic packaging components. Conventional SiC ceramic reinforcements are in the form of discontinuous particles, whiskers and short fibers, or continuous fibers, whereas interpenetrating phase composites (IPCs) are much less common. The latter, once infiltrated with a second phase, transforms into a composite where two distinct, continuous, three-dimensional network structures are formed.

Developing low density composites for use in the transportation industry, specifically in the electronic sector, has a great advantage over monolithic metals and alloys. The advantage of MMCs is their high strength-to-weight and stiffness-to-weight ratio for use in lightweight applications. Moreover, three-dimensional infiltrated structures are said to have good mechanical properties. For example, Raj et al. [1] found

that the toughness of ceramics can be increased by the addition of a ductile metal. They also established that a higher toughness is possessed by a composite where both the metal and ceramic phases form a continuous network as opposed to having the same metal phase volume of discrete, isolated particles distributed in the composite. Analogous to Raj et al., other authors [2] have stated similar findings. To obtain improved mechanical properties, discrete particles of ceramic reinforcement must be homogeneously distributed throughout the matrix, otherwise clusters of ceramic particles (which can form during production of particulate MMCs) can be sources of fracture which are not inherent in continuous ceramic networks in which uniform distribution of reinforcing phase is guaranteed.

It is well known that designers use materials based on standardized, statistically-based, material property data, however this data is not entirely available for MMC's in the composite industry [3]. For this reason, their use has been limited, thus keeping this technology from maturing into large commercial applications. This research anticipates the addition to the pool of knowledge in the composite field. With this addition, MMCs could be applied in a wider range of commercial contexts such as: automotive, aeronautics, space.

### 1.3 Objective

The focus of this research was to gain knowledge of these new materials through a fabrication process and materials characterization. The SiC structure mimicking that of wood was evaluated for its ability to provide porous structure while the MMC will be evaluated for its compression strength, bend strength, impact behavior, thermal

conductivity and coefficient of thermal expansion, as well as compositional and morphological properties. Various common models for predicting Young's modulus, Young's modulus with porosity, thermal conductivity and CTE will be compared against the experimental results. In addition, the results will be compared with commercial as well as literature results of Al/SiC materials employed in the electronic packaging industry.

This new A356/SiC foam composite material will reveal its applicability in the electronic packaging industry, specifically in heat sink/base plate designs. Electronic packaging refers to the overall sealing of integrated circuits (IC) or small electronic circuits sometimes called microchips, in order to protect them against adverse environments. They are found in all electronic equipment such as cell phones, computers, space/satellites and aerospace applications and many other devices. When these circuits are sealed they require a means of heat dissipation. Furthermore, as miniaturization and higher power electronic equipment develops, better cooling systems will be required which in turn requires better packaging materials.

In most electronic packaging designs, the microchip is soldered on top of a ceramic substrate which acts to electrically insulate the chip from the base plate and heat sink. The substrate is soldered to the base plate which provides mechanical strength to the design as well as aids in distributing the heat from the chip to the heat sink. Figure 1.1 illustrates a schematic of an electronic packaging unit. A problem arises due to the thermal expansion mis-match between the chip and the ceramic substrate, the ceramic substrate and the base plate as well as the base plate and the heat sink. Each of these layers have a different CTE (silicon ~4 ppm/°C, ceramics ~4-8 ppm/°C and metal base

plate/heat sink (packaging unit) ~17-24 ppm/°C) therefore, they expand or contract at different rates [4]. Low CTE values provide a stable, more precise material. In packaging, the IC in contact with a substrate and the substrate in contact with the base plate must have matching, or close, CTEs. Otherwise thermal stresses can be induced between the mating parts during fabrication and service, causing failure of the solder or the electronic system. Substrates should be matched to the chip material most commonly used, which is silicon (Si) or gallium arsenide (GaAs); CTE's of 4.2 ppm/°C and 6.5 ppm/°C [5], respectively. Table 1.1 provides a comparison of Al/SiC composites and other electronic packaging material properties, taken from Occhionero et al. [4].

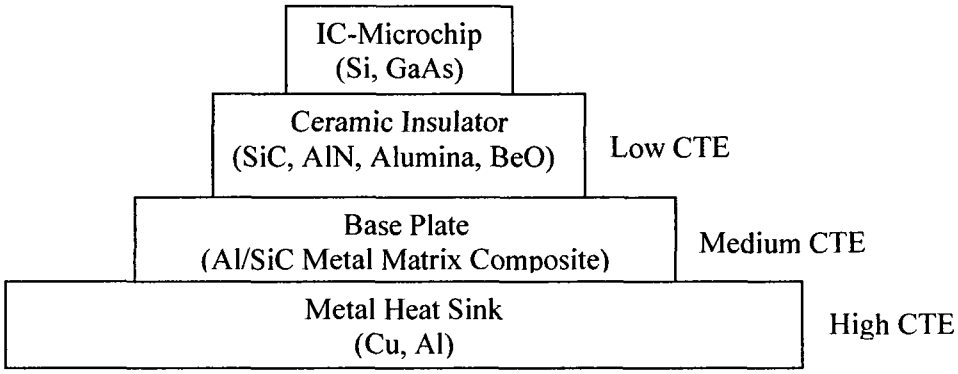


Figure 1.1 Schematic of electronic packaging unit

Packaging materials are required to have: low CTE, high thermal conductivity, low cost, low density and reasonable intermediate mechanical properties. Therefore, producing a new MMC with these properties is an excellent motivation for research. Presently, Kovar (Ni-Fe based alloy), copper and tungsten (Cu-W), copper and molybdenum (Cu-Mo), Cu and Al are used in packaging, base plates and heat sinks [5]. As shown in Table 1.1, the IC materials and the ceramic substrates have matching CTEs;

however, the Cu and Al have much greater CTE values. The Ni-Fe alloy has a matching CTE but has a low thermal conductivity, with a rather high density (weight problem). The Cu-W and Cu-Mo have similar CTEs to the ceramic substrates and thermal conductivities within the desired range, but have relatively high densities which are undesirable for lightweight applications. As a result, much research has been ongoing into the development of Al/SiC materials for they have a low CTE, high thermal conductivity and low density. The majority of SiC utilized for electronic packaging is in the form of discrete particles in an aluminum alloy matrix. However, Elomari et al. [6] found some benefits by bonding SiC particles together to create an Al/SiC composite with a low CTE, rather than dispersed particles. The internal connectivity of the SiC foam struts in this research may prove to have even better results since the struts are one piece, rather than joined particles.

Table 1.1 Conventional electronic packaging material properties [4]

| Material | Material Function | Density ($g/cm^3$) | CTE (ppm/ °C) | Thermal Conductivity (W/m K) |
|---|---|---|---|---|
| Si | IC | 2.3 | 4.2 | 140 |
| GaAs | IC | 5.23 | 6.5 | 54 |
| SiC | Ceramic Substrate | 3.2 | 4.7 | 200-270 |
| AlN | Ceramic Substrate | 3.25 | 4.4 | 180 |
| Alumina | Ceramic Substrate | 3.98 | 6.5 | 20-30 |
| BeO | Ceramic Substrate | 2.9 | 8.0 | 270 |
| AlSiC-7 (Al-Proprietary alloy/>63% SiC) | Packaging | 3.0 | 6.9 | 150 |
| AlSiC-10 (A356/55% SiC) | Packaging | 3.0 | 9.89 | 165 |
| Al-Mg-15%Si/ 54% SiC | Packaging | --- | 9.2 | 166 |
| Al-Mg-15%Si/ 51% SiC | Packaging | --- | 9.4 | 171 |
| Kovar (Fe-29Ni-17Co) | Packaging | 8.4 | 5.9 | 15 |
| Cu-W (10-20% Cu) | Packaging | 15.7-17.0 | 6.5-8.3 | 180-200 |
| Cu-Mo (15-20% Mo) | Packaging | 10.0 | 7-8 | 160-170 |
| Cu | Packaging (heat sink) | 8.9 | 16.6 | 398 |
| Al | Packaging (heat sink) | 2.7 | 23.9 | 205 |

# Chapter 2 Literature Review

## 2.1 Introduction

The reinforcement material employed in this research is in the form of hollow, three-dimensional (3-D) cellular networks. Prior to the discussion of wood and ceramic cells, cellular solid materials are evaluated. The literature review is put together in two parts. The first part provides a short review of the studies conducted in bio-materials, but its principal focus is on the utilization of wood from trees as a precursor to make porous silicon carbide ceramics and further produce an aluminum metal matrix composite. Maintaining the idea of a porous ceramic structure such as the previously mentioned carbonized wood structures, the second part offers a review of experimental techniques attempted and the preferred procedure chosen for combining an aluminum alloy with ceramic foam. A characterization of the Al/SiC composites is done through mechanical and thermal property analysis. These novel materials have two distinct phases and when combined together form two interpenetrating networks; one of aluminum alloy and the other, a ceramic foam. An introduction to Interpenetrating Phase Composites (IPCs) is followed by the latest developments for infiltrating/producing IPCs.

## 2.2 Cellular Structures

Cellular structured materials are available from nature as; wood, bone, sponge, honeycomb structure of a beehive and coral. Through evolution, nature evolved efficient, lightweight load bearing structures, which act to minimize material and maximize strength and stiffness. Inspired by mother-nature, artificial or man-made cellular structures have been copied or closely replicated from natural cellular structures. For a

material that is not 100% solid, opened, closed or both types of pores can exist. Open pores are interconnected within the sample and connected to the surface of the sample, while closed pores are isolated from the surface. To further infiltrate with a light metal, foam with open pores are required.

Cellular structures can be categorized as two dimensional (2-D) or three dimensional (3-D) cellular structures. In 2-D, the majority of the cells are connected in one direction, while 3-D the cells are interconnected in three directions. 2-D honeycomb structures have anisotropic properties indicating the material has different properties in two directions. Generally, wood is orthotropic, that is, its longitudinal properties are different than its transverse or radial properties, however, the transverse and radial tend to have similar properties. In contrast, 3-D structures such as foams, coral, and sponge have isotropic properties indicating the material has the same properties in all three directions.

The mechanical properties of cellular structures are dependent upon relative density, cell shape, cell size and loading state. However, the mechanical properties of the cellular solids depend on its relative density ($\rho^*$);

$$(\rho^*) = \rho/\rho_s \tag{2.1}$$

Where, $\rho$ is the bulk density of the cellular structure, and $\rho_s$ is the density of the fully dense material. As the relative density increases, the cell struts become thicker or more numerous allowing increased load carrying capability. Elastic, plastic and brittle cellular structures produce a similar behavior in compression as the compressive stress-strain curve shown in Figure 2.1. Three regions can be identified: linear elastic, cellular collapse (plateau), and densification. During the linear elastic process the cell wall bends linearly. As the stress level increases, the cell walls yield plastically in bending, which

starts a nonlinear cellular collapse, and continues to deform at a constant stress and increasing strain level where a plateau forms. More and more of the cell walls collapse as the stress is further increased, where densification arises (cellular material begins to act as a solid) and is characterized by a rapid increase in stress [7].

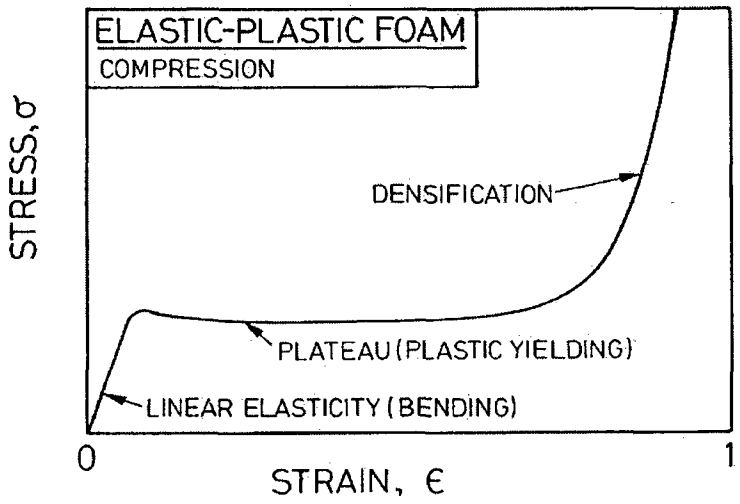


Figure 2.1 Compressive in-plane behavior of an elastic-plastic foam [7]

### 2.2.1 Wood Pore Distribution (Natural)

Trees are classified into softwoods (evergreen or conifers) and hardwoods (deciduous or broad-leaved). Depending on the distribution of vessels or pores in a growth ring, hardwoods are classified as ring-porous, diffuse porous and semi-ring porous whereas softwoods are referred to as non-porous wood since they do not contain vessels. In a ring porous structure, for the same growth ring, earlywood has larger diameter vessels than does the late wood. Diffuse porous woods have a uniform vessel diameter across the growth ring. Semi-ring porous falls between ring and diffuse porous structures. In this arrangement, the vessel diameters have a gradual change from earlywood to latewood. In

softwood such as white pine, the pore distribution is more uniform than hardwoods making it a better material for obtaining more homogeneous mechanical properties within a given direction [8].

Different tree species will have different porous morphologies; as a result extensive varieties of microstructures can be obtained based on the type of wood selected. Natural structures such as wood species are readily available which have the advantage of eliminating a manufacturing step. As will be covered in the review of bio-materials, some research has been done to make use of the hollow cells within certain wood species and are further developed into ceramics. However, a large amount of work is still required as there are approximately 100,000 species of trees in the world [9]. New microstructures for wood-based engineering materials are awaiting discovery.

### 2.2.2 Artificial Ceramic Foam

Various ceramic foam manufacturing routes for different ceramic materials have been reviewed recently [10]. In the second part of this work, open-celled SiC foam was employed as the reinforcement, therefore, the various production techniques are assessed for their feasibility. Manufacturing of SiC open-celled foam can be categorized into three broad groups; foam replication, sacrificial template method and foaming method.

The replication technique can use polymer sponge or polymer foam for the initial porous structure. Once the sponge or foam is coated with the slurry or solution, it is dried and further pyrolyzed in air for the reaction/formation of the ceramic material. A sintering step is used to densify the SiC ceramic struts of the final porous structure. An experiment with ceramic slurry containing a mixture of silicon carbide powder and silica

sol was performed [11]. It was shown that after drying, a second coating of slurry can be applied, but acts to decrease the cell size of the foam. The cell size diameter with one coating was 3.2 mm (3200 μm) with a porosity of 89%. This method is known to cause micro-cracking of the thin strut network structures during pyrolysis. In addition, during the pyrolysis treatment the polymer is deliberately burnt away leaving a hollow strut center, thus reducing the strength of the SiC foam. Using a related preparation technique, a porous polymer preform was infiltrated with a polymeric polysilane SiC precursor solution by dissolving a polymer in a solvent and further pyrolyzed in a nitrogen atmosphere [12]. The polymer solution results in a more homogeneous, dense, pore free strut, but a number of cell windows are covered with a thin ceramic covering. The cell windows range in size from 200-500 μm while the porosity range for this type of foam is between 86-89%.

Similarly, chemical vapor infiltration (CVI)/chemical vapor deposition (CVD), is used to produce a SiC foam [13]. The fabrication technique first involves producing a vitreous carbon foam from pyrolysis of a foamed thermosetting polymer. The SiC foam is made by depositing thin films in the order of 10 to 1000 μm SiC onto the carbon foam using a thermal pyrolysis of methyl-trichlorosilane (MTS), which provides both the silicon and carbon for the SiC layer. The deposition of a solid thin SiC ceramic coating from a gas, is done by both CVI and CVD where CVI process involves deposition on the surface, but inside a porous body while CVD deposit is on surface of a non porous body. This produces a 100% dense, very pure SiC coating for which the strength and density are higher than slurry cast materials. Porosity for this type of foam ranges between 70-

97% and the cell diameters can be between 3-100 pores per linear inch (PPI) (1 inch = 25.4 mm) or average cell diameters of 8500 μm to 254 μm, respectively [13].

The sacrificial template method uses solid fillers that decompose during a heat treatment leaving behind a porous structure. In one method [14], polymer (polymethyl methacrylate) micro-beads of ~20 μm diameter are used as the sacrificial template. Polymer (polysiloxane), phenol resin and micro-beads are mixed thoroughly and pressed into disks. A pyrolysis heat treatment in nitrogen coverts the polymer resin (polysiloxane) to a ceramic (silicon oxycarbide (SiOC)), and the phenol resin to carbon (C). The compact is brought to a high temperature where the reaction between SiOC and C take place to produce SiC. This method produces open cells with dense struts. By adjusting the micro-bead content, porosity ranged between 60 to 95% with cell diameters of 20 μm and smaller. In another method [15], sodium chloride salt was pressed into disks and sintered. The porous compacts were pressure infiltrated with polycarbosilane (PCS). At a temperature of 190°C, in air, the PCS cross-links from the reaction with oxygen (oxidative curing) to transform from a thermoplastic to a thermoset. At a higher pyrolyzation temperature of 1100°C, with argon flow, the PCS thermoset transforms to a 60% porous SiC foam with cell diameters ranging between 10 μm and 100 μm.

The direct foaming method uses a foaming agent for the generation of bubbles in ceramic slurry to produce the foamed material. Porous SiC foams were produced by the foaming method [16]. The SiC ceramic slurry, foaming agent and gelling agent (helps harden or set the porous foam structure) are mixed thoroughly and heated to 70°C. The mixture is poured into a mold to cool and solidify followed by drying and sintering at

25°C and 2120°C, respectively. Porosity ranged from 74% to 88% by varying the amount of gelling agent, while pore diameters of 45 μm to 600 μm were observed.

In conclusion, the slurry replication method, produces thin hollow struts with micro-cracks, not favorable for loading conditions. The polymer precursor solution creates dense struts, but many of the cells are blocked by a thin ceramic membrane which could complicate further light metal infiltration. The SiC foam employed in this research was from the CVI/CVD method, based on the fact that is has good strength, dense struts, the SiC coating is in a pure form and the porosity is available in a variety of pore diameters. Foams produced from the replication method can be easily obtained from a variety of manufacturers while the sacrificial and direct foaming methods are more in the research stage.

## 2.2 Introduction to Wood Morphology

Depending on the species of tree, softwood or hardwood cells come in the form of tracheids, fibers and vessels. In non-tropical regions where there are seasons, at the microscopic level, trees produce earlywood consisting of thin-walled, large diameter cells in the spring and latewood; thicker-walled, smaller diameter cells at the end of the summer. One year's growth is comprised of a section of earlywood and latewood. In addition, two regions can be identified in the cross section of a tree; sapwood is the outer, light-colored wood while heartwood is the darker center of the wood. Over a period of time, as the tree ages the sapwood becomes heartwood.

At the microscopic level, softwood tracheids are hexagonal to rectangular in shape and are the principal cells. In hardwoods, fibers and vessels have a circular profile

and dominate. Universally, these cells are short in length, with a hollow center and tapered closed ends. When positioned one above the other, they form conducting channels. Both softwoods and hardwoods have their longitudinal and horizontal cells connected through pits of varying types. Tracheids are connected by tapered closed ends, where many more pits are concentrated in this area than throughout its length. Typical circular pits are termed, "bordered pits" which have a rounded membrane sitting in its center that acts as a valve, providing pathways for liquid flow between neighboring cells in the living tree as shown in Figure 2.2.

When a differential pressure occurs between two neighboring cells, a halt or activation of liquid flow occurs through the pit by moving the membrane over the pit aperture, effectively closing off the nutrients. In softwoods, the earlywood membrane consists of a non porous torus surrounded by a porous margo which consists of open spaces between supporting strands connecting the torus and allowing access of particles up to 1 μm [17].

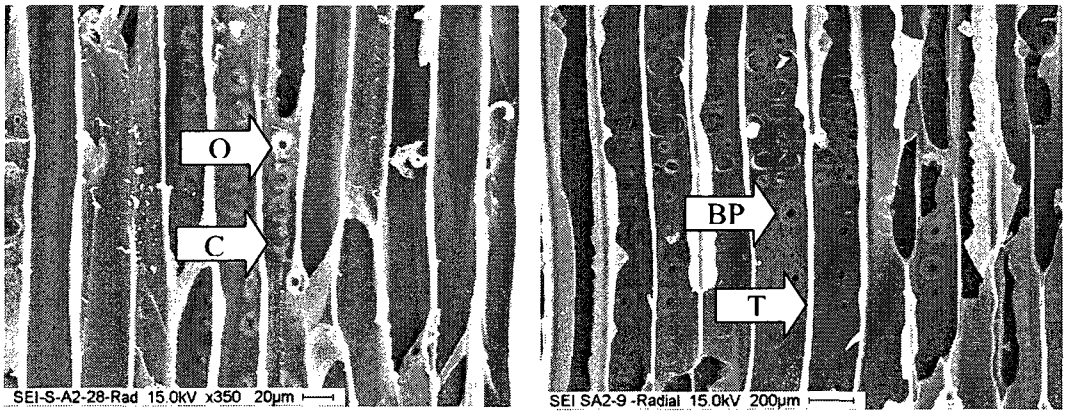


(a) Dry pine wood (b) Carbonized pine wood

Figure 2.2 SEM of: (a) dry and (b) carbonized pine wood showing interconnecting passageways (O-Open pits, C-closed pits, BP-Bordered pit with torus, T-Tracheid wall)

However, as the wood ages, as in latewood, the margo becomes denser until no spaces between the strands are visible. Pit membranes of bordered pits of hardwoods are uniformly micro-porous with nanometer size pores. Similarly, in simple and half-bordered pits of softwoods and hardwoods no torus exists, but simply a membrane. Essential to understanding complete infiltration/penetration into a wood species are the possibility of closed pits (termed 'pit aspirations') occurring due to drying or during transformation from sapwood to heartwood where the torus or membrane seals one of the pit apertures and becomes undistinguishable from the walls of the wood cells.

Permeability is a variable property from specie to specie. A study was conducted on fresh, green softwood Norway Spruce having a naturally high degree of pit aspiration, whereby it was impregnated with linseed oil. It was shown that latewood cells were always filled with oil, but earlywood cells were not completely filled. Furthermore, in some areas, the oil appeared to stop after the last latewood cell in an annual ring as if at a distinct barrier [18]. In another study, it was reported that in softwoods, both air-dried and kiln oven-dried wood, the earlywood bordered pits were all closed, while latewood bordered pits membranes were not aspirated. This is explained by latewood cells being more rigid, thicker celled wall structures so that the surface tension of the sap-air interface during drying is insufficient to seal closed the pit membrane. Hence, latewood is more permeable than earlywood. Applying a heat treatment to dry the wood also affects its permeability. An experiment was conducted where the wood species were heated at different temperatures. It was found that the higher the heat-treatment temperature, the lower the moisture content was observed for pine and spruce exposed to a water absorption test. Pit aspiration in heartwood was found to be an irreversible process,

however in sapwood it is partially reversible, by re-soaking it in water [19]. This statement implies that not all the pits become aspirated since water permeability would not be possible. Exposing air or kiln dried wood to water for a period of time will accumulate water in the wood cells. Absorption of water by either immersion or from moisture in the air is introduced by capillary attraction/forces through the end pores of the wood grains relatively quickly as compared by diffusion through the cell walls. Another reason for water intake of wood is due to its composition. Wood is composed on a dry weight basis of 41-55% cellulose in both softwoods and hardwoods, while lignin makes up 24-33% of softwoods and 19-28% of hardwoods. Hemicellulose forms 23-30% of both softwoods and hardwoods. Swelling is caused by the uptake of moisture or water due to the hydrophilic nature of cellulose and hemicellulose in the cell walls, while the lignin is hydrophobic [20].

Due to pit aspiration, it is difficult to impregnate preservative solutions in wood with aspirated pits. Similar to sap movement in a live tree, wood preservatives use the same passageways in a dead or fallen tree, but with some restriction to aspirated and extractive clogged pits. The topic of this research is linked to the infiltration of wood with preservative solutions since both the silica sol and liquid silicon methods involve filling the wood cells longitudinally and tangentially to produce the SiC structure. When adding preservatives to the wood, sapwood is more easily impregnated with preservatives than heartwood for both softwoods and hardwoods. It was concluded that heartwood has a larger number of closed/aspirated pits. In addition to closure of pit membranes during cutting (felling) or the maturing process of heartwood, extractives or tyloses deposits in the cell walls and cell lumens, obstruct liquid flow [21]. In commercial preservative-

treated wood, the greatest depth possible, even with applied pressure is generally 10 mm. By experience, sectioning a pressure treated plank, the middle is never fully infiltrated.

The purpose of this work is to produce a continuous, porous, SiC ceramic network structure from different wood species by infiltrating the carbonized wood with liquid sol or silicon, followed by a high temperature reaction between the silicon and the carbon to form SiC. The results herein show that it is not possible to obtain a 100% SiC porous structure using either method. In the present study large carbon samples measuring 15 mm x 11 mm x 13 mm (axial, radial, and tangential) were used. Though infiltration was achievable, reproducing the results of other workers [43, 49, 52] in this field was not: this may be due to the sample size studied, the thickness of the specimens or the particular structure of the northern species used which has narrower growth rings than southern grown species.

### 2.3 Background of Bio-Materials

A new class of ceramics produced from biological plant materials has been studied for the past forty years, allowing scientists from all over the world to contribute to this new technology. It has prompted increasing interest in the past decade since the raw materials used to make these ceramics are renewable and cheap, whereas present precursors to high-temperature ceramics use more expensive, non-renewable, petroleum-based products as their starting material. Since the 1970's, researchers [22-33] have been investigating the use of bio-materials to produce ceramic engineering materials out of carbon structures using high temperature processes. The resulting carbon can then be used as a starting material to produce ceramics. The description of carbon material and

the thermal decomposition of lignocelluloses materials to yield carbon/charcoal is thoroughly explained in the thesis of Christopher Byrne [22]. In short, any organic plant material contains mostly polymers such as cellulose, hemicelluloses and lignin. These are converted into carbon by decomposing them through a controlled high temperature treatment.

In early experiments, Lee and Cutler [23] were the first to produce silicon carbide whiskers from rice husks. They found that the SiC produced from rice husks has mostly particle sizes of about 0.1 μm with smaller amounts (~10%) of whiskers. Rice husks have a high silicon content and as a result have been experimented with to produce silicon-derived materials such as; silicon carbide, silica, silicon nitride, silicon tetrachloride, pure silicon and zeolite, however only SiC has been industrialized [24]. Since the work of Lee and Cutler, other studies on conversion to SiC have been reported [25] where silicon-containing coconut shells were used to produce SiC whiskers. The majority of the SiC whiskers produced were of needle-type, however the yield was lower than that from rice husks due to their greater amount of silica. Further advancements in the use of bio-materials were made by Hirose et al., [26] who were the first to produce a new carbon material, which they called "wood ceramics". Through the use of wood or wood wastes such as wood powder, (i.e. sawdust and/or woodchips), they impregnated it with a phenolic resin and pyrolyzed it to produce a porous carbon material. Similarly, Hofenauer et al. [27] produced a silicon/silicon carbide ceramic by silicon liquid infiltration of a pressed board made of beech wood powder and phenolic resin mixture. Their results indicate that the microstructure and properties of this wood-based composite are controlled by resin content and bulk density of the wood.

Other investigations using bio-materials such as natural and cellulose fibers were conducted. Patel and Padhi. [28] presented a feasible procedure for producing ceramic fibers from natural fibers. In this experiment, they successfully produced alumina ($Al_2O_3$) fibers by infiltrating jute fibers with an aluminum salt ($Al_2Cl_6 \cdot 12H_2O$) solution. The fibers produced were not smooth and aligned, therefore, optimizing the fiber structure will be performed in future research. Leute and al. [29] produced a Si-SiC ceramic using SiC powder, graphite, an organic binder, solvent and hemp fibers. The mixture was compacted to form a composite preform and infiltrated with liquid silicon. They observed that the carbonized fibers dissolved completely in the molten silicon, thereby producing SiC crystals.

Krishnarao and Mahajan [30] coated cotton (95% cellulose) fibers with a slurry of silicon nitride ($Si_3N_4$) and heat treated them to produce SiC fibers, however the results show the SiC fibers to be fragile with insufficient strength. Ohzawa et al. [31] infiltrated cellulose fibers obtained from filter paper, recycled paper and cotton fiber cloth preforms, with a gas mixture of $SiCl_4$-$CH_4$-$H_2$ by a pressure pulse chemical vapor infiltration (CVI) process to produce permeable SiC. As the number of pulses increased, the results indicated a decrease in porosity and an increase in flexural strength. Sieber et al. [32] infiltrated silicon into carbonized paper sheets (pure cellulose fibers) to produce SiC sheets. Furthermore, these SiC sheets were infiltrated with a pre-ceramic polymer (polymethylsiloxane) and hot pressed together to form a laminate. These ceramic paper structures have a low density, high stiffness along with non-catastrophic fracture behavior and good high temperature stability. Weisensel et al. [33] used cellulose fibers from filter paper to fabricate a Si-SiC ceramic structure. The carbonized paper was coated with

slurry of phenolic resin-based adhesive. Additionally, the coated carbon sheets were assembled to form a multi-layer structure by warm pressing using a Laminated Object Manufacturing (LOM) machine. The LOM samples were then infiltrated with liquid silicon. It was shown that the porosity, density and pore distribution affect the microstructure of the final product, which can be varied by the temperature and pressure of the LOM as well as the composition of the adhesive.

Throughout these research investigations, a great deal of information has been learned about the development of bio-materials and their potential to contribute to significant improvements in new composite materials.

### 2.4 Ceramics Produced from Wood

This section presents a review of related literature in the area of infiltration of wood species to produce silicon-based ceramic composites. At this time, infiltration can be divided into three categories. The first is by liquid silicon infiltration into carbonized wood, the second is by a gas/vapor infiltration into the carbon wood, while the third technique is by a sol/gel infiltration, which can use wood or carbonized wood.

#### 2.4.1 Melt Infiltration Technique

Greil et al. [34, 35] were among the first pioneers to produce silicon carbide-based ceramics by infiltrating different carbonized tree species such as oak, maple, beech, ebony, balsa and pine with liquid silicon. The method was based on the conventional processing of Si-SiC-materials, which uses petroleum-based carbon preforms and infiltration by capillary action [36]. They found that different wood microstructures produce ceramics with different mechanical properties in the axial, radial and tangential

directions. This is said to be dependent upon the morphology and orientation of the cellular structure of the wood. They also measured weight loss, shrinkage, density and porosity of the wood, carbonized wood as well as the silicon-infiltrated carbon wood.

Similarly, other researchers have experimented with different types of wood. Nagle et al. [37] infiltrated carbonized redwood with liquid silicon. They found that the original carbon cell walls were converted to SiC while residual silicon filled some of the hollow cells. Shin et al. [38] produced a reaction-bonded silicon carbide (RBSC) by infiltrating oak charcoal with liquid silicon. They established that the mechanical properties were comparable with commercially available reaction-bonded Si-SiC products. Sieber et al. [39] infiltrated various types of carbonized wood (oak, maple, beech, ebony, balsa and pine) with liquid or gaseous silicon. They concluded that the liquid infiltration method yields SiC composites with some of the residual porosity filled with excess silicon, whereas the gaseous infiltration results in a single phase SiC ceramic with 20-50% open porosity.

Singh [40] infiltrated carbonized Indian mango wood with liquid silicon and found the compression strength in the axial direction to be about four times that of the transverse directions. Testing at elevated temperatures revealed the Si-SiC ceramic maintained high axial strengths up to the melting point of silicon. In another paper, Singh infiltrated carbonized African bubinga, maple and mahogany [41] with liquid silicon. They found the flexural strength to be comparable with a commercially available reaction bonded silicon carbide (Cerastar RB-SiC). Zollfrank et al. [42] showed that liquid silicon melt infiltration into carbonized beech and pinewood produced three different phases: silicon carbide from the reaction with carbon, residual silicon which fills the pores, and

isolated regions of amorphous residual carbon. They found pine to have volume fractions of 60% SiC, 30% Si and 10% C, similarly, beech had 57% SiC, 38% Si and 5% C. They referred to the final material as a Si-SiC-ceramic. Interestingly, Esposito L. et al. [43], used carbon samples measuring 25 mm x 25 mm x 10 mm high to produce a 100 vol.% SiC structure from obece wood using amounts of silicon powder in excess of 27.7 wt.%. Based on this study, it may be possible to produce similar results using pine wood.

### 2.4.2 Gas/Vapor Infiltration Technique

Vogli et al. [44] were among the first research teams to experiment with gas/vapor infiltration of carbonized wood. They analyzed the porosity changes due to the infiltration of carbonized oak with silicon monoxide (SiO) vapor. They concluded that this method for manufacturing SiC ceramics was able to produce open pores with diameters as small as 1μm. In another paper, Vogli et al. [45] infiltrated carbonized pine, oak and rattan with Si and SiO vapor. They found the SiO infiltration yields a material with higher porosity and lower compression strength compared with Si infiltration. Qian et al. [46] produced SiC ceramics by infiltrating carbonized basswood with silicon vapor. They observed the final SiC ceramic to have two phases, SiC was the major phase while a minor phase of free carbon existed. The silicon vapor infiltration cycle took 8 h for the SiC content to increase to 95% as opposed to 1 to 3 h for the infiltration/reaction time of liquid infiltration into the carbonized wood.

### 2.4.3 Sol/Gel Infiltration Technique

The sol/gel infiltration process is performed on wood or carbonized wood and can be infiltrated by either cyclic infiltration or repeated infiltration. During a cyclic infiltration

process, each infiltration/drying step of the carbon specimen is followed by a carbothermal reaction (ceramization) until it is entirely converted to a ceramic [47]. Ceramization is a term employed to describe a high temperature heat treatment to transform the infiltrated carbon/$SiO_2$ preform into a SiC structure. Ota et al. [48] produced SiC ceramic by vacuum infiltrating oak charcoal with neat tetraethyl orthosilicate (TEOS) and hydrolyzing it to form silica ($SiO_2$)-gel. The treatment process of infiltration, hydrolysis and drying steps were repeated one to six times before being heated at an elevated temperature (ceramization) to form SiC ceramic. The carbon content decreased and the SiC increased for each successive processing treatment. However, the final phases were SiC and carbon. A final step was used to burn off the residual carbon, which produced a porous SiC structure. In a similar procedure, Klinger et al. [49] infiltrated different carbonized woods to produce a SiC ceramic using different particle-sized silica sols of $SiO_2$. Their results suggest highly porous ceramics can be produced. Herzog et al. [50] infiltrated wood as well as carbonized beech and pine with different silica sols. Infiltration/drying and ceramization were repeated until the weight percent of $SiO_2$ necessary for full conversion to SiC had been supplied. He observed the differential shrinkage in a single infiltration is difficult to control for the infiltrated wood followed by pyrolysis. This may be explained by the fact that fully infiltrated wood cells shrink less than those that are empty.

The second method is referred to as the repeated infiltration process. The carbon specimen is repeatedly infiltrated with the sol, followed by a drying stage until a sufficient amount for full conversion has accumulated. This is followed by a high temperature ceramization to convert to a ceramic. Vogt et al. [51] performed a single

vacuum infiltration of carbonized beech and pine with a liquid $SiO_2$-sol. After infiltration, the specimens were dried followed by a ceramization to convert them to SiC ceramic. It was found that several infiltration/ceramization steps are required for complete conversion of carbon to SiC. Other researches such as Qian et al., [52] have infiltrated carbonized Tilia amurensis wood to produce a SiC ceramic using a TEOS silica sol. They found that five repeated infiltration cycles produced a porous SiC ceramic.

To conclude the literature review for the infiltration techniques employed to produce wood-based silicon carbide ceramics; the liquid infiltration produces a dense, low porosity, two phase Si-SiC composite, the gas infiltration produces a more porous single-phase SiC composite, but the template thickness is limited to approximately 10 mm thereby limiting the size of the components. The sol/gel approach also produces porous single-phase SiC composites with greater than 10 mm thickness; however it requires repeated infiltration steps.

## 2.5 Introduction to Interpenetrating Composites

In this study, the aluminum metal matrix composite (MMC) is composed of an aluminum alloy for the matrix phase and a silicon carbide (SiC) ceramic as the reinforcement phase. Conventional SiC ceramic reinforcements are discontinuous particles, whiskers and short fibers, or continuous reinforcements such as fibers or, less familiar, as interpenetrating phase composites (IPCs). The latter, once infiltrated with a second phase, transforms into a composite where two distinct, continuous, three-dimensional network structures are formed. One is the reinforcement and the other is the matrix. Different authors use a variety of acronyms for describing a 3-D network with two distinct interconnected phases such as; "C4" (co-continuous ceramic composite), "3-3 composites" because both phases

have connectivity in three dimensions, and "3-DNRMMCs" (metal matrix composites reinforced by three dimensional (3-D) network structure). Research interest is growing in producing and testing these IPC ceramic/metal structures [53-60]. However, there is a lack of data in this field regarding an aluminum alloy/SiC foam infiltration and its composite mechanical and thermal property measurements have not been attempted to date as far as the author is aware. Distinct, unique properties may prove rewarding.

### 2.5.1 Natural Three Dimensional Ceramic Foam Replication

Nature has developed biological ceramics with diverse pore sizes, shape and strut thicknesses. Moreover, a vast supply of three-dimensional ceramic networks is available in the environment. Similar to information presented in the first part of this literature review, bio-materials grown in nature are also available as ceramic-forming skeletal organisms. They possess high volume fractions, high fracture toughness, compressive strength and anisotropy [61]. These ceramic structures are composed of calcite, a crystalline form of calcium carbonate of which they are made from, which has been found to be easily dissolved with acid solutions. It was discovered that replicating these remarkable configurations and changing their composition with a better material is in our best engineering interest. One example of nature's three-dimensional structures that has been replicated to produce man-made porous structures, emanates from the coral reef. White et al. [62] developed a process called "replamineform" in which they were successful in producing the exact copy of an original coral skeleton as an alumina replicate. In a later publication, Skinner et al. [63] followed the same procedure but produced a flexible piezoelectric PZT (Lead Zirconate Titanate)/silicone composite material using a coral as the template.

## 2.6 Processing of Current Metal/Ceramic MMCs

Popular fabrication techniques used for manufacturing present day aluminum MMCs are based on the infiltration method. Pressure, pressureless and vacuum infiltration are the most common techniques for filling porous preforms as they are able to produce high yield, near net-shape composites. In short, pressure-assisted infiltration such as squeeze casting, uses a piston to mechanically force the liquid melt into a preform [64]. A second type of pressure-assisted infiltration uses an inert pressurized gas to force the liquid metal into the preform [65]. Mechanical assistance uses pressures of approximately 65-100 MPa while inert pressurized gas systems use lower pressures, 2-35 MPa, however, all function on the same principle and are needed to force molten metal into the narrow pore structure found in high volume fraction particle preforms. Pressureless infiltration, also known as capillary driven infiltration is carried out by immersing the ceramic into a molten aluminum alloy bath containing high silicon content, at atmospheric pressure [66]. Vacuum infiltration is also a low-pressure process carried out just below atmospheric pressure [67].

Light metal IPCs can be manufactured using similar arrangements as standard MMCs. The porous ceramic reinforcement of IPCs is produced by different novel techniques as will be explained in the subsequent paragraphs. Low viscosity, liquid aluminum infiltration into a porous preform is the most practical method for infiltrating IPCs and will be considered here. Deciding which method to use depends on the matrix/reinforcement wetting behavior, brittleness of the reinforcement such that a high pressure may damage it, and the viscosity of the melt. In addition, the mechanical

properties may vary depending on the manufacturing method employed as the amount of final porosity will affect the strength of the composite.

## 2.7 Recent Developments for Infiltrating/Producing IPC's

In recent years, a number of fabrication routes have been developed for producing IPC's and are explained below. Some techniques produce a separate ceramic body followed by an infiltration, while in other methods the ceramic and metal are merged together. An earlier publication by Clarke [68], who first proposed IPC's and reviewed common processing routes and hypothesis on future approaches to making interpenetrating phase composites. Each method depends on the reinforcement strength, reactivity/compatibility of the ingredients and the feasibility of the method.

### 2.7.1 Foam Replication Method

Lange et al. [53] developed a method for producing a ceramic porous body for infiltration with a liquid metal. The porous body is manufactured by pressure infiltration of aqueous alumina slurry into a reticulated polyurethane foam, followed by a pyrolysis heat treatment in air to incinerate the polymer and produce a channel network. A final squeeze casting step is performed with an aluminum/magnesium alloy to produce the final composite. In a similar process, Peng et. al. [69] utilized commercially available alumina foam as well as foam produced using a two part polyurethane foam compound, mixed with an alumina powder. Both foams were infiltrated with an aluminum alloy using a squeeze casting method and their microstructures examined. They found both foams to be well infiltrated, however the struts are significantly different. Commercial foam struts are dense, forming two distinct phases of aluminum and alumina, while the sintered ceramic

foam generates porous struts where the melt infiltrates the foam cells as well as the strut network. More recently, Shouren et al. [70] produced a porous silicon nitride ceramic skeleton by immersing a number of polymeric foam specimens into a bath of silicon nitride slurry. The samples were then sintered for different lengths of time to produce porosities varying from 80-94%. The porous ceramic bodies were further infiltrated with an aluminum/magnesium alloy. The largest Young's modulus and fracture toughness were obtained with 6% volume fraction reinforcement as compared to the unreinforced aluminum/magnesium alloy. The least amount of reinforcement showed greater properties due to the inherent porosity in the as-received skeletal foam struts.

### 2.7.2 Foam Coating Method

Brown et al. [54] coated open-celled polyurethane foam with a thin layer of alumina which maintained an opened, alumina-free, empty space as compared to the foam replication method which fills the entire void space of the polyurethane foam with alumina. In general, the foam coating method can produce higher porosity preforms having low volume fractions of ceramic reinforcement networks, while the foam replication method produces ceramic preforms with lower porosities and higher reinforcement contents [71].

### 2.7.3 Reactive Metal Penetration (RMP)

Reactive metal penetration, reactive metal infiltration, oxide displacement reaction or liquid phase displacement method are all synonyms describing an *in-situ* chemical reactive method for producing IPC's by a chemical reaction forming the metal/ceramic interpenetrating microstructure. Breslin et al. [55] were the first to develop an $Al_2O_3$/Al

co-continuous composite by a liquid phase displacement method. A dense silica preform is deposited into a liquid bath of aluminum where the silica and aluminum react to produce a 65 vol% alumina ceramic reinforcement interpenetrated with an aluminum-silicon matrix. This process was found to be near-net shape with the final components having the same size and dimensions as the silica precursor. It was established to have good wear properties with a thermal conductivity of about twice that of steel and a coefficient of thermal expansion less than steel, making this new material ideal for brake rotors. In a later paper, Loehman et al. [72] developed a reactive metal infiltration process whereby, a dense mullite ($Al_6Si_2O_{13}$) ceramic preform was immersed into a liquid aluminum bath in order to produce a near-net shape alumina network intermingled with an aluminum/silicon alloy. As compared to the mullite and aluminum precursors, they determined the increase in strength, modulus and hardness of this new composite is due to the alumina skeleton while the aluminum phase is responsible for improved toughness. Chen et al. [73] also used RMP to produce a wear resistant $Al_2O_3$/Al co-continuous composite by inserting silicon carbide particulates during the fabrication of the silica precursor. After reacting the silicon carbide/silica with the aluminum alloy, the ceramic structure shows phases of alumina and randomly distributed silicon carbide particles while the matrix is composed of phases of aluminum, silicon and aluminum/silicon alloy. In a related experiment, La Vecchia et al. [74] produced an $Al_2O_3$/Al co-continuous composite containing 63vol% alumina by reacting silica in a molten bath of pure aluminum. Strong bonding at the metal/ceramic interface as well as the continuous ceramic reinforcement results in the composite having a high stiffness, as well as high

bend and compression strengths, but with a low tensile strength due to small amounts of residual porosity as compared to pure aluminum properties.

Pavese et al. [75] recently used RMP on two commercially pure, cordierite-based ceramics to produce co-continuous composites. The cordierite preforms are reacted in a bath of pure aluminum, producing an alumina/spinel ($Al_2O_3/MgAl_2O_4$) ceramic reinforcement surrounded by an aluminum/silicon matrix alloy. The mechanical properties are lower than those using silica as a preform, but not by a substantial amount. Their reasoning was because of the spinel present having a lower Young's modulus than alumina; nevertheless, the cost of cordierite is much less than silica.

### 2.7.4 Direct Metal Oxidation (DIMOX$^{TM}$)

Newkirk et al. [56] developed a composite for the Lanxide® Corporation using the DIMOX$^{TM}$ (direct metal oxidation) process which employs a powder-less process. In this method, a molten metal is oxidized. Growth dopants are used in the metal alloy or on its surface to promote rapid oxidation and produce a porous oxide layer. Two types of composites can be produced to create the three-dimensional interconnected ceramic; first a ceramic/metal composite is produced when an oxide layer forms in an outward direction from the melt. As the process progresses, the liquid metal moves through the porous oxide layer forming a ceramic reinforcement and metal as the matrix. The second composite is formed when reinforcement fillers such as particles, fibers, whiskers or preforms are placed on top of the molten metal. In this way, the matrix is a mixture of ceramic and metal as explained in the first case, but progressively grows through the added reinforcement instead of an oxide layer. In this first publication, 20 cm thick

composites have been reported. To determine the mechanical properties of the DIMOX™ composite, Aghajanian et al. [76] conducted an experiment to evaluate the Lanxide® $Al_2O_3$/Al composite and compare them to a commercially available dense alumina. While the dense alumina was harder and stronger in compression, the composite was superior in flexure, toughness and had a better resistance to thermal shock due to the aluminum phase.

### 2.7.5 Pressing and Sintering of Powders: Squeeze Casting

Etter et al. [77] infiltrated commercially available graphite preforms with eutectic aluminum alloy using a squeeze casting technique. After infiltration, porosity for the composites was less than 1 vol.%. It was shown that the infiltrated graphite preform mechanical properties; flexural strength, Young's modulus and fracture toughness, are enhanced as compared to the porous graphite alone, but not greater than aluminum alloy. Zeschky et al. [78] produced an organosilicate (Si-O-C) ceramic/magnesium metal interpenetrating phase composite. Silicon and silicon carbide powders were added as fillers to the polymer powder prior to the foaming process and generated a rigid thermoset foam. The magnesium alloy melt was infiltrated by squeeze casting and a complete infiltration was obtained. In contrast to Etters' results, this composite had 50% increase in flexural strength and Young's modulus as compared to the unreinforced metal alloy.

### 2.7.6 Pressing and Sintering of Powders: Gas Pressure

Prielipp et al. [57] produced $Al_2O_3$/Al composites using an argon, gas pressure metal infiltration process. The ceramic preforms produced were alumina powder, pressed and

sintered, as well as slip cast slurries of alumina powders. This produced a dense and a more porous alumina ceramic preform, respectively. The fracture strength and fracture toughness of the $Al_2O_3$/Al composites proved to be much higher than both the alumina preforms which is attributable to the addition of the aluminum matrix. For example, the Young's modulus for 25vol% aluminum/alumina content was 260 GPa as compared to 400 GPa for alumina and 70 GPa for aluminum. Balch et al. [79] produced open-celled SiC foam starting from infiltration of a polymer into a porous sodium chloride compact. After dissolution of the salt, the compact was transformed into SiC by pyrolysis. Subsequently, the SiC foam was gas pressure infiltrated with pure aluminum. No interfacial reactions were observed between the reinforcement and matrix which is attributable to the low preform temperature of 350 °C. However, 3 vol% porosity in the SiC foam was found to be due to the closed porosity within the SiC foam, originating from the gas evolved during the foaming processing. Final composite porosity was not analyzed. Travitzky [80] gas pressure infiltrated pure aluminum into alumina pressed powder preforms to produce an $Al_2O_3$/Al composite with an interpenetrating network. Preforms with open porosity ranging between 12 and 34 vol.% were produced. The bending strength of the composite decreased with increasing amount of the aluminum phase, whereas the fracture toughness increased with increasing volume fraction of aluminum. Etter et al. [81] infiltrated commercially porous graphite preforms with pure aluminum as well as an aluminum/silicon alloy using gas pressure infiltration. Both preforms were infiltrated using a pressure of 8 MPa of inert gas. Residual porosity remains in the composite due to inhomogeneous infiltration which may be caused by insufficient pressure, thus a squeeze casting process is proposed for future work. The

flexural strength for the aluminum/graphite and aluminum-silicon/graphite composite was 100.9 MPa and 105.3 MPa, respectively, indicating little influence of the matrix on the strength behavior.

### 2.7.7 Pressing and Sintering of Powders: Pore-Forming Agents

Pore-forming agents are pyrolysable particles combined with ceramic powders that are burnt away during a heating process to produce a porous ceramic structure. In this technique, the pore-forming pyrolizable agents influence the pore size and shape. Mattern et al. [58] listed a summary of pore-forming agents used in previous works such as; carbon fibers and flakes, wax, as well as suspensions of polyvinylchloride and polyethylene. Their research employed direct squeeze casting to infiltrate alumina foam with an aluminum/silicon alloy. The foam was manufactured using an aqueous alumina suspension and pyrolysable pore-forming agents such as potato and maize starch. They were added in such amounts to obtain between 50% and 67% open porosities. The maize starch foam produces a more homogeneous microstructure which the authors assume is due to different amounts of swelling from the starch particles when in contact with water. As a result, the maize starch-formed composite revealed a larger bend strength.

### 2.7.8 Pressing and Sintering of Powders: Self-Propagating High-Temperature Synthesis (SHS) Reaction

The previous processes utilize aluminum alloys as the matrix due to their low melting points and densities. It has also been attempted to produce IPC's containing higher temperature resistant materials as the reinforcement phase. The SHS technique, also known as combustion synthesis or thermal explosion has been thoroughly reviewed by Yi

et al. [82]. In general, it has been employed to produce refractory materials such as ceramics (nitrides, borides and carbides) and ceramic composites. In short, a mixture of reactant powders is compacted and heated in a furnace until an ignition temperature is reached. Once the ignition occurs, the processing time is in the order of seconds for the powders to consolidate. The final product is of high porosity due to the existing pores in the compact as well as those formed during the combustion process. The difficulty in this process concluded by the authors is achieving a highly dense product. In a later publication, Travitzky et al. [83] employed the SHS route to produce an $Al_2O_3$-TiAl (alumina-titanium aluminide) IPC. $TiO_2$ (anatase or titanium dioxide) and Al powder were mixed, and pressed to produce a green compact disk. Following thermal explosion, the end material has two separate networks of alumina and titanium aluminide. Fracture toughness of the composite was measured to be higher than the alumina ceramic but lower than the TiAl.

### 2.7.9 Pressing and Sintering of Powders: Three Dimensional Printing

Also known as rapid prototyping, this method can produce three dimensional porous ceramics from a computer model [84]. Complex, brittle ceramic parts can be manufactured without the use of tooling as is required in machining of metals. In general, rapid prototyping is used to visualize a three dimensional (3D) product (a prototype), produce a pattern for a mold or directly as a tool. In principle, the part created is done by a layered printing method where individual layers of ceramic powder and binder material are each applied simultaneously. The sequence is repeated until the part is complete. A final sintering is used to remove the binder and consolidate the powders. Melcher et al. [60] produced a dense $Al_2O_3$/Cu interpenetrating composite using 3D-printing

technology. Alumina powder, dextrin (starch) powder and a dispersant were mixed to form a slurry, printed into preforms and sintered. The porous alumina preforms were infiltrated with a copper alloy using a pressureless process. The composite flexural strength, fracture toughness and Young's modulus were found to be greater than for the sintered preform.

### 2.8 Summary

Literature review revealed that the majority of IPC's are manufactured from $Al_2O_3$/Al. It is clear that in materials with closed pores or if closed pores are formed during infiltration of the molten metal, this may promote inhomogeneous materials. The major mechanical properties sought were; fracture toughness, Young's modulus (stiffness) and flexural strength. The results are promising in that the composites possess unique mechanical properties as compared to the ceramic or metallic phases alone. For example, the low density ceramic phase provides increased modulus, flexural strength, wear resistance, and low CTE, while the metallic phase improves the toughness and ductility as well as the thermal conductivity of the composite. The outcomes of the various research that have been conducted on IPCs show the two distinct phases complement one another. Although other reinforcement-metal combinations have been studied, no publications, to the authors' knowledge, have reported the mechanical properties of an IPC manufactured with a SiC ceramic foam reinforcement and vacuum infiltrated with an aluminum alloy.

# Chapter 3 Material Infiltration Procedure

## 3.1 Introduction

This research project's aim is to produce porous SiC ceramic network, infiltrated with an aluminum alloy. The reason for studying such a material is to produce a new composite for potential use in applications such as electronic packaging. This novel composite is anticipated to be lighter than current materials in use. In addition, due to differing compositions, attachment problems arise in packaging materials where the base plate is difficult to solder to the above ceramic substrate as well as to the heat sink below. This Al/SiC foam composite is assumed to be easily soldered to both of these materials since it contains two networks where the soldering material can attach itself; a ceramic and aluminum alloy three-dimensional network.

## 3.2 Fabrication of SiC from Pyrolyzed Wood

The first portion of this research entails producing a porous SiC ceramic with the morphology of the hollow cell structure in the wood and subsequent infiltration with an aluminum alloy. The bio-materials processing route is shown in Figure 3.1. The experimental procedure involves the use of locally sourced (Eastern Canada) Eastern White pine, American beech and Sugar maple wood as precursors. Kiln dried lumber measuring 20 mm x 20 mm x 915 mm were purchased from a local sawmill and cut into cubes measuring approximately 20 mm x 20 mm x 20 mm. Crack-free carbon samples were produced by initially drying the cubes at 103°C for 24 h in a tube furnace under argon atmosphere and then pyrolyzing in the same tube furnace at a heating rate of 1°C/min up to 500°C, followed by 5°C/min up to 800°C for 1 h in argon atmosphere. A

further pyrolysis was carried out in a graphite furnace with a heating rate of 8.75°C/min up to 1400°C for 1h, under vacuum atmosphere. Before and after pyrolyzation, change in weight and geometrical dimensions were recorded.

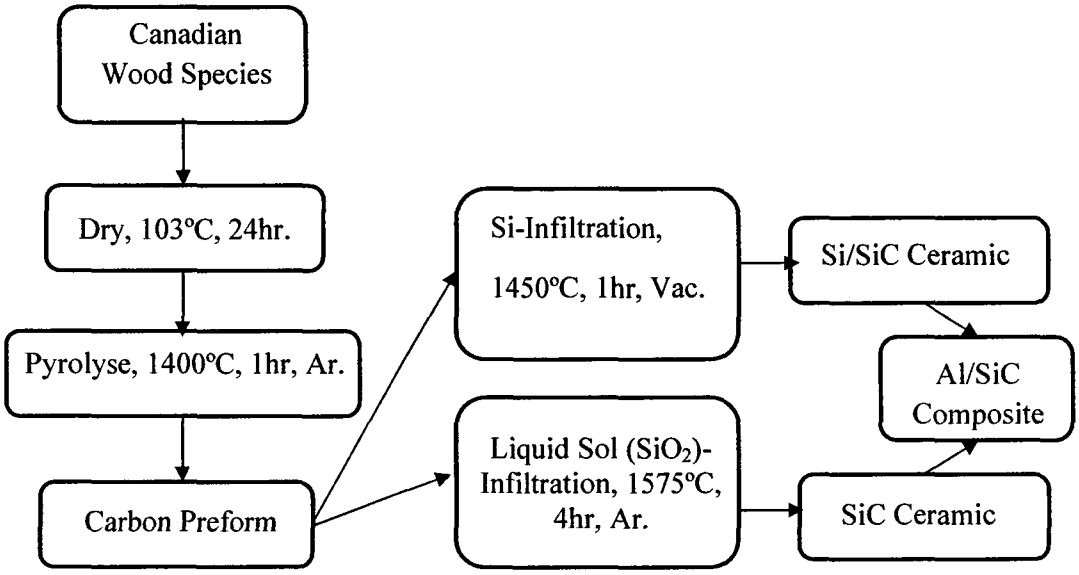


Figure 3.1 Experimental procedure for the production of SiC from wood

### 3.2.1 Silica Sol Infiltration

Two techniques have been developed for silica sol ($SiO_2$) infiltration into carbonized wood preforms and are characterized as either cyclic infiltration or repeated infiltration [47]. During a cyclic infiltration process, each $SiO_2$ infiltration/drying step of the carbon specimen is followed by a carbothermal reaction (ceramization) until it is entirely converted to a ceramic. The second is referred to as the repeated infiltration process. The carbon specimen is repeatedly infiltrated/dried with the sol until a sufficient amount has accumulated, verified by an insignificant incremental weight change. This is followed by

a high temperature ceramization to convert to a ceramic. For example, three repeated infiltrations, indicates the sample was infiltrated/dried three times consecutively. The water-based sol used was Levasil® 50/50% with a mean $SiO_2$ particle diameter of 50nm, supplied by H. C. Starck Inc.

The carbon samples of pine, beech and maple were deposited in a glass beaker, loaded down with small weights to prevent them from floating and sol was poured over the specimens until they were immersed. The beaker was placed in a desiccator and a vacuum of 35 mbar (abs) (26 mm Hg) was applied for 30 minutes at room temperature. For both cyclic and repeated infiltration, the samples were first removed from the sol and left to dry at atmospheric temperature for 12 hr followed by a slow heating rate of 1°C/min up to 100°C and held 12 hr under argon atmosphere to slowly remove the water from the $SiO_2$ solution. A slow drying rate was required; otherwise from experience, during a fast heating rate, the water in the sol evaporates too quickly which "pushes out" the sol, visible as white "flaking" on the exterior of the sample and low infiltration rates measured after drying. Ceramization was carried out at 1575°C, for 4 hr in 70 l/hr (1.16 l/min) flowing argon atmosphere. Optical microscopy, SEM, Energy Dispersive Spectroscopy (EDS) and X-ray diffraction (XRD) were used to study the final structure.

### 3.2.2 Ultra Structure and Silica Sol Analysis

The tracheid/fiber diameters for the pine, beech and maple wood range from 12-54 μm, 30-70 μm and 8-85 μm, respectively. Theoretically, 160 silica particles with diameters of 50 nm placed side by side can fit in a 8 μm fiber cross-section, therefore infiltration into these carbonized wood species is possible longitudinally. In the radial direction, the

earlywood pine bordered pit strand spacing in the margo is reported to be 1 μm, hence, 20 silica particles could fit between the filaments. Measured from an electron microscope image, a bordered pit membrane diameter was 17 μm, torus diameter of 8 μm with an aperture diameter of 5.4 μm. Correspondingly, about 108 silica particles could enter through the pit aperture. In Maple and Beech, the pores in pit membranes range from about 0.005 to 0.17 μm in diameter [85]. Theoretically, silica particles could not pass through a 0.005 μm pore and only about 3 particles could go through a 0.17 μm pore. The pit channel aperture diameter in maple was measured to be 0.45 μm diameter so that 9 silica particles could fit in this diameter. Given these measurements, radial and tangential infiltration may be more difficult to attain since cells are tapered-closed, end to end, and the only means of infiltrating is through pits along their lengths and ends.

### 3.2.3 Liquid Silicon

In the present work, the porous carbon pine preforms were infiltrated with liquid silicon provided by melting a -325 mesh, 99% silicon powder (Sigma-Aldrich Canada, Ltd.). The approach of this study was to investigate the possibility of producing a semi-porous, to porous, SiC structure with the silicon reacting with all the carbon preform. To accomplish this, an excess amount of silicon powder (2.5x, 3x, 4x, 5x, and 6x), beyond that necessary for complete conversion of C to SiC was deposited in a boron-nitride crucible, and the carbonized wood was placed on top of the bed of powder. The crucible was heated in a graphite furnace to 1450°C for 1 hr in a vacuum atmosphere. Optical microscopy, SEM and XRD were used to study the final structure.

### 3.2.4 Wood Ceramic Characterization

To analyze the microstructural changes during silica and silicon infiltration, a scanning electron microscope (SEM), JOEL 840A, was used with an acceleration voltage of 10-15 kV. For looking at different depths of the silicon infiltrated carbon pine, an optical microscope was used at low magnification to view a minimum of one growth ring. Different elements on the surface and in the pores of the silica-infiltrated samples were identified using EDS. Phase composition of the silica-oxidized and silicon-infiltrated samples was determined by XRD by first turning the samples into powder using a pestle and mortar, as given in Figures 6.21 and 6.26, respectively.

## 3.3 Formation of A356 Aluminum Alloy/SiC Foam Composite

By maintaining a reinforcing ceramic network structure, the second portion of this research entails the use of commercially available SiC foam. The ceramic foam/aluminum alloy infiltration procedure is shown in Figure 3.2. The matrix and reinforcement employed are described in the following section.

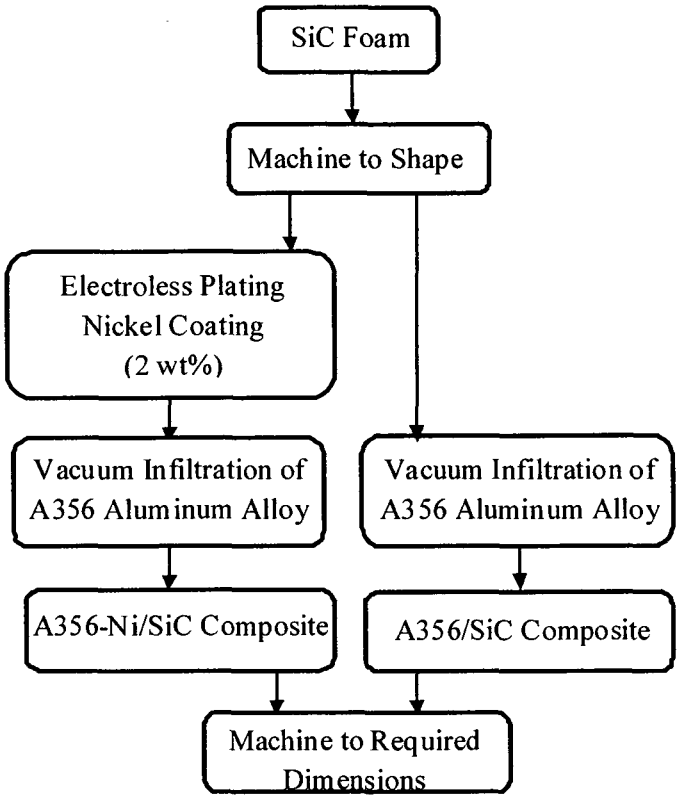


Figure 3.2 Experimental procedure for the A356/SiC foam composite

### 3.3.1 A356 Aluminum Alloy Matrix

The commercial A356 aluminum alloy matrix was an ingot donated by Alcan Inc. and cut into 2.5 mm cubes for re-melting in a small SiC crucible. This aluminum alloy is a sand casting alloy used for its low melting point between 555-615°C and hypoeutectic property. In addition, the composites' physical and mechanical properties can be compared to commercially available A356/SiC particle composites, and other research publications. The A356 Al-Si casting alloy selected is a medium strength, heat-treatable alloy with good ductility and corrosion resistance. It is a very fluid alloy and excellent for casting thin sections. Compared with alloy 356, A356 has the same level of alloying elements, but the 'A' indicates less impurities, hence it is stronger and more ductile. The

physical properties of the A356 aluminum alloy are listed in Table 3.1 [86], while the composition of the A356 aluminum alloy is given in Table 3.2 as per Alcan's chemical composition analysis report.

Table 3.1 Physical properties of the A356 aluminum alloy [86]

| Property | Value |
|---|---|
| Young's modulus (E) | 72.4 GPa |
| Density (ρ) | 2.71 $gcm^{-3}$ |
| Melting range (T) | 555-615 °C |
| Poisson's ratio (υ) | 0.33 |

Table 3.2 Elemental composition of the A356 aluminum alloy, wt%

| Al | Si | Fe | Cu | Mn | Mg | Ni | Zn | Ti | Pb |
|---|---|---|---|---|---|---|---|---|---|
| 92.262 | 7.10 | 0.10 | 0.006 | 0.01 | 0.38 | 0.003 | 0.008 | 0.13 | 0.001 |

### 3.3.2 SiC Foam

The reinforcement is commercially available Ultrafoam$^{TM}$, 100 pores per inch (PPI), SiC ceramic foam purchased from Ultramet as a rectangular solid of 203 mm x 102 mm x 25.4 mm ( 8 inch x 4 inch x 1 inch). In order for the foam specimens to match the inner diameter of the quartz tube, specimens were cut to approximately 12.5 mm x 12.5 mm square at various lengths depending on the mechanical test required. The major commercial use of these SiC ceramic foams are in molten metal filtration industry, but are utilized in this research for their low density, and three-dimensional network structure as shown in Figure 3.3. The physical properties of the as-purchased ceramic SiC foam are given in Table 3.3, as specified from the manufacturers' data sheet [87].

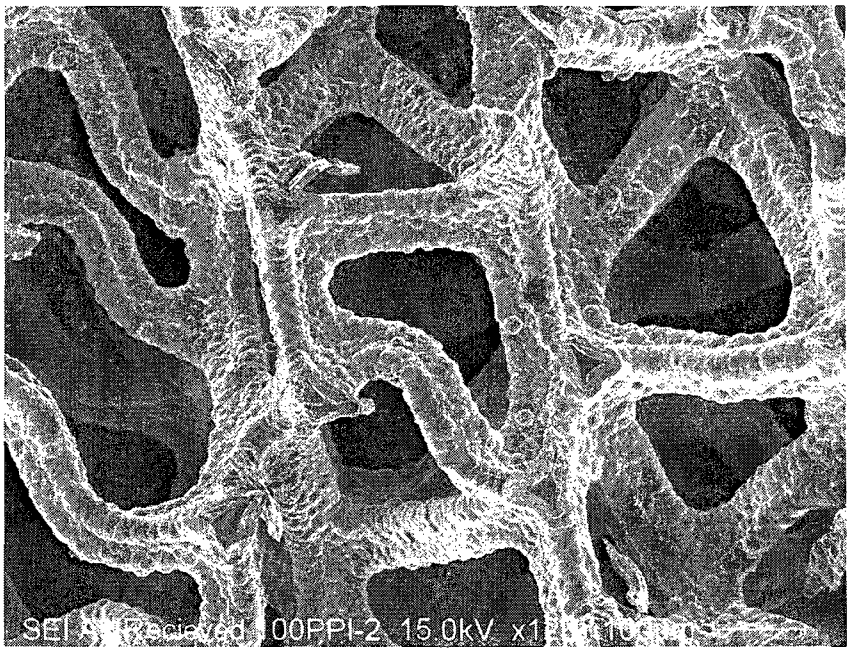

Figure 3.3 SEM image of as-received SiC 100 PPI foam microstructure

Table 3.3 Physical properties of the ceramic SiC foam [87]

| Property | Value |
|---|---|
| Young's modulus in compression (E) | 6.89 GPa |
| Compressive strength ($\sigma_y C$) | 8.96 MPa |
| Foam bulk density ($\rho$) | 0.37 $gcm^{-3}$ |
| Theoretical (ligament) density ($\rho$) | 3.2 $gcm^{-3}$ |
| Maximum temperature use (T) | 1650°C |
| Poisson's ratio ($\upsilon$) | 0.22 |

The SiC foam reinforcement stems from their in-house fabrication technique involving the initial production of vitreous carbon foam from pyrolysis of a foamed thermosetting polyurethane polymer. A representative of the polyurethane foam

producer, Foamex International Inc., stated in a phone conversation that during the manufacturing process of the polyurethane foam, the cells are opened to a proprietary specification. Furthermore, they do not have test data for the amount of open pores, but suggested their foams are 99% open pores.

Employing a Chemical Vapor Infiltration (CVI) process, the carbon foam is transformed into a SiC foam by depositing thin films in the order of 10 to 1000 μm of SiC onto the carbon foam using a thermal pyrolysis of methyl-trichlorosilane (MTS), $CH_3SiCl_3$, which provides both the silicon and carbon source for the SiC. As the gases (Si and C) pass over the carbon substrate, they react to deposit as a solid SiC phase. The inner carbon core remains, surrounded by a SiC thickness since the carbon structure functions only as a substrate for the material being deposited. The thin film deposited strengthens the carbon foam by 70% to 100% [13]. Due to the difficulty in polishing the A356/SiC composite, a sample was sent to JEOL USA for polishing using their Ion-beam Cross Section Polisher. The sample was imaged with a 6610LV, which is a variable pressure W-filament. Secondary (SEI) and the backscatter (BEC) electron detector images were obtained. Shown in the cross-section of the SiC foam strut, Figure 3.4[1], the core is carbon while the thick gray layers are SiC. At closer magnification, Figure 3.5[1], the structure is composed of layers. Each SiC layer is separated by a thin dark carbon interface layer. It is stated, that full structures or alternating layers can be produced where the multilayer composites act to increase the strength and toughness [88].

[1] Courtesy of JEOL USA Cross Section Polisher

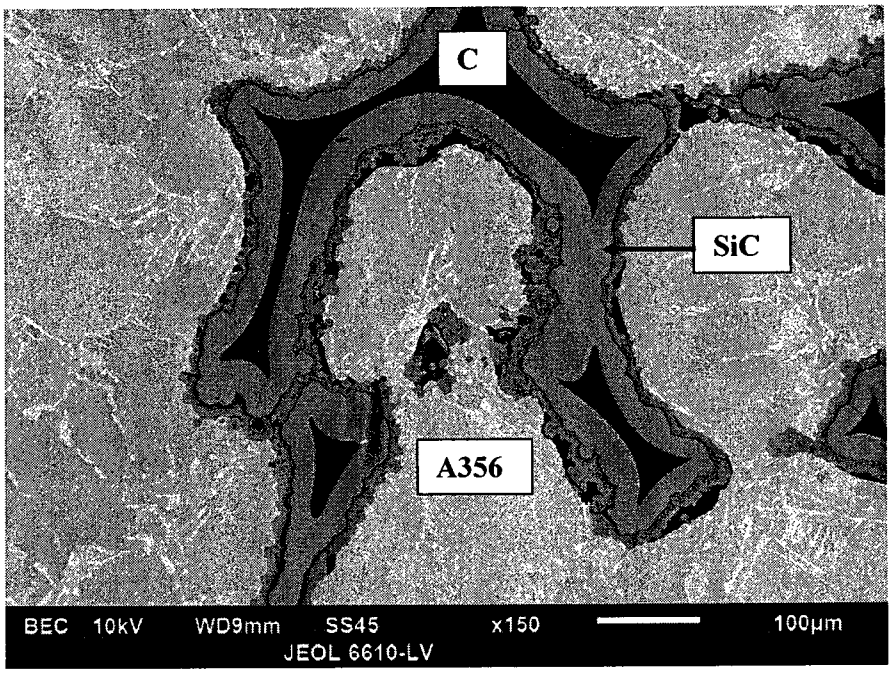


Figure 3.4 Cross-section SEM image of the SiC/C strut microstructure

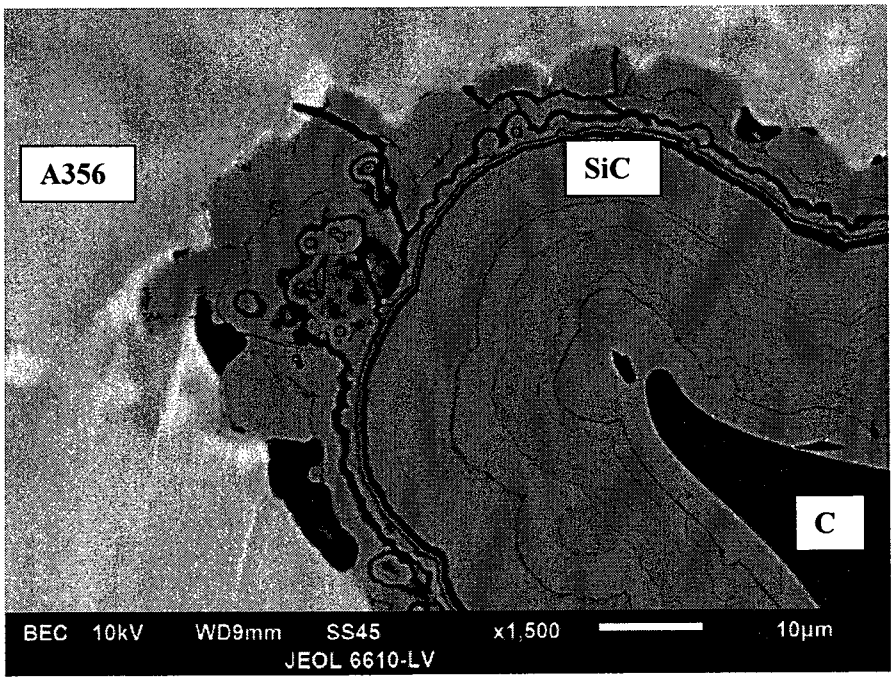


Figure 3.5 Higher magnification of the SiC layer

### 3.3.3 As-Received Foam Strut Composition

The as-received foam is sold by the supplier as SiC foam. Verification of this statement is important as the properties of the final composite will depend on the initial material accuracy. SEM micrographs were taken of a cross-section of the as-received SiC foam. Using an elemental distribution X-ray map, the research revealed two-phase struts; the center being a carbon core surrounded by a SiC shell as shown in Figure 3.4. To understand the approximate dimensions and amount of each phase of the SiC foam, optical microscope images were taken of 20 randomly selected cross-sectional shapes of varying geometries at 20x and measured using image analysis software (Motic Image Plus 2.0 ML). The SiC strut coating thickness varied between 2.6-13.1 μm for an average thickness of 4.3 μm. The area ratio of carbon to SiC of each strut cross-section was measured and an average taken. The SiC coating and carbon center were found to have an average area of 796 $\mu m^2$ and 249 $\mu m^2$, respectively. Assuming linear consistency this would give volume fractions of 0.24 and 0.76 for carbon and SiC, respectively.

However, due to strut junctions, there may be more carbon in these areas of the foam. This was verified by oxidizing the carbon from the SiC/C as-received foam. It is stated that vitreous carbon can be used in air up to 600°C without degradation [89]. Therefore, to determine the mass fractions of the SiC and carbon in the as-received SiC/C foam, it was oxidized at 700°C for one hour. Prior to oxidation, the SiC CVD powder (crushed into powder form) weighted 0.574 g, while after oxidation, the powder sample weight was 0.081 g. This is assuming a $SiO_2$ film has not formed on the SiC as will be discussed in Section 6.2.3. Cowlard et al. [89] determined the bulk density of carbonized vitreous (glassy) carbon to be 1.47 $gcm^{-3}$. The theoretical solid CVD SiC has a density of

3.21 $gcm^{-3}$ [90] while the density of a CVD SiC layer grown on a vitreous carbon substrate was measured to be 3.21 $gcm^{-3}$ after removal of the carbon [91]. The same authors have also established that CVD SiC is known as a dense, porosity free ceramic, hence the identical densities. Employing the appropriate densities and knowing the mass of each constituent, the volume fraction of the SiC and carbon are 0.77 and 0.23, respectively.

Porosity is a measure of open voids (open and closed) or the volume occupied by the total voids in a sample. Porosity measurements on the SiC foam are performed for two reasons; one, porous materials will affect the mechanical properties of the final product as compared to a solid material; two, to determine the open porosity of the foam so that an estimate of amounts of matrix and reinforcement of the final composite can be calculated.

The water absorption method based on Archimedes's principle (ASTM C20-00) [92], was used for determining the open porosity ($P_{open}$). The water saturation liquid filling method measures the open porosity of the sample as opposed to the total porosity, since liquid water cannot enter closed pores. The closed porosity ($P_{closed}$) is calculated by the difference between the total and open porosity using Equation 3.1. The total porosity ($P_{total}$) was calculated based on the relative density of the composite; Equation 3.2, where the relative density is equivalent to the ratio of the bulk density ($\rho_{bulk}$) of a substance to the theoretical density ($\rho_{theo}$) of solid material calculated using Equation 3.3. The open porosities of three foam samples were directly measured using Archimedes method, Equation 3.4 and averaged. W, D and $V_T$ are the saturated weight, dry weight and exterior volume, respectively.

The two phase theoretical strut solid density ($\rho_{theo.\ strut}$) composed of vitreous carbon and CVD SiC was calculated using the Rule of Mixtures (ROM), Equation 3.5. Employing a theoretical CVD SiC density ($\rho_{SiC}$) of 3.2 $gcm^{-3}$[90], a vitreous carbon density ($\rho_c$) of 1.54 $gcm^{-3}$ [87] and the volume fractions of carbon ($V_c$) and SiC ($V_{SiC}$) from the oxidization test, of 0.23 and 0.77, respectively, the strut density is calculated to be 2.82 $gcm^{-3}$. The foam bulk density was obtained by geometrical volume and dry mass measurements of three samples giving a value of 0.32± 0.003 $gcm^{-3}$, hence, the calculated total porosity is 88.65%. The results are tabulated in Table 3.4.

$$(P_{total} = P_{open} + P_{closed}) \tag{3.1}$$

$$P_{total} = (1 - \text{Relative Density}) * 100\% \tag{3.2}$$

$$\text{Relative Density} = (\rho_{bulk} / \rho_{theo}) \tag{3.3}$$

$$P_{open} = (W - D)/ V_T) * 100\% \tag{3.4}$$

$$\rho_{theo.\ strut} = \rho_c V_c + \rho_{SiC} V_{SiC} \tag{3.5}$$

Table 3.4 As-received SiC foam porosity values

| Total Porosity (Calculated) $P_{Total}$ (%) | Open Porosity (Measured) (ASTM C20-00) $P_{Open}$ (%) | Closed Porosity (Difference) $P_{Closed}$ (%) |
|---|---|---|
| 88.65 | 87.67 ±0.19 | 0.98 ±0.19 |

### 3.4 Matrix/Reinforcement Reaction Kinetics

For liquid metal infiltration, the ability of a liquid to spread on a solid surface depends on the capability of the liquid to wet the surface. Wetting is characterized as how well a liquid spreads over a solid surface or penetrates the pores of a preform. Good contact provides suitable bonding between the SiC solid ceramic and the aluminum melt during the infiltration process. Wettability is determined by the contact (or wetting) angle (θ) as shown in Figure 3.6.

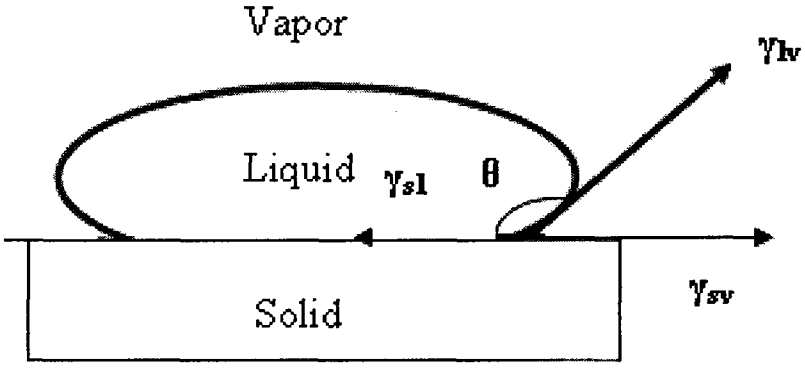


Figure 3.6 Contact angle of a liquid drop on a solid surface

Considering equilibrium of the forces in a system, the liquid, solid and gaseous states are related by three different interfaces; liquid/solid, solid/vapor and liquid/vapor and this relationship is referred to as the Young-Dupre equation, Equation 3.6;

$$\gamma_{sv} = \gamma_{sl} + \gamma_{lv} \cos \theta \qquad (3.6)$$

where, $\gamma_{sv}$ is the surface tension of the solid-vapor interface, $\gamma_{sl}$ is the surface tension of the liquid-solid interface, $\gamma_{lv}$ is the surface tension of the liquid-vapor interface, and θ is the contact angle and describes the wettability. Complete wetting occurs when $\theta = 0$, partial wetting when $0 < \theta < 90°$ and non wetting when $\theta \geq 90°$ [93]. For good wetting, infiltration occurs spontaneously, otherwise, a positive or negative pressure is required to

push or pull the liquid into the porous material, respectively. Pressure is not the only parameter used for providing optimum wetting; it depends on a variety of conditions; including temperature, time, matrix alloying and surface geometry.

The wetting behavior of pure aluminum on single crystal SiC has been evaluated by a sessile drop method [94]. The transition was observed at 740°C after 15 minutes at $1*10^{-8}$ torr. They found the wetting angle decreases for shorter contact time as temperature increases. In addition, at lower temperatures the contact time must be increased to obtain the same wetting angle [94]. Depending on the SiC substrate, θ varies considerably. Han et al. [95], reported θ at 750°C and $10^{-4}$-$10^{-5}$ torr, between pure aluminum and reaction bonded SiC as 82° while on sintered SiC it was 127° for identical conditions. Depending on the nature of the SiC, the wetting properties reported from researchers vary considerably, as some declare the SiC source while others just state SiC as the substrate. For example, reaction bonded SiC has about 10% free silicon, which promotes wetting of aluminum on SiC, whereas sintered SiC contains no free silicon.

At the melting temperature of aluminum, SiC is thermodynamically unstable and reacts with molten aluminum to form aluminum carbide ($Al_4C_3$) at the Al/SiC interface and excess silicon as shown in Equation 3.7. The excess silicon formed dissolves in the aluminum melt forming a liquid Al-Si alloy.

$$Al + 3SiC \rightarrow Al_4C_3 + 3Si \qquad (3.7)$$

The reinforcement-matrix interface plays an important role for load transfer from the matrix to the reinforcement. $Al_4C_3$ forms a brittle phase thus lowering the composite mechanical properties by reducing the bond strength at the interface. Aluminum carbide

is also hydroscopic by reacting with moisture in the atmosphere to produce corrosion or aluminum hydroxide as shown in Equation 3.8.

$$Al_4C_3 + 12\ H_20 \rightarrow 3CH_4 + 4Al\ (OH)_3 \quad (3.8)$$

Alloying aluminum with silicon improves the wettability, and is a key contributor in preventing $Al_4C_3$ formation. However, too much silicon embrittles a composite and lowers its mechanical properties. A minimum of 7 wt% Si in aluminum at 700-750°C was reported to be stable with SiC as no $Al_4C_3$ was produced during infiltration [96]. Similarly, another study indicated formation of $Al_4C_3$ using 7 wt% Si but at 850°C [97]. On the other hand, a maximum of 12.6 wt% Si, in excess of the eutectic Al/Si composition, causes a surplus of silicon to precipitate [98]. Therefore, hypoeutectoid Al/Si alloys should be used such as the commercially available A356 aluminum/silicon casting alloy having a composition of 7 wt% silicon. In addition, roughening the surface of a substrate increases the wetting angle, thus decreasing the wettability. This can be explained by the air/moisture being trapped below the drop of liquid, the larger the cavities, the more air, resulting in a higher contact angle. In contrast, in an industrial setting surfaces are not polished, are not clean and may not be at atmospheric conditions, unlike the results of sessile drop tests where the surfaces are flat, polished, cleaned and the wetting angle is measured under high vacuum [99]. As shown in Figure 3.7, at high SEM magnification, the SiC foam surface in this study is not smooth which may contribute to wettability reduction.

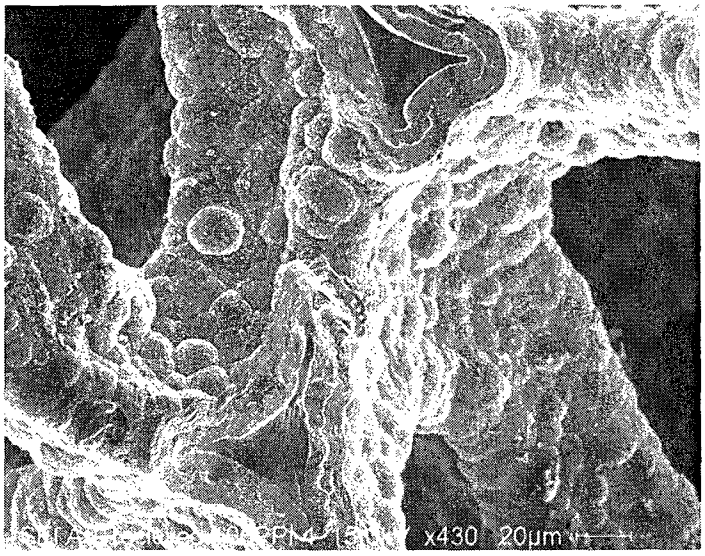


Figure 3.7 SEM of foam strut surfaces showing a rough profile

### 3.4.1 Pore Diameter for Aluminum Flow

The maximum pore diameter for infiltration without an external pressure can be calculated using capillary driven flow, using the Washburn equation, Equation 3.9 [100]. It assumes the flow of the melt penetrating the foam network is equivalent to a collection of cylindrical capillaries where P is the driving pressure required to infiltrate a pore of diameter, d and is calculated using Equation 3.10.

$$d_{max} = 4\gamma \cos\theta / P \tag{3.9}$$

$$P = \rho gh + P_{atm} - P_{vac} \tag{3.10}$$

Using an infiltration depth, h of 0.1 m and literature data for the infiltration properties at the melting point of pure aluminum, 660°C (surface tension $\gamma$ = 860 $mJm^{-2}$ [101], and melt density of $\rho$ = 2140 $Kg/m^3$ [102]), for a pressureless infiltration at atmospheric level, the driving pressure is the hydrostatic pressure, $\rho gh$ in the capillary or narrow tube and is equal to 2140 Pa for the above melt density. If $\theta$ = 82°, using Equation

3.9, pores with a maximum diameter of 23 μm (0.023 mm) are required for spontaneous infiltration. Each pore of the 100 PPI foam, has an approximate diameter of 0.254 mm, therefore, for these conditions, it is not possible to infiltrate the SiC foam with pure aluminum just using capillary action. Owing to the 3-dimensional foam network, consisting of unequal pore diameters and series of restricted passages through which the liquid has to flow, a forced impregnation of the melt by applying a small vacuum/external pressure is required.

### 3.5 Electroless Nickel Coating

When the ceramic surface is not compatible with the liquid matrix, a surface treatment in the form of a metallic coating on the reinforcement can be applied to decrease the wetting angle and promote wetting. Hashim et al. [93] reported nickel to be the most widely used metal coating for use with aluminum-based composites. However, the amount of nickel present in the aluminum has a significant impact on the stiffness of the composite. It is reported that adding 2 wt% nickel into pure aluminum increases the strength of the base metal but also reduces the ductility [103].

The coating technique for this research uses electroless nickel plating or autocatalytic chemical reduction where a chemical reaction bath is used to deposit metallic nickel ions onto a substrate. The quality of the coating depends on the solution concentrations, temperature and potential of hydrogen (pH) level. The main types of electroless nickel plating are nickel-phosphorus (Ni-P) and nickel-boron (Ni-B). In this study, Ni-B is used as the plating medium based on the process of Ni-P. The deposit that will form on the SiC substrate is a nickel boron alloy with 90-99.9 percent nickel and the

remainder boron [104]. Phosphorous is not used since it produces an aluminum-phosphorous compound [105], instead only small traces of boron are present.

### 3.5.1 Ceramic Substrate Surface Pretreatment

In order to obtain a high-quality metal coating onto the surface of the silicon carbide ceramic, a suitable surface preparation of the substrate must be achieved; otherwise this can lead to a lack of adhesion. In summary, cleaning is done to remove organic oils, grease and oxide films from the samples using acetone. Etching is used to roughen the SiC surface using nitric acid. Sites for the tin and palladium to adhere to the SiC for subsequent nickel coating will not form if the surface is not rough. A sensitization is carried out with a solution containing tin (Sn). The Sn ions attach themselves to the SiC surface. These act as catalyst sites for the subsequent palladium (Pd) activation step. Activation is done with a solution containing palladium (Pd) ions. The Pd replaces the Sn ions and acts as a catalyst for the ensuing deposit of nickel. Surfaces of ceramics are not catalytically active, therefore an activation treatment is required to make them catalytic by introducing a catalytically active metal [104]. The last step in the pretreatment preparation is a drying of the substrates to dry out any aqueous solution.

Chemical ingredient quantities for this five step pretreatment procedure was modified from the work of Leon et al. [106], which used 100 g of SiC powder. However, the same molarity for 3 g (or 12.5 mm x 12.5 mm x 60 mm) of SiC foam was kept for the 100 g of SiC powder from Leon et al. The chemicals and amounts are shown in Table 3.5.

Table 3.5 Composition of pretreatment solutions

| | |
|---|---|
| Cleaning: | |
| Acetone ($CH_3COCH_3$) | 20 ml |
| Micro-roughness: | |
| Nitric acid ($HNO_3$) | 20 ml |
| Sensitization: | |
| Distilled water | 250 ml |
| Tin (II) chloride anhydrous ($SnCl_2$) | 1 g |
| Hydrochloric acid (HCl) | 4 ml |
| Activation: | |
| Distilled water | 250 ml |
| Palladium (II) chloride ($PdCl_2$) | 0.025 g |
| Hydrochloric acid (HCl) | 0.25 ml |

### 3.5.2 Experimental Pretreatment Procedure

In all steps, the SiC foam is deposited into each separate solution, manually agitated with a glass rod and simultaneously put in an ultrasonic bath to remove any air bubbles within the porous structure, followed by rinsing with distilled water.

1. Cleaning step:

The SiC foam samples were cleaned with 20 ml of acetone for 15 min., and rinsed four times.

2. Micro-roughness step:

Micro-roughness was obtained by etching in 20 ml of Nitric acid for 15 min.

3. Sensitization step:

Sensitization step was carried out in a solution of anhydrous Tin (II) Chloride ($SnCl_2$) and Hydrochloric acid. In 250 ml of distilled water, 1 g of $SnCl_2$ and 4 ml of HCl were added and mixed with a magnetic stirrer at room temperature for 20 min. The SiC foam specimens were deposited into the solution for 20 min followed by a single rinse.

4. Activation step:

The sensitized substrate was activated in a solution of Palladium (II) Chloride ($PdCl_2$) and Hydrochloric Acid (HCl). In 250 ml of distilled water, 0.025 g of $PdCl_2$ and 0.25 ml of HCl were mixed and placed in an ultrasonic bath for 20 min. The specimens were deposited in the solution and manually agitated with a glass rod for 20 min followed by a single rinse.

5. Drying step:

All samples were dried at 90°C, 4 h.

### 3.5.3 Ceramic Substrate Nickel Plating

The pretreated SiC foam samples were electrolessly nickel-coated. The original recipe is for 1 liter of distilled water for 15 g of SiC powder [106]. However, it is modified for 250 ml of distilled water, and 3 g of SiC foam (or 12.5 mm x 12.5 mm x 60 mm) specimen. The chemicals and amounts used are listed in Table 3.6.

Table 3.6 Composition of nickel plating solutions

| | |
|---|---|
| Distilled water | 250 ml |
| Nickel (II) chloride ($NiCl_2\,6H_2O$) | 7.5 g |
| Borane dimethylamine complex ($BH_3NH(CH_3)_2$) | 1.05 g |
| Sodium acetate, anhydrous ($NaOOCCH_3$) | 5.75g |

The bath consists of three ingredients: a nickel ion source that consumes electrons; Nickel (II) Chloride ($NiCl_2\,6H_2O$), a reducing agent to supply electrons; Borane Dimethylamine complex ($BH_3NH(CH_3)_2$), and a complexing agent to prevent

bath decomposition and avoid nickel precipitates from forming; Sodium Acetate, anhydrous ($NaOOCCH_3$). In 250 ml of distilled water, for a 0.07 molar (M) concentration, the bath ingredients were consecutively stirred into a beaker with a glass rod in the amounts of 7.5 g, 1.05 g and 5.75 g, respectively. During preliminary trials as shown in Figure 3.8, the concentration of ($BH_3NH(CH_3)_2$), was changed to 0.04 M. This had the advantage of reducing the nickel weight increase in the foam by maintaining the same soaking time. Using a 0.04 M Borane solution, a 2 wt% nickel was obtained, for a 15 second immersion in the bath. The bath was maintained at 70°C and pH of 7.0. After the pre-determined soaking time, samples are removed from the nickel solution, rinsed with distilled water and dried at 50°C, argon atmosphere for 12 h. The samples were kept in a desiccator until infiltrated with aluminum, to prevent oxidizing the nickel.

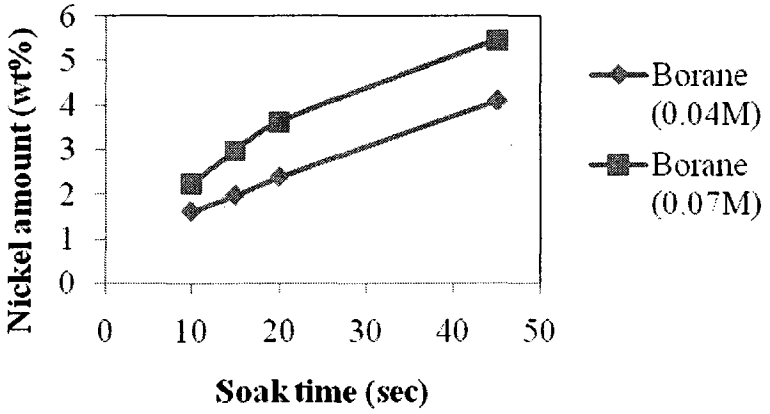


Figure 3.8 Amount of nickel content in the foam

### 3.6 Composite Infiltration Procedure

This research focuses on how a cellular structure can be used to produce new metal matrix composites. Numerous techniques for producing interpenetrating phase composites (IPC's) are given in the literature review. In this study, vacuum infiltration

was employed for its controllable air flow and low pressure application on the preform. The author has found no published information on vacuum infiltration of an aluminum melt into silicon carbide foam to date. Therefore, trial and error investigations were carried out to develop the infiltration process.

### 3.6.1 Description of Infiltration Apparatus

Some researchers use quartz tubes to vacuum infiltrate a melt into packed reinforcement powders for easy removal of the samples [107]. A similar apparatus [67] for infiltrating aluminum into a SiC powder compact was designed and built in-house for this research because of its simplicity and inexpensive hardware. A schematic and a digital photograph are shown in Figures 3.9 and 3.10, respectively.

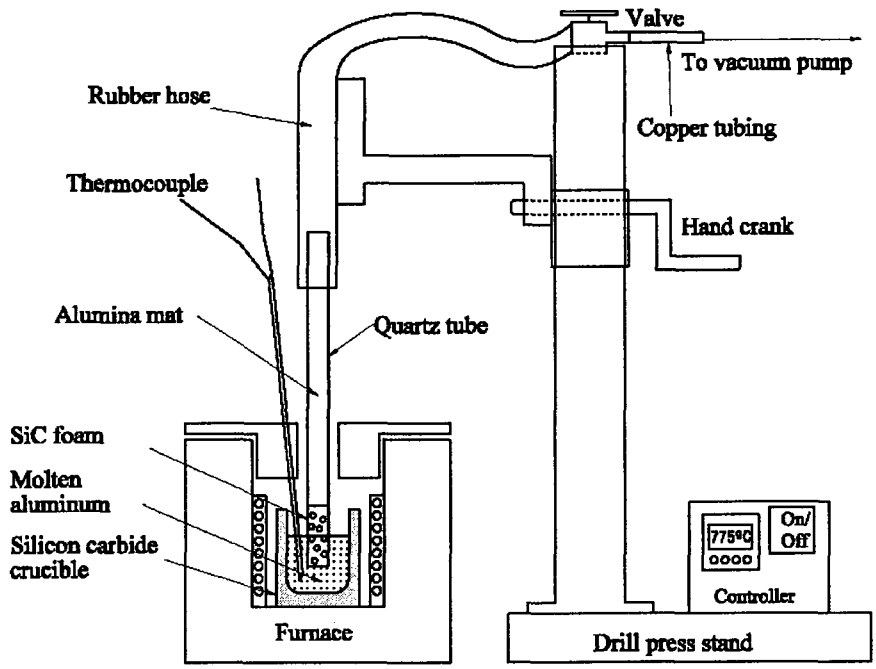


Figure 3.9 Schematic diagram of the vacuum infiltration apparatus

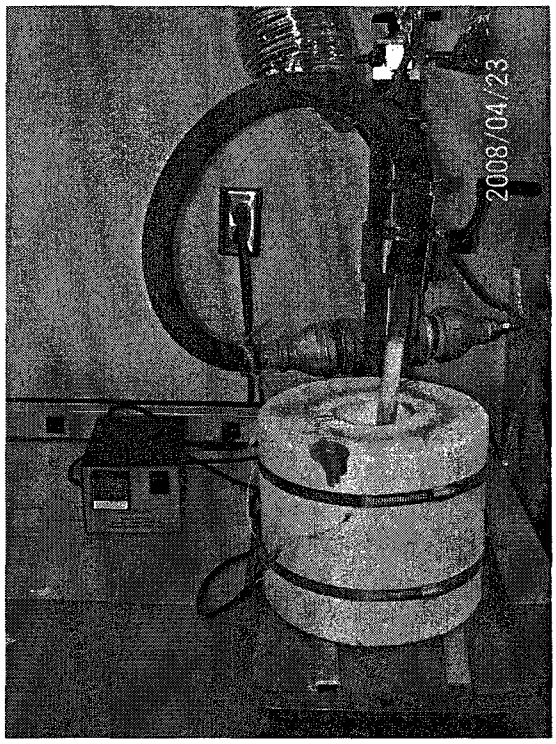


Figure 3.10 Digital photograph of the vacuum infiltration setup

The apparatus consists of a 25.4 cm drill-press support stand (head assembly removed), containing a rack and pinion system for adjusting the height of the specimen in and out of the melt. A 0.9525 cm diameter copper tubing connects the Leybold rotary vane vacuum pump (TRIVAC®-B/D8B) to the Swagelok 3-way ball valve, as well as the flow metering valve with vernier handle, and fittings. A 7.62 cm diameter, 10.16 cm long, galvanized steel pipe with appropriate end fittings are assembled into the system to act as a "catch-can" or a safeguard to prevent liquid aluminum from entering the pipes and pump of the vacuum system. A 15.625 mm inner diameter (ID), black vacuum rubber tubing (VWR®) was used to connect the quartz tube to the vacuum system. The outer diameter (OD) of the quartz tube and ID of the rubber tubing were chosen so as to make a tight fit.

Heating is carried out with an electrical resistance furnace (Heaters Controls & Sensors Ltd.) equipped with a maximum temperature of 1000°C. It comprises a two part, 180 degree semi-cylindrical ceramic heater, 120 V, 400 W, with a 7.62 cm ID x 10.16 cm heated height. The ceramic heater is surrounded by a 24.13 cm OD x 20.32 cm height insulation package and the heating is monitored using a lab controller with type K thermocouple. The aluminum was melted in a silicon carbide crucible (Morganite Crucible Inc., Starrbide, model; A Shape AS 1 CLM 454, bilge) with a top OD of 6.985 cm and height of 9.207 cm with an operating temperature of 700-850°C.

### 3.6.2 Description of Infiltration Constituents

Many experiments were carried out in order to determine the best infiltration procedure. The following materials were employed in all experiments, but configurations and amounts vary. To obtain sufficient sample sizes for standard ASTM mechanical property measurements, quartz tubes measuring 17 mm ID x 19 mm OD x 122 cm long were cut into 21 cm lengths (G.M. Associates, Inc.). The SiC foam was cut into rectangular cross-sections of 12.5 mm x 12.5 mm specimens to match the inner diameter of the quartz tube. Aluminum foil sheets 14 cm x 14 cm (Fisher Scientific) were used to wrap the preforms prior to inserting them into the quartz tube to prevent the high temperature mortar from entering into the porous structure. Alumina fiber, purchased from Zircar Ceramics Inc., was used as a sealant around the square sample as well as employed as a melt flow retardant above the sample. High temperature stove & gasket cement/mortar (Imperial Manufacturing Group$^{TM}$), resisting temperatures of up to 1149°C had a twofold use; (i) bind/solidify the preform to the quartz tube and (ii) act as a sealant between the square preform and cylindrical quartz tube. To prevent the alumina fibers from entering the

vacuum system, a 170 mm long, 2.22 mm diameter metal holding rod (made from a coat hanger) with a spiral at the end of approximately the same ID as the quartz tube was fabricated.

All samples for mechanical property measurement were machined to size (Precimax Ltd.). Polycrystalline diamond (PCD) milling inserts were used (APKW 100304 PDR, Grade ID 8, from Norvik Tooling Inc.). The insert is specific for machining aluminum composites and provides excellent surface finish results between 63-125 μm. Cutting parameters proposed by the supplier were; cutting speed of 242 m/min (800 SFM), feedrate of 0.1016 mm/tooth (0.004 inch per tooth) and a depth of cut 0.5-1 mm (0.02-0.04 inch).

### 3.6.3 Trial and Error Experiments

Several trial and error experiments were carried out in order to obtain an optimum infiltration, with as low porosity as possible. Here are a few learning errors during the preliminary infiltration phase;

- It was found that the high temperature stove & gasket cement had better flow characteristics while expanding less during drying than the Pyromix® high temperature mortar/cement.
- Inserting only 15 mm of the SiC foam inside the quartz tube, rather than the entire length, produced better infiltration results. Figure 3.11 (a-c) shows the stages in sample preparation for vacuum infiltration of aluminum. Figure (a) shows the 15 mm inserted SiC foam length into the quartz tube. Figure (b) shows the aluminum foil wrapped around the SiC foam and alumina fiber in-between the foam and tube. Figure (c) show the inserted SiC foam into the quartz tube after the

application of the high temperature stove gasket cement. If the entire sample is inserted, it becomes difficult to obtain a perfect seal around the 60 mm length foam. During infiltration, the aluminum tends to escape from the side of the tube without penetrating the foam.

- It was hypothesized that melting the quartz tube around the SiC foam, by employing an acetylene torch would provide an air-tight seal around a square cross-section as shown in Figure 3.12. However, during infiltration, the aluminum followed the side wall of the quartz tube to the top of the sample without penetrating the sample.
- Alumina fiber was found to aid in providing a seal between the circular ID of the quartz tube and the square cross-section of the foam as well as having an important role for controlling the flow of the melt through, above the sample and up the quartz tube. The alumina slows the speed of the melt flow and allows better infiltration since the melt has the opportunity to flow with restriction.
- For a better vacuum control, a more precise metering valve was positioned ahead of the ball valve since the ball valve provided too much flow even at its lowest setting.
- Instead of inserting the entire length of the sample into the melt, it was found that lowering the sample in 5 minute steps gave better infiltration results for both nickel and non-nickel coated samples.
- The aluminum/silicon alloy with approximately 2 wt% nickel coating provided better results. A higher vacuum was required for A356 aluminum alloy without nickel, which may have produced higher porosity since the aluminum did not

have time to flow through all the nooks and crannies of the foam, before solidifying.

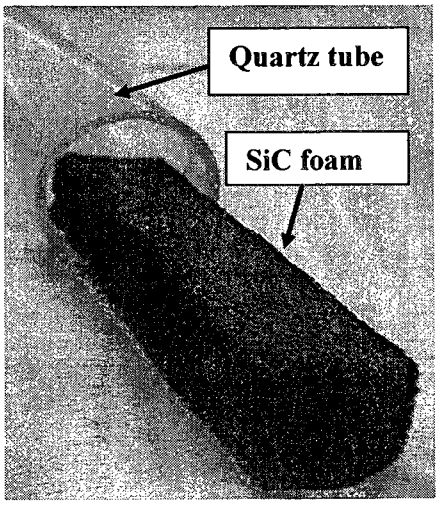


(a). Digital photo of SiC foam 15 mm inside the quartz tube

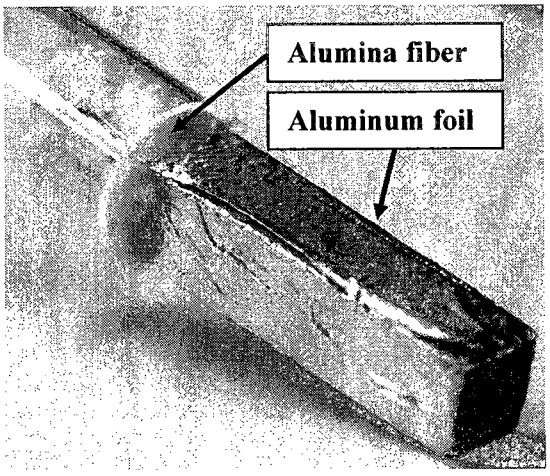


(b). Digital photo of SiC foam wrapped with aluminum foil and alumina fiber

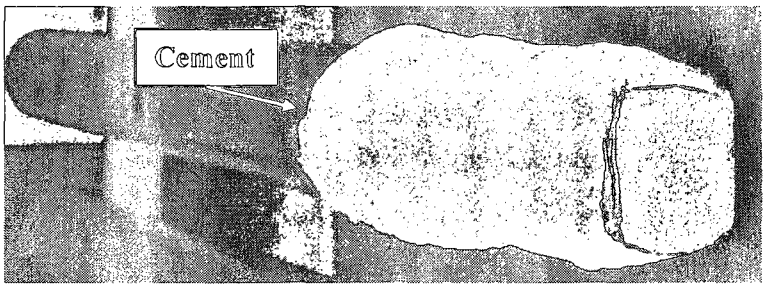


(c). Digital photo of the inserted SiC foam and gasket cement

Figure 3.11 (a-c). Digital photo of sample preparation for aluminum vacuum infiltration

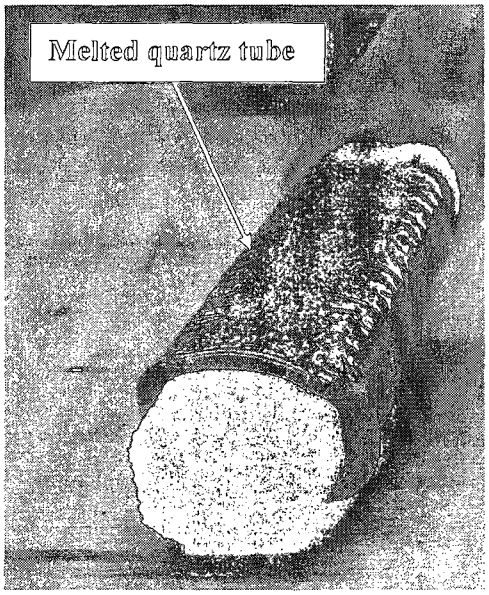


Figure 3.12 Digital photo of quartz tube melted around the SiC foam

The following is the final procedure used for this work; porosity (based on relative density) values ranged from 6-20%. Initial results had high porosity, but as the infiltration process improved, porosity decreased.

- Meter valve opening 0.005 inch.
- Melt temperature (Tm) of 775°C.
- Slightly packed, 12 cm of alumina throughout the length of the quartz tube.
- Before immersion, skim top oxide layer from aluminum melt using a stainless steel spatula.
- Initially submerge approximately 3 mm of the sample end tip in the aluminum melt.
- Every 5 minutes lower the sample into the melt 10 mm (two handle rotation (720°)) .
- Every time the melt flow reaches the top of the specimen, into the alumina, the pump is shut off until aluminum solidifies (10 seconds), then pump is turned back on.
- Continue to lower sample every 5 minutes until sample is immersed (approximately 30 minutes for a 60 mm length sample).
- Gradually apply maximum vacuum once entire sample is immersed, until no flow is visible.
- To prevent solidification shrinkage, remove the sample from the melt by raising the sample 10 mm every 3 minutes until entire sample is out of melt. (approximately 20 minutes for a 60 mm length sample)

The liquid aluminum flow through the SiC foam acts like water in a river. Once the flow begins to move inside the foam, it takes the path of least resistance, remaining in a "corridor" until it reaches the top of the sample to exit into the packed alumina foam. Due to the transparency of the quartz tube, the aluminum flow can be seen so the vacuum

pump can be shut-off to prevent aluminum flow into the set-up. By shutting the vacuum off, it gives a chance for the liquid aluminum to solidify. Once the vacuum is turned back on, the aluminum is presumed to take two directions; (i) some aluminum proceeds to flow where the previous aluminum solidified or (ii) some aluminum takes a different, unfilled path, in the foam. Where the previous aluminum solidified it causes a resistance to flow so the melt is forced to take another path.

## Chapter 4 Mechanical Testing Experiments

The interconnected three-dimensional struts are expected to be more efficient load bearing structures than single isolated solid particles, whiskers or short fibers. It is anticipated that this composite may have higher toughness properties than solid aluminum given the nature of the struts and their interface with the aluminum matrix absorbing the mechanical energy. MMC's in general, are a new type of material and for this reason, there are no acceptable standards yet written. Therefore, researchers observe the work of others and build their own testing procedures accordingly, as well as following ASTM standards as general guidelines.

### 4.1 Compression Test

Both the as-received SiC foam and A356/SiC foam composite were tested in compression. The SiC foam sample was tested on a screw-driven Instron model 3382 (Instron Corp.), with a load cell of 25 kN and cross-head speed of 0.1 mm/sec at room temperature. In order to determine the isotropic behavior of the SiC foam, three rectangular samples measuring 15 mm x 10 mm x 10 mm were cut from each direction, X, Y and Z of the as-received SiC foam, as illustrated in Figure 4.1. The maximum compressive strength was obtained from the position where the linear region ceases and the horizontal plateau begins as observed from the stress-strain curves of Figure 6.37.

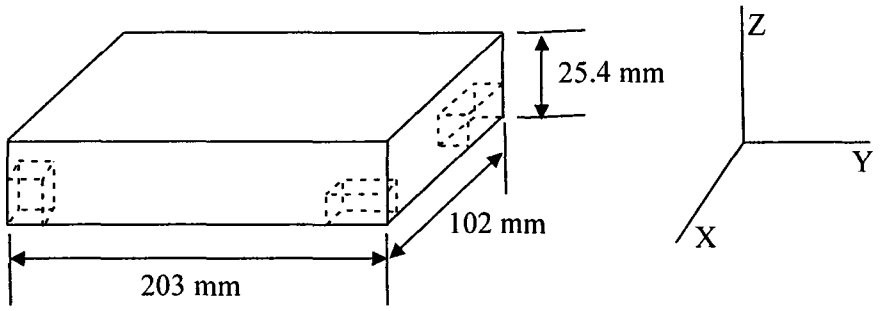


Figure 4.1 Dimensions of as-received SiC foam (203 mm x 102 mm x 25.4 mm)

In MMCs, the matrix and reinforcement have very different coefficients of thermal expansion/contraction, as a result, upon cooling; the two materials cool at different rates producing residual stresses which can cause dislocations to form at the ceramic/metal interface. If the residual stresses are greater than the yield stress of the matrix, the composite experiences plastic yielding and work-hardening on cooling. That is, the composite will yield at a higher value than the matrix, due to the already high internal stresses present. During MMC manufacturing or an annealing treatment following a cooling to room temperature, residual stresses are formed. For example, it has been shown to be difficult to remove residual stresses from heating an Al/SiC composite to 200°C and cooling it at a slow rate [108]. In the present work, initial compression testing of the Al/SiC foam composite revealed very low values of Young's modulus, therefore, a cycling procedure was performed to stabilize the dislocations in the matrix according to Prangnell et al. [109]. The low cycling, elastic deformation procedure re-distributes (or moves) the dislocations from a high density location (matrix/reinforcement interface) to a lower one without damaging the composite material.

For the low cycle fatigue compression test, the Al/SiC foam composites were initially pre-strained to the yield strength of the material, 50 MPa. (The yield strength of the Al/SiC foam composite was evaluated from conventional compressive stress-strain tests). Measurements of an average of four samples (without nickel) were taken from where the stress-strain curve ceases to be linear to obtain a yield strength of 50.7 MPa ± 9.46). On reaching 50 MPa, the stress was reduced to 2 MPa, followed by six fatigue cycles (or until an absence of hysteresis is observed) from 2 MPa to 10 MPa at 0.1 Hz. After cycling, it was ramped down to 2 MPa and finally ramped to failure. Young's modulus was determined from the slope of the linear, stress-strain region, where the cycling was performed as given in Figure 6.40.

Specimens were machined to a square cross-section of 100 $mm^2$ and 15 mm long, having a length-to-width ratio of 1.5 mm to avoid failure by buckling. A356/SiC foam specimens were machined from the vacuum infiltrated material. Testing was performed on an MTS with a 25 kN load cell, at room temperature with a cross-head speed of 0.0015mm/s (equivalent to a strain rate of 0.0001$s^{-1}$) and no barreling was observed. To obtain strain measurements, a strain gauge (CEA-06-125UW-350, Vishay Micro-Measurements) was installed on the face of each test sample. The Al/SiC (0 wt% Ni) and Al/SiC (2 wt% Ni) compression composite samples have porosities of 8.55% ±0.56 and 6.91% ±0.75, respectively determined by Equations 3.2 and 3.3. Three samples were tested to guarantee reliable results.

### 4.2 Flexural Strength

Flexural strength is the maximum tensile stress of a beam in bending and is a suitable substitute for the tensile test of brittle ceramic materials. Testing was done on a

screw-driven Instron model 3382 (Instron Corp.), with a load cell of 25 kN and cross-head speed of 0.5 mm/min. at room temperature. The four-point bend tests were conducted on the A356/SiC composites according to ASTM 1161-02C [110], as this has been employed by other workers for a graphite/aluminum interpenetrating composite network [77]. The four-point loading configuration is shown in Figure 4.2, where the load and support span are 20 mm and 40 mm, respectively. The dimensions of the rectangular specimens are machined to 6 mm x 8 mm x 50 mm, as shown in Figure 4.3.

The theoretical bend strength for the rectangular specimens is derived from beam theory [111]:

$$\sigma = Mc/I \tag{4.1}$$

Where M is the maximum bending moment, I is the moment of inertia and c is the distance from the neutral axis to the outer surface of the specimen. For a rectangular cross section, the expressions for a four-point loading configuration are given in Equations 4.2-4.4;

$$M = (P/2)\, a \tag{4.2}$$

$$c=d/2 \tag{4.3}$$

$$I = bd^3/12 \tag{4.4}$$

Where P is the break load, a, is the distance between the inner and outer supports (a = L/4), L is the outer support span, d is the thickness and b is width of the specimen. Substituting the above equations leads to the flexural stress formula;

$$\sigma_{4\text{-pt}} = 3\, PL/\, 4bd^2 \tag{4.5}$$

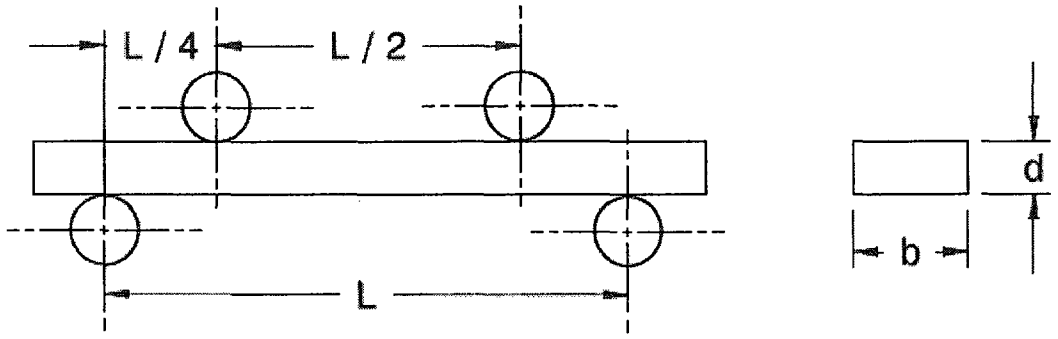


Figure 4.2 Schematic of the four-point bending configuration

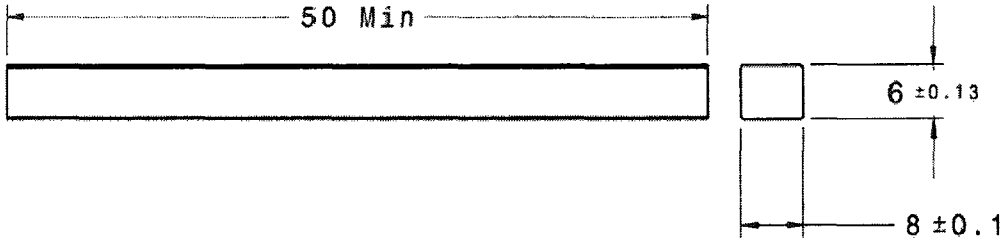


Figure 4.3 Schematic CAD diagram of the rectangular specimen for flexural strength. Dimensions in mm

### 4.3 Charpy Test

For use in lightweight structural applications, the ability of this MMC to withstand impacts is vital to its dependability as a structural material. In addition, the brittle ceramic foam is vulnerable to interior damage from possible impacts. In industry, Charpy test results are not used for design requirements due to the impact energy (toughness) results being sensitive to notch type, geometry and speed of loading. Rather, a Charpy test is a qualitative property for a particular condition and used to compare relative toughness of other engineering materials. It is simple, uses inexpensive equipment and is quick to do. Charpy tests are used to assess a material's fracture resistance, ductility and fracture

appearance. The material toughness or its resistance to fracture is determined by the amount of energy it can absorb during a high strain rate impact.

The cast aluminum and the A356/SiC foam composites were tested according to ASTM E23-02a [112], which was initially developed for metallic materials. Dimensions of the specimens used in this experiment are 10 mm x 10 mm x 55 mm, machined from the ingot and the as-fabricated composite material. Both V-notched and un-notched configurations were tested in order to determine whether the notch had an effect on the new composite material. Notched samples have a 45° V-notch, 2 mm deep, with a 0.25 mm root radius as shown in Figure 4.4, while the un-notched samples are shown in Figure 4.5. Each impact test was performed on an instrumented (SATEC Systems, Inc., model number SI-1B) Charpy, at room temperature, using three samples for each configuration and the results were averaged. The capacity of the machine is 8.4 m-kgs with a hammer weight of 6.1 kg and impact velocity of the hammer arm of 5.4 m/s. The apparatus is equipped with software to provide load versus time as well as absorbed energy versus time graphs. The instrumented Charpy impact test can determine the total absorbed energy ($E_T$) which is the sum of the crack initiation energy ($E_I$) and the crack propagation energy ($E_P$). It will be shown in all Charpy load-time curves, Figure 6.57 and 6.60, the first rise and fall can be neglected as this is due to noise from the hammer impacting the specimens. It is caused by the initial response from the instrument reading the load and time response. The main peak, is the maximum impact load of the specimen, while the remaining peaks are noise from the impact force propagating through the material which is captured by the sensor/detecting instrument.

It is anticipated that the composite will behave in a more ductile manner than a pure brittle ceramic. A previous study on co-continuous $Al/Al_2O_3$ composite employed an un-notched specimen [74] whereas an Al/20 vol% SiC composite used a V-notched specimen [113].

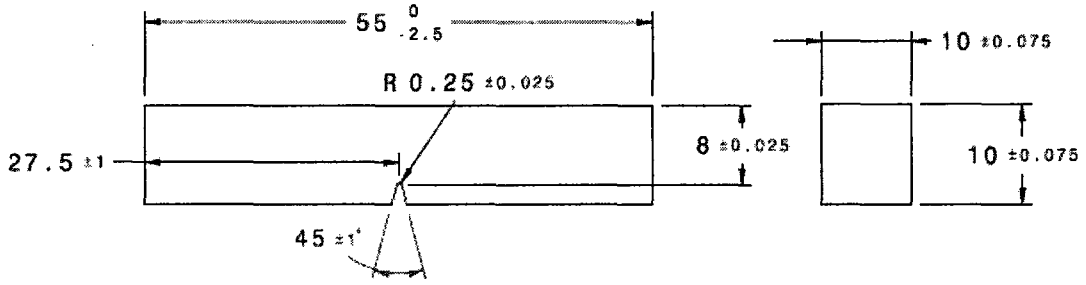


Figure 4.4 Charpy notched test sample. Dimensions in mm

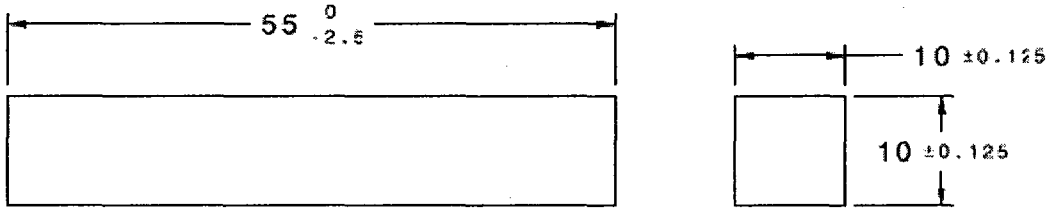


Figure 4.5 Charpy un-notched test sample. Dimensions in mm

### 4.4 Fracture Analysis

Subsequent to the Flexural strength and Charpy testing, fractographic analysis of the fractured surfaces were performed as given in Figures 6.49-6.53 and Figures 6.61-6.63, respectively. Fractography is the analysis of the fractured surface in an attempt to determine the cause of fracture. Fracture surfaces of the broken samples were examined by SEM to determine the fracture properties and failure mechanisms of the composite:

more specifically to help identify the contribution of the matrix and reinforcement as well as their failure behaviors.

### 4.5 Micro-Hardness Test

To confirm the modulus values of the composite phases (A356, SiC and C), hardness and Young's modulus were obtained from a nano-indentation test, performed on a Hysitron Triboscope®, equipped with a Berkovich three-sided diamond pyramid indenter with a tip radius of 100 nm, measured at room temperature. The composite test sample size was approximately 7 mm in diameter, 4 mm high and finished to a smooth and parallel surface by grinding with 240, 320, 400, 600, 800, 1200 and polishing to a mirror finish using colloidal silica (0.05 microns) as the polishing agent.

Hardness and Young's Modulus of the specimen ($E_s$) were evaluated from the unloading curve of the load–displacement data by the technique proposed by W.C. Oliver et al. [114]. The hardness (H) is found from Equation 4.6, where $P_{max}$ is the maximum indentation force, and A is the projected contact area between the indenter, and the specimen at this load. The contact area at maximum load is related to the geometry of the pyramidal indenter and the contact indentation depth, $h_c$ (i.e. $A = 24.5(h_c)^2$). The two parameters ($P_{max}$ and $h_c$) are obtained from the load-displacement curves.

$$H = P_{max}/A \tag{4.6}$$

The modulus of the sample (Es) can be found from Equation 4.7.

$$Es = (1-\nu_s^2) / (1/Er - (1-\nu_i^2)/E_i) \tag{4.7}$$

The poisson's ratio of the sample, $\nu_s$ is required for calculation, a value is assumed for all three materials; A356 aluminum alloy, CVD-SiC and carbon ($\nu_{Al} = 0.33$, $\nu_{SiC} = 0.21$ and $\nu_C = 0.33$, respectively). The diamond indenter elastic modulus, $E_i$, is

1140 GPa and poisson's ratio $\nu_i$ is 0.07. The reduced modulus (Er) accounts for the assumed effect that both the specimen and indenter elastically deform during the measured displacement. It is related to the contact area, A and the initial unloading contact stiffness, S, given in equation 4.8.

$$Er = (\sqrt{\pi}/2)/(S/\sqrt{A}) \quad (4.8)$$

Generally, the region between 20% and 95% of the initial unloading portion of the load-displacement curve is used to determine the slope and thus the contact stiffness.

### 4.6 Thermal Diffusivity

The determination of the thermal diffusivity of the A356/SiC foam composite will establish how quickly the heat will flow through the material and thus change the materials' temperature. Electronic packaging materials with high thermal diffusivities are very efficient for circulating heat flow through the material and are less likely to fail from thermal shock. The thermal diffusivity ($\alpha$) of the composite was measured by a laser flash method using an Xenon Flash apparatus (NETZSCH Model LFA447 Nanoflash) from 25°C to 275°C, in steps of 50°C. Three samples of the composite were tested at one time with 0% nickel and repeated for 2% nickel samples. Square specimens measuring 12 mm x 12 mm x 1 mm were ground to 600 grit. In this technique, the test samples are irradiated on the front side, while the temperature rise is measured on rear side. To improve the absorption of flash energy as well as the emission of infrared radiation to the detector, three graphite coatings were applied to the composite samples.

## 4.7 Specific Heat Capacity

The temperature of an electronic packaging unit must remain stable for a large heat input. The base plate often called a 'heat spreader', acts to spread the heat away from the ceramic substrate. To remove heat quickly, the base plate material will require a low specific heat capacity. In contrast, a heat sink stores heat, therefore it requires a high specific heat capacity material. The heat capacity ($C_p$) of the Al/SiC composite was measured using a differential scanning calorimeter (DSC TA Instruments, model Q10) from 20 °C to 300 °C, in steps of 0.25 °C with a heating rate of 20 °C/min. The samples were made into a powder using a clean metal file. Sample 1; Al/Ni-SiC composite had a mass of 11.4 mg and sample 2; Al/SiC composite had a mass of 10.2 mg. The heating profile employed is as follows; equilibrate at 0 °C, isothermal for 10 minutes, ramp 20 °C/min to 300 °C, equilibrate at 300 °C and isothermal for 10 minutes.

## 4.8 Thermal Conductivity

In electronic packaging applications, high thermal conductivity materials are sought to dissipate or remove the heat quickly from the electrical devices. Thermal conductivity will establish the amount of heat flow through the material. It will be affected by the two different material phases in the composite and its internal structural network. Typical packaging materials have a thermal conductivity of between 15-200 W/m°C as given in Table 1.1 but maximizing this value is a benefit. The composite experimental thermal conductivity (k) is calculated from the experimental thermal diffusivity ($\alpha$), specific heat capacity ($C_p$) and density ($\rho_{comp}$) using Equation 4.9:

$$k = \alpha/\rho_{comp} C_p \qquad (4.9)$$

### 4.9 Coefficient of Thermal Expansion

Electronic packaging materials require low coefficients of thermal expansion (CTE) so their dimensions due to temperature fluctuations do not differ by a great amount. In addition, the materials on either side of the base plate (Figure 1.1) should have similar CTE's to the ceramic substrates above and the heat sink below. The volume fraction of reinforcement is typically 50-70% for attaining low CTE's in electronic packaging materials. The CTE of the composite is expected to be lower than for aluminum alloy since it contains SiC ceramic, and nickel will also reduce the CTE. The CTE of the composite was measured using a thermo-mechanical analyzer (TMA), (TA Instruments model Q400). The CTE was measured from 30 to 300°C with a heating rate of 5°C/min. The specimen measured 11 mm long and 5 mm in diameter.

### 4.10 Composition/Microstructure Analysis Methods

#### 4.10.1 Characterization Analysis Methods

The composition of a crystalline solid or powder can be determined by X-Ray Diffraction Spectroscopy (XRD). Each material has a unique X-ray pattern and qualitative analysis can be performed by XRD. The XRD pattern was recorded using an X-ray diffractometer, (X'Pert PRO, manufactured by PANalytical Inc.), with a Cu-Kα radiation produced at 35 kV and 20 mA over a 2θ angle scanning range between 15-90°.

#### 4.10.2 Energy Dispersive X-ray Spectroscopy

The morphology of the composite and fractured samples was characterized using Scanning Electron Microscopy (SEM) and an optical microscope. The SEM is a JEOL

840A equipped with an EDS or EDX (Energy Dispersive X-Ray Spectroscopy), model Edax Phoenix system (with a "Sapphire" ultra-thin window for light -element analysis) to measure (qualitative and quantitative) the elemental composition of a sample. SEM is used in this research to produce high resolution, high magnification images of the morphology of the solid surfaces of the specimens. Non-metallic samples were made electrically conductive by coating with a thin conductive layer of metal (e.g. gold) using a sputter coating machine.

# Chapter 5 Modeling Metal Matrix Composites

Modeling is used to theoretically estimate the properties of composite materials based on ideal conditions and a variety of assumptions to further compare to experimental results. For purpose of analysis, simplified shapes and perfect bonding between the matrix and reinforcement is assumed. A common modeling assumption for SiC ceramic particles, is that they are spherical, however commercially available SiC particles do not have a regular shape and are not even spherical. Unrealistic hypothesizes lead to inaccurate predictions. Theoretical models for predicting upper and lower bounds for Young's modulus and thermal properties such as, thermal diffusivity, specific heat, thermal conductivity and CTEs have been developed in order to establish the spread of experimental results for the composite materials.

Various models have been suggested for predicting the elastic Young's modulus of MMCs. Although the literature contains many models for different types of MMC reinforcement such as modeling fibers as cylinders and particles as spheres, there are no model equations for open-cell foam with an elastic filler [115]. Moreover, sufficient investigations have not been done in the field of two-phase interpenetrating composites due to the difficulty in treating a three-dimensional interpenetrating structure [116]. Common analytical models that have been attempted in literature for predicting the Young's modulus for IPC are discussed below.

## 5.1 Common Models for Predicting Composite Young's Modulus

The Rule of Mixtures (ROM) upper and lower bounds are used as a preliminary approximation in nearly all types of reinforcement geometries. As a first assumption, many researchers tend to use the ROM model to predict the axial and transverse Young's

modulus of a two phase composite material arranged as two slabs, side by side. Voigt [117] proposed, when the load is applied in the axial direction, the matrix and reinforcement phases experience the same strain (iso-strain). Similarly, Ruess [118] hypothesized when the load acts in the transverse reinforcement direction, the matrix and reinforcement phases experience the same stress (iso-stress).

These two models assume; (i) a two-phase composite, (ii) homogeneous materials, (iii) both phases have the same Poisson's ratio and both deform elastically, (iv) both perfectly bonded alternating phases are aligned parallel and perpendicular to the axial load direction, respectively. These two models were first conceived for predicting the composite stiffness of two phases, side by side, of unknown micro-structural phase geometry, but known phase volume fractions. They have been found to give good estimates for continuous fiber reinforced composites. Voight obtained the longitudinal or upper limit composite modulus ($E_c^U$) as given in Equation 5.1 (iso-strain).

$$E_c^U = E_m V_m + E_r V_r \tag{5.1}$$

where, U denotes the upper bound, $V_m$ and $V_r$ are the volume fractions of the matrix and reinforcement, respectively. A theoretical equation for obtaining the composite modulus was obtained by modifying Equation 5.1 for a lower reinforcing efficiency of 3-D, isotropic, discontinuous and randomly distributed fibers, as given in Equation 5.2 [119]. The reinforcement efficiency parameter ($K_e$) is 1/5 of an aligned composite in the longitudinal direction.

$$E_c = E_m V_m + K_e E_r V_r \tag{5.2}$$

Reuss obtained the transverse or lower limit composite modulus ($E_c^L$) as given in Equation 5.3, where L, denotes the lower bound (iso-stress).

$$E_c^L = \frac{E_m E_r}{E_m V_r + E_r V_m} \tag{5.3}$$

A tighter envelope is provided by Hashin and Shtrikman [120] upper & lower bounds (HS bounds) which estimate the upper and lower limits for the elastic Young's modulus of a composite. This model assumes; isotropic, homogeneous, two phase composite and both phases deform elastically. The volume fraction of the phases is known but phase geometry and distribution is unknown, therefore no information is given for bonding between matrix and reinforcement. The randomly distributed reinforcement phase is surrounded by a continuous matrix phase, both of unknown geometries.

To obtain the upper and lower elastic modulus (E), they calculated the upper and lower limits of the bulk modulus (K) and bulk shear modulus (G) based on energy methods. For isotropic materials, E, K and G are related by equations 5.4 and 5.5 and 5.6, respectively;

$$K = \frac{E}{3(1-2\nu)} \quad (5.4) \qquad G = \frac{E}{3(1+\nu)} \quad (5.5) \qquad E = \frac{9KG}{3K+G} \quad (5.6)$$

The HS upper bound for the bulk modulus ($K_c^U$) and bulk shear modulus ($G_c^U$) are given in Equations 5.7 and 5.8, respectively.

$$K_c^U = K_r + \left[\frac{V_m}{\frac{1}{K_m - K_r} + \frac{3V_r}{3K_r + 4G_m}}\right] \text{ if } K_r > K_m \tag{5.7}$$

$$G_c^U = G_r + \left[\frac{V_m}{\frac{1}{G_m - G_r} + \frac{6V_r(K_r + 2G_r)}{5G_r(3K_r + 4G_r)}}\right] \text{ if } G_r > G_m \tag{5.8}$$

The HS lower bound for the bulk modulus ($K_c^L$) and bulk shear modulus ($G_c^L$) are given in Equations 5.9 and 5.10, respectively.

$$K_c^L = K_m + \left[\frac{V_r}{\frac{1}{K_r - K_m} + \frac{3V_m}{3K_m + 4G_m}}\right] \text{ if } K_r < K_m \tag{5.9}$$

$$G_c^L = G_m + \left[\frac{V_r}{\frac{1}{G_r - G_m} + \frac{6V_m(K_m + 2G_m)}{5G_m(3K_m + 4G_m)}}\right] \text{ if } G_r < G_m \tag{5.10}$$

## 5.2 Theoretical Model for Predicting Young's Modulus with Porosity

The majority of theoretical models for predicting Young's modulus of porous ceramic materials are based on two phase composites of which one phase is the matrix and other phase is voids or pores. The pores are modeled in a variety of geometries; cubes, spheres, non-spherical and variable pore shape, and orientation. In this research we would have to assume that the aluminum/SiC foam form one part of the composite and the second part is formed by voids which is not a realistic assumption as both aluminum and silicon carbide phases have entirely different properties, unless the Al/SiC material can be homogenized for modeling purposes.

However, by first assuming a two phase composite, the A356 aluminum alloy as one phase and the voids as the other phase, an estimate of the Young's modulus can be determined based on the spherical model given by Equation 5.11. It is an empirical relationship, where $E_o$ is the Young's modulus of the solid material and P is the porosity volume fraction. Equation 5.11 is the Coble and Kingery [121] model which is often

employed to predict the modulus of porous ceramics, but has been used for porous metals.

$$E = E_o (1 - 1.9P + 0.9P^2) \quad (5.11)$$

This spherical model assumes, the material is homogeneous and isotropic, containing randomly distributed spherical pores of the same size and based on a Poisson's ratio of 0.3. For a 8.5% (based on approximate porosity of three compression A356/SiC (0% Ni) samples in Table 6.5) porous A356 aluminum alloy matrix, the modulus obtained from Equation 5.11 (i.e 62.7 GPa) and the SiC foam strut modulus (Equation 5.1: i.e. 243 GPa) is substituted into the ROM and Hashin-Shtrikman models.

In the literature, limited studies have been performed for theoretically determining the modulus of a porous; two phase matrix/reinforcement composite. Cohen and Ishai [122] proposed a cubic model for a three-phase composite encompassing a matrix, a reinforcement and porosity. The model predicts an upper and lower bound based on a cubic model consisting of a solid cubic reinforcement surrounded by a porous cubic matrix. The iso-strain model forms the upper bound while the iso-stress model forms the lower bound. They obtained results within the upper and lower bounds for their model when compared against epoxy/quartz sand composites. In another study [123], of a three-phase polymer concrete system, the predicted compression modulus using the Cohen/Ishai model was in reasonable agreement with experimental values. The model assumes uniform, isotropic material, elastic behavior, and that the loading is applied uniformly at the boundaries. However, it neglects Poisson's effects and bonding between the matrix and reinforcement.

For a two phase matrix/reinforcement with no porosity, the composite modulus ($E_c$) for the upper limit is found from the iso-strain cubic model as given by Equation 5.12, where $E_m$ is the modulus of the matrix with no porosity, $V_f$ is the volume fraction of the reinforcement, m, is the reinforcement to matrix modulus ratio. For two phases, comprising of matrix with porosity, the composite modulus with porosity ($E_{cp}$) is given by equation 5.13, where $V_v$ is the volume of the voids or porosity. Substituting $E_{cp}$ for $E_m$ into Equation 5.12, the modulus for the three phase composite is obtained and given by Equation 5.14, where [$m^* = E_f/E_{cp}$].

$$E_c = E_m \left[1 + \frac{V_f}{\frac{m}{m-1} - (V_f)^{1/3}}\right] \tag{5.12}$$

$$E_{cp} = E_m\left(1 - V_v^{2/3}\right) \tag{5.13}$$

$$E_{c3} = E_m\left(1 - V_v^{2/3}\right)\left[1 + \frac{V_f}{\frac{m^*}{m^*-1} - (V_f)^{1/3}}\right] \tag{5.14}$$

For the same cubic configuration, the composite modulus ($E_c$) for the lower limit is found from the iso-stress model for a two phase composite with no porosity, as given by Equation 5.15. The modulus of the matrix with porosity is given by Equation 5.16. Similarly, the three-phase composite is given by Equation 5.17.

$$E_c = E_m \left[\frac{1+(m-1)(V_f)^{2/3}}{1+(m-1)\,(V_f^{2/3} - V_f)}\right] \tag{5.15}$$

$$E_{cp} = E_m \left[\frac{1 - V_v^{2/3}}{1 - V_v^{2/3} - V_v)}\right] \tag{5.16}$$

$$E_{c3} = E_m \left[ \frac{1 - {V_v}^{2/3}}{1 - {V_v}^{2/3} - V_v)} \right] \left[ \frac{1+(m^*-1)(V_f)^{2/3}}{1+(m^*-1)\,({V_f}^{2/3} - V_f)} \right] \quad (5.17)$$

### 5.3 Modeling of Thermal Properties

Similarly to modeling of the Young's modulus for a two-phase composite, the literature does not contain theoretical thermal property models for three-dimensional network structures. Current available models are for two-phase isotropic fiber/particulate materials. For purposes of a first, rough estimate, the following thermal properties were calculated using the ROM parallel and series models.

#### 5.3.1 Thermal Diffusivity

Thermal diffusivity ($\alpha$) is a measure of how fast a material can change its temperature and is calculated using Equation 5.18, where $\rho_{comp}$ is the density of the composite, while the thermal conductivity ($k_c$), Equation 5.20 and specific heat capacity ($C^c_p$), Equation 5.19 are obtained from their respective ROM equations.

$$\alpha. = k/\rho_{comp}\, C_p \quad (5.18)$$

#### 5.3.2 Specific Heat Capacity

Specific heat capacity ($C_p$) is a measure of energy required to raise the temperature of a certain mass by one degree. The ROM for determining the specific heat of various aluminum MMC's was used and results were close to the experimental [124], thus Equation 5.19 was employed in this research for determining the $C_p$ of this composite where subscripts c, m, and r refer to the composite, matrix and reinforcement,

respectively. This equation is accurate for continuous fibers in transversely isotropic composites where the matrix is considered to be isotropic and the reinforcement is anisotropic.

$$C^c_p = (V_r\ C^r_p + V_m\ \ C^m_p) \tag{5.19}$$

### 5.3.3 Thermal Conductivity

To determine the heat flow through the composite, parallel or along the fiber direction, the parallel ROM is given in Equation 5.20 [125], where k, is the thermal conductivity and V is the volume fraction of each phase.

$$k_c = k_r\ V_r + k_m\ V_m \tag{5.20}$$

When the heat flow through the composite is perpendicular or transverse to the fiber direction, the series ROM is given by Equation 5.21 [125].

$$kc\ = \frac{1}{\left(\frac{Vr}{kr} + \frac{Vm}{km}\right)} \tag{5.21}$$

Both of these models consider the composite to be homogeneous, completely dense, the fiber/reinforcement to be continuous and matrix to be isotropic, however, it does not reflect the reinforcement shape/geometry. It also presumes, there is no phase transformation at the interface between the matrix and reinforcement.

The Effective Medium Theory (EMT) model is employed to predict the thermal conductivity of this composite as given by Equation 5.22 [126], where $V_r$ and $V_m$ are the volume fraction of the reinforcement and matrix, $k_r$ and $k_m$ are the thermal conductivities

of the reinforcement and matrix and K is the thermal conductivity of the composite as a whole. The EMT model assumes a heterogeneous material, where the two phases are distributed randomly. The components are a mixture of continuous and discontinuous phases.

$$Vr\frac{kr-K}{kr+2K} + Vm\frac{km-K}{km+2K} = 0 \tag{5.22}$$

### 5.3.4 Coefficient of Thermal Expansion

Two models were chosen to determine which existing model best describes the experimental CTE of this composite. The Rule of Mixtures (ROM) is widely used as a first upper limit approximation and has been employed for the CTE of a ceramic metal composite [127] to estimate the linear coefficient of thermal expansion (CTE) in the transverse direction of a two-phase composite material, given by Equation 5.23. This model assumes no thermal interaction (the phases are not constrained by each another) and similar modulus values between the matrix and the reinforcement. Each phase expands or contracts at different rates. During expansion, the model assumes equal stresses (or no stress transfer between the matrix and reinforcement) throughout the two phases in the composite (iso-stress).

$$\alpha_c = \alpha_r V_r + \alpha_m V_m \tag{5.23}$$

Where $\alpha_c$ , $\alpha_r$ and $\alpha_m$ are the CTE of the composite, fiber/reinforcement and matrix, respectively. The fiber volume fraction is given by $V_r$ and the matrix volume fraction by $V_m$.

The Turner [127] equation estimates a lower limit of the linear CTE in the longitudinal direction of a two-phase composite material, given by Equation 5.24, where K is the bulk modulus of each phase. This model assumes thermal interaction (the phases are constrained by each other) and dissimilar modulus values between the matrix and the reinforcement. Each constituent dimension is assumed to change, expand or contract at the same rate as the overall composite. The model assumes equal strains (no strain transfer between the matrix and reinforcement) throughout the two phases in the composite (iso-strain). When $K_m = K_r$, the Turner model is equal to the ROM model.

$$\alpha c = \frac{\alpha m\, Vm\, Km + \alpha r\, Vr\, Kr}{Vm\, Km + Vr\, Kr} \tag{5.24}$$

# Chapter 6 Experimental Results

## 6.1 Pyrolysis of Wood Species

The pyrolysis process produces a carbon structure retaining the same morphology as the original wood, though with some shrinkage. The final carbon specimens were approximately 15 mm x 11 mm x 13 mm (axial, radial, and tangential) in size. Subsequent to pyrolysis at 1400°C, shrinkage and weight gain from the accumulated $SiO_2$ were measured with their respective standard deviations and are shown in Table 6.1. An average of three samples of each species was geometrically measured, weighed and the average taken. The shrinkage is anisotropic with the tangential direction having the most shrinkage as compared to the axial and radial directions for pine, beech and maple. However, the weight loss due to pyrolysis is approximately the same. After ceramization, a weight loss in the carbon/$SiO_2$ composite is observed for all wood species samples due to the production of the carbon monoxide (CO) gas escaping from the composite as will be discussed in section 6.2.1.

Table 6.1 Microstructural changes of different Canadian wood species following pyrolysis at 1400°C, followed by infiltration of $SiO_2$

| Wood species | | Pine | Beech | Maple |
|---|---|---|---|---|
| After Pyrolysis (1400°C) | | | | |
| Linear shrinkage (%) | Axial | 21 ± 0.42 | 21 ± 0.21 | 21 ± 0.06 |
| | Radial | 28 ± 0.37 | 33 ± 0.46 | 32 ± 0.37 |
| | Tangential | 32 ± 0.02 | 43 ± 0.88 | 42 ± 0.70 |
| Bulk density ($g/cm^{-3}$) | | 0.25 ± 0.002 | 0.57 ± 0.012 | 0.54 ± 0.003 |
| Weight loss (wt%) | | 78.3 ± 0.16 | 77.5 ± 0.10 | 78.5 ± 0.034 |
| After $SiO_2$ infiltration (non-ceramized) | | | | |
| Weight gain (wt%) | 2 repeated | 215 ± 3 | 72 ± 6 | 88 ± 4 |
| Bulk density ($g/cm^{-3}$) | infiltrations | 0.69 ± 0.01 | 0.84 ± 0.03 | 0.75 ± 0.04 |
| Weight gain (wt%) | 2 cyclic | 243 ± 9 | 90 ± 5 | 117 ± 3 |
| Bulk density ($g/cm^{-3}$) | infiltrations | 0.60 ± 0.08 | 0.80 ± 0.04 | 0.58 ± 0.03 |

### 6.2 Silica Sol Infiltration Results

Levasil 50 sol ($SiO_2$) was used in this study based on previous results by Herzog et al. [50] who indicated that porous SiC samples could be obtained, and to increase the amount of silica per infiltration it is preferred to use water-based sols over alcohol-based sols. Moreover, "cyclic" infiltration produces a more efficient infiltration of the liquid sol than the "repeated" infiltration. The $SiO_2$ accumulations in the present study indicate similar findings in terms of efficiency, as presented in Table 6.1. In an attempt to reproduce the results of other researchers, both repeated and cyclic infiltration were carried out on three specimens of carbonized pine, beech and maple tree species. Theoretically, the $SiO_2$ to carbon mass ratio for full conversion to SiC is 1.67 or a stoichiometric accumulation of 167 wt% $SiO_2$. As shown in Table 6.1, this study revealed

that two repeated infiltrations resulted in a dry $SiO_2$ accumulation of 215 wt% ± 3 (56 wt% in the first uptake and 159 wt% in the second uptake) for pine, 72 wt% ± 6 (26 wt% in the first uptake and 46 wt% in the second uptake) for beech and 88 wt% ± 4 (31 wt% in the first uptake and 57 wt% in the second uptake) for maple. Other researchers [128] carried out repeated infiltration with different sols (tetraethyl-orthosilicate-TEOS, zirconium n-propoxide-ZNP and titanium isopropoxide-TTiP) into carbonized pine which resulted in low weight gains after multiple infiltrations and they concluded that the pores clogged after several infiltration/drying cycles. The stoichiometric amount required for pine was achieved, however, beech and maple did not reach their required amounts. As shown in Figure 6.1, an SEM cross-section at half the cube high (~7.5 mm) was taken to observe the silica accumulation into the carbonized wood, after one repeated infiltration phase (or three infiltration/dry cycles). For an uptake of 56 wt% silica, the infiltration is not uniform, some tracheids are filled with silica, while others are empty. Similarly, in Figure 6.2, some tracheids are completely filled with silica along the longitudinal direction, while others are unfilled. In the same way, a number of tracheids and fibers in the carbonized beech are filled with silica, while others are unfilled as shown in Figure 6.3 and 6.4. To have a complete conversion to SiC, the silica distribution should be more homogeneous. The ideal would be to have all pores filled with silica.

The $SiO_2$ accumulation for the two cyclic infiltrations of pine in the present work is 243 wt% ± 9 (74 wt% in the first uptake and 169 wt% in the second uptake) while beech resulted in 90 wt% ±5 (40 wt% in the first uptake and 50 wt% in the second uptake). This contrasts to a previous study where two cycles with Levasil 50 were sufficient for obtaining the stoichiometric amount in carbonized beech wood [49] (their

first infiltration produced an $SiO_2$ accumulation of 86 wt%, while their second infiltration produced an additional 90 wt% $SiO_2$, for a total of 176 wt% $SiO_2$, well above the required amount). Similarly, another study by the same group of researchers achieved, after two cyclic infiltrations of pine and beech, a total of 220 wt% (105 wt% in the first uptake and

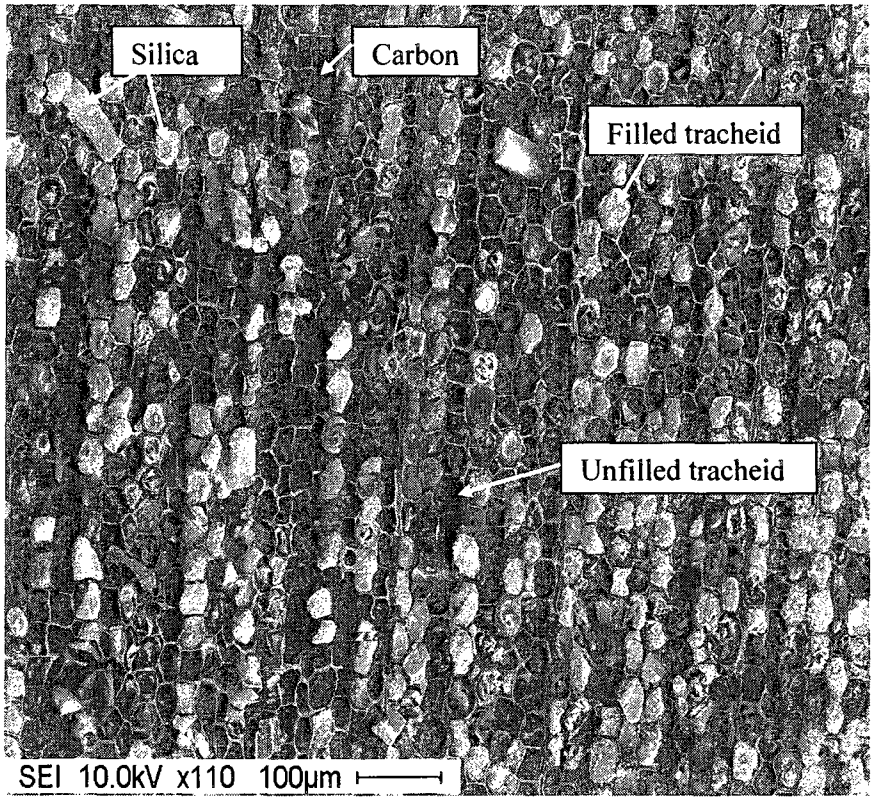


Figure 6.1 Cross-section direction of infiltrated silica into carbonized pine

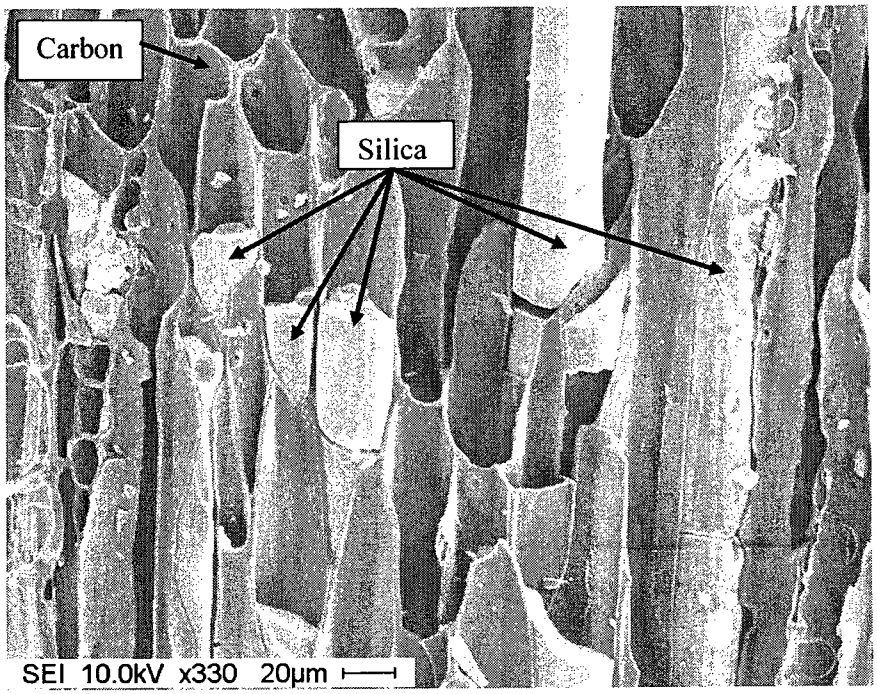


Figure 6.2 Longitudinal direction of infiltrated silica into carbonized pine

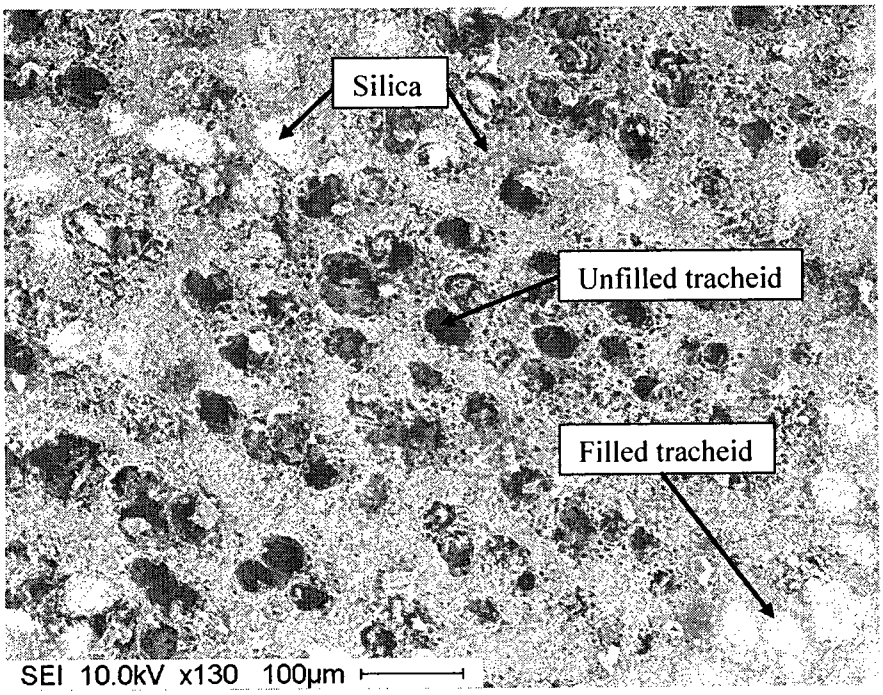


Figure 6.3 Cross-section direction of infiltrated silica into carbonized beech

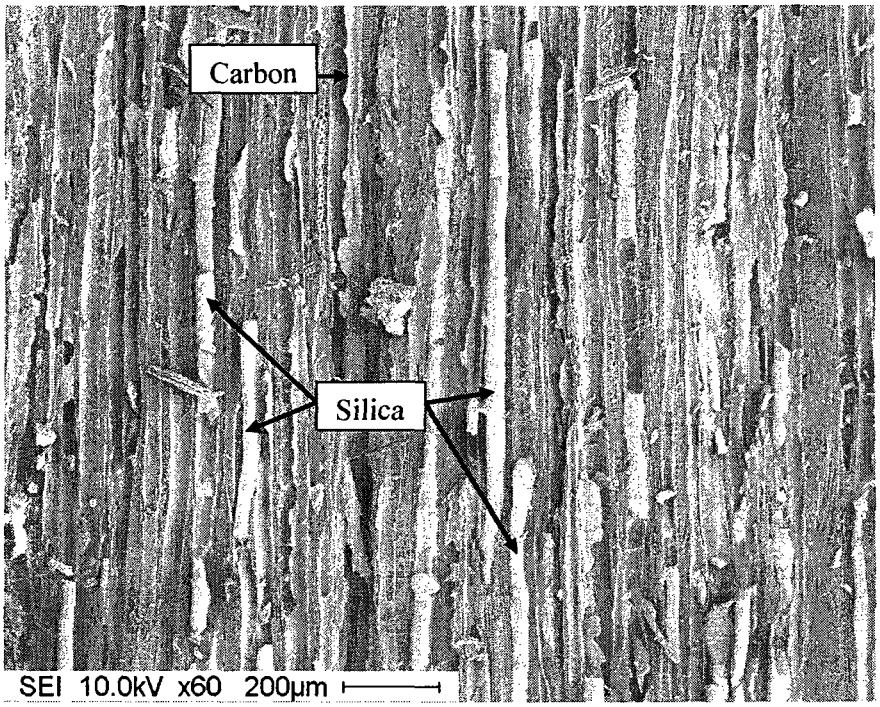


Figure 6.4 Longitudinal direction of infiltrated silica into carbonized beech

110 wt% in the second uptake) and 141 wt% (68 wt% and 78 wt%) $SiO_2$ accumulation, respectively [50]. In the present study another trial was conducted for two cyclic infiltrations of $SiO_2$ into carbonized maple, which showed a weight gain of 117 wt% ± 3 (37 wt% in the first uptake and 80 wt% in the second uptake). Although pine samples from both infiltration methods have enough $SiO_2$, beech and maple have insufficient quantities. The cyclic infiltrated pine sample theoretically has enough $SiO_2$ to fully convert the carbon to SiC, however after the second ceramization, an oxidation in air at 700°C for 1 hr was carried out in which a weight loss of 20% indicated that carbon remained after ceramization. No further work in terms of infiltration with molten metal was done on these samples since they could not be fully converted into SiC using either

of the two methods. The following describes the work done to determine the limiting reasons for this incomplete ceramization.

After two cyclic ceramizations, all three samples were cross-sectioned at approximately 7.5 mm (half the cube height in the longitudinal direction) using a diamond saw blade and ground finished to 1200 grit. SEM micrographs were taken in the axial direction for one growth ring (or annual ring) as well as the longitudinal direction for pine, beech, and maple, Figure 6.5 shows the filled, non-aspirated, latewood cells and the mostly unfilled, aspirated earlywood cells. Similarly, in Figures 6.6 and 6.7 the small diameter tracheids/fibers are filled while the larger vessel earlywood cells are unfilled. In Figure 6.7, SiC whiskers have grown in some of the large vessels.

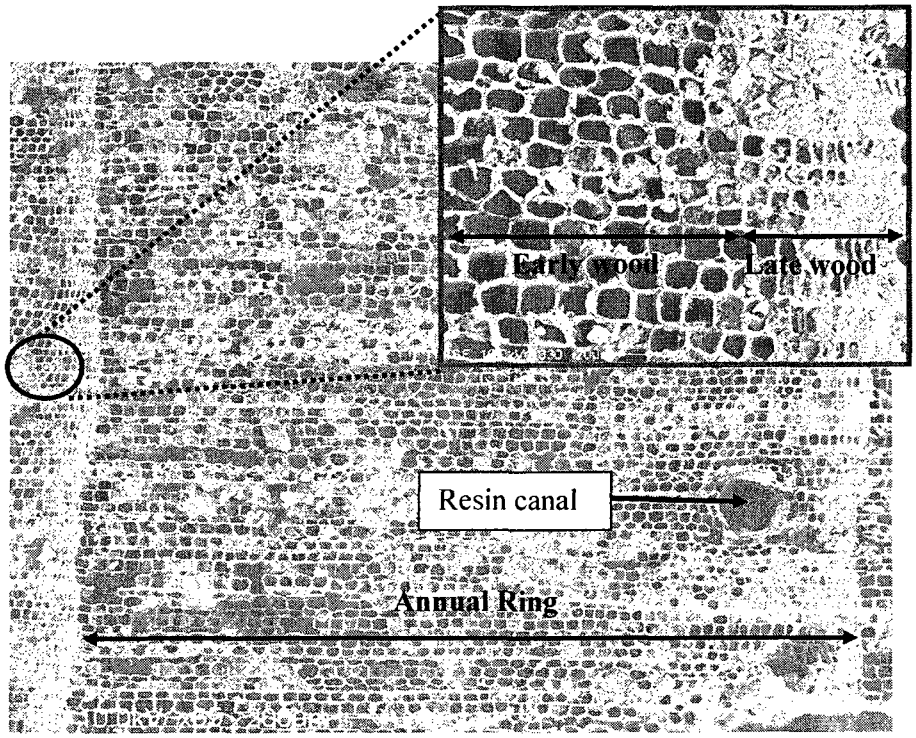


Figure 6.5 Axial direction of ceramized pine, showing one growth ring

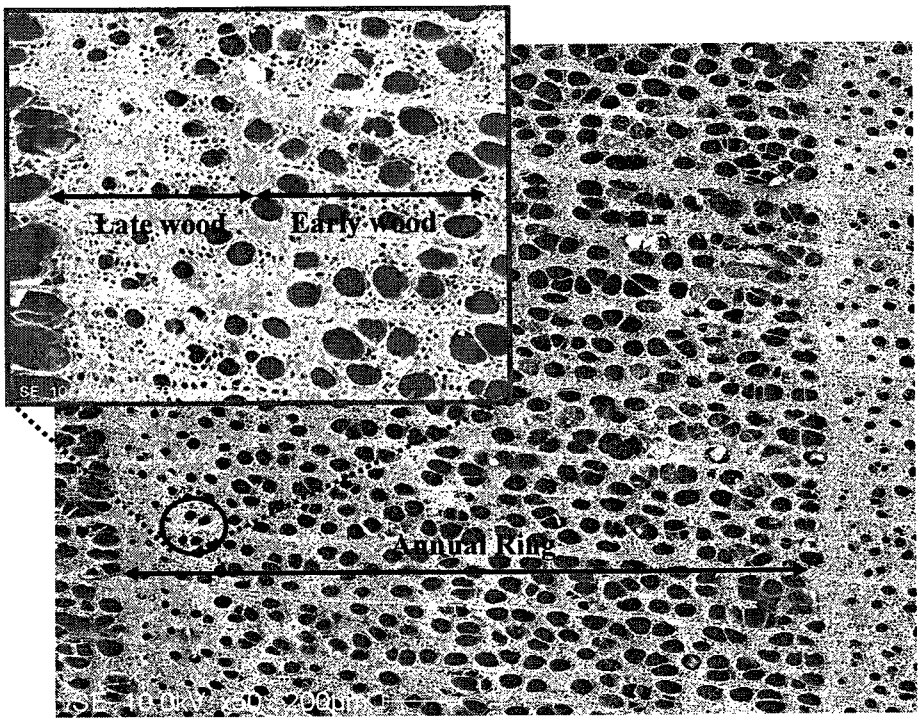


Figure 6.6 Axial direction of ceramized beech, showing one growth ring

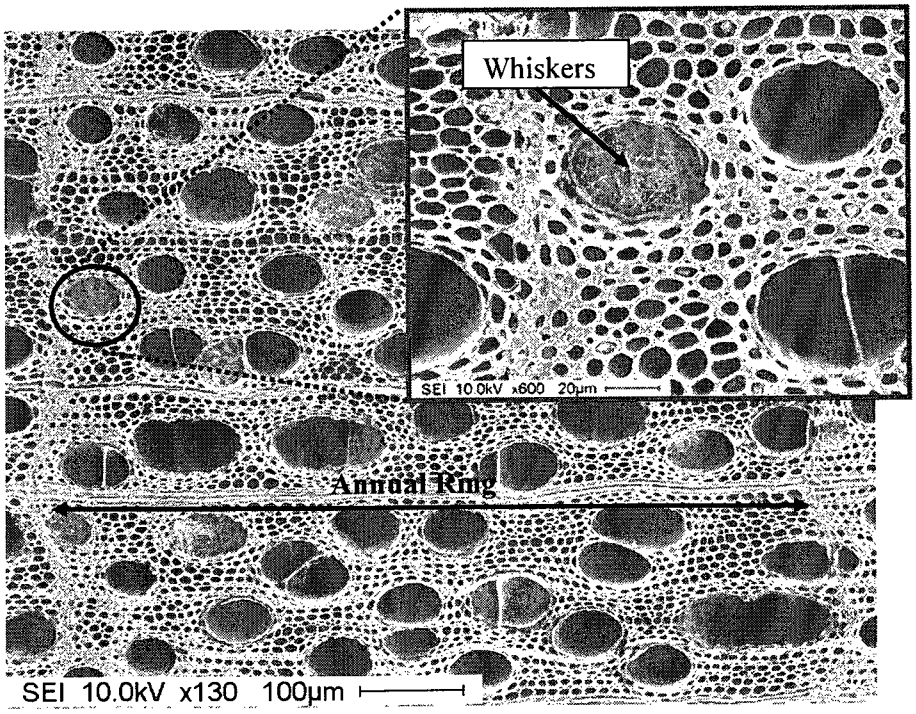


Figure 6.7 Axial direction of ceramized maple, showing one growth ring

EDS, spot analysis was used to analyze the $SiO_2$ remaining in the tracheids/fibers, the grains/particles grown on the inner walls of the tracheids/fibers, and the wall regions in-between the tracheids/fibers for all three species following ceramization. The results indicate mainly carbon and silicon and small amounts of oxygen elements. This signifies that SiC has formed, however it is not homogeneously dispersed throughout the structure. In the axial direction of the ceramized pine, Figure 6.8, a reaction between $SiO_2$ and carbon has occurred (discussed in section 6.2.1) as illustrated by the space between the tracheid wall and unreacted silica. As opposed to an absence of a gap after the $SiO_2$ is infiltrated and dried as given by Figure 6.9. In Figure 6.10, 6.13 and 6.15, the circular SiC grains forming on the interior of the tracheid wall are growing individually, thus producing a porous SiC structure. EDS demonstrated that carbon was remaining between the SiC grains as shown in Figure 6.10, 6.12 and 6.16. In addition, although some regions have been well infiltrated with $SiO_2$ as revealed by the numerous grain formations, other regions have less SiC grain structures as shown in Figure 6.18, with a majority of the walls being carbon.

During the SEM microstructure observation, a high density of SiC whiskers in certain tracheids/fibers and vessels were discovered as shown in Figure 6.8 for pine, Figure 6.11 for beech and Figure 6.15 for maple. The length and diameter of the whiskers are approximately 2 to 50 μm and 250 nm, respectively. Whiskers have been found after the reaction at high temperatures for a variety of wood species and sol types. For example, pine wood and TEOS [129], carbonized bamboo and TEOS [130], pine wood and sodium silicate [131], carbonized cedar with TEOS [132], pine and poplar dry wood with TEOS [133], carbonized basswood with SiO gas [134], carbonized tilia amurensis

wood with TEOS [52], and carbonized oak with SiO gas [44]. However, in this study, carbonized pine, beech and maple wood infiltrated with Levasil sol have also produced SiC whiskers. From the location of the SiC whiskers in the center of the tracheids, away from the solid carbon, it is presumed, the whiskers are not formed from a solid-solid reaction but one of a gas phase reaction between the SiO (g) and CO (g) as given in Equation 6.1. In a similar work, SiC whiskers were produced in the pores of a carbon foam from the evaporation of silicon powder [135].

$$SiO\ (g) + 3CO\ (g) \rightarrow SiC\ (s) + 2CO_2\ (g) \qquad (6.1)$$

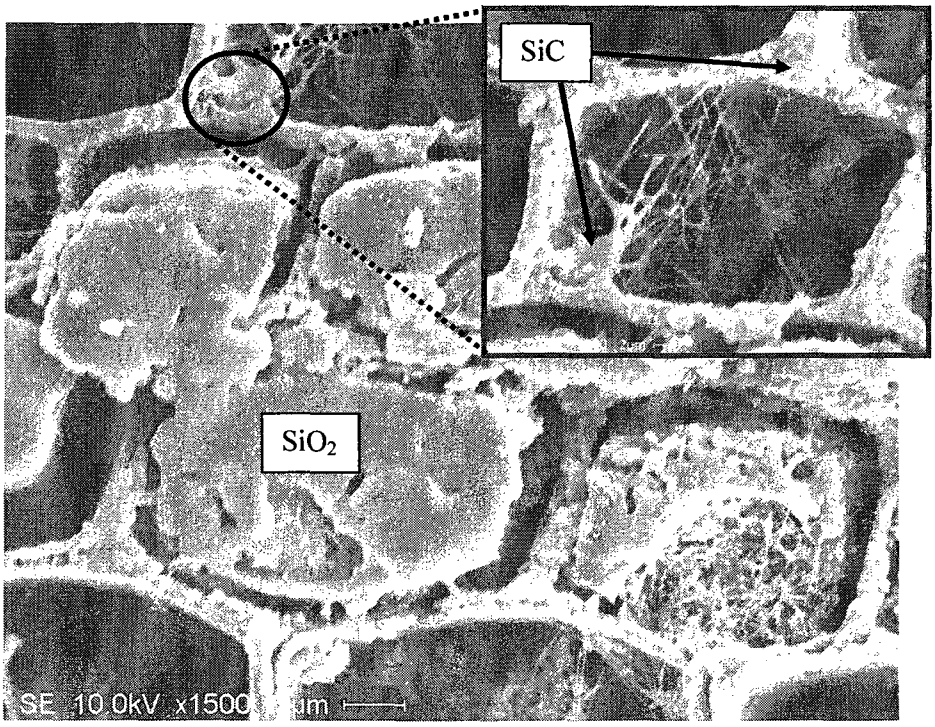


Figure 6.8 Magnified view of the silica in ceramized pine, axial direction, after reaction

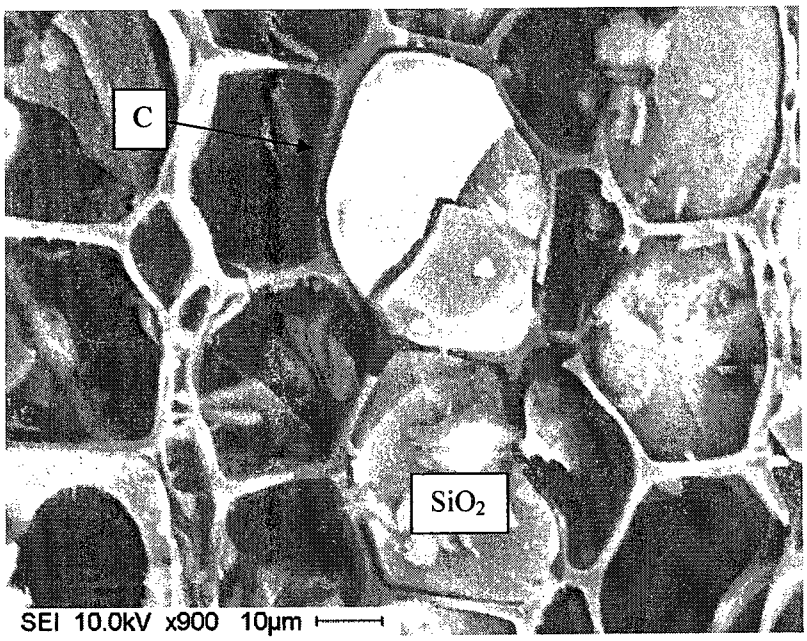


Figure 6.9 Magnified view of the silica in carbonized pine, axial direction, after drying

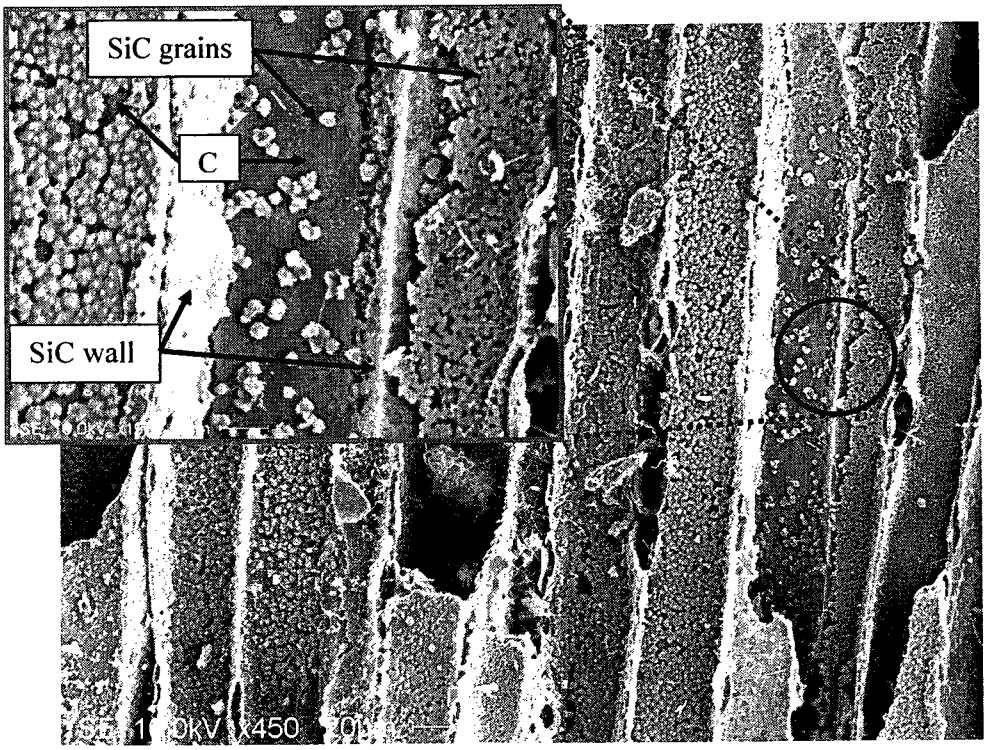


Figure 6.10 Longitudinal direction of ceramized pine

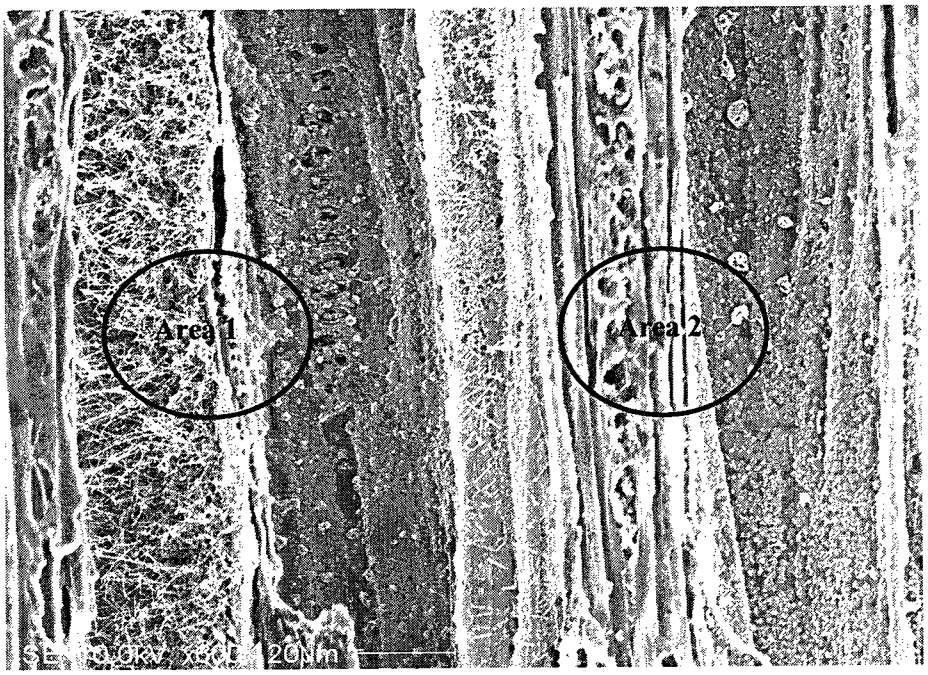


Figure 6.11 Longitudinal direction of ceramized beech

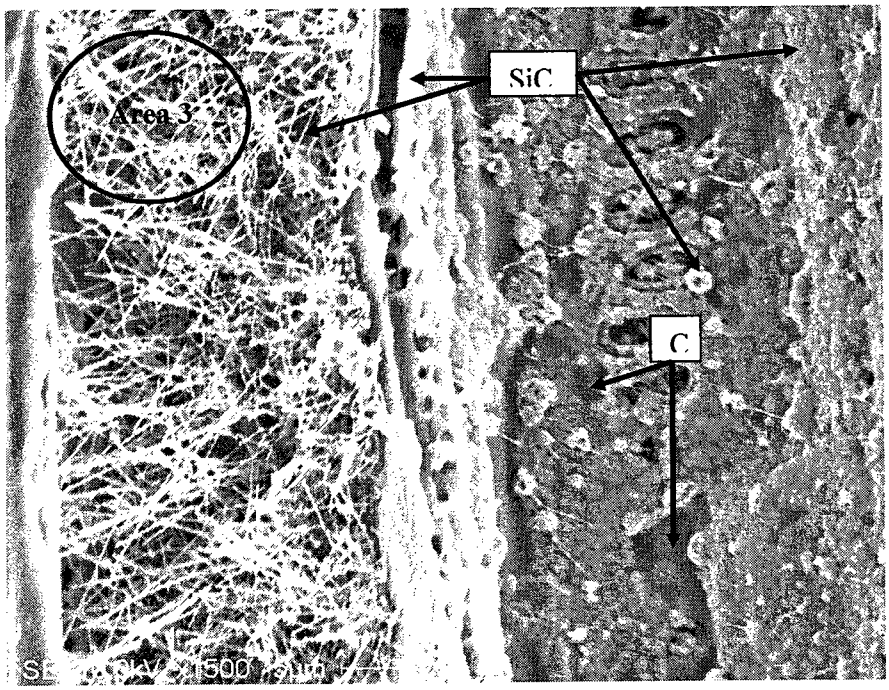


Figure 6.12 Longitudinal direction of ceramized beech, magnified area 1

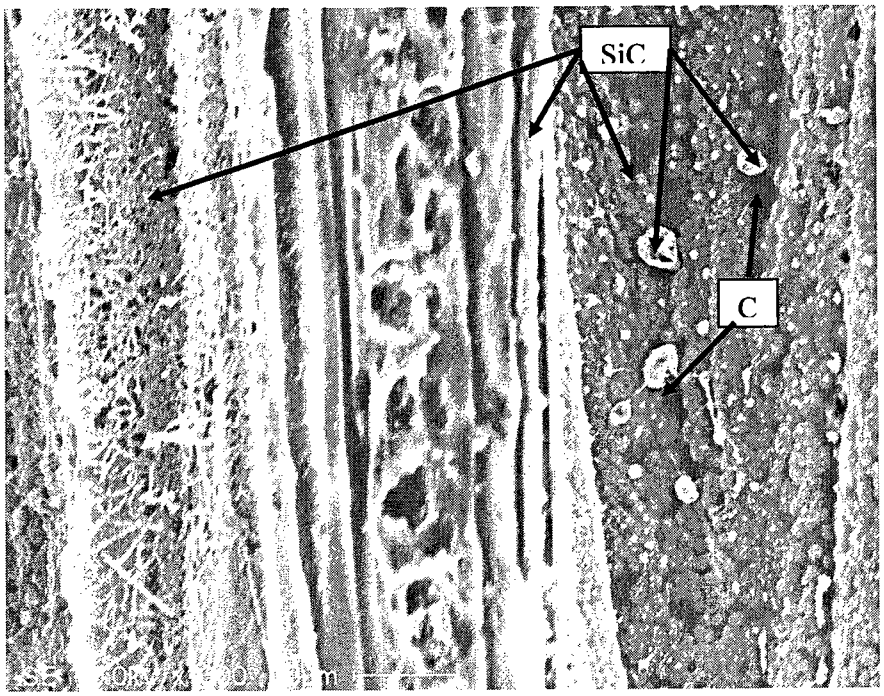


Figure 6.13 Longitudinal direction of ceramized beech, magnified area 2

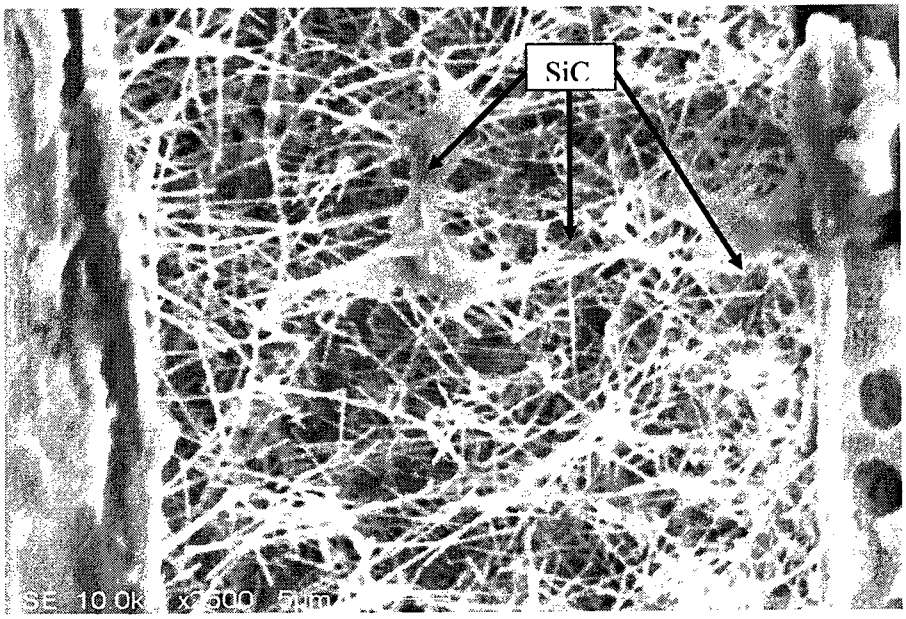


Figure 6.14 Longitudinal direction of ceramized beech, magnified area 3

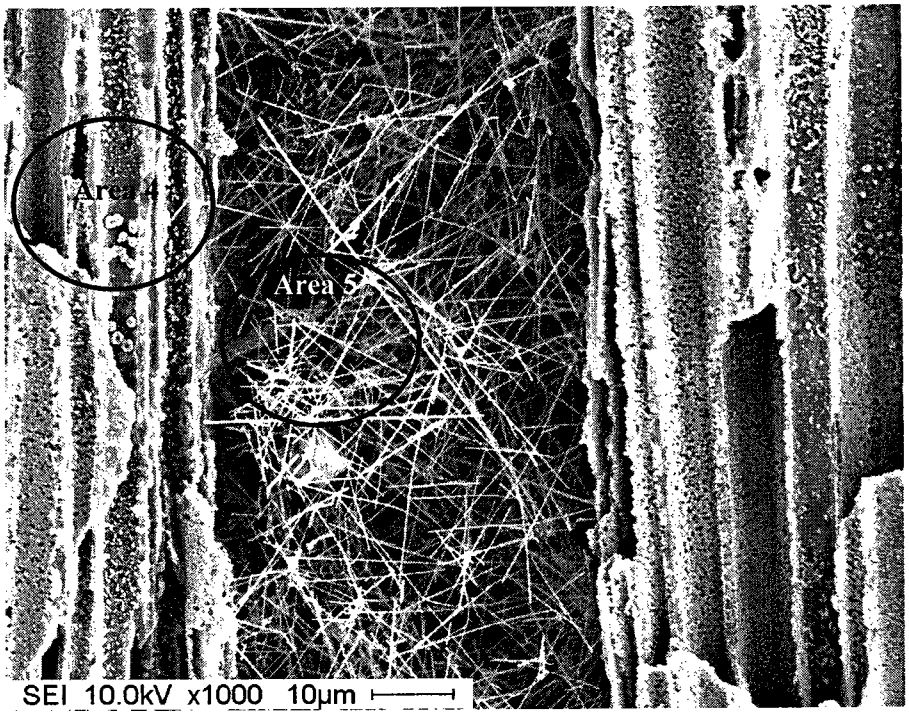


Figure 6.15 Longitudinal direction of ceramized maple

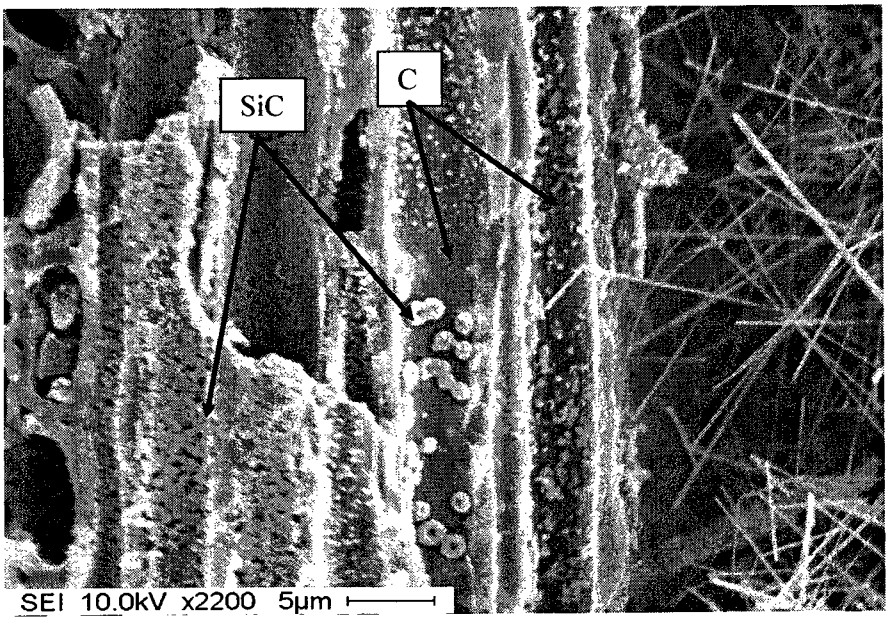


Figure 6.16 Longitudinal direction of ceramized maple, magnified area 4

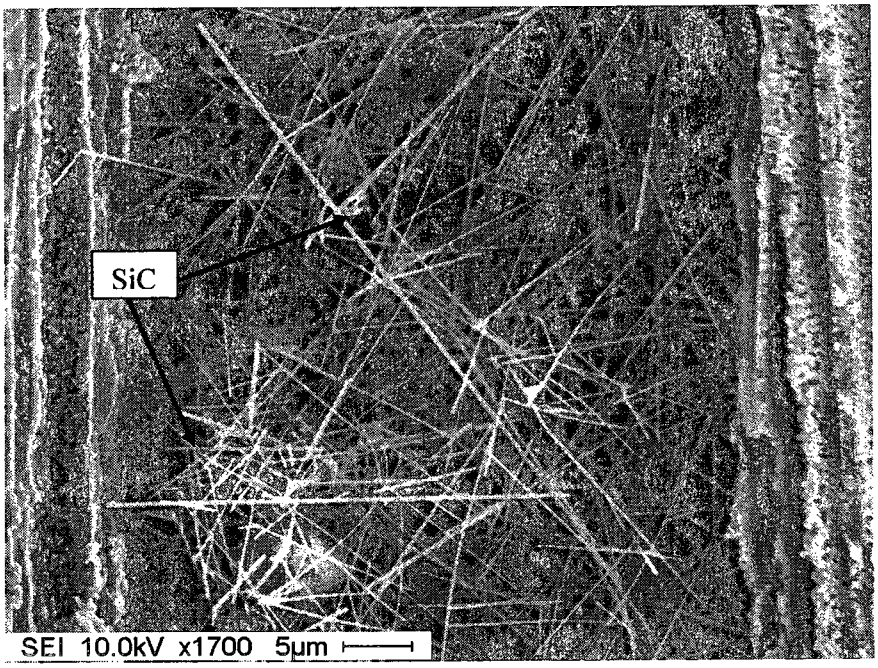


Figure 6.17 Longitudinal direction of ceramized maple, magnified area 5

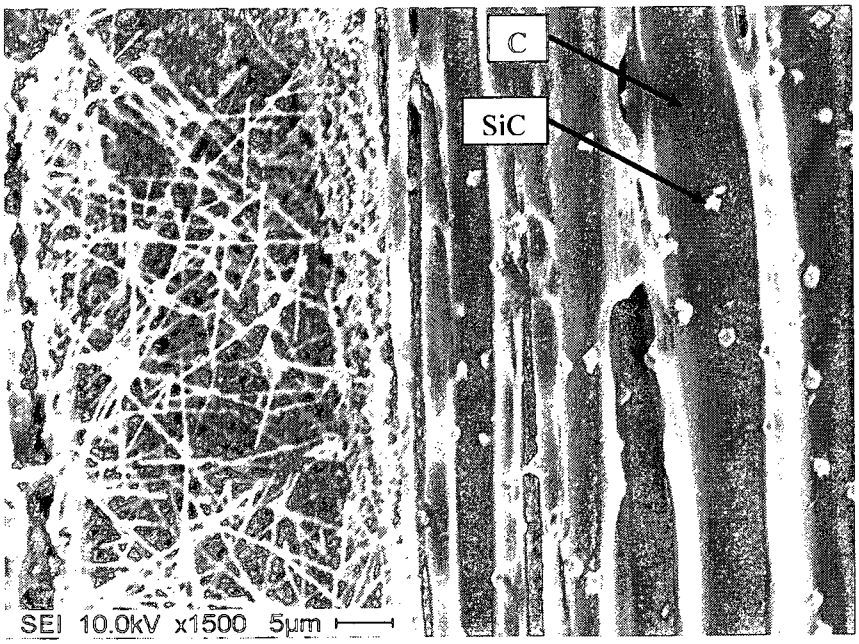


Figure 6.18 Longitudinal direction of ceramized maple, low infiltration region

### 6.2.1 Ceramization Reactions

After ceramization, a weight loss of the samples was recorded. These losses are normal due to the reactions taking place. The reactions generate SiO (g) and a large amount of CO (g), involving weight losses in the form of decomposition of the carbon substrate reacting with oxygen as given by Equations (6.2-6.7):

$$SiO_2\ (s) + 3C\ (s) \rightarrow SiC\ (s) + 2CO\ (g) \quad (6.2)$$

$$SiO_2\ (s) + C\ (s) \rightarrow SiO\ (g) + CO\ (g) \quad (6.3)$$

$$SiO_2\ (s) + CO\ (g) \rightarrow SiO\ (g) + CO_2\ (g) \quad (6.4)$$

$$SiO\ (g) + 2C\ (s) \rightarrow SiC\ (s) + CO\ (g) \quad (6.5)$$

$$CO_2\ (g) + C\ (s) \rightarrow 2CO\ (g) \quad (6.6)$$

$$2SiO_2\ (s) + SiC\ (s) \rightarrow 3SiO\ (g) + CO\ (g) \quad (6.7)$$

As CO gas is formed, weight is lost from the carbon substrate being oxidized and removed from its surface. This causes a strength reduction and degradation of the carbon preform. The ceramized tracheids/fibers could in fact be thinner than the initial carbonized structure. For example, in producing a quantity of one mole of SiC, three times more carbon moles are required for the reaction in Equation 6.2 to take place; therefore our carbonized structure will lose approximately 2/3 of its weight as CO gas. In contrast to an amount of carbon powder, which can be varied for SiC powder production, the amount of carbon available for the reaction is fixed from the wood structure.

After dehydration of the liquid silica sol, the reaction between $SiO_2$ and C to form SiC requires two main reactions; solid-solid and gas-solid, as reported by Krstic V. D. [136]. Initially as both the $SiO_2$ (s) and C (s) are in physical contact, they react with one another at 1400°C [137], where a weight loss occurs from the oxidization of carbon into carbon monoxide CO (g), as given in Equation 6.2. In addition, at 1500°C [137], $SiO_2$ (s) reacts with C (s) to completely vaporize into the SiO (g) and CO (g) by equations 6.3. At 1400°C [136], the CO (g) generated reacts with $SiO_2$ (s) to produce SiO (g) and carbon dioxide ($CO_2$ (g)), governed by the reaction of Equation 6.4. The SiO (g) generated further reacts with C(s) at 1450°C [137], Equation 6.5, to produce SiC and CO (g). The $CO_2$ (g) also reacts with the carbon structure to form additional CO (g) as given by Equation 6.6. These reactions continue until the $SiO_2$ or the carbon is completely consumed. To fully covert the carbon preform, a replenishment of $SiO_2$ is performed during a second infiltration. However, adding more silica may destroy the existing SiC by the excess $SiO_2$ (s) reacting with the formed SiC at 1520°C [137], Equation 6.7.

As given by Equation 6.5, SiO (g) formation is beneficial to the formation of SiC. Once the solids in Equation 6.2 are no longer in intimate contact as shown in Figure 6.8, the reaction ceases and Equation 6.5 is the predominate reaction forming SiC. Provided the silica sol is uniformly distributed throughout the carbon preform and the SiO gas reaches the carbon, a full conversion is theoretically possible. A significant amount of CO (g) is formed during all these reactions (Equations 6.2-6.7). An increased concentration of CO (g) slows the reaction rate of Equation 6.2 from occurring; thus to improve the kinetics of the reaction, CO (g) concentration must be reduced by carrying it away from the furnace via the argon flow. Unfortunately, at the same time as CO (g) is

removed, SiO gas is also taken out of the system but this is required above 1450°C for the formation of SiC, by equation 6.5. Some researchers have indicated that controlling the CO (g) removal while allowing the SiO (g) reaction requires a flow rate of 90 $cm^3$/min. [138]. If the SiO gas leaves the system, a low yield of SiC will occur. In addition, the reaction condition required for SiO (g) to react and form SiC, before it disappears into the argon flow was reported to be between 1460-1660°C [137]. In the present work we ceramized at 1575°C, which is within this temperature range.

### 6.2.2 SiC Layer Growth

Initially, the SiC forms on the surface of the carbon tracheids through a solid-solid reaction as well as a gas-solid reaction. In the solid-solid reaction, once a SiC layer is formed, the growth process continues via the carbon atoms and silica molecules (solid) diffusing through the SiC layer along its grain boundaries. The diffusion coefficient of carbon through SiC is $10^{-9}$ $cm^2$/s [139], while the diffusion of Si through SiC is much slower $10^{-14}$ $cm^2$/s at 1900°C [140]. As a result of the carbon atoms diffusing faster than the silicon atoms, the SiC layer grows towards the center of the tracheids [141].

The mechanism presented above shows that as SiO gas is evolved, further SiC layer forms through a gas-solid reaction of SiO. The SiO either initiates the SiC growth on the bare carbon surface or continues the SiC layer development. Similar to silica molecules, the SiO gas molecules diffuse through the SiC layer and react with the carbon atoms diffusing in the opposite direction [142]. As opposed to the diffusion rates in the solid reaction, the diffusion rate of silicon oxide gas (SiO) is faster than that of carbon [143]. The SiO gas diffusion/growth continues until the entire carbon structure is SiC.

From reactions of equations 6.2 to 6.5, the growth dynamics of the SiC can be proposed to proceed in the following manner. With reference to the initial interface between the carbon and silica, the carbonized wall of the tracheids is converted into SiC in two different directions as shown in Figure 6.19. Initially, the carbon diffuses into the silica forming SiC "inward" of the initial interface and SiO gas. Subsequently, the SiO gas diffuses through the formed SiC into the carbon layer, reacting to form an additional SiC layer which is growing "outward" of the initial interface. After a certain elapsed time, the SiO concentration starts diminishing. At that time more carbon has the chance to diffuse through the SiC to form an additional layer inwards. The same process repeats until either the carbon or the $SiO_2$ is depleted. This way the SiC layer is growing in both inward and outward directions from the initial interface in a sequential manner.

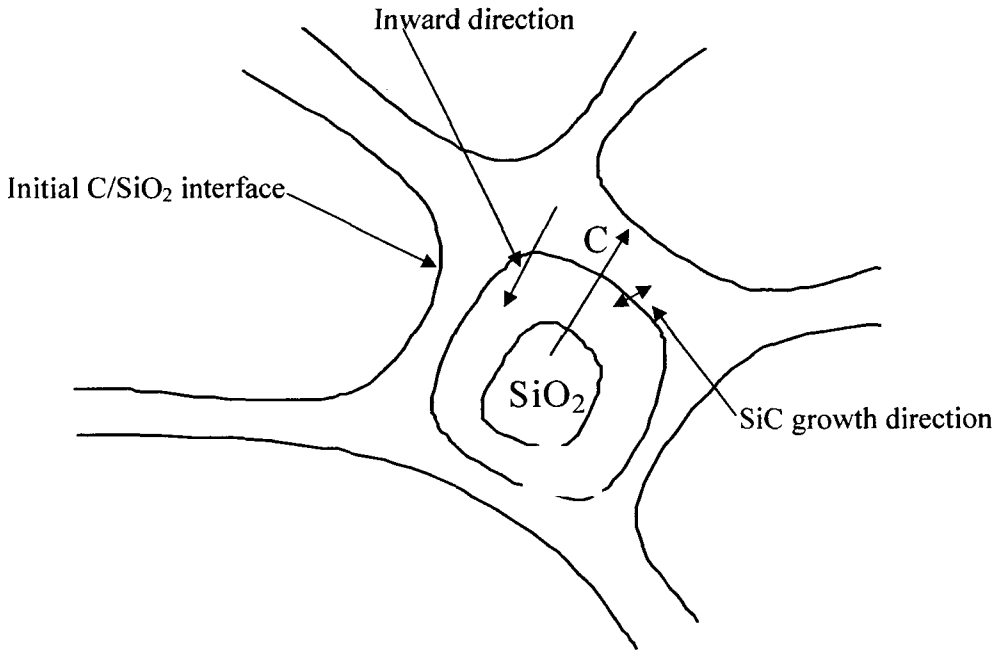


Figure 6.19 Schematic diagram of SiC growth in carbonized wood

### 6.2.3 Oxidizing

Research into the infiltration of silica sol into different carbonized wood has been previously studied with claims for producing a full conversion to SiC structure [49,50]. However, when infiltrated with the Levasil sol, a final sintering or oxidation step is performed in order to remove any excess carbon prior to obtaining a 100% SiC structure. During SiC synthesis, carbon is lost through CO gas evolution in addition to this oxidizing step in the final stage to produce the pure SiC. Although a quantity of carbon has reacted with silicon, some non-reacted carbon which previously maintained the structural integrity disappears through the final oxidation process.

A protective coating on SiC is a film of $SiO_2$(s) formed by reacting SiC with oxygen in an oxidizing heat treatment above 1200°C [144]. On submitting SiC at 700°C for 1hr, it was reported that little oxidation occurred with a film thickness of 25 nm, but increased to 58 nm at 900°C for 1hr [145]. Assuming the $SiO_2$ formed a defect free, homogeneous layer on the continuous SiC structure, the $SiO_2$ would prevent the oxygen from diffusing preserving the carbon structure since the oxygen diffusivity coefficient into silica is very low [146]. However, as shown in Figure 6.10, the SiC formed contains defects such as a discontinuous grain structure, where voids and pin-holes can allow oxygen to migrate to the carbon structure. The oxygen will diffuse inward to react with the carbon, while CO or $CO_2$ gas will diffuse outward through the defects. This would make the final ceramized product less solid, with thinner tracheid walls and struts, with more porous tracheids and overall, a weaker structure.

Oxidation of the pine, beech and maple was done in order to determine the final structural integrity. The weight losses were 20%, 26% and 19%, respectively. After 1 hr

oxidation at 700°C to remove residual carbon, the cellular maple structure, for example, is intact; however, the cells are no longer bonded together as shown in Figure 6.20. All three samples reveal the same trend in oxidized structure with XRD results indicating mostly peaks of SiC (Figure 6.21) in the final structure. It is assumed after the oxidation step, the carbon rich areas have dissociated leaving a "Swiss Cheese" effect alongside the SiC structure. This outcome weakens the structure and it is not possible to further infiltrate with for example, a liquid metal since the oxidized structure is very brittle and fragile.

It was concluded that the flow rate of argon during ceramization is very important. If the flow is too high, the SiO gas formed will leave the structure without sufficient time to react with the carbon. Research for infiltrating silica sol into various pyrolyzed wood species was done at diverse argon flow rates; 70L/h [47, 49, 50], 19L/h [51] and 12L/h [48], while 90 $cm^3$/min (5.4L/h) was reported to give optimum results for the production of SiC by reacting carbon with silica [138]. It was observed that larger argon flow rates did not favor SiC yield while smaller flow rates decreased the SiC yield. In this work a typical flow rate of 70L/h was employed.

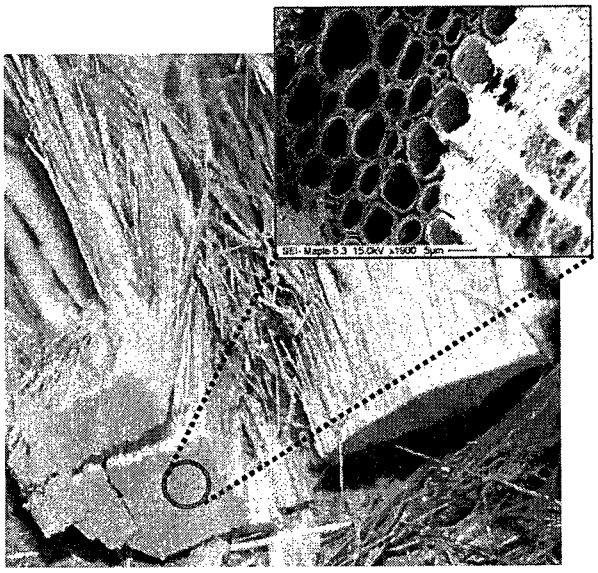

Figure 6.20 Digital image of final oxidized (15x11x13) $mm^3$ maple with magnified SEM

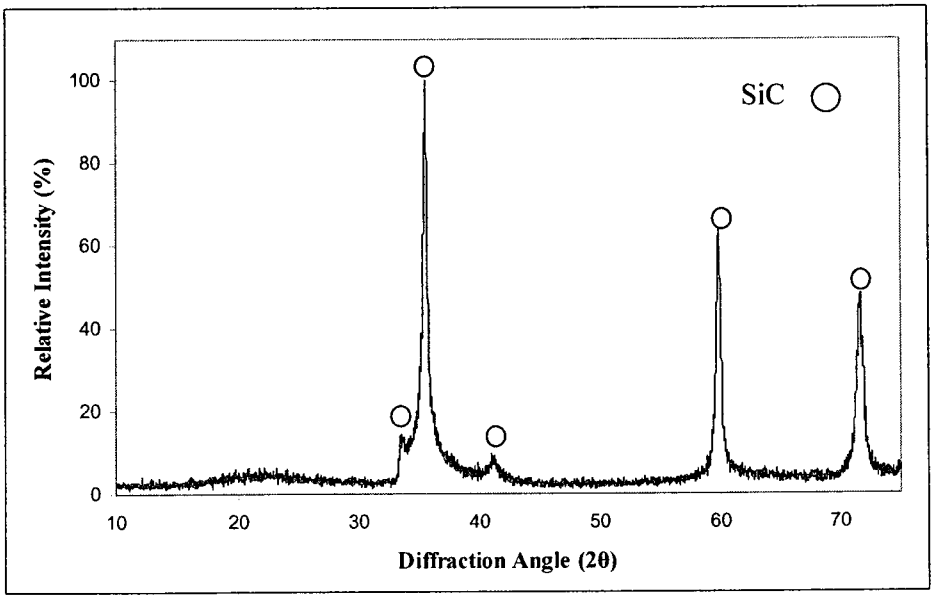


Figure 6.21 X-ray powder diffraction results after oxidation at 700°C, 1 hr for maple

### 6.3 Effect of Climate on Wood Morphology

As the infiltration process was similar to that used by other workers [50], the assumption is that the different results are due to differences in the wood cell morphology. On the large scale, climate may not have a great effect on wood mechanical properties, but at the micro-structural level, where penetration of a liquid is important, the effects may be more pronounced. The observations from the literature suggest there is possible variation at the microscopic level. Morphology characteristics can be influenced by water supply, temperature and growth location.

Heartwood for the most part is dead. In contrast, the amounts of sapwood (earlywood and latewood) in the tree ring width can change. In general, for trees grown in areas where seasons exist, spring is when there is an abundance of water. At this time, the cells divide rapidly, featuring thin, porous walls and large diameters increasing the ring width. At the end of the summer, under less favorable conditions or when the wood is produced slowly, when there is less water, cell division and cell enlargement cease, the walls of the last-formed cells begin to thicken gradually [147]. It is anticipated that climate change can affect this growth process. Soil moisture (water supply) and temperature throughout the growing season, are the most important variables for determining annual ring width development and thus cell sizes. For example, a dryer year can cause a smaller ring width and an earlier transition from earlywood to latewood [148]. For our purposes of altering the carbon structure to a SiC structure, this may be important in terms of cell wall thickness, such that thin earlywood cells are more porous and are less dense than the thicker latewood cells, thus explaining the reason for less pit aspirations in latewood than early wood.

Growth geography would also alter the amount of earlywood and latewood. Assuming a pine specie grows in two different climates; one in Southeast Canada and the other in near equatorial South America. The presence of earlywood and latewood is visible in both, however it is apparent that the South American tree has more earlywood and much less latewood cells, if any, since the season is more constant. In softwood and hardwood species, pit size, number of pit openings, cell diameter and length are all factors affecting the permeability of the wood structure [149]. For instance, it is assumed that long and large diameter cells have more pit membranes than short and narrow ones [150]. In addition, it was found in sugar maple, small diameter vessels had smaller pit membrane pores than larger diameter vessels which suggests that the diameter of the cells are related to the size of the pit membranes [151].

From the light color of the wood employed in this research, sugar maple and american beech were both from the sapwood, since the heartwood in these species are both visibly reddish brown. In contrast, eastern white pine forms sapwood and heartwood but there is no distinct color to differentiate them. Therefore, selected regions of the outer tree diameter, shown as dotted lines in Figure 6.22 were used to ensure samples are of sapwood and not of heartwood. Smith [152] found the treatability of eastern white pine with chromate copper arsenate (CCA) in the sapwood was good while a significant amount was able in the heartwood. One way to determine if the Eastern Canada-sourced wood species have different wood cell morphology is to obtain some samples from very different climatic regions and test them.

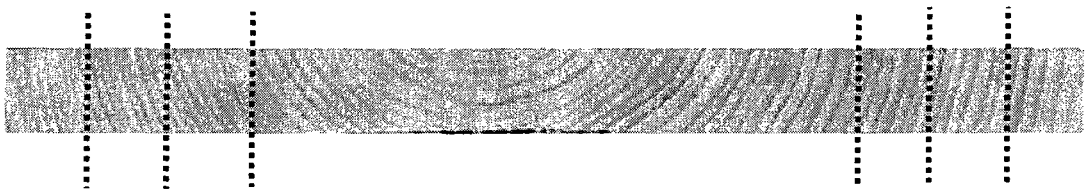

Figure 6.22. Image of the Eastern white pine board measuring 12 in wide x 1 in thick

### 6.4 Liquid Silicon Infiltration Results

When infiltrating with molten silicon, results indicate that at different depths, different porosities exist. A carbonized pine sample was infiltrated with a supply of three times the stoichiometric amount of silicon (3x). Figure 6.23 is a schematic showing the relation between sample infiltration direction and grinding depths involved in this study.

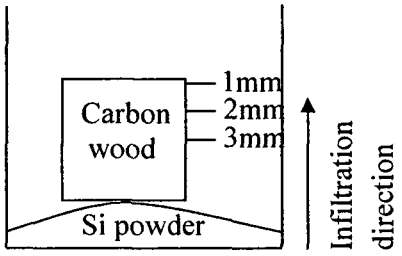


Figure 6.23 Schematic of infiltration direction and ground depths

After silicon infiltration, optical microscope images for three positions beginning at 1 mm below the top of the cube to a 3 mm depth, opposite the infiltration front were taken as given in Figure 6.24. At each of these three levels, the sample was ground and finished to 1200 grit.

Figure 6.24, illustrates the porosity at varying depths; the black color is un-reacted porous carbon wood while the light gray color is the infiltrated silicon/carbon structure.

In addition, SEM images were taken to illustrate the Si, SiC, and C regions, for an infiltrated sample ground to approximately 2 mm, as shown in Figure 6.25. The magnified area clearly indicates filled latewood cells, while earlywood cells remain unfilled. Even for a supply of three times the stoichiometric amount of silicon, only partial conversion to SiC is observed in Figure 6.25. At a depth of 2 mm, small diameter latewood trachieds are filled (dark gray areas), while larger earlywood tracheids (black colored areas) are empty.

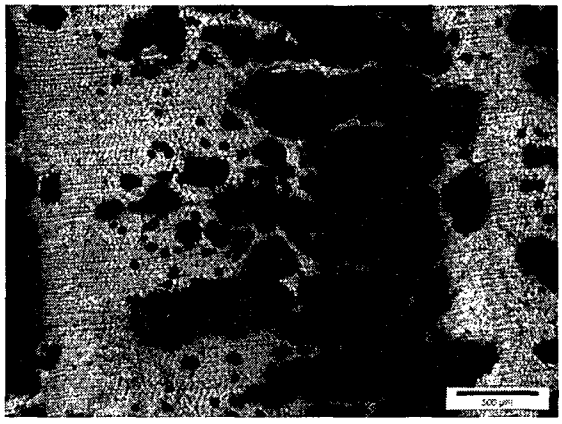

(a) Ground depth of 1 mm

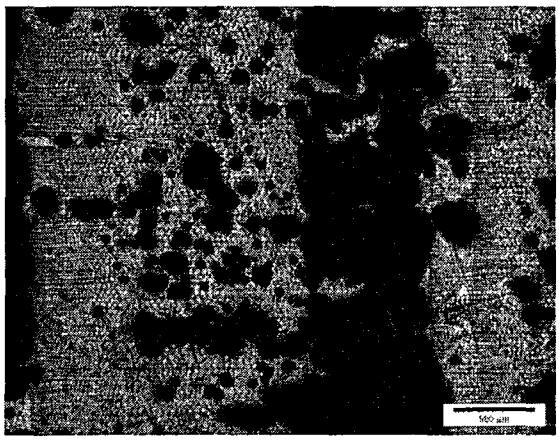

(b) Ground depth of 2 mm

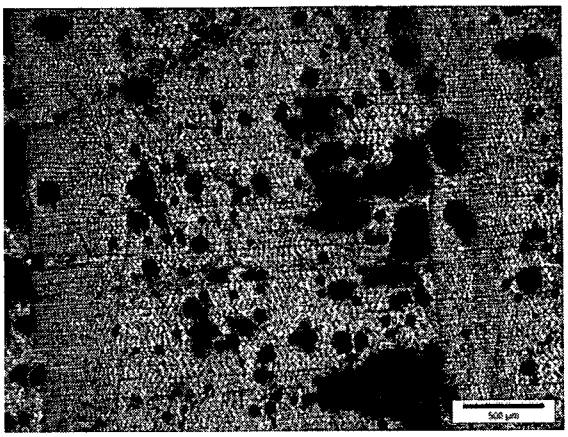

(c) Ground depth of 3 mm

Figure 6.24 Optical microscope images of 3x silicon infiltration at varying depths

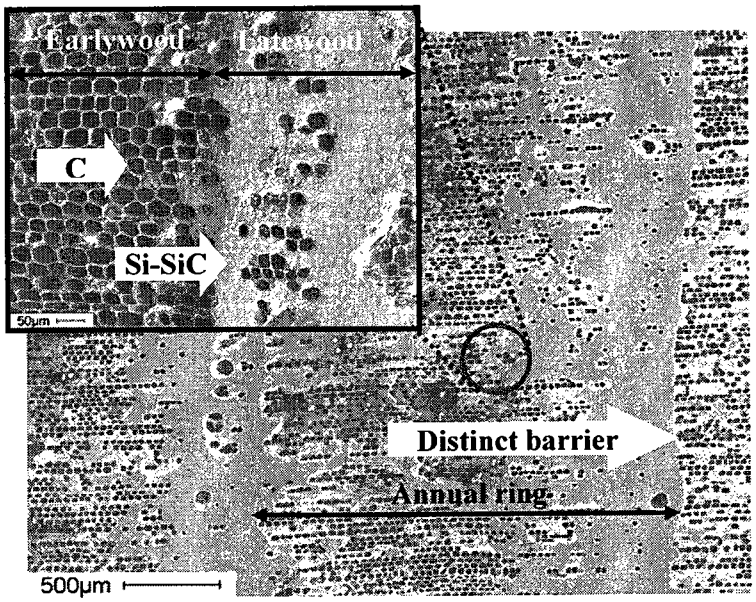


Figure 6.25 SEM of carbonized pine subsequent to 3x infiltration, with magnified area (C: Carbon and Si-SiC: Silicon and silicon carbide)

The phenomenon of pressureless, spontaneous silicon infiltration into carbonized wood species and related reaction kinetics was examined by Greil et al. [34]. These

authors demonstrated that by capillary flow, the size of the pore diameter dictates the infiltration rate. Smaller diameter pores (2-20 μm) require less time to fill up then larger pores, however a maximum diameter exists where pores remain unfilled. Using literature data, for properties of silicon at 1600°C and Equation 3.9, they obtained a maximum pore diameter of 60 μm. Smaller than this value, the pores are estimated to be full of silicon. Results of the present study indicate similar findings as shown in Figure 6.25.

After 3x silicon infiltration into carbonized pine, the composition of the composite was verified. An oxidation treatment at 700°C for 1 hr, was followed by crushing the sample into powder form for XRD measurement as given in Figure 6.26. The phase composition is approximately 60 vol.% SiC and 40 vol.% silicon and no residual carbon is present.

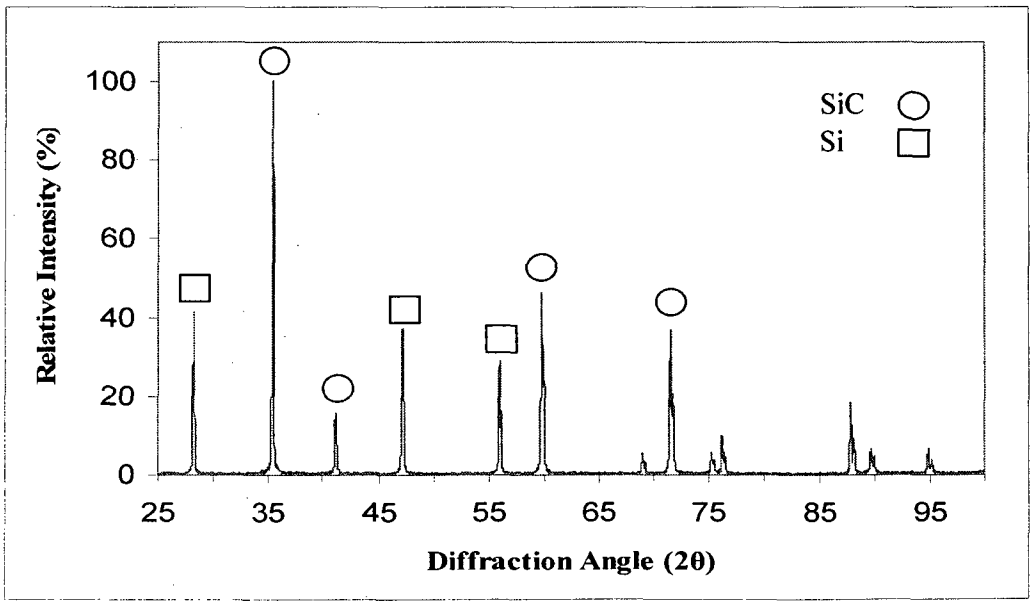


Figure 6.26 XRD powder pattern after oxidation of silicon-infiltrated carbon pine at 1450°C

In order to obtain a full, non-porous structure, four or more times the stoichiometric amount of Si is required as shown in Figure 6.27. Excess silicon is required in order to fill the cell diameters and to compensate for the silicon that is loss in the form of vapor and the final coating remaining on the inside of the crucible. The micrographs were taken at half the cube height in order to inspect the microstructure. The dark gray areas are silicon carbide, the lighter gray is residual silicon, while the black spots are unreacted carbon. It is not possible to obtain a uniformly porous structure using molten silicon and carbonized pine. For smaller amounts of silicon powder, the small diameter latewood cells are full of silicon and the larger earlywood cells are empty, whereas for larger amounts of silicon the entire annual rings are filled. It appears there is no ideal amount for producing a silicon carbide porous structure. In either case, the silicon completely fills the smaller carbon wood cells first.

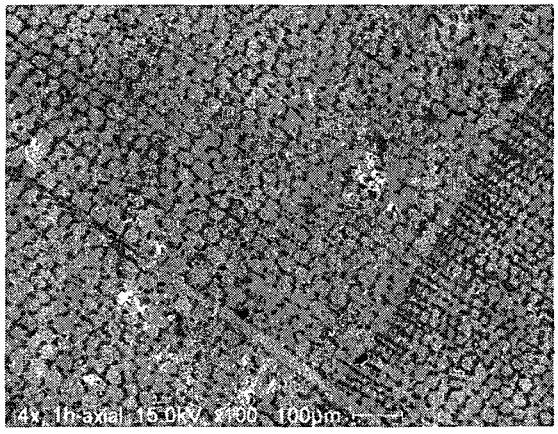


a) Axial direction

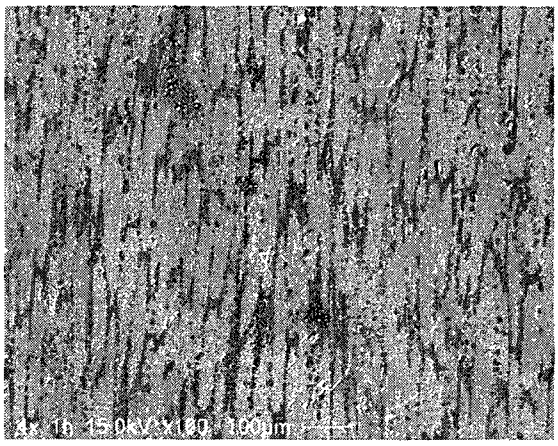

b) Radial direction

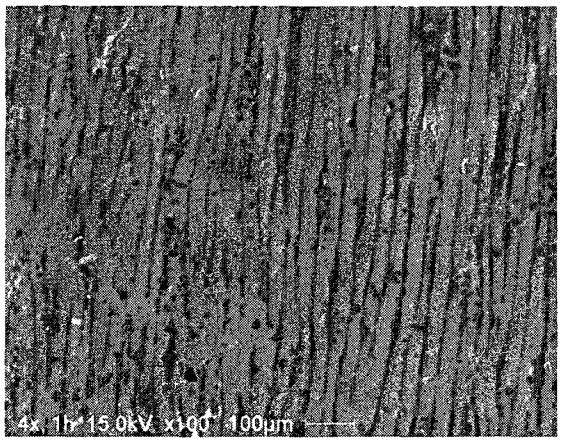

c) Tangential direction

Figure 6.27 SEM micrographs of the Si-SiC for 4 times stoichiometric amount, at 1450°C

### 6.4.1 Silicon Reaction

The melt infiltration for the conversion processes of solid SiC (s) is a liquid-solid and a gas-solid reaction. The reaction between liquid silicon Si (l) and solid carbon C (s) was carried out at 1450°C. SiC is produced above the melting point of silicon, 1414°C, when in contact with the carbon preform as given by the reaction in Equation 6.8. As soon as the silicon is liquid, capillary forces drive the liquid silicon into the longitudinal direction

of tracheid/fiber cells of the carbon preform. In the same way, the liquid silicon also penetrates through the open pits in the cell walls in the radial and horizontal directions. This spontaneous wetting results from the low wetting angle (40-50° for vitreous (glassy) carbon at 1426°C, vacuum atmosphere) between the carbon and silicon [153] Between the temperature range of 1430-1450°C [154], once the two material are in contact, the liquid silicon immediately reacts with the carbon to form a thin SiC layer at the Si/C interface. The diffusion coefficient of carbon in liquid silicon is fast with a value of $5.3*10^5 cm^2/s$, at 1497°C [36]. This solid layer hinders further reaction, therefore to maintain the reaction, the Si and C atoms must diffuse through the SiC formed layer. This process continues until the entire carbon structure is transformed to SiC with residual silicon at the center of the cells. At higher temperatures of 2077°C, Pampuch et al.[36] proposed the SiC crystals are formed by dissolution of carbon into the liquid silicon. Upon cooling, the silicon reacts with the dissolved carbon to form the SiC crystals. A thin layer of silicon was observed on the interior walls and cover of the boron-nitride crucible employed for this experiment. This indicates the gaseous silicon (SiO (g) and Si (g)) may play a minor part in the conversion of the carbon preform into SiC as given by Equation 6.5 and 6.9, respectively.

$$C\,(s) + Si\,(l) \rightarrow SiC\,(s) \tag{6.8}$$

$$C\,(s) + Si\,(g) \rightarrow SiC\,(s) \tag{6.9}$$

### 6.5 Summary of Silica and Silicon Infiltration of Carbonized Wood

In both silica and silicon infiltration, if a stoichiometric amount of silica or silicon is used, some latewood and most earlywood cells remain open resulting in an incompletely

transformed SiC structure. Therefore, complete porous SiC structures were not able to be produced. The same phenomenon has been reported during a study of linseed oil infiltration into Norway Spruce; latewood cells were always filled with oil, but earlywood cells were not completely filled. Similar to our results, the oil segregated to the latewood first and appeared to stop after the last latewood cell in an annual ring [10]. This study shows that a porous SiC structure mimicking that of wood is not possible by these routes. The proper amount of silica for full, 100% conversion to a porous SiC structure was not able to be sufficiently drawn into the tracheids, fibers and vessels of the different wood species. Silicon infiltration did not produce a 100% porous SiC structure, rather a mix of solid carbon, silicon and silicon carbide if excess of silicon is used. As stated earlier, dried wood and heartwood of most wood species contain certain amounts of aspirated pits. However, Figure 6.27 indicates the possibility of infiltrating both latewood and earlywood cells in carbon pine wood. There are two possible reasons for this: first, if the sample contains heartwood, not all pits are closed, thus allowing flow to neighboring tracheids, second, this specimen may come from the sapwood rather than heartwood, which has improved infiltration from the non-aspirated pits. If less silicon is employed, the small diameter latewood cells were filled first while the larger earlywood cells were not filled. In addition, the porosity at different depths vary considerably. The suggestion to use a greater amount of silicon to produce a semi-porous Si-SiC or 100% SiC structure was not possible as claimed by Esposito et al. [43] for their obece wood species. To generate a metal matrix composite by further infiltrating a light metal using this method seems impossible due to the impermeable Si-SiC structure. However, liquid aluminum in contact with solid silicon can react to produce an Al/Si alloy. For pure

aluminum, the initial dissolution of silicon into aluminum will occur quickly, since at the beginning of the reaction, no silicon atoms are present. The maximum solubility of silicon in aluminum is 17 wt.% at a temperature of 660°C. At this amount, the solubility limit is reached, aluminum in proximity to the Al/Si interface is saturated with silicon and further dissolution proceeds very slowly which is not a feasible approach.

### 6.6 A356/SiC Foam Infiltration Results

The results for the second portion of this study are presented below. Infiltration of an aluminum alloy into porous SiC foam was carried out. Selected mechanical and thermal properties were tested in order to determine the properties of this new material.

#### 6.6.1 Density and Porosity of the Composite

The theoretical density of the two phase Al/SiC foam composite ($\rho_{theo.\ comp}$), without nickel, was calculated using the ROM, Equation 6.10. The two-phase theoretical strut solid density ($\rho_{SiC/C}$ or $\rho_{theo.\ strut}$) was calculated to be 2.82 $gcm^{-3}$ (from section 3.3.3). Based on an open porosity of 87.67%, the volume fraction of aluminum ($V_{Al}$) and foam ($V_{SiC/C}$) is 0.873 and 0.127, respectively. Therefore, the Al/SiC foam composite ($\rho_{theo.\ comp}$) theoretical density is calculated to be 2.72 $gcm^{-3}$. The bulk density was obtained from the average of three (15 mm x 10 mm x 10 mm) A356/SiC specimens by taking their individual masses and dividing by their respective volumes as well as compared against the same three samples measured by the Archimedes method (ASTM C20-00) [92], given in Table 6.2.

$$\rho_{theo.\ comp.} = \rho_{Al} V_{Al} + \rho_{SiC/C} V_{SiC/C} \qquad (6.10)$$

Table 6.2 Comparison of theoretical and bulk density for the A356/SiC composite

| Theoretical (ROM) $\rho_{theo.\ comp}(gcm^{-3})$ | Calculated = mass/volume $\rho_{bulk}\ (gcm^{-3})$ | Measured ASTM C20-00 [92] $\rho_{bulk}\ (gcm^{-3})$ |
|---|---|---|
| 2.72 | 2.58 ±0.13 | 2.52 ±0.18 |

Current electronic Al/SiC packaging materials have bulk densities, typically between 3 and 17 $gcm^{-3}$ [4] as shown in Figure 6.28. This Al/SiC foam composite has a lower bulk density than common Al/SiC packaging materials since the density of the foam strut is 2.82 $gcm^{-3}$ rather than SiC particulates which have a density of 3.28 $gcm^{-3}$. The drop in density is due to the carbon interior of the foam strut and also due to the reduced volume fraction of SiC (12% vs 50-70%). Typical electronic packaging material density could thus be reduced from 3 $gcm^{-3}$ to a bulk density of 2.52 $gcm^{-3}$, which has the advantage of decreasing the weight of a packaging component by 16%.

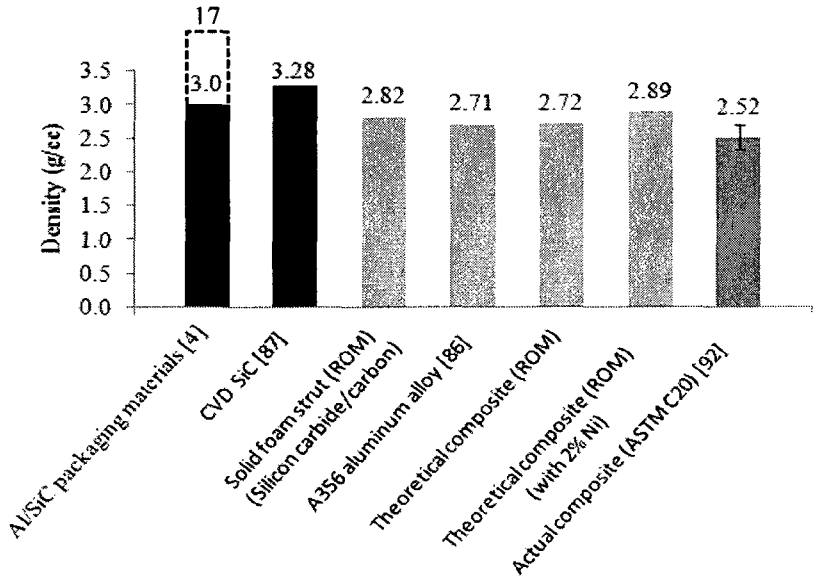


Figure 6.28 Comparison of various bulk density values

Porosity of the composite was evaluated assuming the Al/SiC foam composite theoretical density of 2.72 g/cm$^3$ (based the ROM for a solid foam strut density of 2.82 gcm$^{-3}$), and the measured bulk density of 2.52 ±0.18 g/cm$^3$, based on Archimedes's method (ASTM C20-00) [92]. The total porosity of the composite is 7.35 ±0.18 %, evaluated using Equations 3.2 and 3.3. The open porosity of the same three samples was found using Equation 3.4, while the closed porosity was calculated by the difference between the total and open porosity, Equation 3.1. Results are tabulated in the Table 6.3.

Porosity formation in aluminum can be due to the release of hydrogen from the melt and/or solidification shrinkage during cooling. Hydrogen is a product from the reaction of moisture ($H_2O$) in the atmosphere with the aluminum. It can enter the aluminum melt during stirring or pouring, but could also be present from the as-received ingot from the foundry. Porosity from hydrogen gas bubbles will form spherical holes in the solidified structure if not removed from the melt [155]. Degassing is a method used to remove the hydrogen bubbles and reduce the porosity of aluminum castings. It can be done by inserting a lower partial pressure inert gas into the molten aluminum, or adding solid pellets, based on Chlorine which decompose and release a lower partial pressure gas. For example, the inserted gas can be nitrogen. Hydrogen gas bubbles have a high partial pressure and will tend to flow into the lower pressure nitrogen gas bubbles. Nitrogen being a light gas will rise quicker through the melt and out to the atmosphere. Infiltrating molten aluminum at high pressure can reduce the porosity from hydrogen gas, since the solidifying metal is maintained under pressure. Sievert's law [156] states that the absorbed hydrogen (H) in the melt is proportional to the square root of the partial pressure of hydrogen (P), but also increases with temperature as given by Equation 6.11:

$$H = (P)^{0.5} \exp (C_1/T + C_2) \quad (6.11)$$

In the same way an increase of hydrogen amount is absorbed into the melt as the partial pressure and temperature of hydrogen increases, in a vacuum atmosphere, the hydrogen diffuses out of the melt as pressure and temperature decrease causing gas porosity to form. In this work, the as-received ingot was melted in a crucible such that no stirring or pouring was involved helping reduce the hydrogen gas input into the aluminum melt. The vacuum used in this work was very low which acts to reduce the chance of voids from gas porosity as indicated in Figure 6.12. Comparable to the vacuum set-up employed in the current work, porosities ranged between 1-5% for an aluminum alloy vacuum infiltrated into SiC particulate preforms in other studies [157].

Figure 6.29 shows areas of porosity due to solidification shrinkage shown as a gap between the SiC/Al interface and small un-infiltrated areas, however, the majority of the composite is well infiltrated. Solidification shrinkage of aluminum alloy in castings is due to the volume change during the phase transformation from liquid to solid. The solidification shrinkage of pure aluminum is 7%, while for aluminum casting alloys ranges between 5 to 6% [158]. Shrinkage can be compensated by feeding molten aluminum into the open-celled preform during solidification. In the present study, this was accomplished by slowly (1 cm every 3 minutes) raising the infiltrated composite out of the aluminum melt. Therefore, full infiltration is possible with this method, however porosity will exist in small amounts due to the inherent shrinkage of aluminum. Changing to a positive pressure such as a squeeze casting method could improve the void content, but may damage the foam structure.

Table 6.3 Composite porosity values

| Total Composite Porosity (Calculated) $P_{Total}$ (%) | Open Composite Porosity (Measured) (ASTM C20-00) $P_{Open}$ (%) | Closed Composite Porosity (Difference) $P_{Closed}$ (%) |
|---|---|---|
| 7.35 ±0.18 | 1.46 ±0.23 | 5.89 ±0.05 |

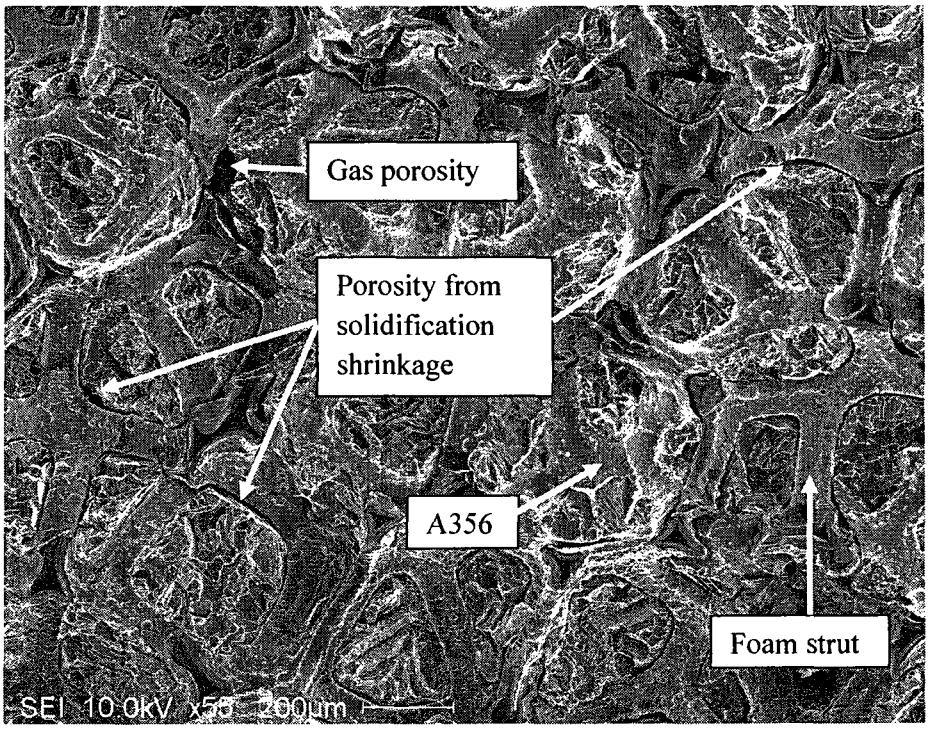


Figure 6.29 SEM porosity appearance in the Al/SiC foam composite

### 6.6.2 Nano Indentation

Micro-hardness measurements were performed on the Al/SiC composite in order to verify the hardness and Young's modulus of the composite components. The struts of the foam utilized in this study consist of a carbon interior, enclosed with a layer of SiC. The

reason for this is that the precursor foam is first produced from a polyurethane which is then turned into a vitreous carbon foam and further coated using a CVD/CVI process within a temperature range of 800-1500 °C [13].

Mechanical property values of the carbon interior and SiC coating for this specific 100 PPI foam struts are not available in literature, whereas those for A356 aluminum alloy are easily available. Determining the strut's solid modulus is important to obtain accurate values when comparing the mechanical properties of the final Al/SiC composite against various models and other materials. Properties from nanoindentation studies show diverse results depending on how the material was manufactured. CVD/CVI SiC depends greatly on the processing parameters used, e.g. deposition temperature, pressure, and chemical reagents utilized. For instance, a study was conducted to produce a CVD SiC by pyrolysis of methyl-trichlorosilane in a hydrogen atmosphere, where a Young's modulus of 466 GPa was obtained [90]. In contrast, Flannery et al. [159] used nanoindentation to measure the modulus of a plasma-enhanced chemical vapor deposited (PECVD) silicon carbide coating to be 56 GPa. Generally, polycrystalline SiC ceramic Young's moduli values can range between 300-450 GPa depending on the processing conditions such as; hot-pressed, self-bonded, sintered, reaction-sintered as well as the manufacturing temperature [160]. Young's modulus obtained from nanoindentation of various carbon types ranging from 2-32 GPa were tabulated in the work of Diss et al. [161].

Each indentation experiment consisted of three phases as described below. Upon surface contact, the indenter is loaded at a constant rate of 200 μN/s to peak load of approximately 924 uN. The penetration depths of 14 nm (SiC), 16 nm (C) and 140 nm (Al) were observed. The peak load is held constant for 5 seconds and subsequently

unloaded at a rate of 5 μN/s. The indentation behavior of the A356 aluminum alloy, and the cell wall materials (SiC and carbon) are depicted in the load-displacement curves, Figure 6.30. The carbon, being harder than the aluminum, shows a lower penetration depth for the same applied load, whereas the SiC is stiffer and harder than the preceding materials and the penetration depth is much less. Three indentation point measurements at constant intervals of 20 μm where made on the aluminum matrix as well as the carbon and SiC cross-sectional regions of the foam strut to obtain an average assessment. From the manufacturer, Hysitron Inc., nanoindentation moduli results are known to be accurate to within 10%. There was very little variation in the measurements as indicated by the low standard deviations as given in Table 6.4. This data agrees well with those found in the literature. For instance, employing a nanoindentaion technique, a glass carbon film had a modulus of 30 GPa [161], while a CVD SiC coating had a modulus of 354 ± 30 GPa [162]. Figure 6.31, shows SiC with an indentation depth of 14 nm. The marker on the right-hand side of this figure, refers to the height in nanometers (nm) of the surface topology. The white color area represents a high region where the material uplift/or pile-up due to the Berkovich indenter occurred. The dimensional height of the triangular indenter is approximately 1 μm.

When the peak load is held constant for five seconds the displacement or penetration depth increases. The indenter movement ranges between 5-10 nm depending on the material being tested, aluminum or silicon carbide. Aluminum will creep more than SiC, but the exact amount of creep will depend on the loading rate, probe geometry, peak force, and the properties of that particular specimen, but it is normal behavior for many materials. The reason for incorporating a hold segment into the load function is to

minimize any effects of creep during unload, which is the segment used to calculate hardness and modulus.

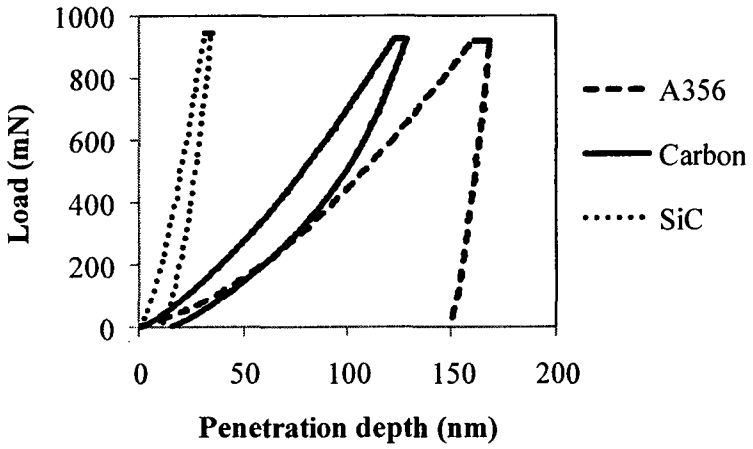


Figure 6.30 Load-penetration depth curves for the A356/SiC foam composite

Table 6.4 Nanoindentation hardness and Young's modulus results

| Nano-indentation | Modulus (GPa) | Hardness (GPa) |
|---|---|---|
| **A356 matrix** | **71 ±2.0** | **1.55 ±0.08** |
| **SiC coating** | **307 ±23.7** | **57 ±8.99** |
| **Carbon interior** | **27 ±2.1** | **6 ±0.50** |

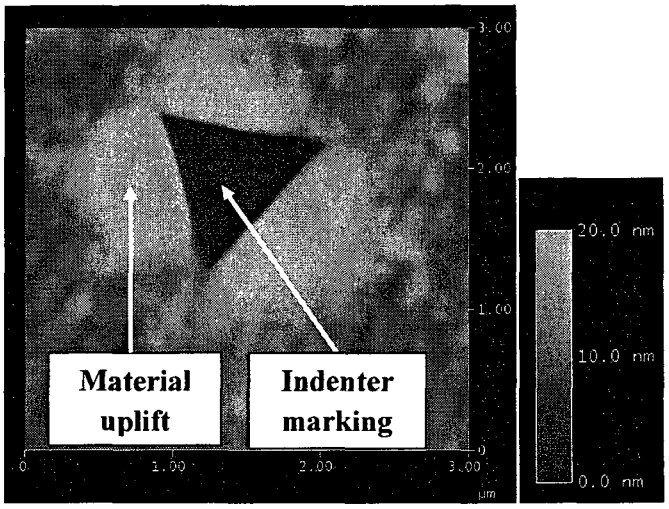


Figure 6.31 Image of the nanoindentation on the SiC strut coating

### 6.6.3 Composition Analysis Results

In this research, XRD was used to verify contamination in the melt of the vacuum infiltration experiments as well as to verify for brittle phase aluminum carbide ($Al_4C_3$) as given in Figure 6.32. As stated earlier, a large number of researchers use quartz tubes to infiltrate aluminum into a bed of packed ceramic powders. It was found that silica ($SiO_2$) contained in the quartz tube dissolves in the aluminum melt to produce free silicon and alumina. Due to this observation it was suggested to change the melt after several experiments [107]. The high temperature cement coating used in this research contains sodium silicate ($Na_2SiO_3$) and similarly may react with the aluminum as given by Equation 6.12. However, XRD results do not show any contamination after ten SiC foam infiltrations, as revealed in Figure 6.32.

$$Na_2SiO_3 + 2Al \rightarrow Si + Al_2O_3 + 2Na \qquad (6.12)$$

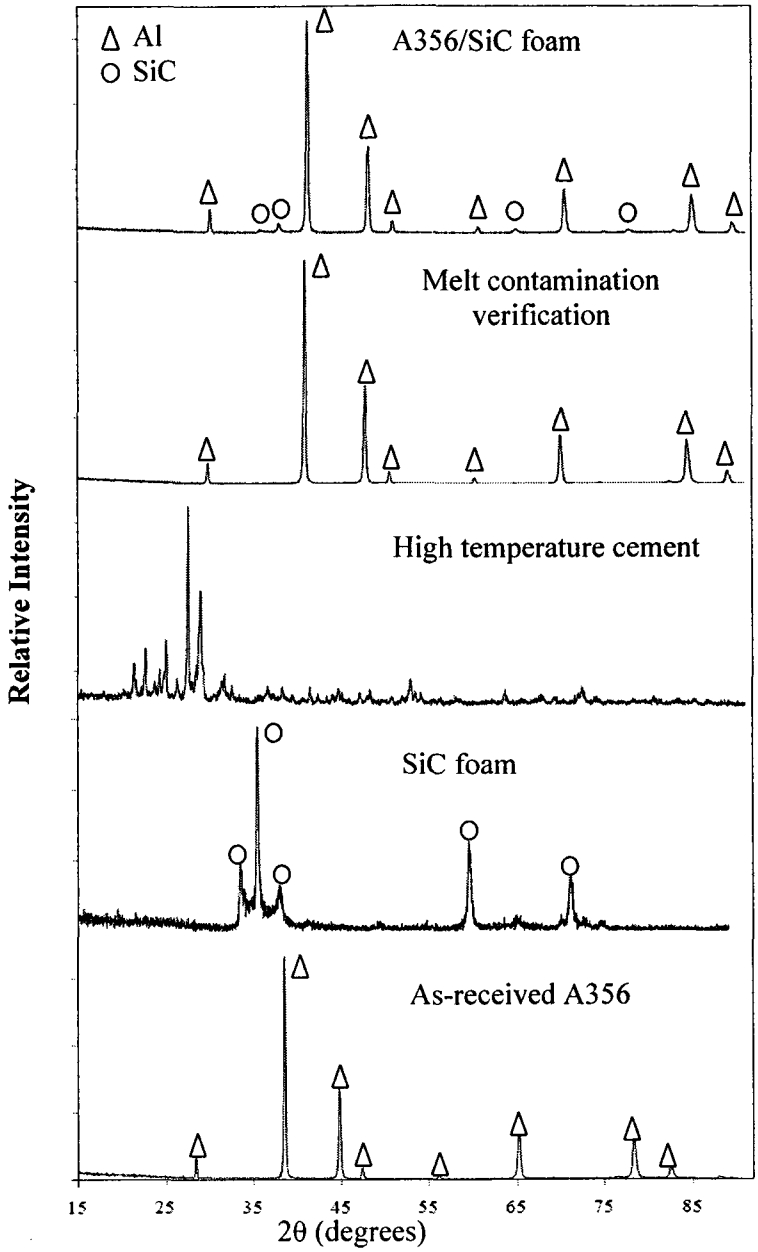


Figure 6.32 XRD comparison result

XRD was performed on the as-received A356 aluminum alloy, oxidized SiC foam, high temperature cement, melt in the crucible after ten infiltrations and the A356/SiC foam composites with and without nickel as shown in Figure 6.32. In addition, XRD was performed on the A356/SiC, 2 wt% nickel composite in order to determine if

any Ni-Al intermetallics form. The results show an identical XRD diffraction pattern as the A356/SiC foam composite without nickel in Figure 6.32, indicating that the amount of nickel is below the detection limit of the XRD detector. According to the Al-Ni phase diagram, it requires more than 40 wt% of nickel in aluminum to form intermetallic compounds. Some observations from Figure 6.32 are;

- The most intensive peak in the high temperature cement is not observed in the sample or in the crucible melt.
- The SiC foam alone and the A356 /SiC foam peaks show the presence of SiC phase.
- No $Al_4C_3$ was detected at the Al/SiC interface in the A356/SiC foam composite.

### 6.6.4 A356 Aluminum Alloy Grain Structure

The as-cast A356 Al/SiC foam composite sample was first ground to 1200 grit, followed by polishing to 1 micron with mono-crystalline diamond suspension as shown in the optical micrograph (100x) of Figure 6.33. Upon cooling, the aluminum grains have grown in the form of dendrite structures. Between the SiC struts, the grains have formed long and narrow outlines. However, closer to the interface of the struts, the dendrites or grain growth is obstructed by the solid SiC strut network. As the dendrites grow, the solid strut network cannot move with the growing dendrites, so the grains tend to grow/deform around them.

The sample was then etched for 5 seconds in a mixture of 1 mL Hydrofluoric acid and 200 mL of distilled water according to ASTM E 407 [163]. Images of the etched surface were obtained using SEM and EDS was used to determine the silicon areas. The

microstructure of the as-cast alloy A356 is shown in Figure 6.34. The silicon is dispersed between the aluminum dendrite structure and has a course acicular morphology. Some micro-pores have developed at the grain boundaries.

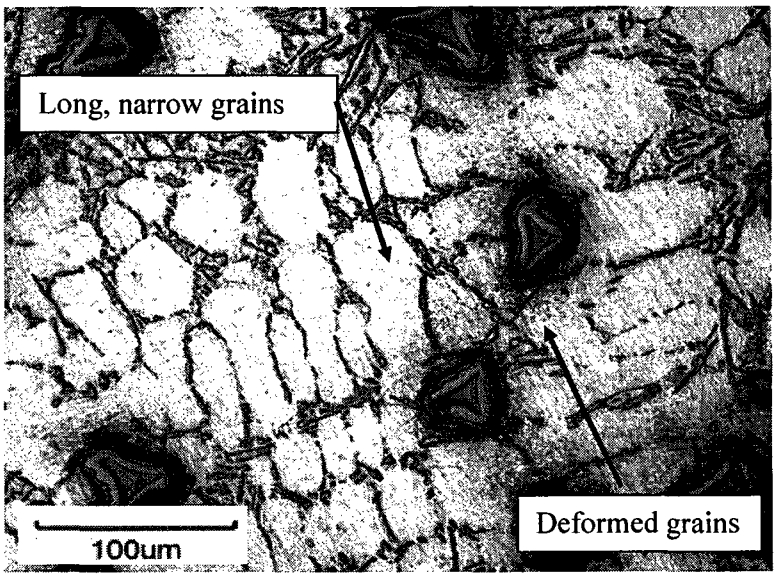


Figure 6.33 As-cast optical microstructure of the A356/SiC foam composite prior to etching

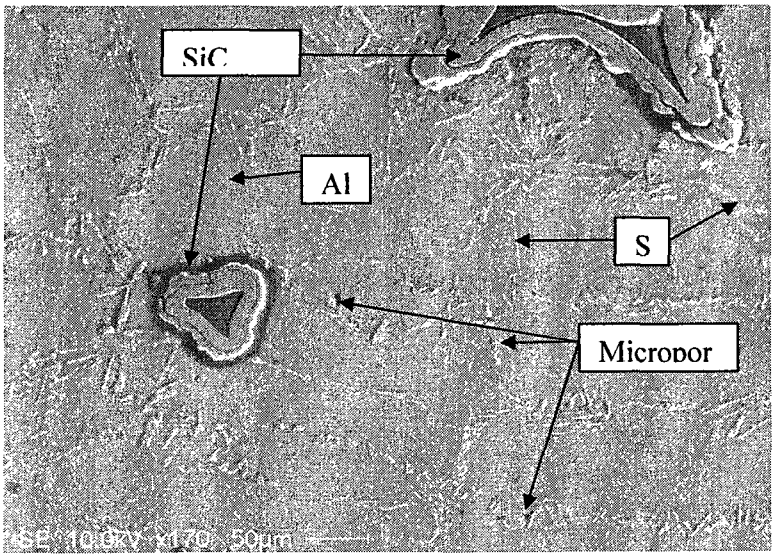


Figure 6.34 As-cast SEM micrograph of A356 Al/SiC foam composite after etching

Compositional analysis was performed on an Al/Ni-coated SiC foam composite sample as given in Figure 6.35. Some micropores exist due to solidification shrinkage. Figure 6.36 (a) shows a magnified SEM image of Figure 6.35 along with the corresponding composition element distribution X-ray map images (b-e) for element identification. The carbon map is given in (b), the aluminum map in (c), the silicon map in (d) and the nickel map in (e). X-ray mapping was performed on the A356 nickel coated SiC foam composite in order to determine the location of the nickel. From the nickel map, it appears the nickel has remained on the outer surface of the SiC foam as it shows up as a definitive line. The nickel coating did not dissolve and segregate around the grain boundaries in the aluminum matrix. The x-ray maps also show the center of the foam to be carbon and the eutectic silicon in the aluminum. Even with a nickel coating, some porosity still exists, possible due to solidification shrinkage.

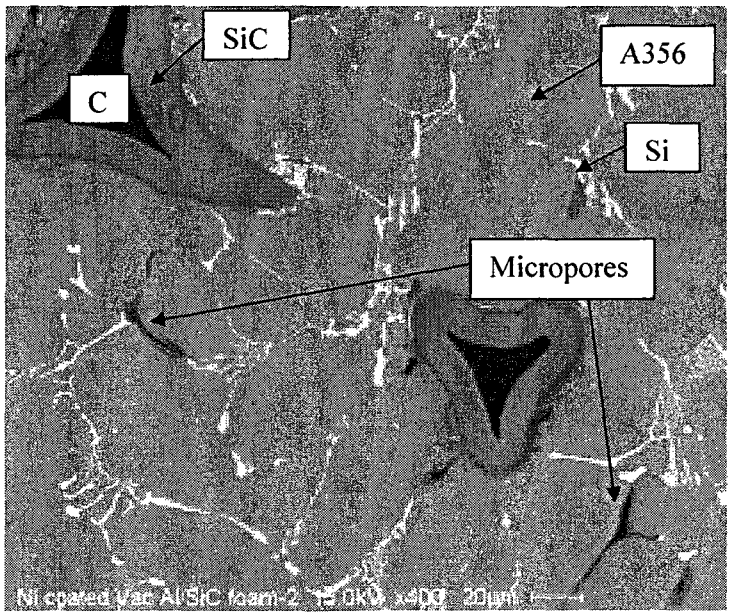


Figure 6.35 SEM image of an A356, nickel coated SiC foam composite

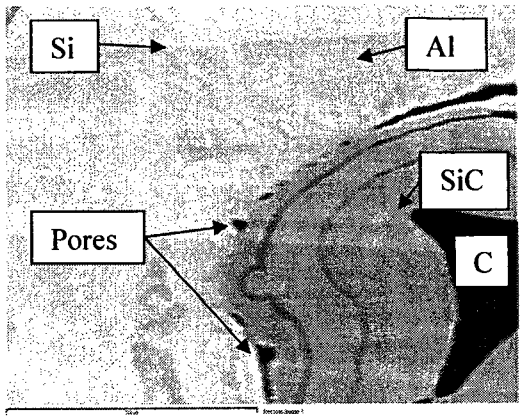


(a)

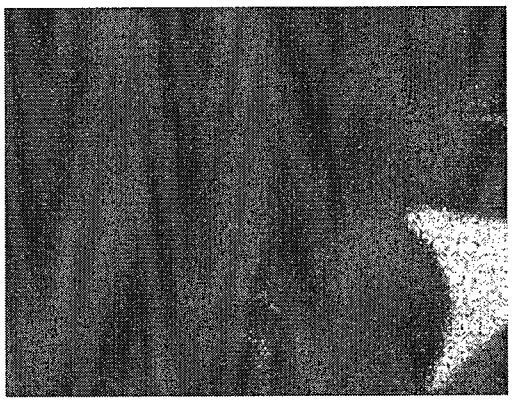

Carbon Ka1_2

(b)

Aluminum Ka1

(c)

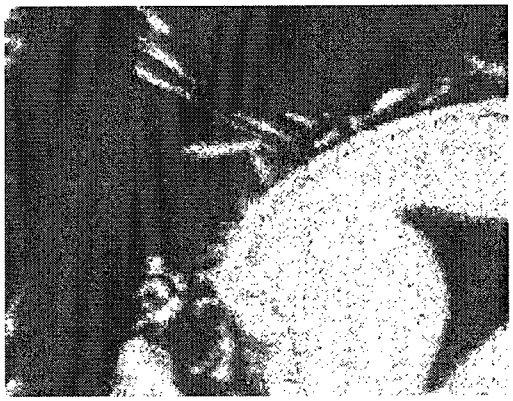

Silicon Ka1

(d)

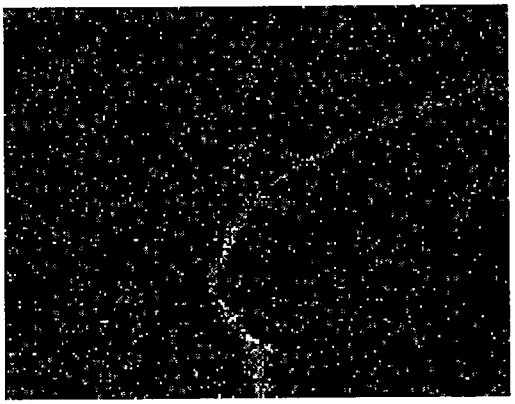

Nickel Ka1

(e)

Figure 6.36 SEM image (a) and X-ray map images of A356, nickel coated SiC foam composite (b-e).

### 6.6.5 Compression Test

Figure 6.37, is a typical compressive stress-strain curve for the SiC ceramic foam. Initially, as the cross-head of the Instron machine contacts the specimen, the load increases linearly until a small plateau is reached. The samples begin to crush and damage is observed on the top and bottom of the sample as broken ceramic material. The X and Z directions have similar strengths, while Y direction is stronger. To ensure isotropic properties, the samples were cut from the X and Z directions.

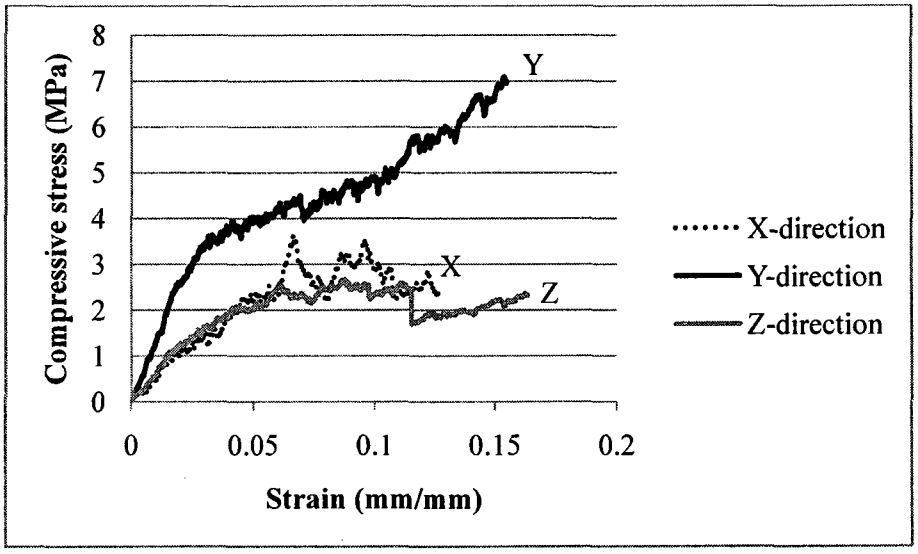


Figure 6.37 Typical stress-strain curve of the SiC ceramic foam showing the three strength directions, X, Y and Z

The engineering stress was obtained by dividing the axial force by the initial cross-sectional area of each sample. The axial strain was evaluated using one strain gage placed in the longitudinal direction as shown in Figure 6.38.

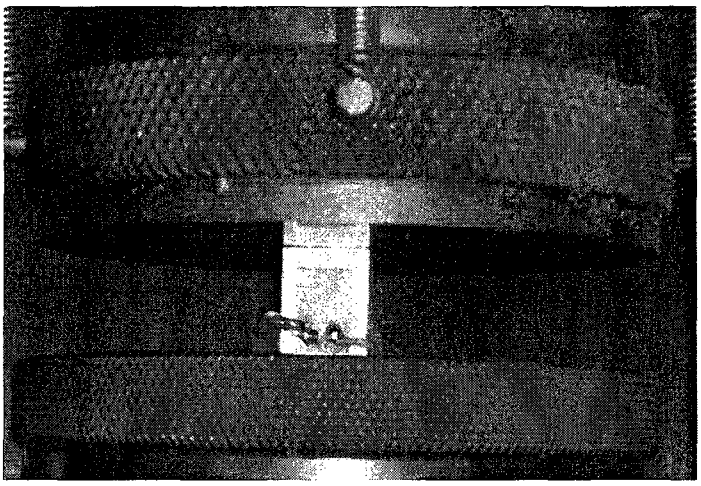

Figure 6.38 Digital photo of compression testing in the MTS machine

The typical compression behavior for the Al/SiC foam composites is given in Figure 6.39, for composites with 0 wt% nickel and 2 wt% nickel and the modulus values are tabulated in Table 6.5. The moduli were calculated from the linear slope of the stress-strain region between the loads of 200 N to 1000 N (~2-10 MPa). For example, the 2 wt% nickel composite corresponds to strains of about 0.01% (100 micro-strain), as shown in the magnified areas of Figures 6.40.

The 0 wt% Ni and 2 wt% Ni Al/SiC foam composites have average Young's moduli of 76.36 ±1.51 GPa and 80.60 ±2.55 GPa, respectively. Addition of nickel increases the average composite stiffness by 5.5 %. This new composite (without nickel) has a 9.1% higher stiffness than the A356 aluminum alloy matrix material, indicating the SiC network is making the composite stiffer. Although the composite has low reinforcement concentration (approximately 12 vol%), an increased stiffening does occur. In literature, Young's modulus of typical Al/SiC particulate MMCs employed for packaging materials range from 167 GPa to 192 GPa for 55 vol% and 63 vol% SiC,

respectively [4]. The two-phase theoretical strut modulus composed of vitreous carbon and CVD SiC was calculated using the ROM, Equation 5.1. In literature theoretical CVD

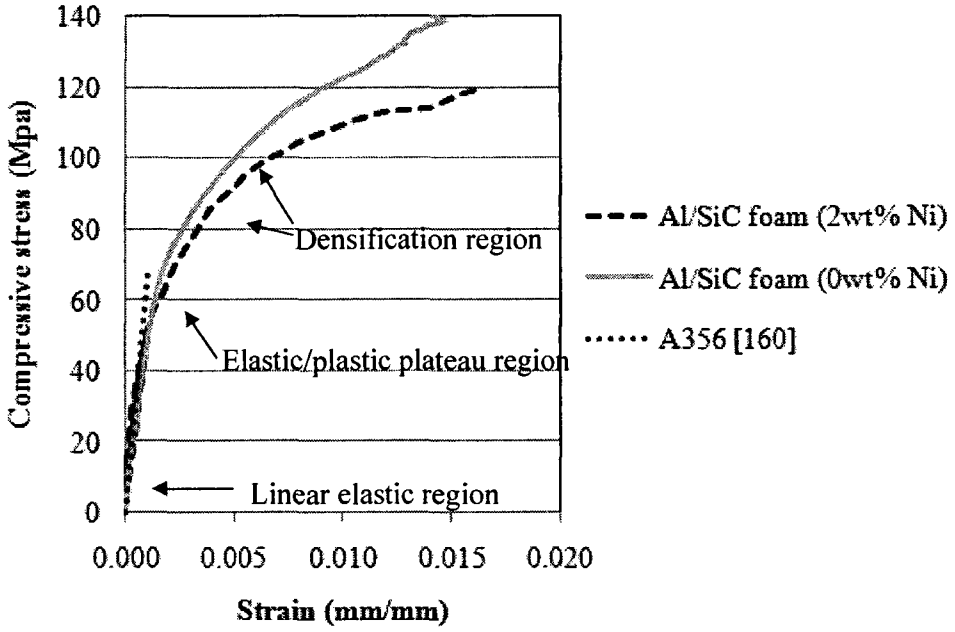


Figure 6.39 Compressive stress-strain results

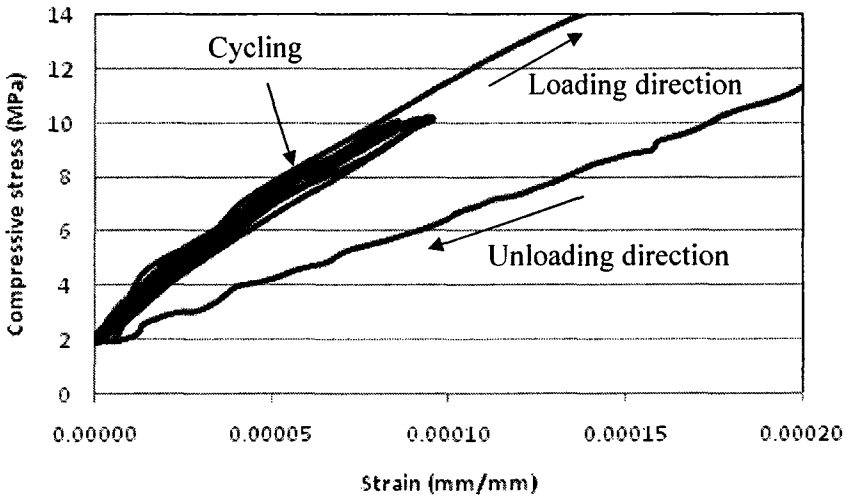


Figure 6.40 Magnified region of compressive stress strain curve for 2 wt% nickel

Table 6.5 Experimental Young's modulus results with porosity

| Samples | Porosity (%) | Average porosity (%) | Standard deviation (±) | Composite Young modulus (Gpa) | Composite average Young modulus (%) | Standard deviation (±) |
|---|---|---|---|---|---|---|
| 0% Nickel | | | | | | |
| 1 | 9.22 | | | 76.34 | | |
| 2 | 7.86 | | | 78.22 | | |
| 3 | 8.58 | 8.55 | 0.56 | 74.53 | 76.36 | 1.51 |
| 2% Nickel | | | | | | |
| 4 | 6.26 | | | 77.58 | | |
| 5 | 6.51 | | | 83.81 | | |
| 6 | 7.97 | 6.91 | 0.75 | 80.42 | 80.60 | 2.55 |

SiC modulus is 415 GPa [164], and vitreous carbon moduli is 20.7 GPa [89]. In this study, employing the nanoindentation technique, the results for SiC are 307 GPa and 27 GPa for carbon, while the volume fractions of carbon and SiC from the oxidization test, of 0.23 and 0.77, respectively, the strut modulus is calculated to be 243 GPa. This value is lower than the modulus of solid CVD SiC of 415 GPa, since the interior of the strut is composed of lower modulus carbon. The results are compared in Figure 6.41.

In this case, the addition of the SiC network into the aluminum alloy resulted in an increase of stiffness. The SiC struts being stiffer than the aluminum alloy, are assumed to hold the load until they break under the applied load at approximately 5000 N (or 50 MPa) as shown in Figure 6.39. At this point the matrix takes over and establishes the stress-strain behavior. The A356/SiC foam composites show a general trend as established by previous authors for a two-phase composite material [165]. The curves follow a pattern having an initial linear elastic deformation where strut wall bending

occurs. As the stress level increases, the brittle struts reach their peak strength value and gradually buckle reaching a short elastic-plastic plateau. Upon further loading, the matrix begins to carry the load and plastically deforms in a ductile manner. As the stress increases, the strain increases due to bending, buckling, collapsing and crushing of the struts, thereby densifying the composite.

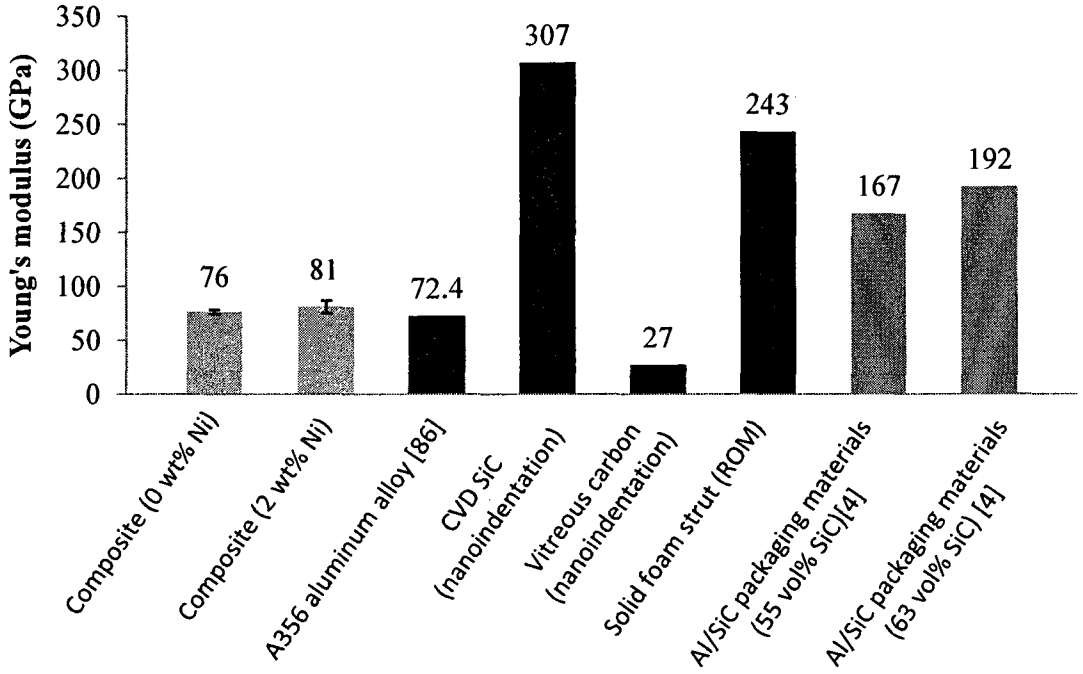


Figure 6.41 Comparison of various Young moduli values

To understand how failure of the struts occurred subsequent to compressive loading, the internal damage was observed using SEM images. A representative microstructure of the composite prior to compression testing is given in Figure 6.42. A typical sample evaluated at 3.3% strain (initial sample height is 15 mm, and final height is 14.5 mm) was cross-sectioned in the longitudinal direction, parallel to the load

direction as shown in Figure 6.43. The micro-structural damage is dominated by broken, cracked and delaminated SiC struts. The matrix deforms into circular profiles having larger diameters then the original foam pores as given in Figure 6.43. Figures 6.43 and 6.44 show the majority of the strut cross-sections fractured at 45° to the loading direction which is representative of shear fracture in compression. When loaded axially, ductile materials are known to fracture at a 45° plane from shear stresses, while brittle materials fail from normal stresses at 0° or perpendicular to the load direction. In Figure 6.44, the fractured crack has moved through the SiC layer into the carbon strut interior indicating a good interface bonding, as the load is transferred from the matrix to the reinforcement.

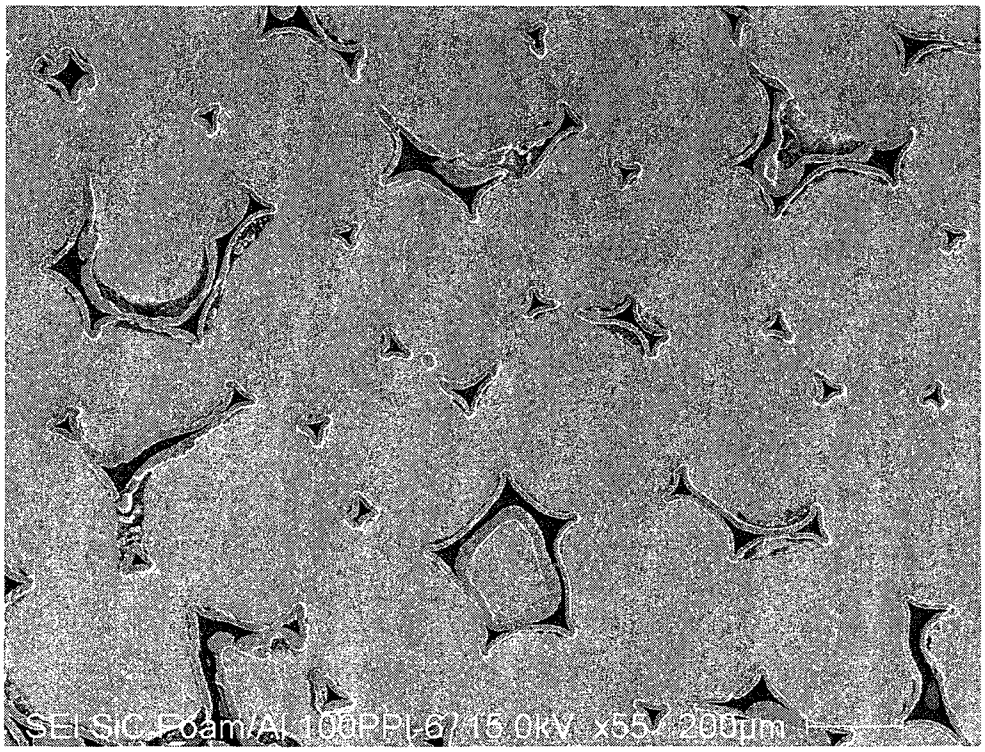


Figure 6.42 Typical microstructure prior to compression testing

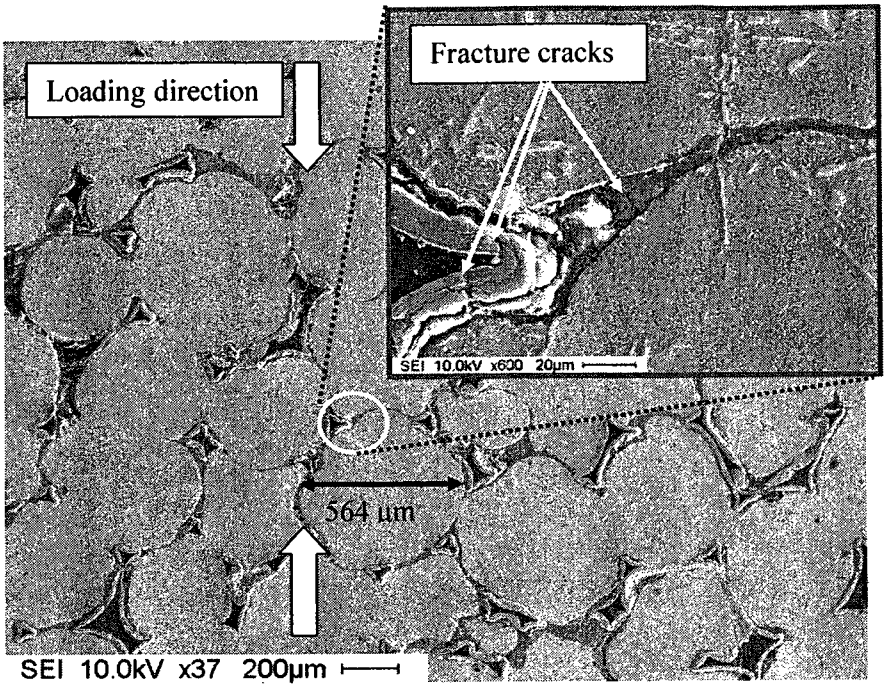


Figure 6.43 Typical microstructure subsequent to compression testing

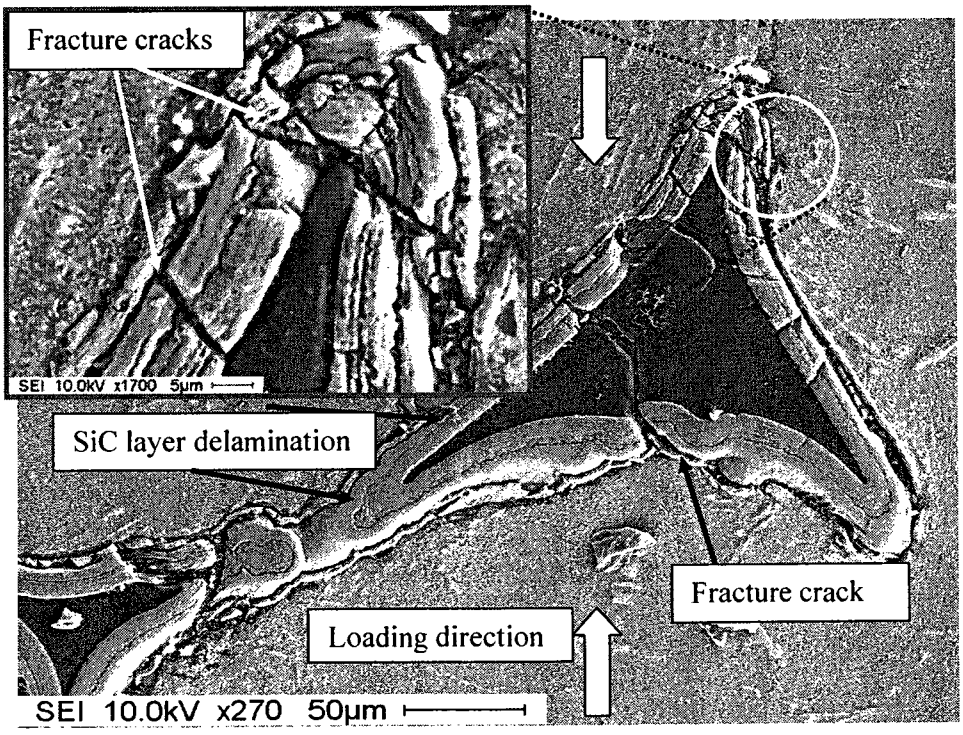


Figure 6.44 Magnified area of a fractured strut in compression

### 6.6.6 Flexural Strength Test

The four-point bending fixture was produced in-house and is shown in Figure 6.45. The local fracture of the Al/SiC composites occurred on the tension sides of the samples as shown in Figure 6.46.

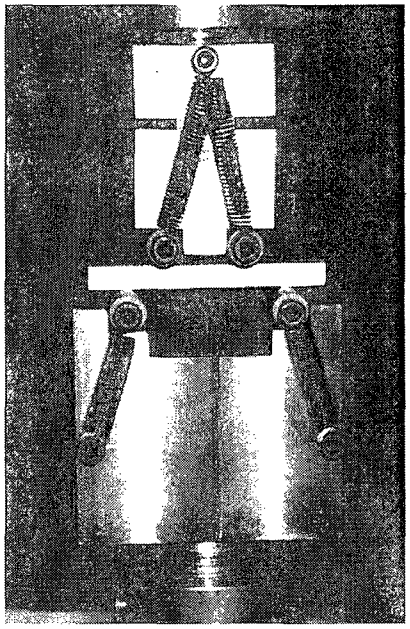

Figure 6.45 Digital image of 4-point bending fixture

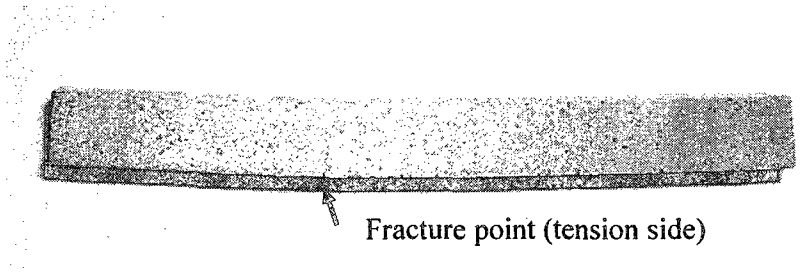


Figure 6.46 Digital image of the Al/SiC foam fractured sample

All sample geometries were ground finished to 600 grit silicon carbide paper on four sides to remove any stress concentrations due to machining. Samples with 0% and

2% nickel were tested to measure the flexural strength of the composite. The maximum or break load of each sample was obtained from the data acquisition system. The experimental flexural strength results for the A356/SiC foam composite of varying porosities, along with typical Al/SiC (70 vol% reinforcement) and A356 aluminum alloy are presented in Figure 6.47 and tabulated in Table 6.6.

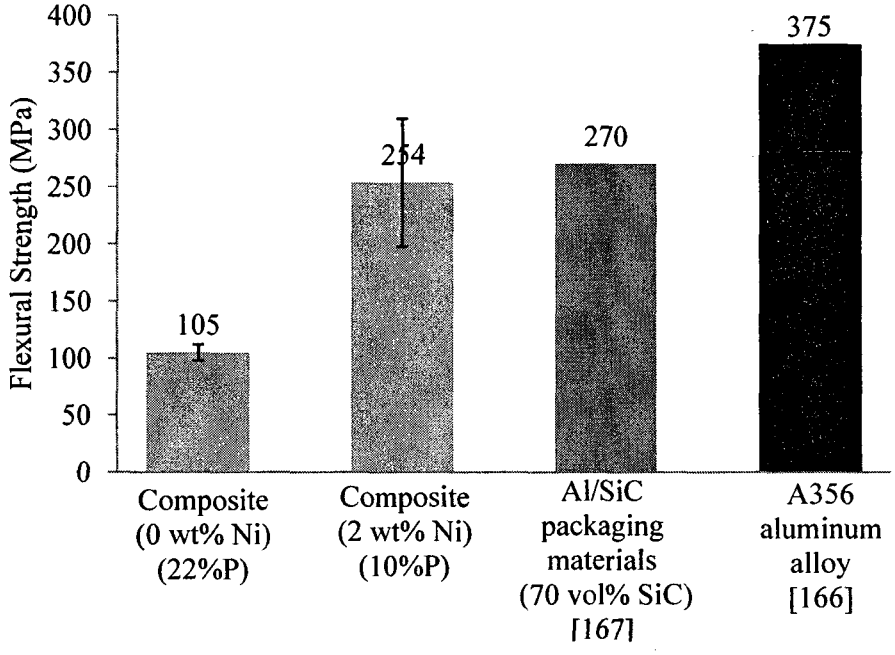


Figure 6.47 Comparison of various flexural strength values

Table 6.6 Experimental flexural strength results with porosity

| Samples | Porosity (%) | Break load (N) | Flexural strength (MPa) | Average flexural strength (MPa) | Standard deviation (±) |
|---|---|---|---|---|---|
| 0% Nickel | | | | | |
| 1 | 23.7 | 750 | 103.23 | | |
| 2 | 22.6 | 788 | 97.41 | | |
| 3 | 21.3 | 820 | 115.49 | 105.38 | 7.53 |
| 2% Nickel | | | | | |
| 4 | 6.5 | 2139 | 332.20 | | |
| 5 | 10.6 | 1210 | 230.68 | | |
| 6 | 14.4 | 1322 | 199.39 | 254.09 | 56.69 |

The flexural strength of an A356 aluminum alloy is reported to be 375 MPa [166] and Al/SiC (70 vol% SiC) MMC is currently employed in electronic packaging base plates with a bend strength of 270 MPa [167]. Looking at individual results (Figure 6.48), for a 14% porous composite, flexural strengths of 160 MPa and 199 MPa were obtained for 0% nickel and 2% nickel respectively. Therefore, adding 2% nickel increased the strength by 24%. The highest flexural strength occurs at 332 MPa, for 6.5% porosity (Table 6.6) composite.

The flexural strength results of this study are in the same range as a previous study on nickel-coated SiC particles, vacuum infiltrated with an Al-5.9 wt% Si-0.23 wt% Mg alloy. For composites containing 50 vol% SiC particles and an average of 5 wt% Ni, the average flexural strengths varied between 118 MPa and 156 MPa [67].

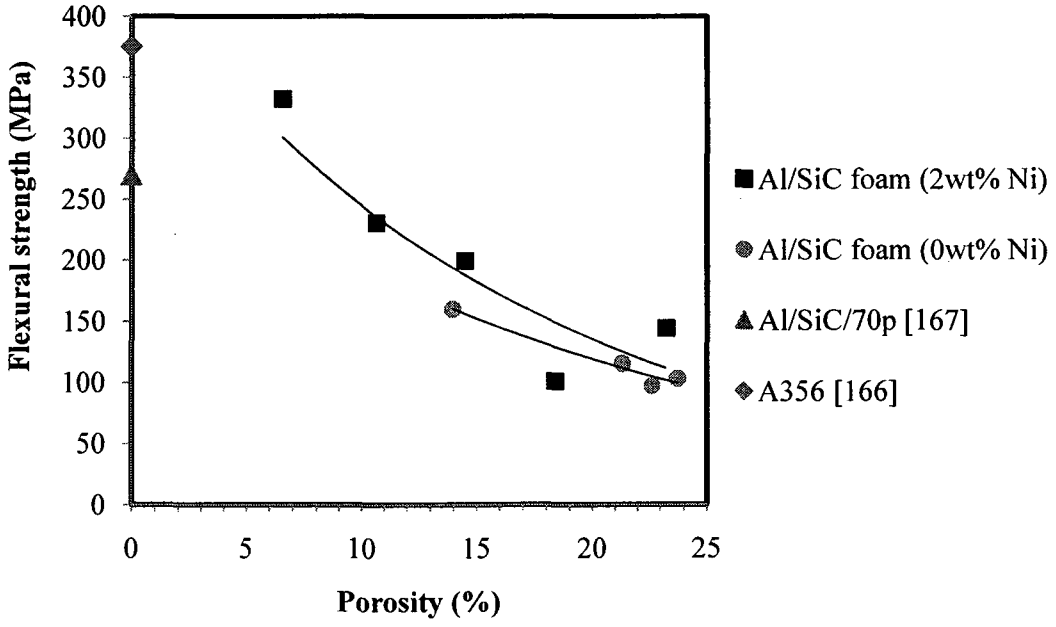


Figure 6.48 Flexural strength versus porosity for individual tests performed

Lower strength values are due to porosity and the brittle ceramic struts. However, with only 12% SiC reinforcement and 6.5% porosity, this material is comparable to typical Al/SiC MMC with 70% SiC. The standard deviation value for the 2% nickel coated samples is quite large, however if the number of samples is increased, the standard deviation range should decrease. In a similar study, various aluminum alloys incorporating 60% SiC particles were four-point bend tested using five samples of each composition. The standard deviation was as high as ±63.1 for an Al-Cu alloy [168]. If porosity of the Al/SiC foam samples in this study was decreased, the overall flexural strength would increase and be comparable to other similar literature materials. Pores are considered as flaws in the material and contribute to weak points and stress concentrations throughout the composite.

### 6.6.7 Fractographic Analysis of Flexural Test

Subsequent to the four-point bend test, the fractured surfaces were analyzed. SEM was employed to determine the failure mechanisms of the Al/SiC foam composite, while EDS spot analysis was used to determine if the SiC struts have detached entirely from the aluminum or the multi-layers structure of the strut arrangement have de-bonded from one another. Figure 6.49 shows the general fracture surface area in bending of the A356 matrix and SiC reinforcing struts. The A356 aluminum-silicon alloy matrix show signs of mixed fracture. Cleavage regions are shown as flat areas and are related to brittle failure while some dimpling also occurs and are related to ductile failure. A356 alloy with its 7wt% silicon content was utilized due to its good flowability characteristics for casting as well as preventing intermetallic $Al_4C_3$ from forming; however brittle silicon particles in the aluminum matrix tend to deteriorate the ductility of the aluminum. Since silicon is

more brittle than the aluminum, it tends to fracture before the ductile aluminum. Three different fractured regions can be observed from the SiC reinforcement strut; in some areas the SiC struts have detached from the matrix indicated by the Al/Si phases, while in other areas, the matrix has un-bonded from the SiC strut as indicated by the C/Si phases. Yet, in other areas, the multilayered SiC struts have cracked and de-bonded from one another as is indicated in the Figure 6.50. Some solidification shrinkage porosity (P) at the Al/SiC interface is observed. Figure 6.50 shows regions depicting crushed struts and missing SiC layers of the multi-layered struts. In Figure 6.51, magnified area 1, and in Figure 6.52, magnified area 2, the presence of cracked struts indicates the interface bonding in this area is good and the load is transferred from the matrix to the reinforcement. Magnified region 2, Figure 6.52 shows a fracture of the multi-layered strut, de-bonding of a single layer from both the matrix and its reinforcement and a missing layer, presumably attached to the second fractured portion of the flexural test specimen. Areas with missing layers, indicate a strong interface bond between the SiC layer and the matrix but a lower bond strength between the individual SiC layers. In some areas of the SiC foam such as in Figure 6.51, and Figure 6.52, convex dimpled regions on the surface of the SiC foam are few while in other regions, Figure 6.53, the convex dimples are numerous. The difference is assumed to be due to the manufacturing process.

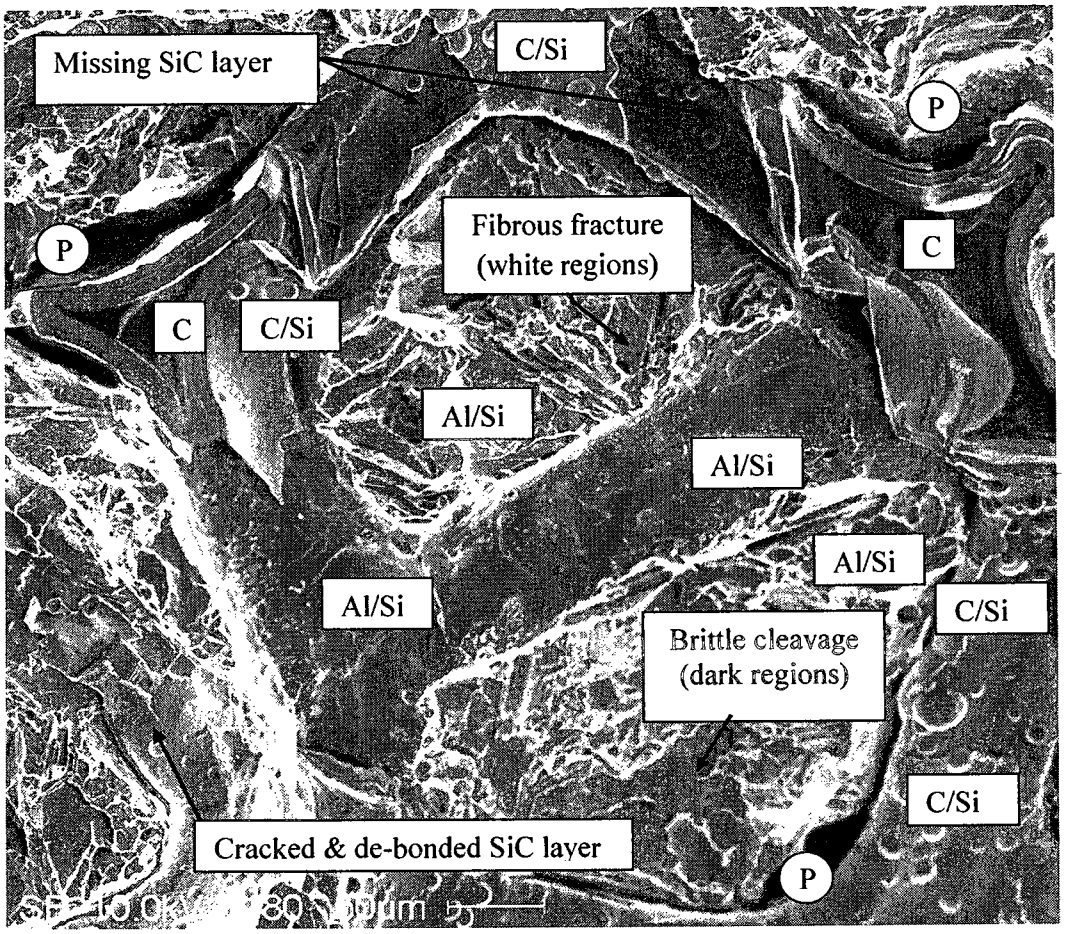


Figure 6.49 SEM flexural fracture surface of Al/SiC foam composite

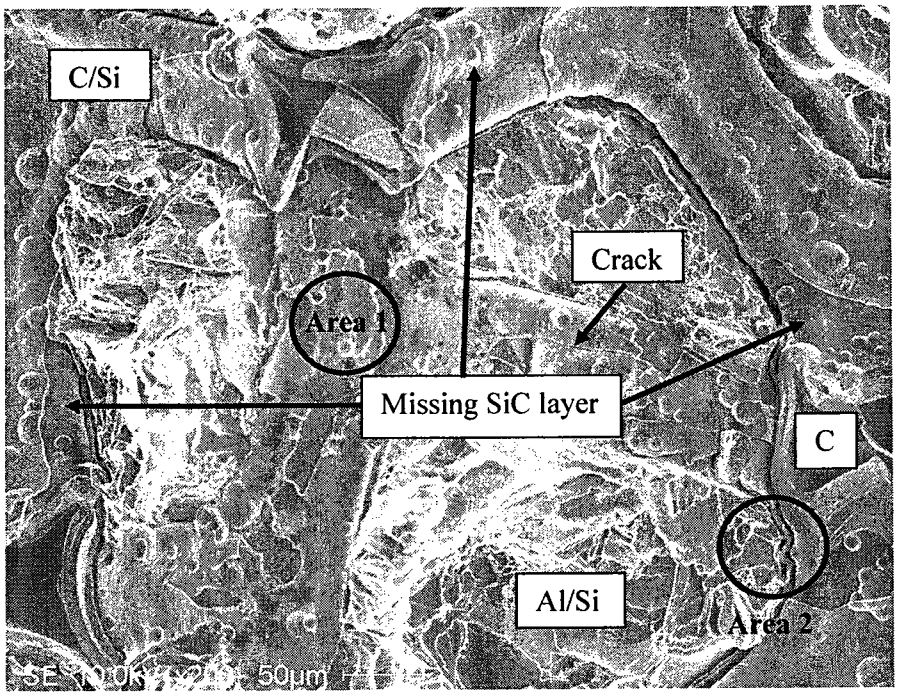


Figure 6.50 SEM region of cracked struts (flexure)

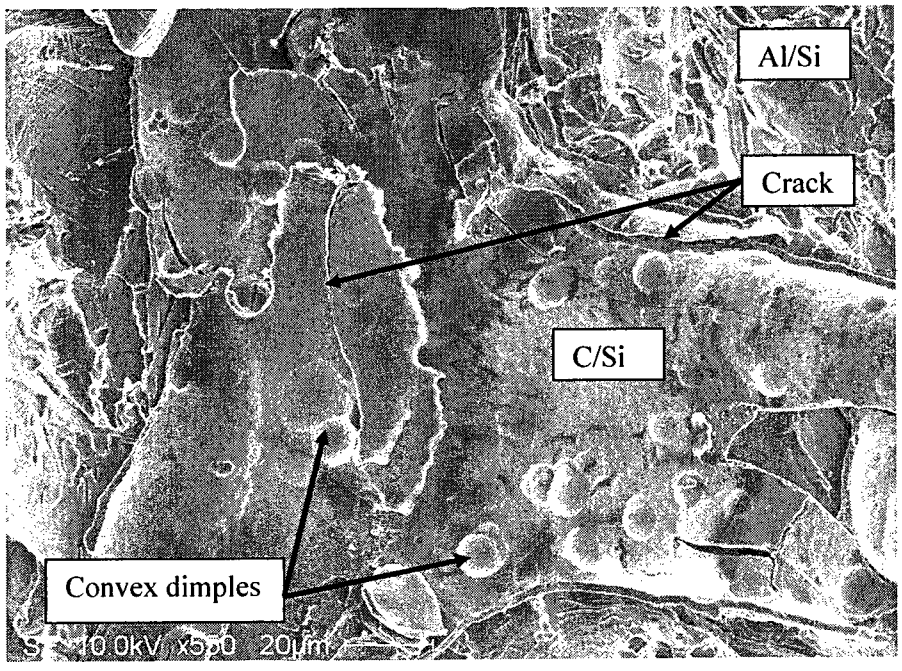


Figure 6.51 Magnified region of area 1

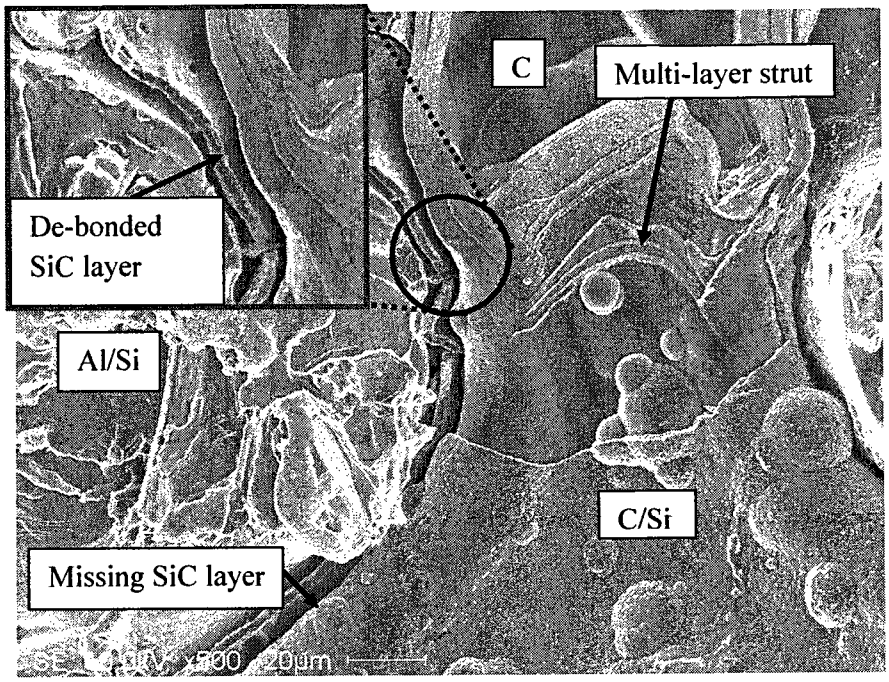


Figure 6.52 Magnified region of area 2

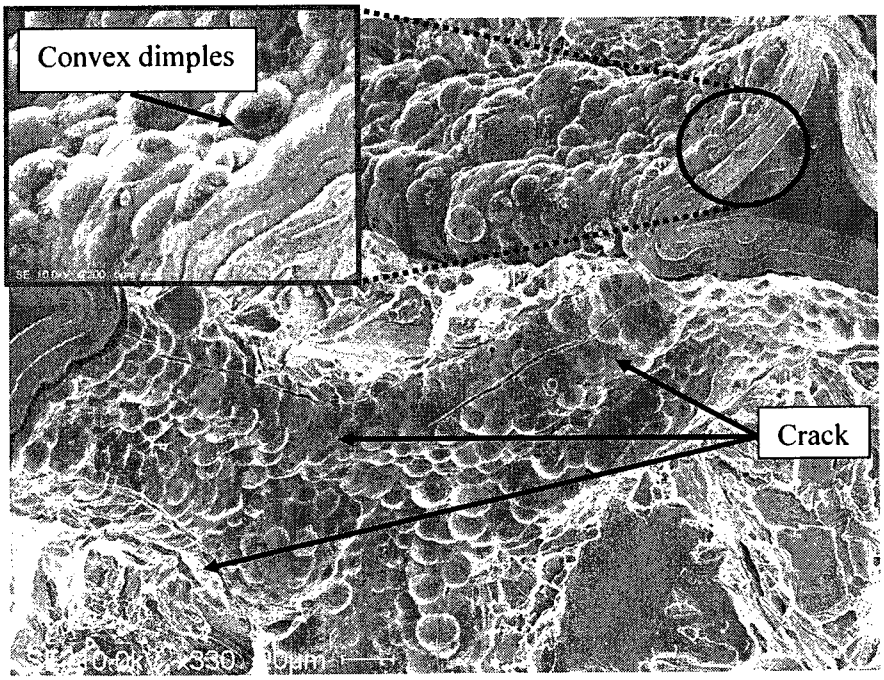


Figure 6.53 Convex dimples in outer surface of the SiC foam strut

### 6.6.8 Charpy Test

The material toughness or its resistance to fracture is determined by the amount of energy it can absorb during a high strain rate Charpy impact test. The total impact energy for A356/SiC foam composite specimens ranged from 1.23-1.34 J for notched and un-notched samples, respectively as given in Table 6.7. These are typical energies for IPCs as reported for an $Al_2O_3$/Al composite of 1.3 J [74]. Figure 6.54, shows the impact strength results for notched and un-notched Charpy specimens with 0% and 2% nickel. The results are compared against literature data [169] for un-notched A356 aluminum alloy. The reduction in toughness from the as-received A356 aluminum alloy is due to the presence of the SiC strut 3-D network structure, as it acts as stress concentrations making the composite more fracture sensitive than the pure matrix.

Both notched A356/SiC foam composites with 0 % and 2% nickel have the same impact energies of 1.23 J. Similarly, the un-notched 0% and 2 % nickel samples have impact energies of 1.25 J and 1.34 J, respectively that are close to one another. This suggests that adding a 2 wt% of nickel does not affect the impact energies to a great extent. By adding a notch to the A356/SiC (0% Ni) composite, the impact energy reduced by 1.6%. In addition, by incorporating the ceramic network structure, the impact energy of the notched samples decreased by 70%, from the A356 aluminum alloy.

Table 6.7 Experimental Charpy results with porosity

| 0% Nickel (notched) | Porosity (%) | Average porosity (%) | Standard deviation (±) | Total impact energy (J) | Average impact energy (J) | Standard deviation (±) |
|---|---|---|---|---|---|---|
| 1 | 8.86 | | | 1.03 | | |
| 2 | 9.69 | | | 1.44 | | |
| 3 | 17.85 | 12.13 | 4.06 | 1.23 | 1.23 | 0.17 |
| 0% Nickel (un-notched) | | | | | | |
| 1 | 9.54 | | | 1.29 | | |
| 2 | 13.02 | | | 1.25 | | |
| 3 | 17.05 | 13.20 | 3.07 | 1.22 | 1.25 | 0.03 |
| 2% Nickel (notched) | | | | | | |
| 1 | 10.97 | | | 1.08 | | |
| 2 | 16.58 | | | 1.32 | | |
| 3 | 22.46 | 16.67 | 4.69 | 1.28 | 1.23 | 0.11 |
| 2% Nickel (un-notched) | | | | | | |
| 1 | 11.77 | | | 1.69 | | |
| 2 | 13.83 | | | 1.21 | | |
| 3 | 14.91 | 13.50 | 1.30 | 1.12 | 1.34 | 0.25 |
| A356 (notched) | | | | | | |
| 1 | 1.28 | | | 2.39 | | |
| 2 | 1.68 | | | 2.13 | | |
| 3 | 1.15 | 1.37 | 0.23 | 1.80 | 2.10 | 0.24 |

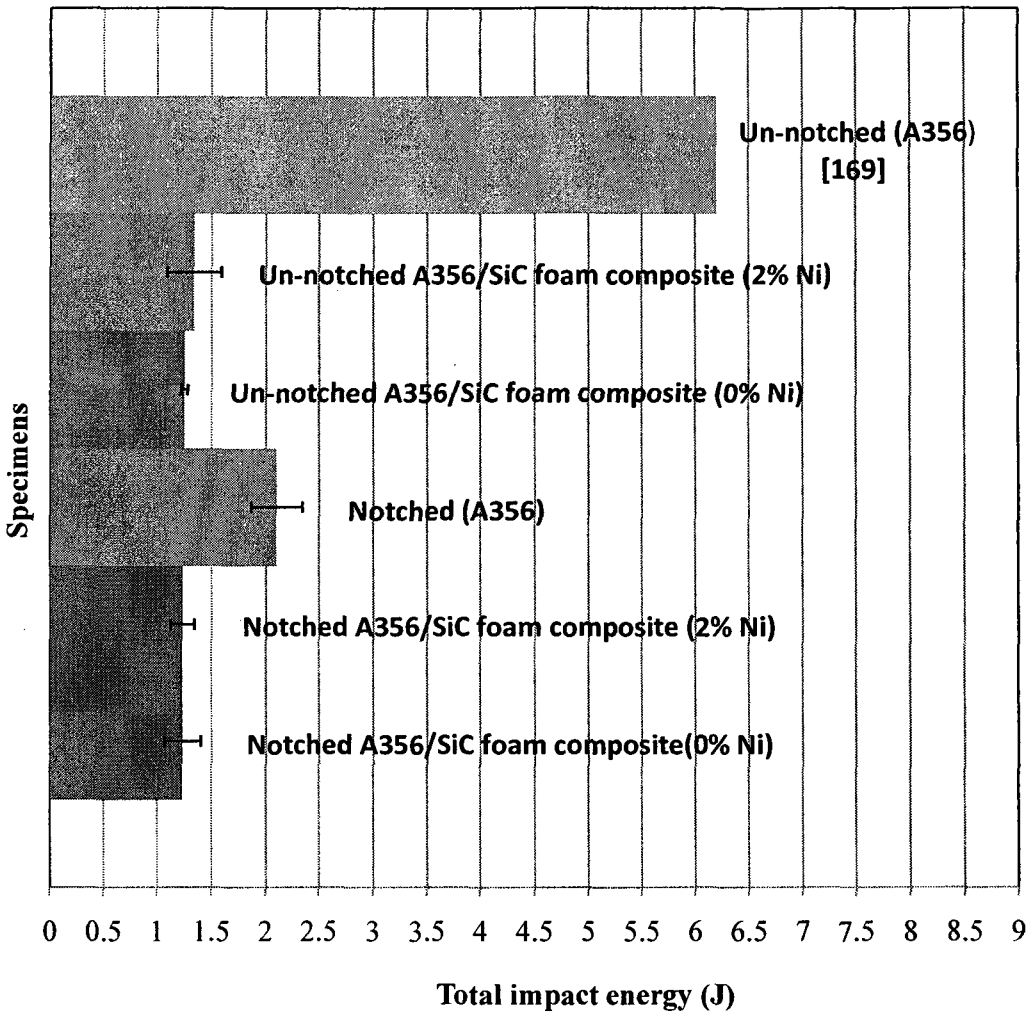


Figure 6.54 Impact energy for V- notch and un-notched Charpy samples

### 6.6.9 V-Notched A356/SiC Foam Composite

The fractured V-notched A356/SiC composite Charpy samples show a relatively horizontal break as given in Figure 6.55, while the cross-sectional fractured surface for notched A356/SiC composite with 0% nickel is shown in Figure 6.56. The 2% nickel composite has a similar trend to Figure 6.56. Pores are shown as black spots while the filled aluminum is gray. Both 0% and 2% nickel, notched composites show relatively flat

surfaces indicating the fracture mode to be brittle. Due to the brittle nature of the SiC ceramic, the composite impact energy was lower than the un-reinforced A356 aluminum alloy. The addition of a 3-D SiC foam reinforcement causes the composite impact energy

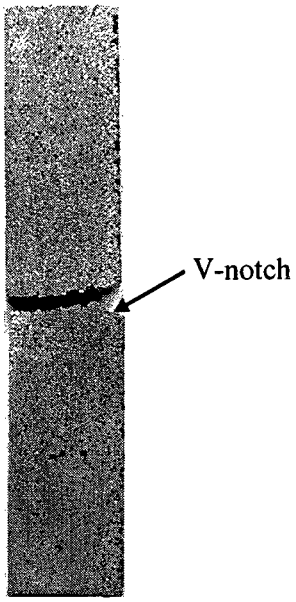


Figure 6.55 Digital image of the V-notched A356/SiC Charpy impact test specimen

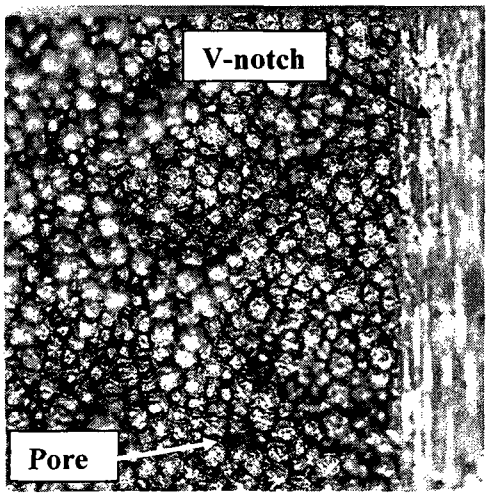


Figure 6.56 Digital image of charpy fracture surface for V-notched A356/SiC composite with 0% nickel

to decrease by 41% for the notched samples with 0% and 2% nickel addition.

The total absorbed energy shown in Figure 6.57 for a notched composite with 0% nickel and an average of three specimens for each test, gave a value of 1.23 Joules ±0.17 (0.69 ft-lb). The 2% nickel has a very similar trend to Figure 6.57 and has an average total absorbed energy of 1.23 Joules ±0.11 (0.69 ft-lb). This suggests, the addition of only 2% nickel does not affect the toughness of this composite.

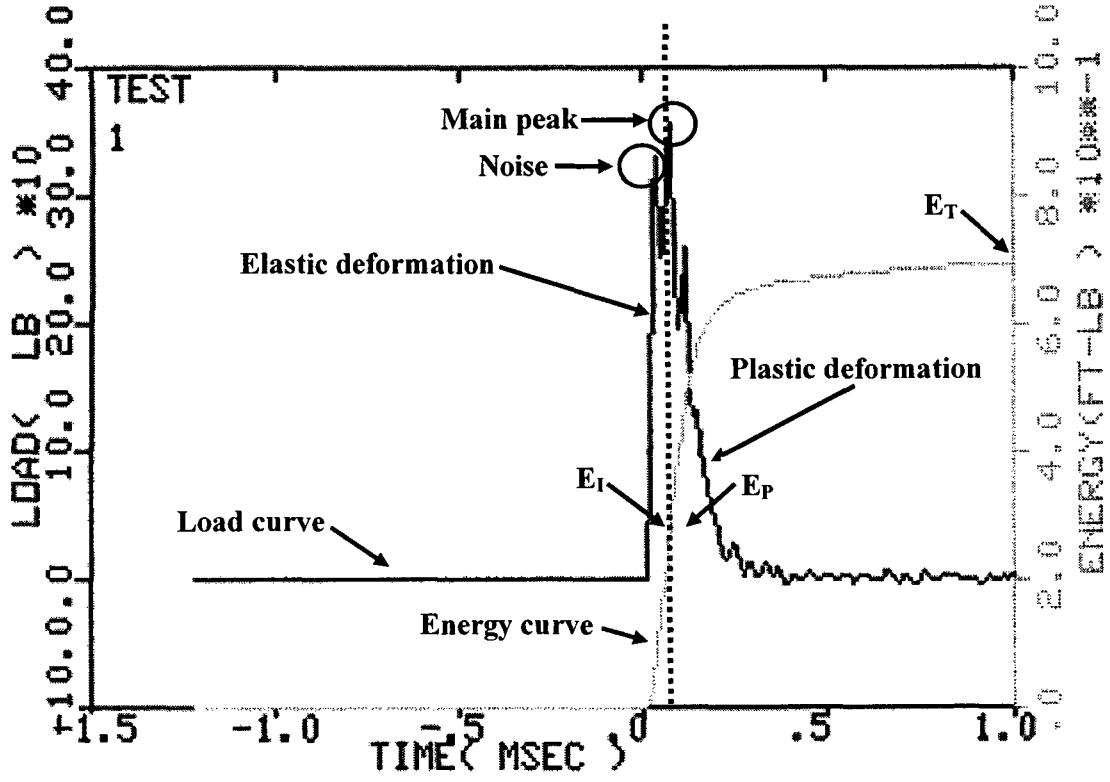


Figure 6.57 Charpy impact Load/Energy-Time curve for the notched A356/SiC composite containing 0% nickel

### 6.6.10 Un-Notched A356/SiC Foam Composite

Similarly, the fractured un-notched A356/SiC foam composite Charpy sample shows a relatively horizontal break as given in Figure 6.58 while, the cross-sectional un-notched A356/SiC composite surface with 0% nickel is shown in Figure 6.59. In the same way as the V-notched A356/SiC samples, the 2% nickel un-notched composite has a similar trend to Figure 6.59. Both un-notched composites also show relatively flat surfaces. Notched and un-notched sample have similar impact energies indicating an absence of notch sensitivity.

The curve in Figure 6.60 shows both, the load-time curve and the energy-time curve for the notched A356/SiC foam composite. The load curve can be divided into two regions; elastic and plastic deformation separated by the dashed line. It produces little elastic (almost no yielding observed) and plastic deformation as both the load increase and decrease curves respectively, are roughly vertical, straight lines. This sharp peak is indicative of a brittle material. The total absorbed energy (total area under the load-time curve) was read directly from the computer print-out. The total absorbed energy shown in Figure 6.60 for an un-notched composites with 0% and an average of three specimens for each test, produced a value of 1.25 Joules ±0.03 (0.86 ft-lb). Crack initiation energy (area under the load-time curve up to maximum load) and crack propagation energy (area under the load-time curve subsequent to maximum load) occur in a short time as depicted by their small areas under the load-time curve. The 2% nickel has a very similar trend to Figure 6.60 and has an average total absorbed energy of 1.34 Joules ±0.25 (0.80 ft-lb). Similar to the notched samples, this suggests, the addition of only 2% nickel does not affect the toughness of this composite.

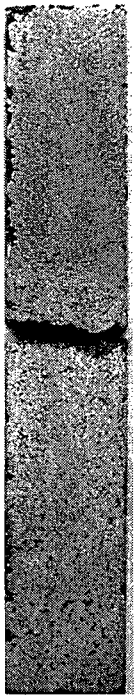

Figure 6.58 Digital image of the un-notched A356/SiC Charpy impact test specimen

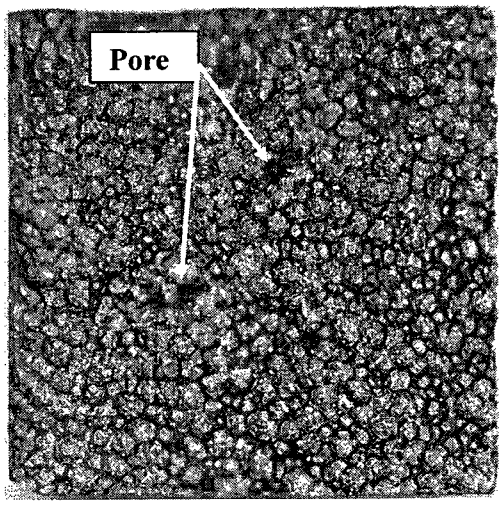


Figure 6.59 Digital image of charpy fracture surface for un-notched A356/SiC

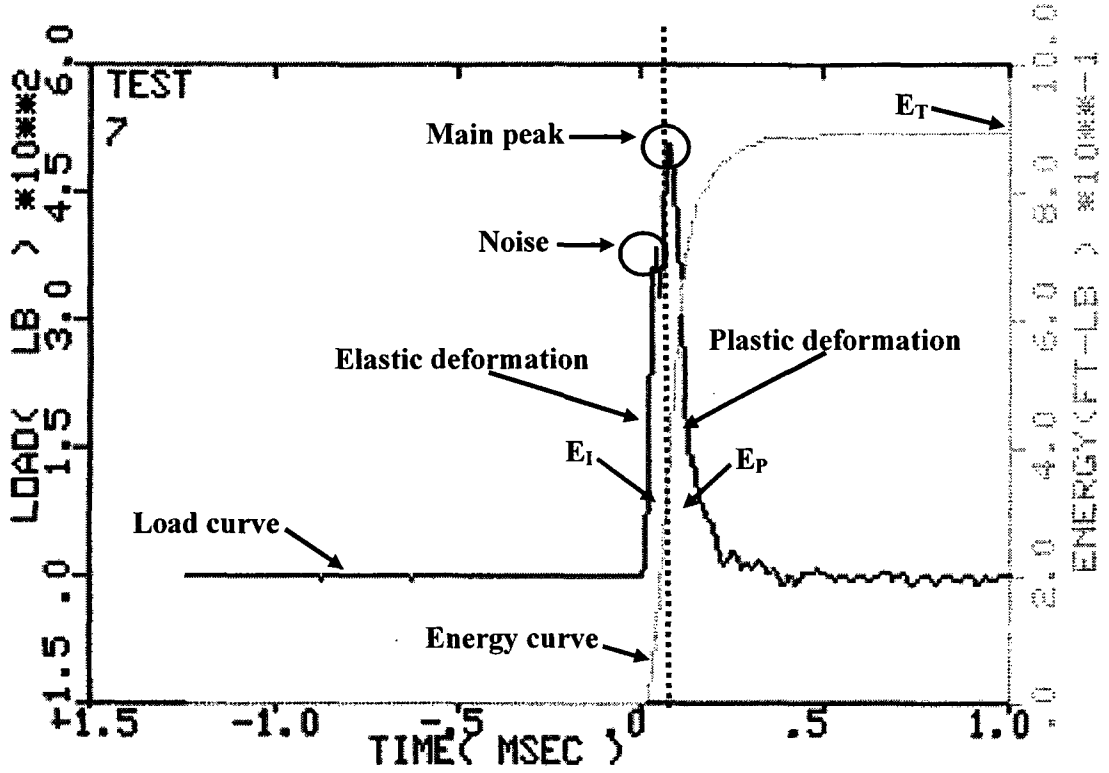


Figure 6.60 Charpy impact Load/Energy-Time curve for the un-notched A356/SiC composite containing 0% nickel

The lowered impact energy from un-reinforced A356 aluminum alloy is an indication of a more brittle composite. In un-notched samples, the total absorbed energy is a measure of the crack initiation plus crack propagation, while notched samples measure crack propagation energy. These impact results suggest this material is slightly notch sensitive since both configurations have similar total absorbed energies. In comparison to discontinuous short fiber and particulate MMC's, scaffold effects of 3-D network struts during loading are not free to move independently, without breaking first.

All Charpy samples fractured in a brittle manner and have low impact toughness as indicated by the shape of the narrow load-time curves. Every tested specimen, notched

and un-notched has a low $E_I$ signifying how easily it is to initiate a crack and a low $E_P$ indicating the ease at which a crack can propagate (hard/brittle metal behavior). It can be concluded that both the matrix and reinforcement are brittle in nature individually, and when combined together.

### 6.6.11 Charpy V-Notched and Un-notched Fracture Analysis of A356/SiC Foam Composite

The A356/SiC foam composite Charpy notched and un-notched, fracture surfaces show similar fracture modes as those of the flexural strength test as shown in Figure 6.61. Silicon tends to increase the brittleness of the aluminum alloy and is seen as darker, larger surface area regions, while the white areas depict the more ductile regions. There are much more brittle, flat surfaces than dimples which explains the low impact values obtained. Moreover, the 2wt% nickel content does not show any major differences in the fractured regions of the micrographs. Identical behavior as the non-reinforced A356 aluminum alloy, the Al/SiC composite matrices illustrates fibrous fracture and brittle cleavage. SiC struts also have the same fracture failures as the flexural fractured sample. They show signs of layer de-bonding from their layered structure as given in magnified region of area 1, Figure 6.62. In other areas, some struts are missing a layer of SiC indicating SiC layer interdelamination. Yet, in other regions such as magnified region of area 2, Figure 6.63 the SiC strut did not remain attached to matrix. From an area analysis of Figure 6.61, an estimate SiC strut de-bonding from matrix is 75% and 25% for inter-layer de-lamination.

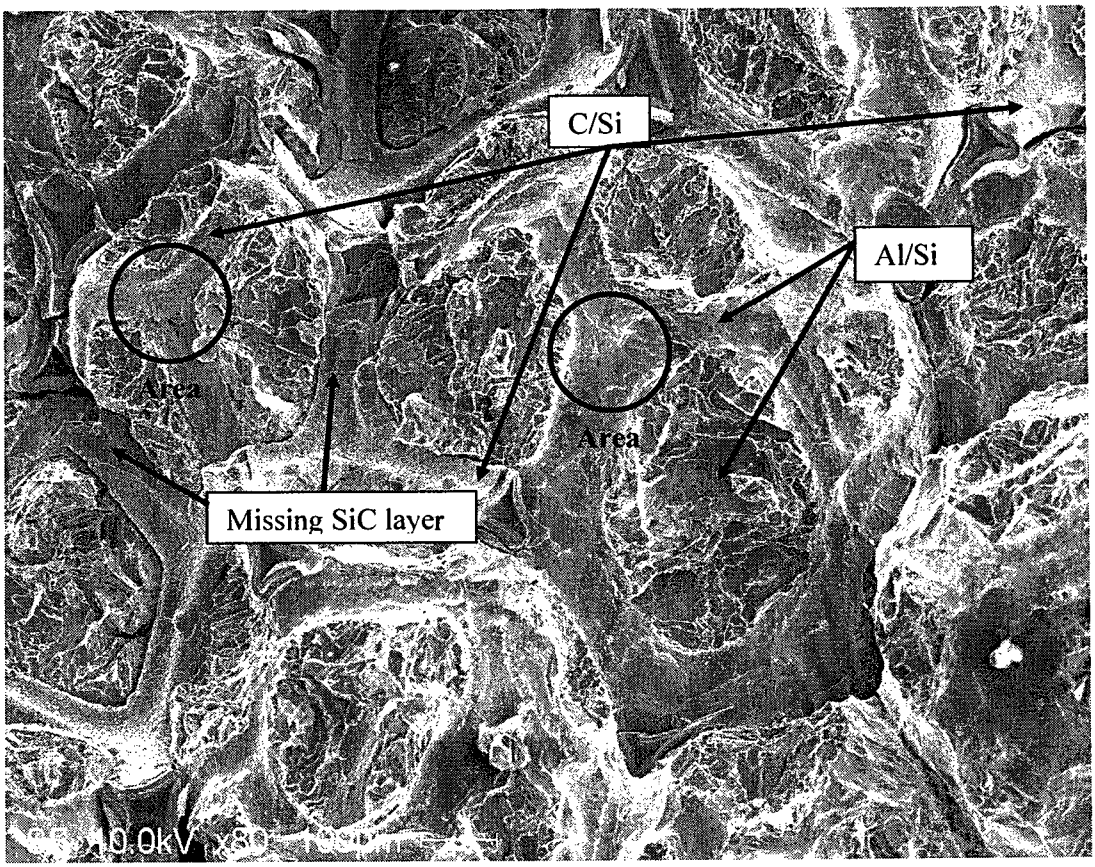


Figure 6.61 SEM microstructure of the Charpy un-notched A356/SiC composite with 0% nickel

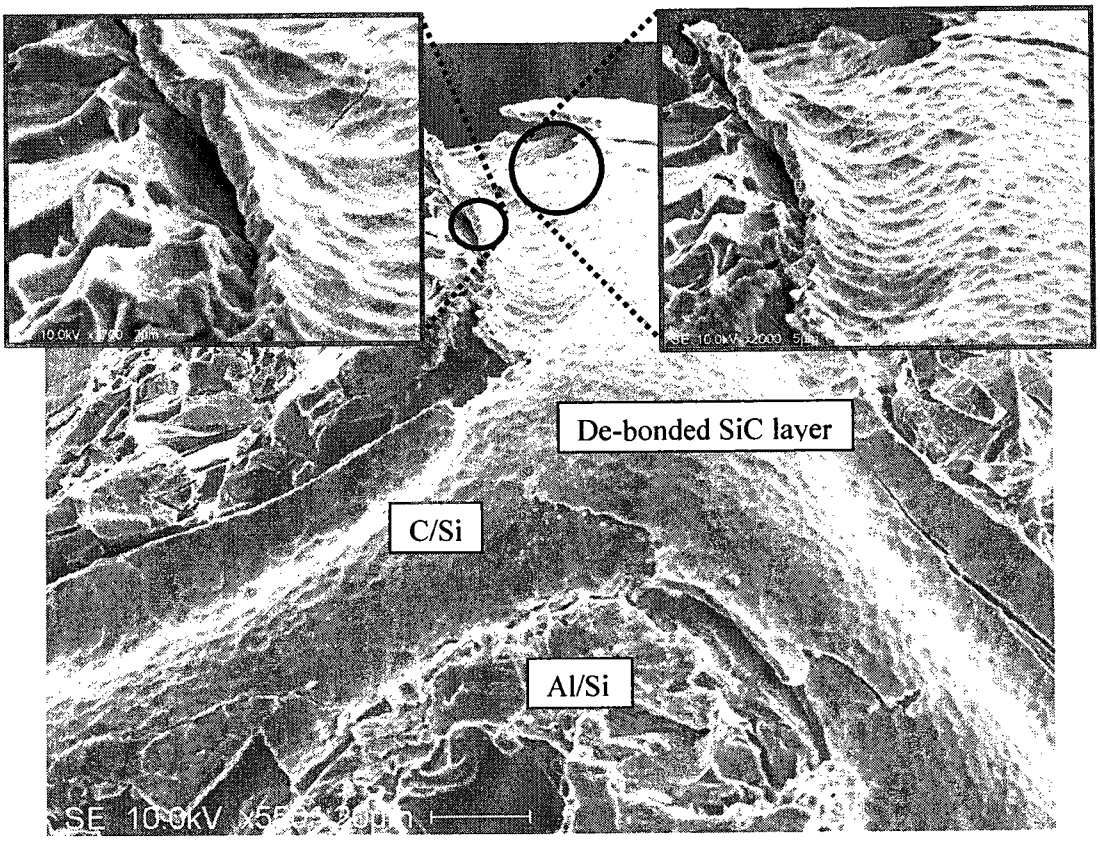


Figure 6.62 Magnified area 1, de-bonded SiC layer remains attached to matrix

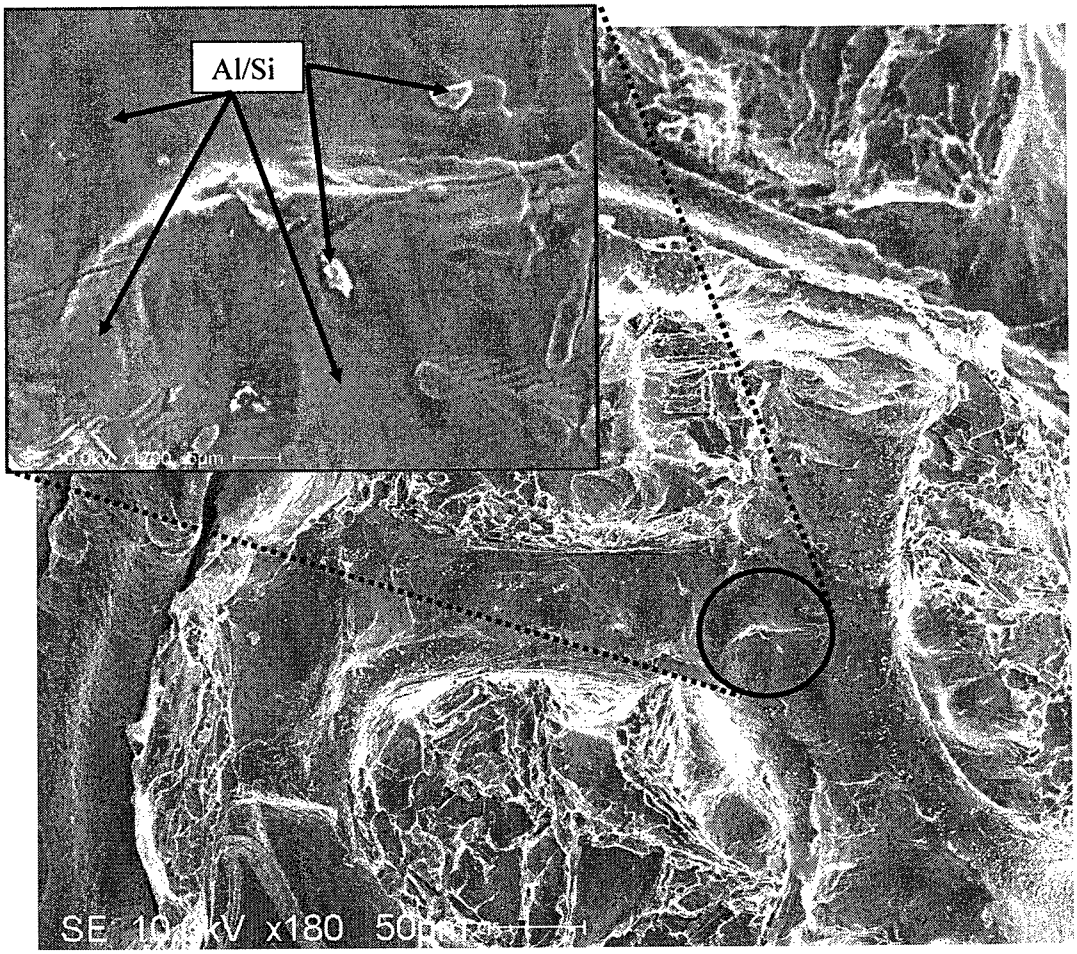


Figure 6.63 Magnified area 2, de-bonded SiC strut did not remain attached to matrix

### 6.6.12 Thermal Diffusivity

The thermal diffusivity results are graphed in Figure 6.64 and compared to published literature. For comparison to literature data, the thermal diffusivity of A356 [170], CVD SiC [171] and nickel [172] are plotted in Figure 6.64. The data shows that the flow of heat will diffuse faster in an aluminum alloy than in nickel. Materials with lower thermal diffusivities, conduct the heat more slowly. It is anticipated that by adding nickel to the composite, the thermal diffusivity will be lowered as nickel conducts heat at lower rate than aluminum.

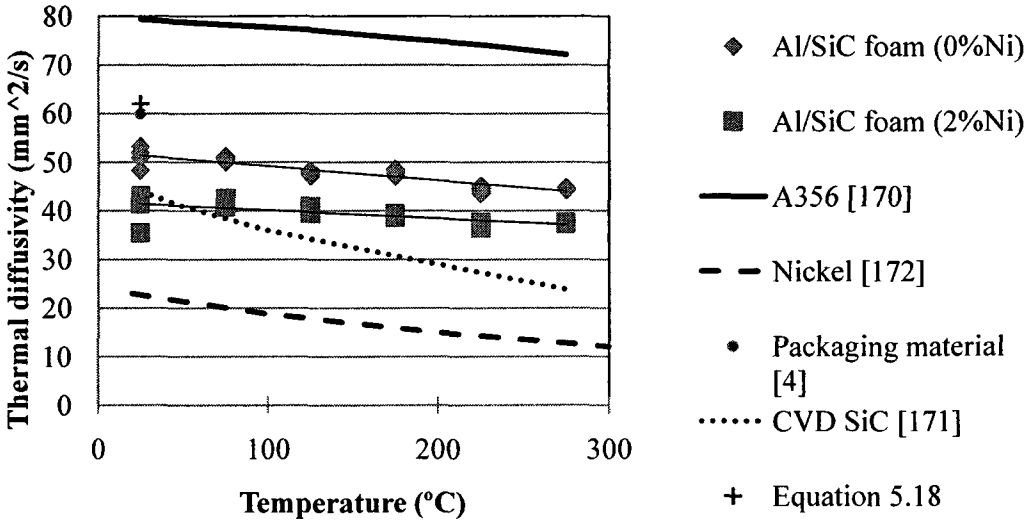


Figure 6.64 Thermal diffusivity as a function of temperature

The results for the Al/SiC composite are slightly lower than the common thermal diffusivity of conventional packaging materials. For example, typical Al/SiC packaging materials with 65% SiC particulate content have high thermal diffusivities of 60 $mm^2/s$ [4], at ambient temperature. The thermal diffusivity of the Al/SiC foam composite decreases as temperature increases, following the trend of A356 aluminum alloy, CVD

SiC and nickel. A temperature increase from 25°C to 275°C, brings about a thermal diffusivity decrease of 6.5 $mm^2/s$ or a 12% difference for 0 wt% nickel and a 3.1 $mm^2/s$ or a difference of 8% for 2 wt% nickel samples. Similarly, the A356 aluminum alloy from literature has a thermal diffusivity decrease of 9%. With the addition of 2 wt% nickel the diffusivity of the composite is decreased by approximately 10.5% at room temperature, compared to the 0% nickel composite. In an electroless Ni-plated coating placed on top of a SiC/Al particulate composite, the thermal diffusivity at ambient temperature, as reported by Zhao et al. [173] was lower by 17% for non-coated SiC/Al samples. Their study showed nickel to decrease the thermal diffusivity which is corroborated here. If the porosity of approximately 7% (Table 6.3) in the A356/SiC foam composite is reduced, the thermal diffusivity will increase. The experimental results show the heat flowing through the network structure is slower than unidirectional fibers and high volume fraction of dispersed particles. This can be attributed to the increased surface area of the ceramic struts.

### 6.6.13 Specific Heat Capacity

Aluminum has a higher specific heat capacity compared to nickel, while SiC is in-between at ambient temperature, as given in Figure 6.65. Typical Al/SiC packaging materials with 65% $SiC_p$ content have a specific heat capacity of 0.78 J/g°C [4], at ambient temperature (25°C), while the composite in this study, with 0% nickel has a specific heat capacity 0.79 ±0.035 J/g°C but with only 12 vol% SiC. The Al/SiC foam with 2% nickel has a specific heat capacity of 0.67 ±0.063 J/g°C In contrast, Kovar (Fe-29Ni-17Co) is used in electronic packaging as it has one of the lowest CTE (5.9 ppm/°C [4]), but also has a low specific heat capacity of 0.43 J/g°C [174].

The results are compared against literature values for aluminum alloy A356 [175], typical SiC (0.68 J/g°C) [176] and nickel, [172], as plotted in Figure 6.65. Both specific heat capacities of Al/SiC and Al/Ni-SiC increase with temperature, following a similar trend as A356 aluminum alloy and nickel. By adding 2% nickel, the specific heat capacity decreased by 15%, from 0.79 J/g°C to 0.67 J/g°C, at ambient temperature. Therefore, a slight addition of nickel in the composite would be beneficial for use in electronic packaging base plates as it would have a low specific heat capacity typical of Kovar materials.

The SiC ceramic material has a low specific heat capacity. Therefore, by increasing the connectivity as compared to unidirectional fibers and isolated, dispersed particles will in fact reduce the ability of the composite to store heat as observed in the experimental results.

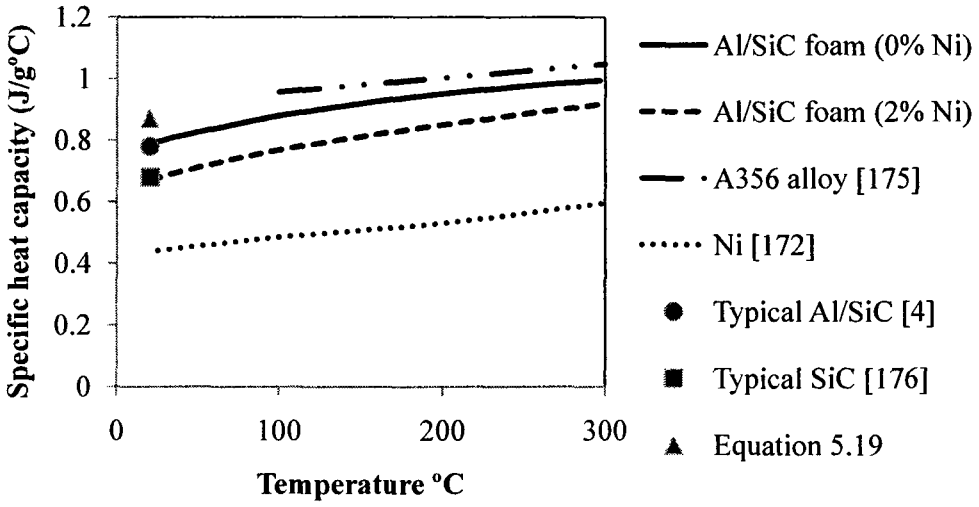


Figure 6.65 Specific heat capacity of the Al/SiC composite vs. temperature

### 6.6.14 Thermal Conductivity

Thermal conductivity results for the Al/SiC results 0 wt% Ni and with 2 wt% Ni are plotted in Figure 6.66. The results are compared against literature values for aluminum alloy A356 [175], nickel [172] and 100 PPI SiC foam (120 W/m°C) [87]. The Al/SiC thermal conductivity of current base plate packaging materials range between 150-171 W/m°C [4], for an average of 163 W/m°C as illustrated in Figure 6.66. As the temperature increases from 0 °C to 300 °C, the thermal conductivity of aluminum increases, however it decreases for nickel. In the literature, thermal conductivity values for SiC range from 40 W/m°C for C/SiC [177] to 180 W/m°C for typical SiC [176]. At 25°C, the composite without nickel, has a thermal conductivity of 97 ±1.28 W/m°C, however it should be above 120 W/m°C, while with 2 wt% nickel, the thermal conductivity is 87 ±5.77 W/m°C. The low thermal conductivity values are due to porosity in the Al/SiC composite. Porosity acts as an insulator. Therefore, by reducing the porosity, the thermal conductivities will increase.

Even though this material has a low thermal conductivity, Kovar has an even lower thermal conductivity of 17.3 W/m°C [174], and is still employed as a packaging material. The thermal conductivity increases for the Al/SiC composite, as the temperature increases. For 0 wt% Ni, the increase from 25 °C to 275 °C is approximately 24% while for 2 wt% Ni, the increase is 16%. Moreover, by adding 2wt% Ni, the thermal conductivity drops by 10% at 25°C.

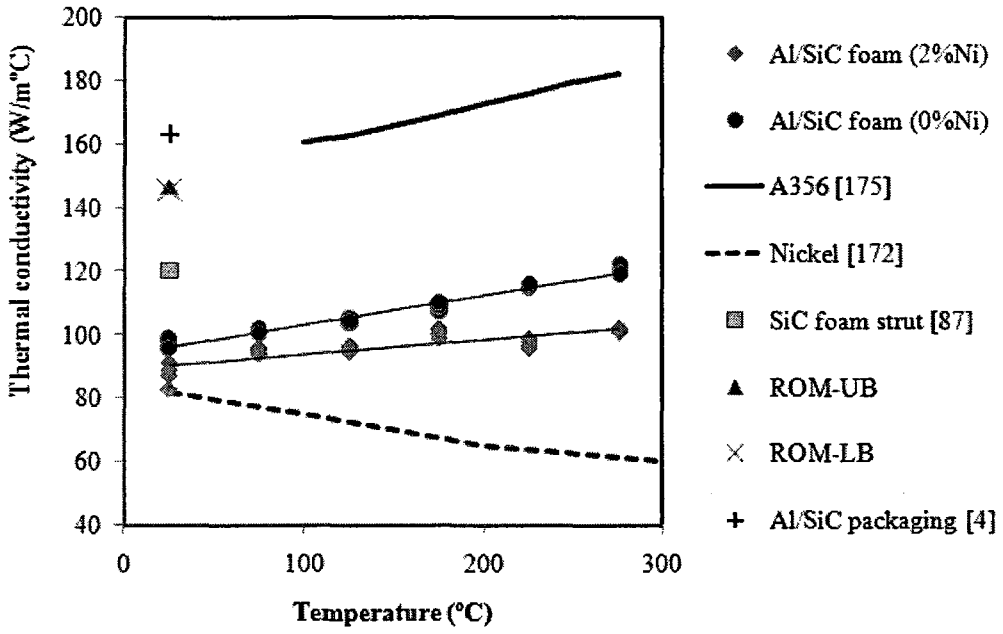


Figure 6.66 Thermal conductivity of the Al/SiC composite versus temperature

### 6.6.15 Coefficient of Thermal Expansion

The results of CTE versus temperature are plotted in Figure 6.67. A359/SiC MMC was used since literature data was not found for A356 in this temperature range. Published CTE values for the matrix alloy, ceramic reinforcement and nickel addition, as well as Duralcan SiC/A359 aluminum alloy composites with 10% and 40% SiC particulate reinforcement [178] are plotted for comparison. The CTE from 25 to 300°C for aluminum alloy A359 [178] and nickel [179] gradually increase linearly with temperature, whereas 100 PPI SiC foam has a constant CTE of 4.5 ppm/°C [87] within this temperature range. The experimental results show, with the addition of 2 wt% nickel, the CTE of the composite decreased by 6.7%, from 9.6 ±0.045 ppm/°C (0 wt% nickel) to 9.0 ±0.485 ppm/°C at ambient conditions (25°C) as shown in the region of the drawn

circle, of Figure 6.68. By incorporating a SiC foam into the aluminum, the CTE of the aluminum is decreased considerably, more specifically by 55% (from 21.1 to 9.6 ppm/°C), at ambient temperature. The Al/SiC foam composite expands at a high rate (9.6 to 18 ppm/°C) up to a temperature of 75°C, but is less sensitive at higher temperatures from 75 to 300°C. Similarly, typical Al/SiC particle electronic packaging materials ranges between 7 to 12 ppm/°C [4] for ambient temperatures, as given in Table 1.1.

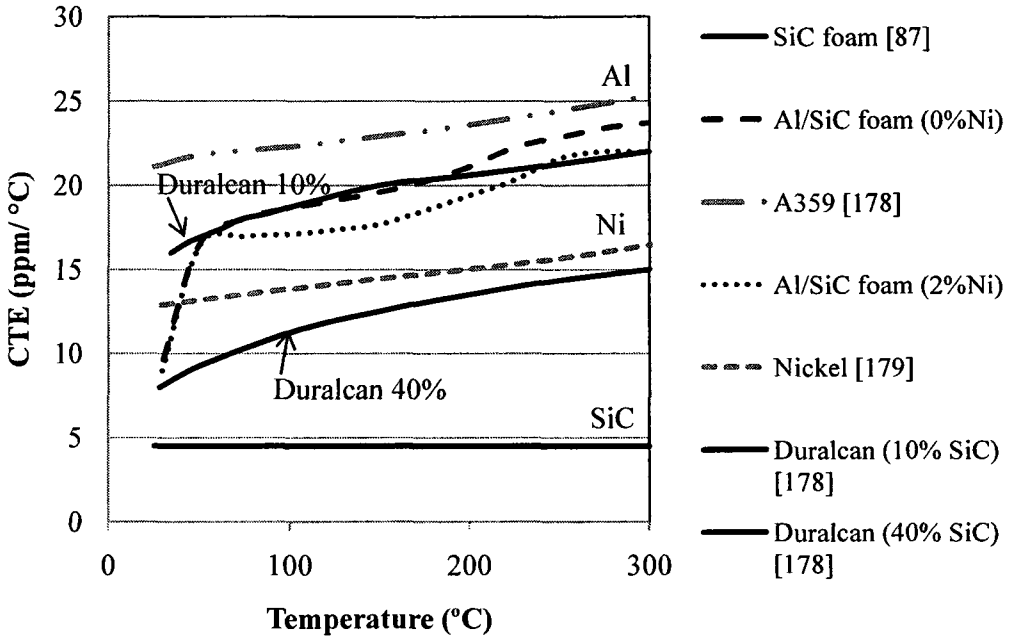


Figure 6.67 CTE versus temperature for the Al/SiC foam composite

For electronic packaging the CTE should be close to that of silicon or gallium arsenide; 4.2 ppm/°C and 6.5 ppm/°C, respectively. In this study, the A356/SiC foam has a CTE of 9.0 ppm/°C, with 2% nickel at ambient temperature which is within the range of literature data, but with only 12 % volume fraction reinforcement. Changing the aluminum alloy, for example from A356 (7.1% Si) to an A359 (8.5% Si) would increase the silicon content and help reduce the CTE even more.

At low temperatures, below 50°C, the initial CTE curves of the Al/SiC foam composite exhibits a very different behavior to Duralcan A359/SiC with 10-40 vol% SiC particles [178]. In this A356/SiC foam composite, the CTE initially rises sharply, then tapers to gradually increase with temperature. Once the rapid change in CTE has occurred, the behavior is similar to particulate reinforced Al/SiC MMCs. The reason for a sharp initial increase in CTE of the Al/SiC foam composite is due to MMC misfit strains at the Al/SiC interface, which have been well studied [180]. The strains arise due to a large variation between the aluminum and SiC CTE (5:1). After vacuum infiltration, the composite aluminum and SiC cool at different rates, thereby contracting at different rates. These thermal stresses generate dislocations at the Al/SiC interface. Therefore, during initial heating of the CTE test, below 50°C, a majority of the dislocations (or residual stresses) are annihilated/removed, allowing the CTE rate to increase rapidly. As the temperature gets closer to the melting point of aluminum (660°C), or greater than 300°C, the composite CTE gets closer to that of the CTE of the aluminum. This phenomenon suggests that the dislocations from the differential thermal stresses have been removed and thus allows the atoms to move more freely. As shown in Figure 6.67, both Duralcan composites with 10% and 40% SiC reinforcement do not show such a severe change in CTE initially as the Al/SiC foam composite of this research. The CTE slope in the Al/SiC from 25°C to 75°C is more pronounced in the rigid SiC network structure than the SiC particles. This can be explained by the network structure having more surface area, therefore is able to generate much more misfit strains at the Al/SiC interface.

## Chapter 7 Experimental Evaluation with Existing Models

The theoretical models for Young's modulus with and without porosity as well as thermal properties such as thermal diffusivity, specific heat, thermal conductivity and CTE, were able to predict reasonably well the experimental results (±10%) using the various upper and lower bounding limitations. Precise model predictions depend on accuracy of the variables within the composite, such as: volume fraction and distribution of each phase, homogeneity, elastic deformation of phases, perfect bonding between phases and also on the assumption used in defining the model such as idealized geometry and isotropic properties. For these reasons, it is difficult to model experimental results as too many variables must be taken into account.

### 7.1 Young's Modulus

The modulus of the A356 aluminum alloy matrix and the two-phase (C/SiC) theoretical strut reinforcment used in both ROM and HS Bound models is 72.4 GPa [86] and 243 GPa (from nanoindentation results using Equation 5.1), respectively. In the HS Bounds, Poisson's ratio was 0.33 for the matrix and 0.22 for the reinforcement. The compressive Young's modulus experimental results at 12% volume fraction of SiC reinforcement, are compared against the ROM and HS Bound in Figure 7.1. For a 12% reinforcement, the theoretical ROM upper and lower bound predict a modulus of 93 GPa and 79 GPa, respectively, while the theoretical HS upper and lower bounds predict a tighter envelope for a modulus of 87 GPa and 83 GPa, respectively. The experimental A356/SiC (0wt% Ni) composite has a modulus of 76.36 ±1.51 GPa for a 8.5% porous (Table 6.5) composite and the A356/SiC (2wt% Ni) composite has a modulus of 80.60 ±2.55 GPa with an 6.9 % porosity (Table 6.5) as compared in Figure 7.2. The A356/SiC (2wt% Ni)

composite falls within the ROM upper and lower bounds, however the A356/SiC (0wt% Ni) composite falls outside these limits. The HS Bounds overestimate the experimental results. The experimental results for the Al/SiC foam (0%Ni) falls outside the theoretical ROM bounds, by a difference of 4% (76 GPa versus 79 GPa), indicating a good first approximation. To determine if this material follows these models, the percent volume (% Vol) of SiC composition of the foam would need to be varied. Each model has many assumptions accounting for the errors. The theoretical idealized structures in the models do not take into account SiC foam cell geometry, strut size, orientation of the constituent, quality of interfacial bonding between the matrix and reinforcement and amount of porosity.

The ROM upper and lower bounds are based on the iso-stress and iso-strain (slab) models while the Hashin-Shtrikman upper and lower bounds are based on a randomly distributed reinforcement phase, surrounded by a continuous matrix phase. Therefore the 3-D, IPC structure of the Al-SiC foam cannot be approximated accurately by either of these models. For example, in the ROM, the poisson's ratio of the two phases; aluminum (0.33) and SiC (0.22) differ by 50%, rather than having identical values. Both phases are not arranged alongside each other as in the slab model, but rather they are two, three-dimensional structures intertwined among each other. Similarly, the experimental results fall outside the Hashin-Shtrikman (HS) bounds, possibly due to not considering the phase geometry and distribution within the composite. For example, HS Bounds were used to predict elastic properties of an alumina/aluminum composite and compared with experimental results [181]. The experimental Young modulus values lay close to the lower HS Bound, but according to the authors should have been higher. The reason

suggested may be due to the geometries of the real structure differ substantially from the model. A later study [71] showed the experimental data to be within the HS Bounds, for an Al-$Al_2O_3$ composite, but could not predict exactly for individual compositions. In addition, literature suggests for 3-D, isotropic, discontinuous and randomly distributed fiber composite, an efficiency parameter (Ke) can be used to predict the Young's modulus. For the A356/SiC foam composite, prediction of the modulus fails since the model is for a 3-D discontinuous fiber composite and not a continuous 3-D network structure.

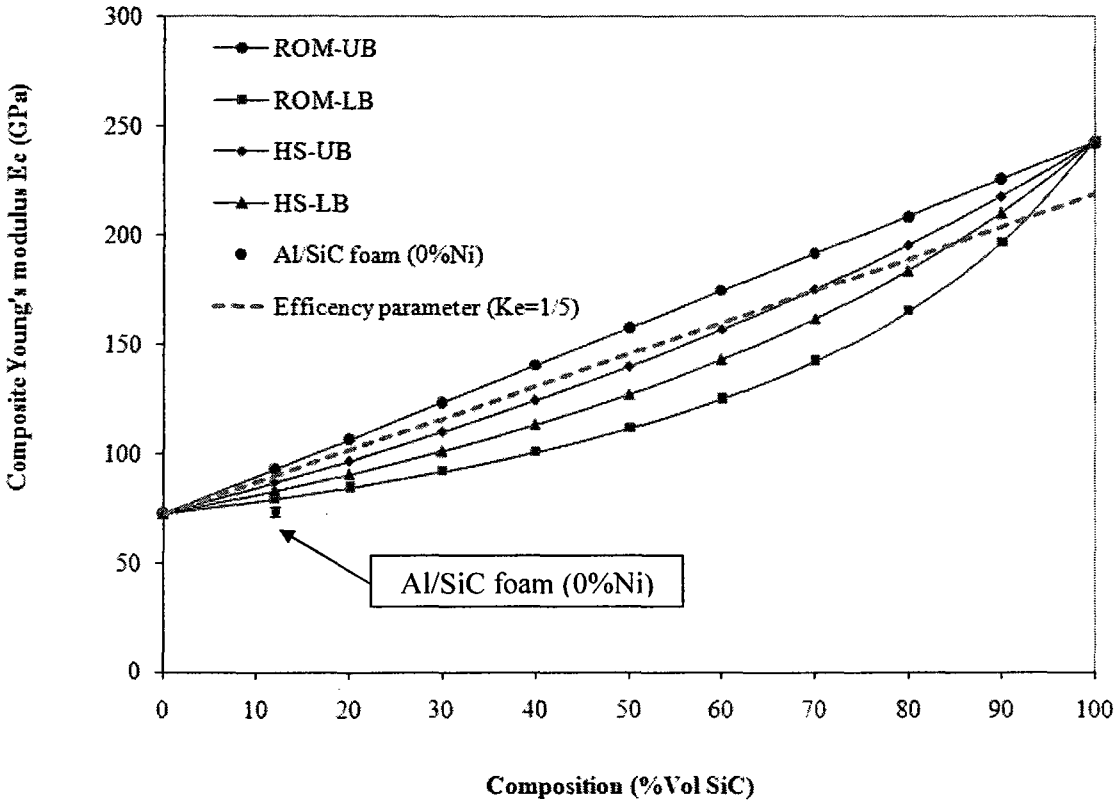


Figure 7.1 Young's modulus as a function of volume fraction reinforcement

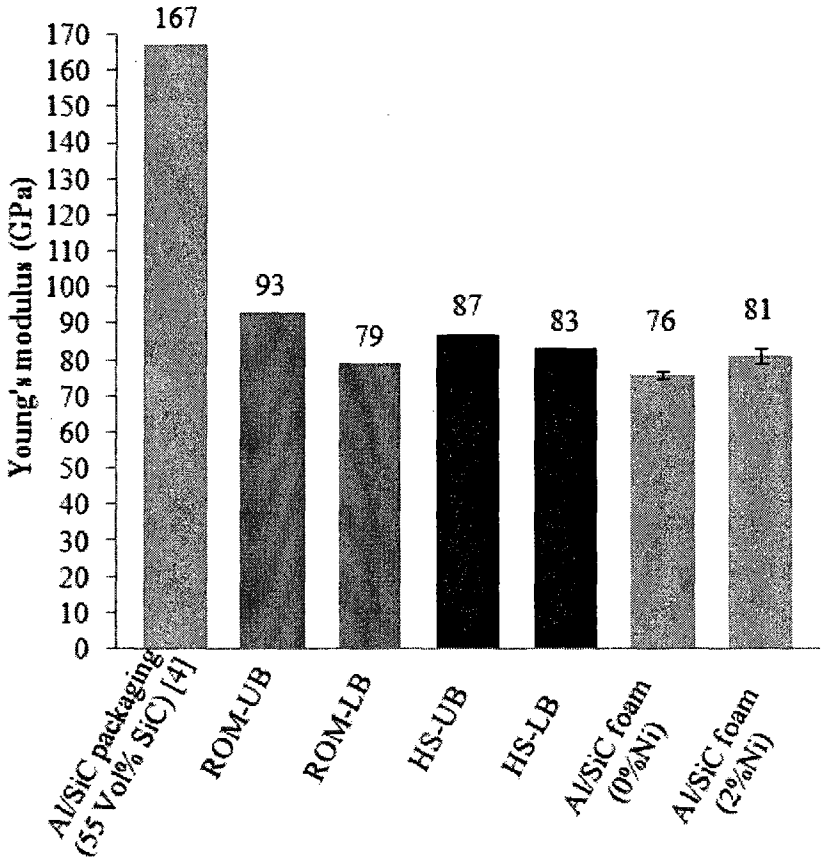


Figure 7.2 Theoretical models and experimental modulus for a 12 vol% reinforcement

## 7.2 Young's Modulus with Porosity

Based on a porous aluminum matrix of 8.5% the spherical model modulus obtained is 62.7 GPa (Equation 5.11) and the strut modulus is 243 GPa (from nanoindentation, Equation 5.1). For a 12% reinforcement, substituting these two moduli values into the ROM and Hashin-Shtrikman, the theoretical ROM upper and lower bound predict a modulus of 84 GPa and 69 GPa, respectively, while the theoretical HS upper and lower bounds predict moduli of 77 GPa and 73 GPa, respectively as given in Figure 7.3. The experimental A356/SiC (0wt% Ni) composite has a modulus of 76.36 ±1.51 GPa for a

8.5% porous composite. Taking into account the porosity in the matrix, the modulus obtained from the theoretical ROM and HS bound models are lowered. The experimental results fall within the ROM upper and lower bounds, while the A356/SiC (0wt% Ni) composite is within the HS bound, but the A356/SiC (2wt% Ni) composite is outside these limits. Although the experimental is within the envelope of the bounding models, the theoretical values do not match with the experimental, possibly due to the actual non-spherical pore shape and the overall difference in microstructure of the composite. It is difficult to model the actual pore size, pore shape and its distribution throughout the composite as it can be random from part to part, but the values obtained are reasonable as a first approximation.

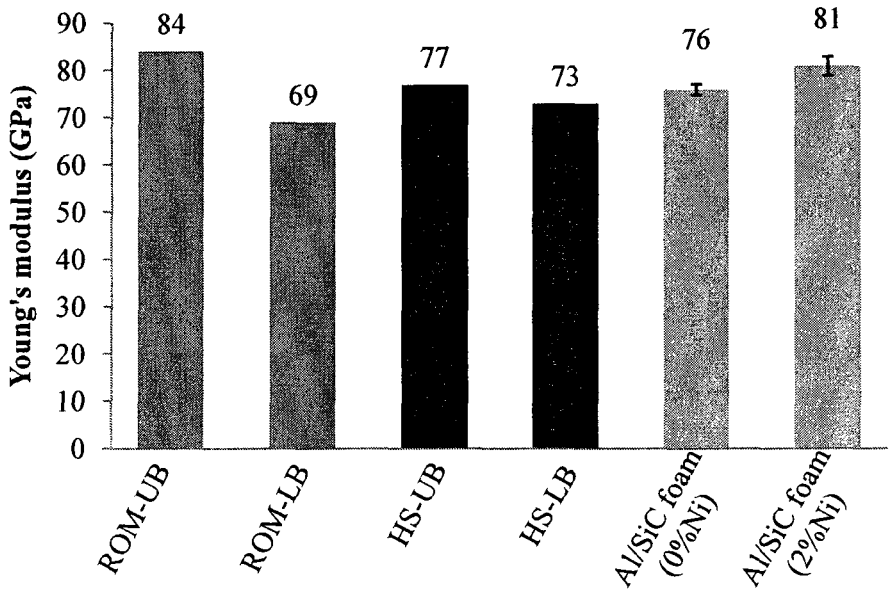


Figure 7.3 Spherical model (5.10) incorporated into the ROM and Hashin-Shtrikman results

The Cohen and Ishai cubic model, takes into account porosity, and predicts upper and lower bounds using the data for the two phase SiC foam and A356 aluminum alloy material as shown in Figure 7.4. Identical values of modulus for matrix and reinforcement as employed in the ROM and Hashin-Shtrikman are used in this model, 72.4 GPa and 243 GPa, respectively. For 12 vol% reinforcement, and a 8.5% porous composite, the cubic model predicts upper and lower moduli of 82 GPa and 68 GPa , repectively. The experimental A356/SiC (0wt% Ni) composite has a modulus of 76.36 ±1.51 GPa for a 8.5% porous composite, as given in Figure 7.5. The experimental results fall within the cubic upper and lower bounds but fail to accurately predict the modulus. This is possibly due to the simplified assumptions made and the cubic geometry of the model is not the actual shape of the three dimensional network of the foam.

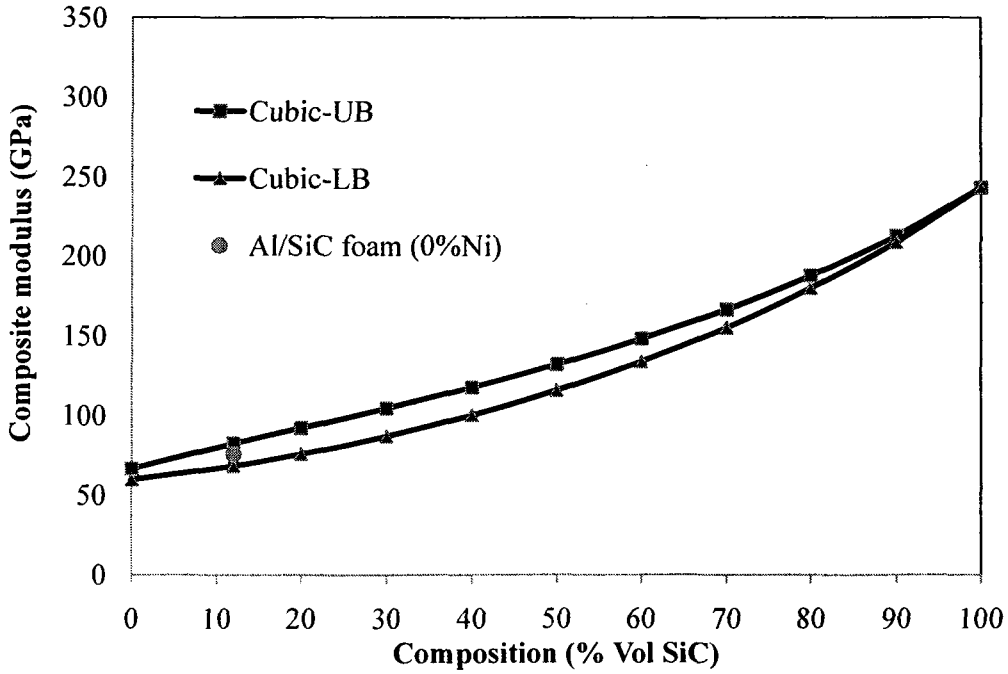


Figure 7.4 Composite modulus as a function of volume fraction reinforcement

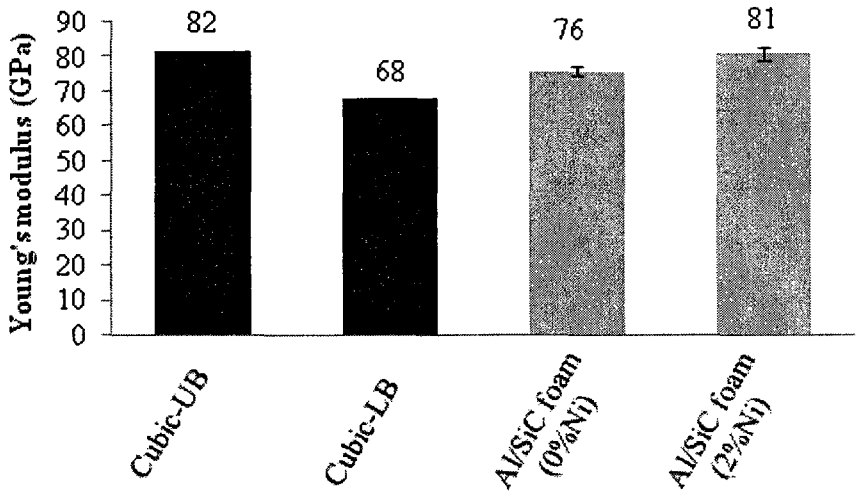


Figure 7.5 Theoretical cubic model and experimental modulus for 12 vol% reinforcement

### 7.3 Thermal Properties

The following thermal properties were obtained for an ambient temperature condition (25°C), with varying reinforcement composition.

#### 7.3.1 Specific Heat Capacity

The relationship between the specific heat capacity and reinforcement composition prediction is given in Figure 7.6. The specific heat capacity of the composite decreases as the volume fraction of SiC increases, resulting from the lower $C^r_p$ of SiC. That is, the Al/SiC foam composite requires less heat input to change its overall temperature. The specific heat capacity at 25°C for typical SiC reinforcement ($C^r_p$) and A356 matrix ($C^m_p$) are 0.68 J/g°C [176] and 0.90 J/g°C, respectively. The experimental measured specific heat capacity for the Al/SiC (0% Ni) composite with 12% reinforcement is 0.79 ±0.035

J/g°C, while the ROM of typical SiC and A356 composite ($C^c_p$) estimates a value of 0.87 J/g°C.

For a C/SiC strut, the theoretical SiC and vitreous carbon specific heat capacities are 0.68 J/g°C [176], and 0.71 J/g°C [182], respectively. The volume fractions of carbon and SiC from the oxidization test, are 0.23 and 0.77, respectively. Utilizing these values, the C/SiC strut specific heat capacity ($C_p^{strut}$) is calculated with the ROM to be 0.69 J/g°C. This value is very close to that used for typical SiC, assuming the reinforcement strut is pure SiC. This suggests the amount of carbon in the strut core does not have any great effect on the specific heat capacity of the composite. The percentage difference between the experimental and theoretical specific heat capacity value is 10%. This is due to the porosity present in the composite. Therefore, employing the ROM as a first approximation is good start.

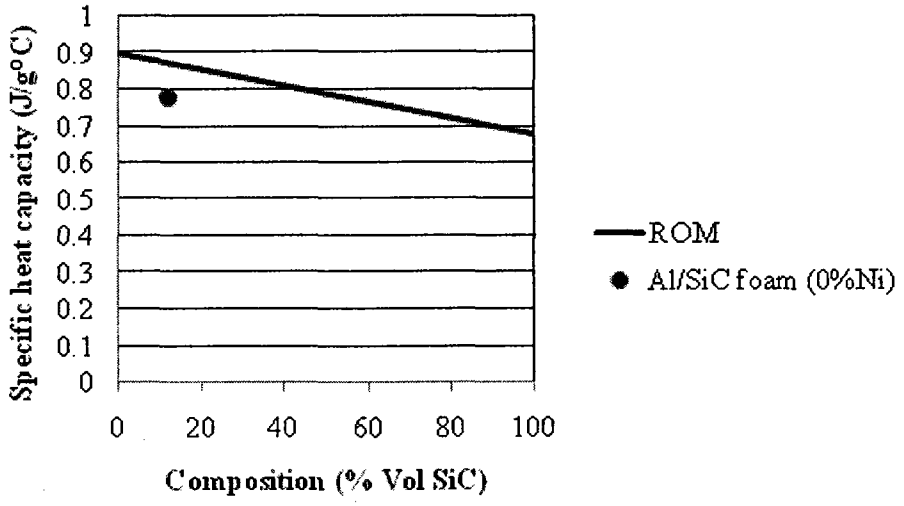


Figure 7.6 Composite specific heat capacity as a function of volume fraction reinforcement

### 7.3.2 Thermal Conductivity

ROM upper and lower bounds were obtained for the thermal conductivity of the composite ($k_c$) with respect to reinforcement content as given in Figure 7.7. In both bounds, the thermal conductivity of the composite decreases as the volume fraction of SiC increases, resulting from the lower conductivity of SiC. That is, the ability of the Al/SiC foam composite to conduct heat decreases. At 25°C, the thermal conductivities of the SiC foam reinforcement ($k_r$) and A356 aluminum alloy matrix ($k_m$) employed in the calculation are 120 W/m°C and 150 W/m°C, respectively. For simplicity, the reinforcement and matrix are assumed to be isotropic. The SiC foam core contains carbon, but only represents a small volume fraction of material as compared to the overall volume of the composite. Therefore, it is assumed to have negligible effect on the overall thermal conductivity of the composite. For 12% reinforcement, the Al/SiC (0%Ni) composite experimental thermal conductivity obtained is 97 W/m°C ±1.28, the ROM upper and lower bounds provide a value of 146.40 W/m°C (Equation 5.20) and 145.63 W/m°C (Equation 5.21), respectively, while the EMT predicts a value between the upper and lower ROM of 146.17 W/m°C (Equation 5.22). The ROM assumes a fully dense, unidirectional slab/plate structure, while the experimental has 7.3% porosity with a 3-D network structure. Similarly, the EMT model assumes the two phases are distributed randomly, but fails to predict the experimental.

The thermal conductivity values predicted by the ROM and EMT models are very close to one another. For the two phases, there is not a large change in thermal conductivity as the volume fraction of reinforcement increases. SiC has a high thermal conductivity as compared to other ceramics, close to that of A356 aluminum alloy. For

example, aluminum oxide has a thermal conductivity of 35 W/m°C [183] which is about three times lower than SiC. Therefore, SiC is a good material for applications requiring high thermal conductivities.

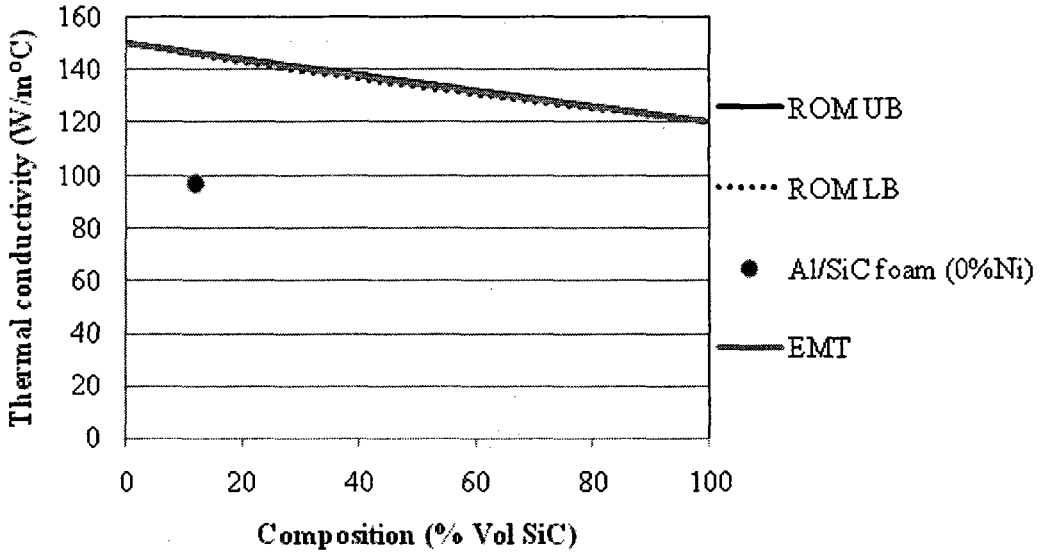


Figure 7.7 Composite thermal conductivity as a function of volume fraction reinforcement

### 7.3.3 Thermal Diffusivity

The Al/SiC foam composite thermal diffusivity was calculated using Equation 5.18 and plotted against the reinforcement content as given in Figure 7.8. The composite material parameters in Equation 5.18 were thermal conductivity, Equation 5.20, composite density, Equation 6.10 and specific heat capacity, Equation 5.19. At ambient temperature, according to Equation 5.18, the thermal diffusivity decreases linearly from 61 $mm^2/s$ to 55 $mm^2/s$ as the SiC content increases. This is expected, since the thermal conductivity and specific heat capacity for aluminum are greater than the SiC. Using Equation 5.18, the Al/SiC foam composite with 12% reinforcement should have a thermal diffusivity of

60.5 $mm^2/s$. The results indicate, at ambient temperature, the heat will flow through the Al/SiC foam composite quicker if the SiC content is lower. For comparison, at 25°C, the literature thermal diffusivities of typical SiC reinforcement [171] and A356 aluminum alloy [170] matrix are 44 $mm^2/s$ and 79 $mm^2/s$, respectively. The experimental measured thermal diffusivity for the Al/SiC (0% Ni) composite with 12% reinforcement is 51 ±1.82 $mm^2/s$, while with the addition of 2% Ni it is 40 ±3.04 $mm^2/s$. There is a 18 % error between calculated and experimental.

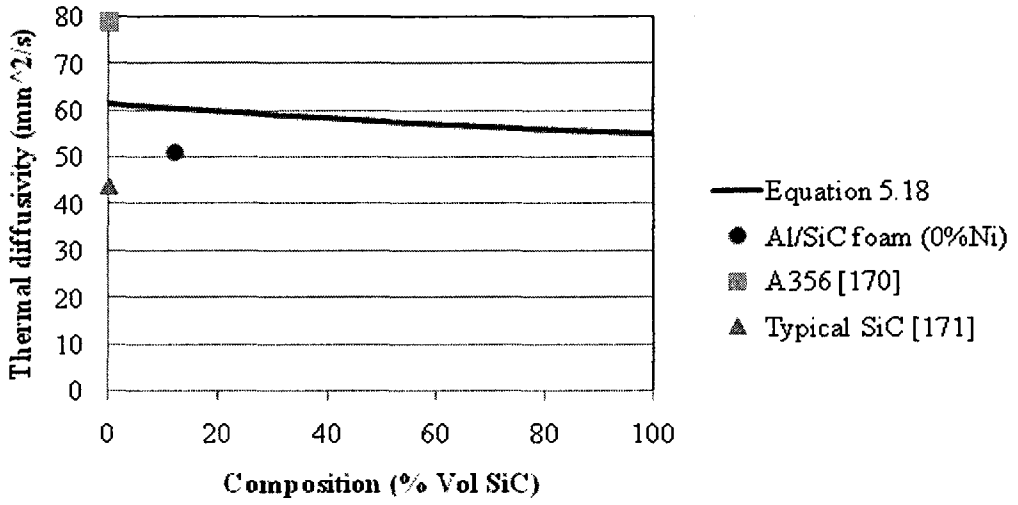


Figure 7.8 Composite thermal diffusivity as a function of volume fraction reinforcement

### 7.3.4 Coefficient of Thermal Expansion (CTE)

The ROM and Turner models were used to predict the composite CTE with respect to volume fraction of SiC at ambient temperature of 25°C, as given in Figure 7.9. The CTE of SiC 100 PPI foam reinforcement ($\alpha_r$) and A359 aluminum alloy matrix ($\alpha_m$) employed in the models are 4.5 ppm/°C [87] and 21.1 ppm/°C [178], respectively. The CTE of A359 aluminum alloy was used since A356 aluminum alloy was not found in literature,

but is not expected to differ significantly. As expected, both CTE models show a decrease in CTE as the amount of SiC is increased, as a consequence of the low CTE of the SiC. The bulk modulus A359 matrix ($K_m$) and SiC reinforcement ($K_r$) values used in the models were also obtained from literature [178], as 68.4 GPa and 227 GPa, respectively. The ROM model, Turner model and experimental results, for 12% SiC reinforcement gives a CTE of 19.1 ppm/°C, 15.9 ppm/°C and 9.6 ±0.045 ppm/°C, respectively.

As stated earlier, the SiC foam strut has two phases; carbon and CVD-SiC. The theoretical strut CTE ($\alpha_{strut}$) was also calculated using the ROM. Employing a theoretical SiC ($\alpha_{SiC}$) CTE of 4.5 ppm/°C [178], a vitreous carbon CTE ($\alpha_c$) of 2.2 ppm/°C [89] and the volume fractions of carbon and SiC from the oxidization test, of 0.23 and 0.77, respectively, the strut CTE is calculated from a ROM to be 3.9 ppm/°C. Substituting this

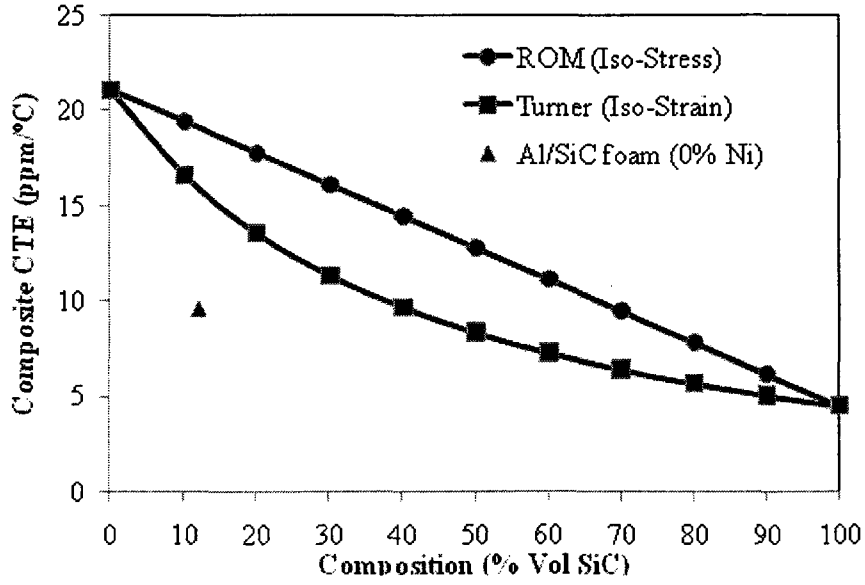


Figure 7.9 Composite CTE as a function of volume fraction reinforcement

strut CTE in the ROM and Turner models, provides estimates of 19.0 ppm/°C and 15.7 ppm/°C, respectively. There is not a substantial difference in CTE based on the two-phase strut, due to the negligible amount of carbon in the network structure.

The experimental results are far away from both theoretical models. The hypothesis for the ROM states that at the interface, there is no transfer of stress between reinforcements and the matrix, but in fact interfacial bonding should be considered. Furthermore, in both models there is no constraint on the shape and distribution of the reinforcement. For two slabs side by side (longitudinal direction being the longest) containing two materials perfectly bonded to one another, the ROM represents the CTE in the transverse direction while the Turner model represents the CTE in the longitudinal direction. The ROM model predicts a larger CTE than the Turner model for the same volume fraction of reinforcement. The reason is that in the ROM, the metal/ceramic phases are independent of one another and are able to expand at their respective rates, without any constraint, while the Turner model, the overall expansion of the composite is constrained by the phase with the lowest CTE. In addition, the surface area of a slab is greater along the length of the slab than transverse to the slab. Therefore, more material can expand in the transverse direction, than the longitudinal direction.

The experimental CTE may be low due to the porosity incurred from solidification shrinkage between the matrix and reinforcement struts. Porosity in the matrix was reported to affect the thermal expansion of an Al/SiC particulate composite [79]. Upon heating, the matrix plastically deforms, expanding into the porous areas thus lowering the CTE of the composite.

In addition, the solid 3-D interconnected network may constrain the matrix and this could be the reason for the lower than expected CTE. That is, the foam prevent the aluminum matrix from expanding placing a limitation on the amount the matrix can expand, as opposed to dispersed particles where they can move much more freely upon expansion.

Table 7.1 The thermal properties at ambient temperature (25°C)

| | Matrix A356 | Reinforcement SiC | ROM (A356/SiC 12 vol%) | Experimental (A356/SiC 12 vol%) | Error (%) |
|---|---|---|---|---|---|
| Specific Heat Capacity (J/g°C) | 0.90 [71] | 0.68 [176] | (Eq. 5.19) 0.87 [124] | 0.79±0.035 | 10.3 |
| Thermal Conductivity (W/m°C) | 150 [71] | 120 [87] | (Upper/Lower) (Eq. 5.20/5.21) 146/145 [125] | 97±1.28 | 33.5/33.1 |
| Thermal Diffusivity ($mm^2/s$) | 79 [170] | 44 [171] | (Eq. 5.18) 61.6 | 51±1.82 | 17.2 |
| CTE | 4.5 [87] | 21.1 [178] | ROM/Turner (Eq. 5.23/5.24) 9.1/15.9 [127] | 9.6 | 5.5/39.6 |

# Chapter 8 Conclusion

## 8.1 Ceramics Produced from Wood

Two routes for obtaining a SiC structure from different wood species were tried. Although procedures reported in previous works were followed, fully open, porous SiC structures from wood precursors were not possible to produce in approximately 15 mm x 15 mm x 15 mm carbon samples. The following conclusions can be drawn:

- It was possible to obtain sufficient $SiO_2$ sol infiltration in these wood species (with a 15 mm cube) however it was not possible to achieve a fully converted SiC porous sample in contrast to results described by previous works using the same methodology. This would indicate that the cellular morphology of these wood samples or the sample size used may be critical factors.
- SEM micrographs of silica-infiltrated carbonized pine wood show latewood cells are filled, while early wood cells are mostly unfilled with silica. Similarly, the small diameter tracheids/fibers of beech and maple are filled while the larger vessel earlywood cells are unfilled. To have a complete conversion to SiC, the silica distribution should be more homogeneous. The ideal would be to have all pores filled with silica.
- SiC grains/particles were observed on the inner walls of the tracheids/fibers. The grains are spherical and growing individually, thus producing a porous SiC structure. Carbon-rich areas remain between the grains. Although some SiC is formed, not enough of a homogeneous SiC layer is formed from the pyrolyzed structure thus producing a "Swiss Cheese" effect after an oxidation treatment.

- During the SEM microstructure observation, a high density of SiC whiskers were discovered in the carbonized pine and beech wood infiltrated with Levasil sol, reacted under an argon flow of 70L/h at 1575°C, suggesting extensive vapor phase reactions.
- In the liquid $SiO_2$ infiltration results of previous works, it seems only selected regions have been published. In future studies of silica infiltrated into wood, it is suggested to incorporate at least one full growth ring or larger in the SEM images. When using natural materials as precursors, it is important to take the microstructure and macrostructure into account. If solid wood is being used as the starting material, then not only is the cell structure, such as tracheid size important but also the size and morphology of the growth rings and position in the tree.
    - Liquid silicon infiltrations show that although SiC is formed, the liquid silicon clogs the majority of the open pores in pine. In addition, different porosities were observed at different depths of the specimen.
    - Pyrolyzed wood used in this research has less thermal stability under oxidative condition than graphite which is explained by the crystallinity of graphite and the amorphous nature of charred wood. The carbonized wood species were pyrolyzed at 1400°C, whereas, above 1800°C, is where the carbon charcoal changes to a graphite structure. It could be concluded that more CO gas would evolve from the charcoal wood than if it was a pure graphite sample, thus resulting in a greater weight loss for the carbonized samples.

### 8.2. A356/SiC Foam Interpenetrating Phase Composites

A manufacturing technique was developed for producing a novel IPC material. It consists of vacuum infiltrating an A356 aluminum alloy into a SiC ceramic network. Mechanical

and thermal properties were investigated as well as its microstructure. The material possesses attractive requirements for electronic packaging. Ideal packaging materials have low densities, typically less than 3 $g/cm^3$. It was possible to produce a 2.52 $g/cm^3$A356/SiC composite due to the low density SiC foam. A component built with this material can decrease the weight by 16%. The lowest total porosity obtained using the vacuum infiltration apparatus was 7%. From the micrographs, it appears the porosity is due to some solidification shrinkage at the SiC/Al interface and microporosity. This new composite material has a Young's modulus of about 76 GPa for a reinforcement volume of only 12%, in contrast to typical Al/SiC particulate MMCs employed for packaging materials which have moduli of 167 GPa for 55 vol% reinforcement.

The highest flexural strength of this composite occurred at 332 MPa, for 7% porosity and 12% reinforcement. Typical Al/SiC with 70% volume fraction reinforcement used in electronic packaging materials have a flexural strength of 270 MPa. With an 83% decrease in SiC volume fraction reinforcement, the flexural strength increased by 23%. With only 12% volume fraction reinforcement, the present composite obtained comparable impact toughness as aluminum composites with 50-70% SiC.

The highest thermal conductivity obtained was 97 W/m°C for the A356/SiC foam composite with no nickel content. Ideal thermal conductivities of packaging materials are greater than 100 W/m°C at ambient temperature. Voids act as an insulating medium with low thermal conductivity; therefore, by reducing the porosity using a positive infiltration method, the thermal conductivities will increase.

The A356/SiC foam composite has a CTE of 9.0 ppm/°C, with 2% nickel and 9.6 ppm/°C with 0% nickel at ambient temperature. The CTE requirements for electronic

packaging are between 7.8-10.8 ppm/C. The results are within the range of literature data, but with only 12 % volume fraction reinforcement. However changing the matrix alloy could reduce the CTE even more.

There are no theoretical models to describe the experimental Young's modulus and thermal properties of a three dimensional network structure composite. The existing models for two phase composites were able to predict the properties of this composite to some degree using upper and lower bounding systems, however better models could be developed. In conclusion, an outstanding advantage of this composite is with only 12% volume fraction SiC reinforcement, the present composite obtained comparable mechanical and thermal properties to aluminum composites with 50-70% SiC particulate composites.

### 8.3 Future Work

In the first part of this work, a porous SiC ceramic wood structure was not attainable with the wood species employed. Research on equatorial species may resolve difficulties in tracheid size and growth rings, but negates the benefit of locally sourced constituents. In the second part of this work, an innovative composite material was manufactured and tested for obtaining selected properties. Additional work would have to be done in the areas of thermal fatigue, using a positive pressure infiltration arrangement to reduce porosity, and modeling a three-dimensional network with two and three phases. Other work efforts can be done in;

- Maintaining the same bulk volume, conduct experiments with a variety of foam strut thicknesses to determine if the amount of increased reinforcement content

affects the overall properties of this composite. This can be done by special order or produce the foam in-house.

- Determine wear resistance properties for possible use in wear applications.
- Change the matrix alloy for better elastic deformation, impact toughness and reduced CTE. A356 aluminum alloy was used instead of pure aluminum for its better flow properties, reduce chances of aluminum carbide formation and has better wettability characteristics.

### 8.4 Contributions to Original Knowledge

In both parts of this work, the results of this research have contributed to new knowledge in the field of composite materials. The initial part of this study dealt with producing a porous SiC structure mimicking that of wood using two silicon sources; silicon and silica ($SiO_2$) sol. New knowledge in this field was gained through;

- Evaluation of Canadian wood species for the first time.
- Infiltrating Si into the pyrolyzed wood obtained diverse porosity levels at varying depths within the preform which hindered the formation of a fully porous SiC structure, (this has not been reported on any wood species around the world).
- For the first time, a high density of SiC whiskers were discovered in the carbonized pine, beech and maple wood infiltrated with Levasil sol, and reacted under an argon flow of 70L/h at 1575°C.
- Images of the SiC grain formation in the interior of the tracheid walls, in the longitudinal direction of pine, beech and maple were obtained.

In the second part of this study, a novel A356/SiC composite material was manufactured and characterized for the first time. The properties revealed the material to be a good fit for the transportation industry, specifically in electronic packaging materials. During the initial development and testing, new knowledge was acquired:

- Al/SiC foam composite manufacturing using the vacuum infiltration is a new set-up which is simple and inexpensive.

- Vacuum infiltration of a large foam section measuring 60 mm long and 10 $mm^2$ has not been previously reported with low porosity. Low pressures have the advantage of preventing strut fracture.

- Characterization of A356/SiC foam composite by compression and flexural strength testing, Charpy toughness evaluation and thermal property measurements: thermal diffusivity, specific heat capacity, CTE and thermal conductivity.

- Micro-structural characterization of the fractured surfaces.
- Micro-hardness measurements were performed for the first time on the struts of the SiC/C struts.

- Peeling or SiC layer debonding was observed for the first time in a CVD SiC foam.

This research has provided a lot of new information about the microstructure, mechanical and thermal behavior of an A356/SiC foam composite. The results indicate promising properties for use in the electronic packaging industry, specifically in light-weight applications for automotive, aerospace and space applications.

## REFERENCES


1. Raj R., Thompson L. R., 1994. Design of the microstructural scale for optimum toughening in metallic composites. Acta Metallurgica et Materialia 42 [12] 4135-4142.

2. Liu W. and Köster U, 1996, Microstructures and properties of interpenetrating alumina/aluminum composites made by reaction of $SiO_2$ glass preforms with molten aluminum. Materials Science and Engineering A210 1-7.

3. Department of Defence, Composites Materials Handbook, Volume 17-4A: Metal Matrix Composites.

4. Occhionero M. A., Hay R. A., Adams R. W., and Fennessy K. P., 1999, Aluminum silicon carbide (AlSiC) for cost-effective thermal management and functional microelectronics packaging design solutions, in Proceedings of the 12th European Microelectronics and Packaging Conference, Harrogate, U.K., June 7–9.

5. Moores K. A., Joshi Y. K. 2001. High performance packaging materials and architectures for improved thermal management of power electronics. Future Circuits International 7 45-49.

6. Elomari, R. Boukhili, C. San Marchi, A. Mortensen, D. J. Lloyd. 1997. Thermal expansion responses of pressure infiltrated SiC Al metal-matrix composites. Journal of Materials Science 32, 2131-2140.

7. Gibson L. J. and Ashby M.F., 1988. Cellular solids: structure & properties. Oxford; New York: Pergamon Press.

8. Dinwoodie J. M., 2000. Timber: Its Nature and Behaviour, London; New York, Van Nostrand Reinholdp.

9. Williams N., 1998. Study finds 10% tree species under threat. Science 281, 1426-1427.

10. Studard A. R., Gonzenbach U. T., Tervoort E., Gauckler L. J. 2006. Processing routes to macroporous ceramics: a review. Journal of the American Ceramic Society 89, 1771-1789.

11. Yao X., Tan S., Huang Z. Jiang D. 2006. Effect of recoating slurry viscosity on the properties of reticulated porous silicon carbide ceramics, Ceramics International 32, 137-142.

12. Bao X., Nangrejo M. R., Edirisinghe M. J. 2000. Preparation of silicon carbide foams using polymeric precursor solutions. Journal of Materials Science 35, 4365-4372.

13. A. J. Sherman, R.H. Tuffias, RB. Kaplan. 1991. Refractory ceramic foams: a novel new high temperature structure. Ceramic Bulletin 70 [6] 1025-1028.

14. Kim Y. W., Kim H.D. 2005 Fabrication of open-cell, microcellular silicon carbide ceramics by carbothermal reduction. Journal of the American Ceramic Society 88, 2949-2951.

15. Fitzgerald T. J., Michaud V. J., Mortensen A. 1995. Processing of microcellular SiC foams. Journal of Materials Science 30, 1037-1045.

16. Mouazer R. 2004. SiC foams produced by gel casting: synthesis and characterization. Advanced Engineering Materials 6, 340-343.

17. Robert A. Zabel & Jeffrey J. Morrell, Wood Microbiology: decay and its prevention, Academic Press Inc., San Diego, p. 144-145 WEB TA 423.2 Z33 1992.

18. Thomas Ulvcrona, Henrik Lindberg, Urban Bergsten, 2006. Impregnation of Norway spruce (Picea abies L. Karst.) wood by hydrophobic oil and dispersion patterns in different tissues. Forestry 79 [1] 123-134.

19. Sini Metsa-Kortelainen, Toni Antikainen, Pertti Viitaniemi, 2006. The water absorption of sapwood and heartwood of Scots pine and Norway spruce heat-treated at 170C, 190C, 210C and 230C. Holz als Roh- und Werkstoff 64 192-197.

20. Rowell, R. M., Banks W.B. 1987. Tensile strength and toughness of acetylated pine and lime flakes. British Polymer Journal 19 479-482.

21. Petric B. 1972. Influence of wood structure on the permeability of hardwoods. Sumarski List 96 [9-10] 364-373.

22. Byrne C. E., 1996, Polymer, ceramic and carbon composites derived from wood, Ph.D thesis, Department of Materials Science and Engineering, The John Hopkins University, M.D. U.S.A.

23. Lee J. G., Cutler I. B., 1975. Formation of silicon carbide from rice hulls. American Ceramic Society Bulletin 54, 195-198.

24. Sun L., Gong K., 2001. Silicon-based materials from rice husks and their applications. Ind. Eng. Chem. Res. 40, 5872.

25. Selvam A., Nair N. G., Singh P., 1998. Synthesis and characterization of SiC whiskers from coconut shells. Journal of Materials Science Letters 17, 57-60.

26. Hirose T., Fan T., Okabe T., Yoshimura M., 2002. Effect of carbonizing speed on the property changes of woodceramics impregnated with liquefacient wood. Materials Letters 52, 229.

27. Hofenauer A., Treusch O., Tröger F., Wegner G., Fromm J., Gahr M., Schmidt J., Krenkel W., 2003. Dense reaction infiltrated Silicon/Silicon carbide ceramics. Advanced Engineering Materials 5 11, 794-765.

28. Patel M., Padhi B. K., 1990. Production of alumina fibre through jute fibre substrate. Journal of Materials Science 25, 1335-1343.

29. Leute M., Wilhelm M., Wruss W., 2002. SiC-Si Ceramic composites reinforced with carbonized fibres made of biogenic substances. Key Enginering Materials 23, 261-264.

30. Krishnarao R. V., Mahajan Y. R., 1996. Preparation of silicon carbide fibres from cotton fibre and silicon nitride. Journal of Materials Science Letters 15, 232-235.

31. Ohzawa Y., Hoshino H., Fujikawa M., Nakane K., Sugiyama K., 1998. Preparation of high-temperature filter by pressure-pulsed chemical vapour infiltration of SiC into carbonized paper-fibre preforms. Journal of Materials Science 33, 5259-5264.

32. Sieber H., Friedrich H., Zeschky J., Greil P., 2000. Light weight ceramic composites from laminated paper structures. Ceramic Engineering and Science Proceedings 21, 129-134.

33. Weisensel L., Sieber H., Travitzky N., Greil P., 2004. Fabrication of SiSiC laminar composites by laminated object manufacturing (LOM), in: High Temperature Ceramic Matrix Composites HTCMC-5, Ed.: M. Singh, R.J. Kerans, E. Lara-Curcio and R. Naslain, The American Ceramic Society 437-442.

34. Greil P., Lifka T, Kaindl A., 1998. Biomorphic cellular silicon carbide ceramics from wood I. Processing and Microstructure. Journal of the European Ceramic Society 18, 1961-1973.

35. Greil P., Lifka T, Kaindl A., 1998. Biomorphic cellular silicon carbide ceramics from wood II. Mechanical Properties. Journal of the European Ceramic Society 18, 1975-1983.

36. Pampuch R., Walasek E. and Bialoskorski J., 1986. Reaction mechanism in carbon-liquid silicon systems at elevated temperatures. Ceramics International 12, 99-106.

37. Nagle D.C., Lewis A. and Byrne C.E., 1998. Net-shape advanced polymer, ceramic and carbon composites produced from wood. Materials Technology-Technology Reviews 13, 115-120.

38. Shin D.W., Park S. S., Choa Y. H. and Niihara K., 1999. Silicon/silicon carbide composites fabricated by infiltration of a silicon melt into charcoal. Journal of the American Ceramic Society 82, 3251-3253.

39. Sieber H., Hoffmann C, Kaindl A., and Greil P., 2000. Biomorphic cellular ceramics. Advanced Engineering Materials 2, 105-109.

40. Singh M., 2000. Environment conscious ceramics (ecoceramics). Ceramic Engineering and Science Proceedings 21, 39-44.

41. Singh M. and Salem J.A., 2002. Mechanical properties and microstructure of biomorphic silicon carbide ceramics fabricated from wood precursors. Journal of the European Ceramic Society 22, 2709-2717.

42. Zollfrank C. and Sieber H., 2004. Microstructure and phase morphology of wood derived biomorphous SiSiC-ceramics. Journal of the European Ceramic Society 24, 495-506.

43. Esposito, L., Sciti D., PiancastelliA., Bellosi A, 2004. Microstructure and properties of porous β-SiC templated from soft woods. Journal of the European Ceramic Society 24 533-540.

44. Vogli E., Mukerji J., Hoffman C., Kladny R., Sieber H., and Greil P., 2001. Conversion of oak to cellular silicon carbide ceramic by gas-phase reaction with silicon monoxide. Journal of the American Ceramic Society 84, 1236-1240.

45. Vogli E., Sieber H., and Greil P., 2002. Wood derived porous and cellular ceramics. Ceramic Engineering and Science Proceedings 23, 211-218.

46. Qian J.M., Wang J.P., and Jin Z.H., 2003. Preparation and properties of porous microcellular SiC ceramics by reactive infiltration of Si vapor into carbonized basswood. Materials Chemistry and Physics 82, 648-653.

47. Vogt, U., Herzog, and A. Graule T., 2004. Biomorphic SiC structures from composites by carbothermal reduction of silica-sol infiltrated carbonized wood, in: High Temperature Ceramic Matrix Composites HTCMC-5, Ed.: M. Singh, R.J. Kerans, E. Lara-Curcio and R. Naslain, The American Ceramic Society, 413-418.

48. Ota T., Takahashi M., Hibi T., Ozawa M., Suzuki S., and Hikichi Y., 1995. Biomimetic process for producing SiC "wood". Journal of the American Ceramic Society 78, 3409-3411.

49. Klingner R., Sell J., Zimmermann T., Herzog A., Vogt U., Graule T., Thurner P. Beckmann F. and Müller B., 2003. Wood-derived porous ceramics via infiltration of $SiO_2$-sol and carbothermal reduction. Holzforschung 57, 440-446.

50. Herzog A., Klingner R., Vogt U. and Graule T., 2004. Wood-derived porous SiC ceramics by sol infiltration and carbothermal reduction. Journal of the American Ceramic Society 87, 784-793.

51. Vogt U., Herzog A., Klingner R., 2002. Porous SiC ceramics with oriented structure from natural materials. Ceramic Engineering and Science Proceedings 23, 219-226.

52. Qian J.M., Wang J. P., Qiao G.J., and Jin Z. H., 2004. Preparation of porous SiC ceramic with a woodlike microstructure by sol-gel and carbothermal reduction processing. Journal of the European Ceramic Society 24, 3251-3259.

53. Lange F. F., Velamakanni B.V. and Evans A. G., 1990. Method for processing metal-reinforced ceramic composites. Journal of the American Ceramic Society 73, 388-393.

54. Brown D., Green D., 1994. Investigation of strut crack formation in open cell alumina ceramics. Journal of the American Ceramic Society 77, 1467-1472.

55. Breslin M.C., Ringnalda J., Xu L., Fuller M., Seeger J., Daehn G.S., Otani T., Fraser H. L., 1995. Processing, microstructure, and properties of co-continuous alumina-aluminum composites. Materials Science and Engineering A 195, 113-119.

56. Newkirk M.S., Lesher H. D., White D. R., Kennedy C. R., Urquhart A. W. and Claar T. D., 1987. Preparation of Lanxide™ ceramic matrix composites: Matrix formation by the directed oxidation of molten metals. Ceramic Engineering Proceedings 8, 879-885.

57. Prielipp Helge, Knechtel Mathias, Claussen Nils, Streiffer S. K., Müllejans H., Rühle M., Rödel Jürgen. 1995. Strength and fracture toughness of aluminum/alumina composites with interpenetrating networks. Materials Science and Engineeing A 197, 19-30.

58. Mattern A., Huchler B., Staudenecker D., Oberacker R., Nagel A., Hoffmann M. J., 2004. Preparation of interpenetrating ceramic-metal composites. Journal of the European Ceramic Society 24, 3399-3408.

59. Yi H. C., Moore J. J. 1990. Review self-propagating high-temperature (combustion) synthesis (SHS) of powder-compacted materials. Journal of Materials Science 25, 1159-1168.

60. Melcher R., Martins S., Travitzky N., Greil P., 2006. Fabrication of $Al_2O_3$-based composites by indirect 3D-printing. Materials Letters 60, 572-575.

61. Green David., 2004. Bio-inspired ceramic structures: from invertebrate marine skeletons to biomimetic crystal engineering. Journal of the Australasian Ceramic Society 40, 1-6.

62. White, R. A., Weber, J.N., and White E. W. 1972. Replamineform, a new process for preparing porous ceramic, metal and polymer prosthetic materials. Science 176, 922-924.

63. Skinner D. P., Newnham R.E. and Cross L.E., 1978. Flexible composite transducers. Materials Research Bulletin 13, 599-607.

64. Chen L. G., Shue K. H., Chang S. Y., Lin S. J. 2002. Squeeze casting of $SiC_P$/Al-alloy composites with various contents of reinforcements. Journal of Materials Research 17, 376-385.

65. Altinkok N., Demir A., Ozsert I. 2003. Processing of $Al_2O_3$/SiC ceramic cake preforms and their liquid Al metal infiltration. Composites Part A, 34, 577-582.

66. Xi X. M., Yang X. F. 1996. Spontaneous infiltration of aluminum-silicon alloy into silicon carbide preforms in air. Journal of the American Ceramic Society 79, 102-108.

67. Chung W. S., Lin S. J. 1996. Ni-coated $SiC_P$ reinforced aluminum composites processed by vacuum infiltration. Materials Research Bulletin 31, 1437-1447.

68. David R. Clarke, 1992. Interpenetrating phase composites. Journal of the American Ceramic Society 75, 739-759.

69. Peng H. X., Fan Z., Evans J. R. G., 2000. Novel MMC microstructures prepared by melt infiltration of reticulated ceramic preforms. Materials Science and Technology 16, 903-907.

70. Shouren Wang, Haoran Geng, Jingchun Zhang, Yingzi Wang, 2006. Interpenetrating microstructure and properties of $Si_3N_4$/Al-Mg composites fabricated by pressureless infiltration. Applied Composite Materials 13, 115-126.

71. Moon R. J., Tilbrook M., Hoffman M., 2005. Al-$Al_2O_3$ composites with interpenetrating network structures: composite modulus estimation. Journal of the American Ceramic Society 88, 666-674.

72. Leohman E. R., Ewsuk K. and Tomsia P. A., 1996. Synthesis of $Al_2O_3$-Al composites by reactive metal penetration. Journal of the American Ceramic Society 79, 27-32.

73. Chen M.Y., Breslin M. C., 2002. Friction behavior of co-continuous alumina/aluminum composites with and without SiC reinforcement. Wear 249, 868-876.

74. La Vecchia G. M., Badini C., Puppo D., D'Errico F., 2003. Co-continuous Al/ $Al_2O_3$ composite produced by liquid displacement reaction: relationship between microstructure and mechanical behavior. Journal of Materials Science 38, 3567-3577.

75. Pavese Matteo, Valle Massimiliano, Badini Claudio, 2007. Effect of porosity of cordierite preforms on microstructure and mechanical strength of co-continuous ceramic composite. Journal of the European Ceramic Society 27, 131-141.

76. Aghajanian M. K., Macmillan N. H., Kennedy C. R., Luszcz S. J., Roy R., 1989. Properties and microstructure of Lanxide® $Al_2O_3$-Al ceramic composite materials. Journal of Materials Science 24, 658-670.

77. Etter T., Kuebler J., Frey T., Schulz P., Löffler J. F., Uggowitzer P. J., 2004. Strength and fracture toughness of interpenetrating graphite/aluminum composites produced by the indirect squeeze casting process. Materials Science and Engineeering A 386, 61-67.

78. Zeschky J., Jason Lo, Thomas H., Peter G., 2005. Mg alloy infiltrated Si-O-C ceramic foams. Materials Science and Engineering A 403, 215-221.

79. Balch D. K., Fitzgerald T. J., Michaud V. J., Mortensen A., Shen Y. L., Suresh S., 1996, Thermal expansion of metals reinforced with ceramic particles and microcellular foams. Metallurgical and Materials Transactions 27A, 3700-3717.

80. Travitzky N. A., 2001. Effect of metal volume fraction on the mechanical properties of alumina/aluminum composites. Journal of Materials Science 36, 4459-4463.

81. Etter T., Papakyriacou M., Schulz P., Uggowitzer P. J. 2003. Physical properties of graphite/aluminum composites produced by gas pressure infiltration method. Carbon 41, 1017-1024.

82. Yi H. C., Moore J. J. 1990. Review self-propagating high-temperature (combustion) synthesis (SHS) of powder-compacted materials. Journal of Materials Science 25, 1159-1168.

83. Travitzky N., Gotman I., Claussen N., 2003. Alumina-Ti aluminide interpenetrating composites: microstructure and mechanical properties. Materials Letters 57, 3422-3426.

84. Sachs E., Cima M., Williams P., Brancazio D., Cornie J., 1992. Three dimensional printing: rapid tooling and prototypes directly froma CAD model. Journal of Engineering for Industry. 114, 481-488.

85. Frank W. Ewers, Jack B. Fisher, 1989. Techniques for measuring vessel lengths and diameters in stems of woody plants. American Journal of Botany 76 5 645-656.

86. ASM Metals Handbook, Properties and selection-nonferrous alloys and special-purpose materials. 2000. ASM International volume 2.

87. Ultramet Advanced Materials Solutions. Ultramet™ "UltraCat" open-celled silicon carbide foam property data sheet. 12173 Montague Street Pacoima, California 91331, USA.

88. Bertrand S., Droillard C., Pailler R., Bourrat X., Naslain R., 2000. TEM structure pf (PyC/SiC) multilayered interphases in SiC/SiC composites. Journal of the European Ceramic Society 20 pp.1-13.

89. Cowlard F. C., Lewis J. C. 1967. Vitreous carbon-a new form of carbon. Journal of Materials Science 2 507-512.

90. Jitendra S Goela, Mechael A Pickering et al. 1991. Properties of chemical-vapor-deposition silicon carbide for optics applications in severe environments. Applied Optics 30 [22] 3166-3175.

91. Paccaud O. Derre A. 1995. Silicon carbide coating for carbon materials produced by a pack-cementation process. Journal de Physique IV, Colloque C5, supplement au Journal de Physique II, Volume 5 135-142.

92. Standard Test Methods for Apparent Porosity, Water Absorption, Apparent Specific Gravity, and Bulk Density of Burned Refractory Brick and Shapes by Boiling Water," ASTM Specification C20–00. American Society for Testing and Materials, West Conshohocken,PA.

93. Hashim J., Looney L. and Hashmi M.S.J. 2001. The wettability of SiC particles by molten aluminum alloy. Journal of Materials Processing Technology 119 324-328.

94. Laurent V., Chatain D., Eustathopoulos N., 1987 Wettability of SiC by aluminum and Al-Si alloys. Journal of Materials Science 22 244-250.

95. Han Do-Suck, Jones H., Atkinson H. V. 1993. The wettability of silicon carbide by liquid aluminum: the effect of free silicon in the carbide and of magnesium, silicon and copper alloy additions to the aluminum. Journal of Materials Science 28 2654-2658.

96. Lloyd D. J. 1994. Particle reinforced aluminum and magnesium matrix composites. International Materials Reviews 39 [1] 1-23.

97. Samuel A. M., Liu H., Samuel F. H. 1993. On the Catsability of Al-Si/SiC particle-reinforced metal-matrix composites: factors affecting fluidity and soundness. Composites Science and Technology 49 1-12.

98. Pech-Canul M. I., Katz R. N., Makhlouf M. M. 2000. The role of wetting and pressureless infiltration of SiCp preforms by aluminum alloys. Journal of Materials Science 35 2167-2173.

99. Quéré David 2002. Rough ideas on wetting. Physica A 313 32-46.

100. Washburn E. W. 1921. The Dynamics of Capillary Flow. The Physical Review 17 273-283.

101. Delannay F., Froyen L., Deruyttere A. 1987. Review: The wetting of solids by molten metals and its relation to the preparation of metal-matrix composites. Journal of Materials Science 22 1-16.

102. Xu Hanbing, Jian Xiaogang, Meek T. T., Han Qingyou. 2004. Degassing of molten aluminum A356 alloy using ultrasonic vibration. Materials Letters 58 3669-3673.

103. John E. Hatch, Aluminum: Properties and Physical Metallurgy, Metals Park, Ohio, p. 235.

104. Glenn O. Mallory, Juan B. Hajdu, Electroless plating: fundamentals and applications published by American Electroplaters and Surface Finishers Society Orlando, Fla.: The Society, 1990, p.101 and 11-12.

105. Leon C. A., Drew R.A.L. 2002. The influence of nickel coating on the wettability of aluminum on ceramics. Composites: Part A 33 1429-1432.

106. Leon C. A., Drew R.A.L. 2000. Preparation of nickel-coated powders as precursors to reinforce MMCs. Journal of Materials Science 35 4763-4768.

107. Garcia-Cordovilla C., Louis E, Narciso J. 1999. Pressure infiltration of packed ceramic particulates by liquid metals. Acta Materiala 47 18 4461-4479.

108. Hu J., Luo R.S., Fei D., Yao C. K. 1999. Effect of annealing treatment on the microstruture of matrix in SiC whiskers reinforced aluminum composite. Journal of Materials Science Letters 18 1525-1527.

109. Prangnell P.B., Downes T., Withers P.J. Stobbs W. M. 1994. The deformation of discontinuously reinforced MMCs-II The elastic response. Acta Metallurgica et Materialia 42 3437-3442.

110. ASTM C1161-02C "Standard test method for flexural strength of advanced ceramics at ambient temperature". American Society for Testing and Materials Annual Book of Standards, Vol. 15.01, ASTM, West Conshohocken, PA, 2002.

111. Bengisu M., "Engineering Ceramics" Springer, New York, 2001. p 214-216.

112. ASTM E23-02a, "Standard Test Method for Notched Bar Impact Testing of Metallic Materials", American Society for Testing and Materials Annual Book of Standards, Vol. 3.01, ASTM, West Conshohocken, PA, 2002.

113. Badini C., La Vecchia M., Giurcanu A., Wenhui J. 1997. Damage of 6061 SiC composite by thermal cycling. Journal of Materials Science 32 921-930.

114. Oliver W. C., Pharr G. M. 1992. An improved technique for determining hardness and elastic modulus using load and displacement sensing indentation experiments. Journal of Materials Research. 7 [6] 1564-1582.

115. Kwon Y. W., Cooke R. E., Park C. 2003. Representative unit-cell models for open-cell metal foams with or without elastic filler. Materials Science and Engineering A343 63-70.

116. Feng X. Q., Tian Zhi, Liu Y.H. Yu S. W. 2004. Effective elastic and plastic properties of interpenetrating multiphase composites. Applied Composite Materials 11 33-55.

117. Voigt W. 1889. Ueber die beziehung zwischen den beiden elasticitätsconstanten isotroper körper. Annals of Physics 38 573-585.

118. Reuss A. 1929. Berechnung der fließgrenze on mischkristallen auf grund der plastizitätbedindingungen für einkristall. Journal of Applied Mathematics and Mechanics 9 49-58.

119. Krenchel H. 1964. Fibre Reinforcement Akademisk Forlag, Copenhagen, Denmark.

120. Hashin Z., Shtrikman S. 1963. A variational approach to the theory of elastic behavior of multiphase materials, Journal of Mechanics and Physics of Solids 11 127-140.

121. Coble R.L., Kingery W. D. 1956. Effect of porosity on physical properties of sintered alumina. Journal of the American Ceramic Society 39 377-385.

122. Cohen L. J. and Ishai O. 1967. The elastic properties of three-phase composites. Journal of Composite Materials 1 390-403.

123. Vipulanandan C., Dharmarajan N., Ching E. 1988. Mechanical behaviour of polymer concrete systems. Materials and Structures 21 268-277.

124. Christian J. L. and Campbell M. D. 1972 In: Timmerhaus, K (editor), Proceedings of the 1972 Cryogenic Engineering Conference, Advances in Cryogenic Engineering, vol, 18. Plenum Press, p 175-183, National Bureau of Standards, Boulder Colorado August 9-11, 1972.

125. Thornburgh J. D. and Pears C. D. 1965 Prediction of the thermal conductivity of filled and reinforced plastics. In: ASME Heat Transfer Division, Winter Annual Meeting, 65-WA/HT-4.

126. Wang J., Carson J. K., North M. F., Cleland D. J., 2006. A new approach to modeling the effective thermal conductivity of heterogeneous materials. International Journal of Heat and Mass Transfer 49 3075-3083.

127. Hsieh C. L., Tuan W. H. 2007. Thermal expansion behavior of a model ceramic-metal composite. Materials Science and Engineering A 460-461, 453-458.

128. Rambo C. R., Cao J., Rusina O., Sieber H. 2004. Manufacturing of biomorphic (Si, Ti, Zr)-carbide ceramics by sol-gel processing. Carbon 43 1174-1183.

129. Zhurinsh A., Locs J., Berzina-Cimdina L. 2009. Investigation of the feasibility of pyrolytic obtaining of porous biomorphic SiC ceramics. Journal of Analytical and Applied Pyrolysis 85 544-548.

130. Cheung Teresa L. Y., Ng Dickon H. L. 2007. Conversion of bamboo to biomorphic composites containing silica and silicon carbide nanowires. Journal of the American Ceramics Society 90 559-564.

131. Vyshnyakova K., Yushin G., Pereselentseva L., Gogotsi Y. 2006. Formation of porous SiC ceramics by pyrolysis of wood impregnated with silica. International Journal of Applied Ceramic Technology 3 485-490.

132. Hata T., Castro V. Fujisawa M., Imamura Y. Bonnamy S., Bronsveld P., Kikuchi H. 2005. Formation of silicon carbide nanorods from wood-based carbons. Fullerenes, nanotubes, and Carbon Nanostructures 13 107-113.

133. Shin Y., Wang C., Exarhos G. J. 2005. Synthesis of SiC ceramics by carbothermal reduction of mineralized wood and silica. Advanced Materials 17 73-77.

134. Qian J., Wang J., Hou G., Qiao G. Jin Z. 2005. Preparation and characterization of biomorphic SiC hollow fibers from wood by chemical vapor infiltration. Scripta Materialia 53 1363-1368.

135. Xu S., Qiao G., Wang H., Li D., Lu T. 2008. Preparation of aligned silicon carbide whiskers from porous carbon foam by silicon thermal evaporation. Materials Letters 62 4549-4551.

136. Krstic V. D., 1992. Production of Fine, High-Purity Beta Silicon Carbide Powders. Journal of the American Ceramics Society 75 [1] 170-174.

137. Filsinger D. H., Bourrie D. B., 1990. Silica to Silicon: Key Carbothermic Reactions and Kinetics. Journal of the American Ceramics Society 73 [6] 1726-1732.

138. Narciso-Romero F.J., Rodriguez-Reinoso F., Diez M.A. 1999. Influence of the carbon material on the synthesis of silicon carbide. Carbon 37 1771-1778.

139. Belmonte T., Bonnetain L., Ginoux J. L. 1996. Synthesis of silicon carbide whiskers using vapour-liquid-solid mechanism in a silicon-rich droplet. Journal of Materials Science 31 2367-2371.

140. Kuo S. Y., Virkar A. V. 1987. Modulated structures in SiC-AlN ceramics. Communications of the American Ceramic Society 70 125-128.

141. Johnson J.A., Hrenya C. M., Weimer A. W. 2002. Intrinsic reaction and self-diffusion kinetics for silicon carbide synthesis by rapid carbothermal reduction. Journal of the American Ceramics Society 85 2273-2280.

142. Kim J. W., Myoung S. W., Kim H. C., Lee J. H., Jung Y. G., Jo C. Y. 2006. Synthesis of SiC microtubes with radial morphology using biomorphic carbon template. Materials Science and Engineering A 434 171-177.

143. Rijswik W. V., Shanefield D. J. 1990. Effect of carbon as a sintering aid in silicon carbide. Journal of the American Ceramics Society 73 148-149.

144. Singhal S. C. 1976. Oxidation kinetics of hot-pressed silicon carbide. Journal of Materials Science 11 1246-1253.

145. Mergia K., Lafatzis D., Moutis N., Speliotis T., Apostolopoulos G., Cousin F. 2008. Oxidation behavior of SiC coatings. Applied Physics A: Materials Science & Processing. A92 387-395.

146. Westwood M.E., Webster J. D., Day R. J., Hayes F. H., Taylor R. 1996. Review Oxidation protection for carbon fibre composites. Journal of Materials Science 31 1389-1397.

147. Wimmer R., Grabner M. 2000. A comparison of tree-ring features in picea abies as correlated with climate. IAWA Journal 21 403-416.

148. Dougherty P.M., Whitehead D., Vose J. M. 1994. Environment influences on the phenology of pine. Ecological Bulletins 43 64-75.

149. Wang J. Z., DeGroot R. 1996. Treatability and durability of heartwood, Gen. Tech. Report FPL-GTR-94. Forest Products Lab., Madison, WI, USA. p 252–260.

150. Hargrave K. R., Kolb K. J., Ewers F. W. Davis S. D. 1994. Conduit diameter and drought-induced embolism in Salvia mellifera Greene (Labiatae). New Phytologist 126 695-705.

151. Sperry J. S., Tyree M.T. 1988. Mechanism of water stress-induced xylem embolism. Plat Physiology 88 581-587.

152. Smith W. B. 1986. Treatability of several northern species with chromate copper arsenate wood preservative. Forest Products Journal 36 63-69.

153. Whalen T. J., Anderson A.T. 1975. Wetting of SiC $Si_3N_4$, and carbon by Si and binary Si alloys. Journal of the American Ceramics Society 58 396-399.

154. Zhou H., Singh R. N. 1995. Kinetics model for the growth of silicon carbide by the reaction of liquid silicon with carbon. Journal of the American Ceramics Society 78 2456-2462.

155. Kaufman J. G. 2004. Aluminum alloy castings: properties, processes, and applications. Materials Park, OH: ASM International 49-54.

156. Suh D., Eagar T. W. 1998. Mechanistic understanding of hydrogen in steel welds. Proceedings of International Workshop Conference on Hydrogen Management for Welding Applications, Ottawa, Ontario, Canada 6-8 Oct. 105-110.

157. Sahin Y., Acilar M. 2003. Production and properties of SiCp-reinforced aluminum alloy composites. Composites: Part A 34 709-718.

158. Ahson J. P., gruzleski J. E. 1999. The quantitative discrimination between shrinkage and gas microporosity in cast aluminum alloys using spatial data analysis. Materials Characterization 43 319-335.

159. Flannery F. A., Mourlas N. J., Storment C. W., Tsai S., Tan S. H., Heck J., Monk D., Kim T., Gogoi B. Kovacs G.T.A. 1998. PECVD silicon carbide as a chemically resistant material for micromachined transducers. Sensors and Actuators A 70 48-55.

160. Wang Zhirui, Zhang Ruby J. 1991. Mechanical behavior of cast particulate SiC/Al (A356) metal matrix composites. Metallurgical Transactions 22A 1585-1593.

161. Diss Pascal, Lamon Jacque, Carpentier L., Loubet J. L., Kapsa Ph. 2002. Sharp indentation behavior of carbon/carbon composites and varieties of carbon. Carbon 40 2567-2579.

162. Bellan C., Dhers J. 2004. Evaluation of Young modulus of CVD coatings by different techniques. Thin Solid Films 469-470, 214-220.

163. ASTM E 407-99 "Standard Practice for Microetching Metals and alloys". American Society for Testing and Materials Annual Book of Standards, Vol. 3.01, ASTM, West Conshohocken, PA, 1999.

164. Shackelford J. F., Alexander W. 2001. CRC Materials Science and Engineering Handbook, Second Edition, Boca Raton, FL: CRC Press p 46 and p 507-508.

165. Rohatgi P. K., Kim J. K., Gupta N., Alaraj Simon, Daoud A. 2006. Compressive characteristics of A356/fly ash cenosphere composites synthesized by pressure infiltration technique. Composites Part A 430-437.

166. Hsu Chia-Wen, Chao Chuen-Guang 2002. Effect of heat treatments on in-situ $Al_2O_3/TiAl_3$ composites produced from squeeze casting of $TiO_2$/A356 composites. Metallurgical and Materials Transactions 33B 31-40.

167. Premhmar M. K. 1997. Al/SiC for Power Electronics Packaging, International Symposium on Advanced Packaging Materials. Alcoa Composite Components, Alcoa Center, PA, March 9-12, 162-165.

168. Olivier Beffort, Siyuan Long, Cyril Cayron, Jakob Kuebler, Philippe-André Buffat 2007. Alloying effects on microstructure and mechanical properties of high volume fraction SiC-particle reinforced Al-MMCs made by squeeze casting infiltration. Composites Science and Technology 67 737-745.

169. Jaromi S.A. Jenabali, Dehghan A., Malekjani S. 2004. Effects of optimum amount of Sr and Sb modifiers on tensile, impact and fatigue properties of A356 aluminum alloy. Iranian Journal of Science & Technology, Transaction B 28, 225-232.

170. Overfelt R. A., Bakhtiyarov S. I., Taylor R. E. 2002. Thermophysical properties of A201, A319, and A356 aluminum casting alloys. High Temperatures-High Pressures 34 401-409.

171. Cheng Laifei, Xu Yongdong, Zhang Qing, Zhang Litong. 2003. Thermal diffusivity of 3D C/SiC composites from room temperature to 1400°C. Carbon 41 707-711.

172. Miranzo P., Osendi M.I. 2008. Thermal conductivity of $ZrO_2$-Ni functionally graded coatings. Scripta Materialia 58 973-976.

173. Zhao H. F., Tang W. Z., Li C. M., Chen G.C., Lu F.X., Cai Y. X., Guo H., Zhang R. Q., Zhang P.W., 2008. Thermal conductivity properties of Ni-P electroless plated $SiC_p$/Al composite electronic packaging material. Surface & Coatings Technology 202 2540-2544.

174. Deshayes Y., Bechou L., Danto Y., Laffitte D., Goudard J. L. 2002. Three-dimensional FEM simulations of thermomechanical stresses in 1.55μm laser modules. Physical and Failure Analysis of Integrated Circuits, 2002. IPFA 2002. Proceedings of the 9th International Symposium. 8-12 July 2002.

175. Viswanathan S., Ren W., Porter W. D., Brinkman C. R., Sabau A. S., Purgert R. M. 1995. Metal compression forming of aluminum alloys and metal matrix composites. Oak Ridge National Laboratory, CRADA Number ORNL95-0363.

176. Tsuno Katsuhiko, Irikado Hiroshi, Hamada Kazuo, Kazuhiko Ohno, Ishida Juro, Suyama Shoko, Itoh Yoshiyasu, Ebizuka Noboru, Eto Hiroaki, Dai Yutang, 2004. Reaction-sintered silicon carbide: newly developed material for lightweight mirrors. Proceedings of the 5th International Conference on Space Optics (ICSO 2004), 30 March- 2 April 2004 Toulouse, France.

177. Kowbel W., Champion W., Withers J. C., Shih Wei, 2000. Low cost, high thermal conductivity composite heat spreaders for power electronics. Semiconductor Thermal Measurement and Management Symposium, Sixteenth Annual IEEE 21-23 March.

178. Lemieux S., Elom S., Nemes Ri J., Skibo M. D.. 1998. Thermal expansion of isotropic Duralcan metal-matrix composites. Journal of Materials Science 33 4381-4387.

179. Kollie T. G. 1977. Measurement of the thermal-expansion coefficient of nickel from 300 to 100K and determination of the power-law constants near the Curie temperature. Physical Review B 16 4872-4881.

180. Vogelsang Mary, Arsenault R. J., Fisher R. M. 1986. An in-situ HVEM study of dislocation generation at Al/SiC interfaces in metal matrix composites. Metallurgical Transactions A 17 379-389.

181. Daehn G. S., Starck B., Xu L., Elfishawy K. F., Ringnalda J., Fraser H. L. 1996. Elastic and plastic behavior of a co-continuous alumina/aluminum composite. Acta Materials 44, 249-261.

182. Shinzato K., Baba T. 2001. A laser apparatus for thermal diffusivity and specific heat capacity measurements. Journal of Thermal Analysis and Calorimetry 64 413-422.

183. Barea R., Belmonte M., Osendi M. I., Miranzo P. 2003. Thermal conductivity of $Al_2O_3$/SiC platelet composites. Journal of the European Ceramic Society 23 1773-1778.